UNIVERSITÀ
DEGLI STUDI
DI PADOVA

Sede Amministrativa: Università degli Studi di Padova

Dipartimento di Scienze Chimiche

SCUOLA DI DOTTORATO DI RICERCA IN: SCIENZE MOLECOLARI
INDIRIZZO: SCIENZE CHIMICHE
CICLO XXV

SINTESI E CARATTERIZZAZIONE DI FERRITI NANOSTRUTTURATE

Direttore della Scuola: Ch.mo Prof. Antonino Polimeno
Coordinatore d'indirizzo: Ch.mo Prof. Antonino Polimeno
Supervisore: Dott.ssa. Silvia Gross

Dottorando: Stefano Diodati

Dedicated to the memory of Don Pietro Pengo

(17/11/1926-02/12/2009)

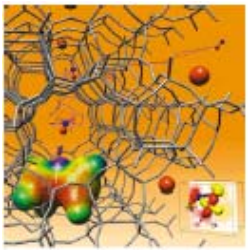

University of Padova

Ph.D. School in Molecular Sciences

Sintesi e caratterizzazione di ferriti nanostrutturate

Synthesis and characterisation of nanostructured ferrites

Student – Stefano Diodati

Advisor – Dr. Silvia Gross

In this thesis, the synthesis of transition and/or metal iron ferrite systems (both in the spinel MFe_2O_4 and perovskite $MFeO_3$ form) through wet-chemistry synthetic routes was explored.

Three specific routes were employed: i) nonaqueous sol-gel synthesis, ii) coprecipitation of oxalates from an aqueous solution and iii) hydrothermal synthesis coupled with oxalate coprecipitation. All three routes successfully allowed to synthesise iron ferrites (though the nature and characteristics of the prepared compounds varied depending on the chosen method).

The spinel ferrites $CoFe_2O_4$, $MgFe_2O_4$, $MnFe_2O_4$, $NiFe_2O_4$ and $ZnFe_2O_4$, as well as the perovskites $MnFeO_3$ and $SrFeO_{3-\delta}$ were obtained as crystalline powders. All powders (except $MgFe_2O_4$) were obtained as pure, single-phase compounds.

The obtained materials were then characterised through a wide array of techniques from the compositional, structural and functional points of view. In particular, bulk atomic ratios were investigated trough ICP-AES (Inductively Coupled Plasma-Atomic Emission Spectroscopy) and compared with surface composition explored through XPS (X-ray Photoelectron Spectroscopy). TGA-DSC (ThermoGravimetric Analysis-Differential Scanning Calorimetry) and microanalysis allowed to study the evolution of the system during calcination and to evaluate the presence of residual organic moieties (from the synthesis precursors) in the materials. XRD (X-Ray Diffraction) and TPXRD (Temperature-Programmed XRD) were employed to investigate powder structure and to calculate average crystallite sizes (through Rietveld refinement), and the data thus obtained was compared with micrographs collected through TEM (Transmission Electron Microscopy). In parallel, XPS, Mössbauer spectroscopy and TPR (Temperature Programmed Reduction) afforded information on the oxidation states and chemical environments of the elements in the material (both in bulk and on the surface).

In the case of spinel ferrites, Mössbauer spectroscopy was particularly useful as it allowed to calculate the degree of inversion of the compounds.

From a functional point of view, SQUID (Superconducting Quantum Interference Device) measurements were employed to study the magnetic properties of the materials, revealing that the cobalt and manganese spinels displayed ferrimagnetic behaviour (as expected), whereas the manganese perovskite was paramagnetic above 35 K (Néel temperature) and displayed ferrimagnetic behaviour below that temperature. Electric characterisations to gain insight on the conduction properties of the materials were carried out through BES (Broadband Electric Spectroscopy). These measurements revealed relaxations at 30 and 90°C in the cobalt and nickel spinels which are compatible with water intercalation within the crystal structure. As far as the manganese perovskite is concerned, the relaxations at 100°C and higher conductivity displayed

compared to the spinels are compatible with ionic conduction. The catalytic activity was investigated through temperature-programmed oxidation of methane (CH_4-TPO), showing that the synthesised cobalt, manganese, magnesium and nickel ferrites were active in the oxidation of methane to carbon dioxide, despite not being stable over several cycles.

The effect of synthetic parameters (such as nature of the precursors, additives, thermal treatment parameters, aging time etc.) on the final structural and compositional nature of the oxides was the object of particular interest.

Based upon the results obtained from these investigations, the synthetic protocols for each route were optimised in order to maximise product purity and yield, as well as to improve synthetic conditions; in particular, efforts were made to lower treatment temperatures and shorten treatment times whilst suffering no losses in terms of product yield and quality. In particular, hydrothermal syntheses of the nickel, cobalt, zinc and manganese spinels were successfully carried out at 75°C with a 4 hour treatment.

In addition, the possible application of the coprecipitation of oxalates from an aqueous solution method to prepare iron ferrites containing two metals was explored: the $Co_{0.5}Mn_{0.5}Fe_2O_4$, $Co_{0.5}Mg_{0.5}Fe_2O_4$ and $Co_{0.5}Mn_{0.5}FeO_3$ systems were successfully prepared and characterised. Measurement of bulk atomic ratios between the three metals in each mixed-metal ferrite (i.e. Co, Fe and either Mg or Mn) revealed that the chosen synthetic route afforded good control over the final stoichiometry of the prepared materials.

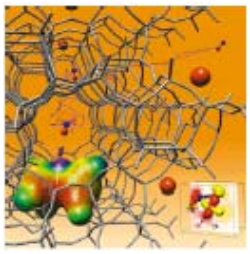

Università degli Studi di Padova

Scuola di Dottorato in Scienze Molecolari

Sintesi e caratterizzazione di ferriti nanostrutturate

Studente – Stefano Diodati

Supervisore – Dott.ssa Silvia Gross

In questa tesi è stata esplorata la sintesi di sistemi di ferriti contenenti ferro e uno o più metalli di transizione o alcalino terrosi (sia in forma di spinello MFe_2O_4 che di perovskite $MFeO_3$) tramite metodi di sintesi per via umida.

Sono state impiegate tre specifiche metodologie di sintesi: i) sintesi sol-gel non acquosa ii) coprecipitazione di ossalati da una soluzione acquosa e iii) sintesi idrotermale accoppiata alla coprecipitazione di ossalati. Tutti e tre i metodi hanno permesso di sintetizzare con successo ferriti di ferro (per quanto la natura e le caratteristiche dei composti preparati siano variati in base alla tipologia di sintesi scelta).

Sono stati ottenuti gli spinelli $CoFe_2O_4$, $MgFe_2O_4$, $MnFe_2O_4$, $NiFe_2O_4$ e $ZnFe_2O_4$, oltre alle perovskiti $MnFeO_3$ e $SrFeO_{3-\delta}$. Tutti i prodotti sono stati ottenuti come polveri cristalline e (con l'eccezione di $MgFe_2O_4$), sotto forma di una singola fase cristallina.

I materiali sintetizzati sono stati successivamente caratterizzati, tramite una vasta gamma di tecniche, dal punto di vista composizionale, strutturale e funzionale. In particolare, il rapporto stechiometrico massivo tra i metalli nei composti è stato studiato tramite ICP-AES (Inductively Coupled Plasma-Atomic Emission Spectroscopy) e confrontato con la composizione superficiale ottenuta tramite XPS (X-ray Photoelectron Spectroscopy). Si è fatto uso delle tecniche di microanalisi e TGA-DSC (ThermoGravimetric Analysis-Differential Scanning Calorimetry) per esplorare l'evoluzione del sistema durante la calcinazione, oltre a valutare la presenza di possibili residui organici (dovuti ai precursori utilizzati durante la sintesi) nei materiali. XRD (X-Ray Diffraction) e TPXRD (Temperature-Programmed XRD) sono stati impiegati per studiare la struttura cristallina delle polveri e per calcolare (tramite raffinamento Rietveld) le dimensioni medie dei cristalliti. I dati così ottenuti sono stati confrontati con le immagini acquisite tramite TEM (Transmission Electron Microscopy). Parallelamente, spettroscopia Mössbauer, XPS e TPR (Temperature Programmed Reduction) hanno fornito informazioni sugli stati di ossidazione degli elementi nei materiali (sia in superficie che nel massivo).

Nel caso delle ferriti in forma di spinello, la spettroscopia Mössbauer è stata particolarmente utile, in quanto ha permesso di calcolare il grado di inversione dei composti.

Dal punto di vista funzionale, misure SQUID (Superconducting Quantum Interference Device) sono state impiegate per studiare le proprietà magnetiche dei materiali, rivelando che gli spinelli di cobalto e manganese presentano (come previsto) un comportamento ferrimagnetico, mentre la perovskite di manganese ha comportamento paramagnetico sopra i 35 K (temperatura di Néel) e ferrimagnetico al di sotto di tale temperatura. Caratterizzazioni dielettriche per ottenere informazioni sulle proprietà di conduzione dei materiali sono state eseguite tramite BES (Broadband Electric Spectroscopy). Queste misure hanno

evidenziato rilassamenti a 30 e 90°C negli spinelli di cobalto e nichel, compatibili con l'intercalazione di acqua all'interno della struttura cristallina. Per quanto concerne la perovskite di manganese, i rilassamenti mostrati attorno a 100°C e la maggiore conducibilità rispetto agli spinelli sono compatibili con la conduzione ionica..

L'attività catalitica dei materiali è stata esplorata tramite l'ossidazione a temperatura programmata del metano (CH_4-TPO), mostrando che le ferriti sintetizzate contenenti cobalto, manganese e nichel sono attive nell'ossidazione del metano ad anidride carbonica, pur non essendo stabili nel corso di cicli successivi.

L'effetto dei parametri di sintesi (quali la natura dei precursori, additivi, parametri termici, tempo di invecchiamento) sulla natura finale (composizionale e strutturale) degli ossidi prodotti è stato oggetto di particolare interesse.

Sulla base dei risultati ottenuti da questi studi, è stato possibile ottimizzare ciascun protocollo di sintesi allo scopo di massimizzare resa e purezza dei prodotti, oltre a migliorare le condizioni di sintesi. In particolare, uno degli scopi principali di questo processo di ottimizzazione è stato quello di abbassare le temperature di trattamento e ridurre i tempi di trattamento termico, senza che al contempo questo causasse perdite dal punto di vista della resa e della qualità dei prodotti. In particolare è stato possibile sintetizzare gli spinelli di cobalto, manganese, nichel e zinco per via idrotermale a 75°C con un trattamento di 4 ore.

È stata inoltre esplorata la possibilità di applicare il metodo della coprecipitazione degli ossalati da una soluzione acquosa alla preparazione di ferriti di ferro contenenti due metalli. Sono stati sintetizzati con successo, e successivamente caratterizzati, i sistemi $Co_{0.5}Mn_{0.5}Fe_2O_4$, $Co_{0.5}Mg_{0.5}Fe_2O_4$ e $Co_{0.5}Mn_{0.5}FeO_3$. La misura dei rapporti stechiometrici massivi tra i metalli in ciascuna ferrite (vale a dire Co, Fe e Mg o Mn) ha mostrato che il metodo di sintesi scelto permette un buon controllo sulla stechiometria finale dei materiali preparati.

List of acronyms

acac - Acetylacetonate [$CH_3COCHCOCH_3^-$]
BES - Broadband Electric Spectroscopy
B.E. - Binding Energy
ccp - cubic closed pack
CH_4-TPO - Temperature Programmed Methane Oxidation
COD - Crystallography Open Database
dc - Direct Current
DICVOL DIChotomy method using VOLume space
DSC - Differential Scanning Calorimetry
EM - ElectroMagnetic
ESCA - Electron Spectroscopy for Chemical Analyses
EXAFS - Extended X-Ray Absorption Fine Structure
fcc - face centre cubic
FWHM - Full Width at Half-Maximum
ICP-AES - Inductively Coupled Plasma - Atomic Emission Spectroscopy
IR - Infra Red
MAUD - Materials Analysis Using Diffraction
MEEM - Maximum Entropy Electron Maps
MRI - Magnetic Resonance Imaging
OAc - acetate [CH_3COO^-]
RF - Radio Frequency
RIXS - Resonant Inelastic X-ray Scattering
RPM - Rotations Per Minute
RT - Room Temperature
SAED - Selected Area Electron Diffraction
SOFC - Solid Oxide Fuel Cells
SQUID - Superconducting Quantum Interference Device
TCD - Thermal Conductivity Detector
TENOH - Tetraethyl Ammonium Hydroxide
TGA - ThermoGravimetric Analysis
TPR - Temperature Programmed Reduction
TPXRD - Temperature Programmed X-Ray Diffraction
UHV - Ultra High Vacuum
UV - Ultra Violet
XAS - X-ray Absorption Spectroscopy
XPS - X-ray Photoelectron Spectroscopy
XRD - X-Ray Diffraction
XRPD - X-Ray Powder Diffraction

Index

1 - Introduction and goals of the thesis

In recent times, modern technology has been characterised by an ever-growing need for new functional materials, the properties of which make them invaluable in many different technological disciplines. Currently, many different fields make extensive use of various types of functional materials (organic, inorganic and hybrid) in order to produce better performing, safer, more sustainable and cheaper products. These fields can span the range from optics (where lenses can be enhanced in order to be thinner and more resistant), to electronics (for faster processors, smaller data storage devices, more sturdy components etc.), to medicine (both in diagnostic medicine and in therapy) and beyond.

In this context, transition metal oxides having either the spinel or the perovskite crystal structure, have been the topic of extensive studies and technological applications due to their relevant and different functional properties (catalytic, optical, electrical, magnetic, etc.) combined with their chemical, thermal and mechanical stability.[1-16]

In particular, among transition metal oxides in general, ferrites, having the general formula $M'_xM''_yO_z$ (M'= Mg, Ca, Sr, Ba, Mn, Fe, Co, Ni etc.; M''= Ti, Fe etc.), represent a class of inorganic materials which is currently experiencing a phase of great development for functional applications, and in particular for magnetic devices.[17-20] Moreover, ferrites currently attract considerable interest due to the interesting functional properties (magnetic, electrical, catalytic) that can be obtained by suitably varying their chemical composition, defectivity and structure.[21-30] The versatility and numerous properties displayed by ferrites, depending both on the structure and on the nature of the M' and M'' metals, make this class of materials suitable for application in an extremely wide variety of different fields, ranging from medicine,[31-34] to catalysis,[35, 36] to oxygen conducting devices,[37, 38] to electronics,[39] to magnetic devices.[17, 19, 32-34]

Since composition, defectivity and structure are closely related to chemical reactivity and functional properties, this important field was not ignored by the nanotechnology revolution. In fact, through the nanosizing of these oxides, innovative behaviours, such as the transition from ionic-electronic conductor to semiconductor, have already been highlighted.[40, 41]

In order to be able to satisfy the needs of modern technology, preparation methods need to be developed that enable the synthesis of the desired compound with a fine control over the compositional, structural and morphological features, and therefore over the properties (both structural and functional) of the final product. These synthesis methods must additionally be fine-tuned in order to optimise the procedure parameters and features (such as low temperatures, high yields, short reaction and treatment times, limited number of steps, limited use of hazardous or toxic complex equipment and ease of execution) whilst at the same time leaving the qualities of the final product unchanged.

Among the synthetic methodologies for the preparation of metal oxides, wet-chemistry routes are particularly appealing, since they afford to tailor the chemical features of the precursors and to use mild reaction conditions; in addition, they yield more uniform products and allow a greater control over a wide range of reaction parameters.[42-44]

In this thesis, the synthesis of mixed metal iron ferrites has been explored through different wet-chemistry methods. Three synthetic routes i.e. i) nonaqueous sol-gel synthesis, ii) coprecipitation of oxalates and iii) hydrothermal synthesis, and combination thereof, have been investigated and implemented.

The materials obtained as a pure crystalline phase were thoroughly analysed through a plethora of complementary techniques with the goal of correlating how the different synthetic parameters affected the different structural and chemical-physical features of the compounds. Such an understanding would enable, in a further step, a fine-tuning of the synthetic process based on the desired characteristics in the product, thus representing a powerful tool also in the scope of high-scale production planning.

A comprehensive characterisation of the systems was performed in this regard. In particular, microstructure and morphology of the prepared materials were investigated by means of Transmission Electron Microscopy (TEM) and powder X-Ray Diffraction (XRD); X-Ray Photoelectron Spectroscopy (XPS) was employed to obtain information on the surface composition and chemical environments of the species in the prepared samples, whereas bulk stoichiometry was assessed through Inductively Coupled Plasma - Atomic Emission Spectroscopy (ICP-AES). Furthermore, Temperature Programmed Reduction (TPR) and Mössbauer spectroscopy were used to shed light on the chemical environments and site geometry of the metals involved, as well as to perform an in-depth investigation on the iron atoms. Differential Scanning Calorimetry coupled with Thermogravimetric Analysis (DSC-TGA) was employed to study how the precursor compounds evolved during the calcination process. Concerning the assessment of the functional properties of the prepared oxides, in view of possible applications in various fields (catalysis, photocatalysis, electrical or magnetic devices), several functional investigations were carried out: methane oxidation measurements (CH_4-TPO) were performed to study the catalytic activity of the oxides; the magnetic behaviour of the synthesised oxides was explored through Superconducting Quantum Interference Device (SQUID) and Broadband Electric Spectroscopy (BES) was employed to assess their dielectric properties.

This thesis spans 7 chapters, the first one being the Introduction. In Chapter 2 the concept of *ferrite* will be described from a structural and functional point of view, as well as the main features and applications of these materials. Chapter 3 will be concerned with the description of the various synthetic protocols employed during this work for the preparation of ferrites. The advantages of wet chemistry routes over solid-state ones will be highlighted and an in-depth description of the three synthetic routes utilised in this Ph.D. thesis will be provided. In Chapter 4 the results concerning the chemico-physical, structural and functional characterisation of the prepared oxides will be presented and discussed. Furthermore, similar products obtained with different methods will be compared in detail and their properties correlated with both synthesis protocol and parameters. Chapter 5 will illustrate the experiments that have been carried out during this thesis and provide a detailed description of the synthesis protocols. Chapter 6 will portray the various analytical techniques employed for the characterisation of the obtained compounds. Finally, Chapter 7 will address the conclusions drawn from this research activity and present the perspectives disclosed by this work.

2 - Ferrites

2.1 - Main features of ferrites

The term *ferrite* is used to describes an extremely wide class of inorganic compounds having the general formula $M'_xM''_yO_z$ (M'=Fe, Ba, Ca, Co, Mg, Mn, Sr etc.; M''=Fe, Ti etc.) and endowed with interesting magnetic characteristics,[1-7, 10, 16, 17, 19] due to which the term ferrite is sometimes informally used to define ferrimagnetic ceramic materials in general.[45] In addition, ferrites also display numerous widely different properties depending on their composition and defectivity.[21-30]

Iron ferrites form a subclass of these materials characterised by the presence of iron as the M'' metal.[46-50] From a chemical point of view, an iron ferrite is defined as a metal oxide were iron is in an oxidation state of III or higher. The most common ferrites are spinels, whose generic chemical formula is MFe_2O_4, where iron is in an oxidation state of III and M is a metal in an oxidation state of II (most commonly Mg, Zn, Mn, Ni, Sr or Fe).[1, 22, 23, 51, 52] They crystallise in an fcc (*face centred cubic*) form [Fig. 2.1.1] and are differentiated into "normal" and "inverse" spinels. In normal spinels the ion having an oxidation state of II occupies tetrahedral positions in the ccp (*cubic closed pack*) lattice formed by the oxygen atoms and the ferric ions occupy octahedral positions. In inverse spinels, ferric ions are divided between tetrahedral and octahedral sites, whilst the M ions occupy octahedral sites. Finally, in mixed spinels, the ratio of iron atoms in octahedral and tetrahedral sites is intermediate between 2:0 and 1:1; a "degree of inversion" γ can therefore be defined, which describes how much the spinel structure tends towards inversion (with $0 \leq \gamma \leq 1$ where 1 indicates an inverse spinel). The occupancy x of the final compound can be calculated as $x = \frac{1-\gamma}{1+\gamma}$, with the metal atoms divided between (tetrahedral) and [octahedral] sites as $(M_xFe_{1-x})[M_{1-x}Fe_{1+x}]O_4$.

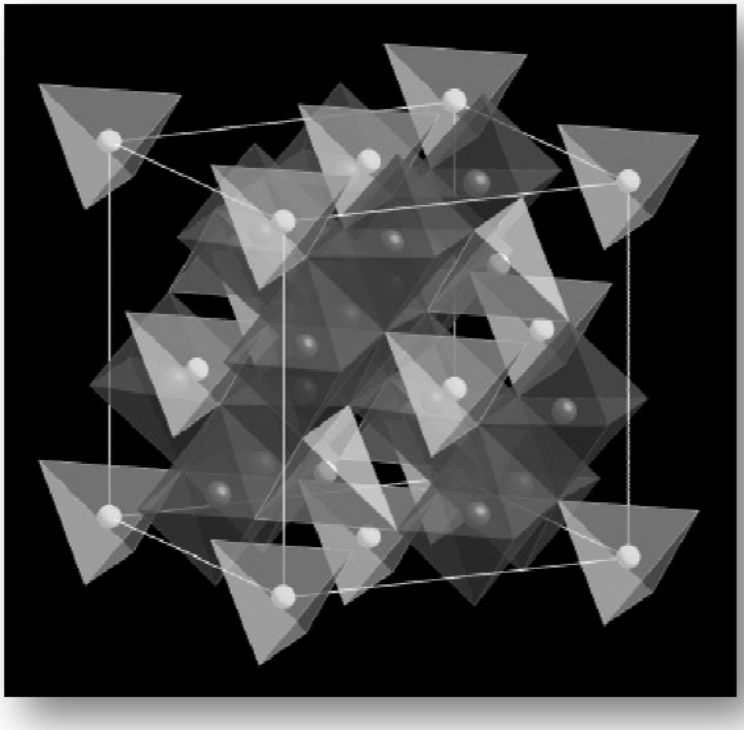

Figure 2.1.1 - *Spinel structure where tetrahedral and octahedral sites have been highlighted*

In inverse spinels, the unpaired electrons belonging to cations located in octahedral sites (in other words the M ions and half of the iron ions) are paired in a parallel fashion, thus creating a ferromagnetic lattice; a second ferromagnetic lattice is similarly created by the parallel pairing of the electron spin from the ions occupying tetrahedral sites (i.e. the remaining iron III ions). The two lattices possess however antiparallel spin. If the cations in the octahedral sites have the same number of unpaired electrons as the cations occupying tetrahedral sites, the balance between the two lattices results in the overall compound having antiferromagnetic properties, otherwise, the compound displays ferrimagnetic behaviour[1]. These oxides, whose formula can be alternatively expressed as $MO\text{-}Fe_2O_3$, can be considered a special case of the larger class of compounds known as hexagonal ferrites, having a generic chemical formula $MFe_{2n}O_{3n+1}$ (or $MO\text{-}nFe_2O_3$).[53]

A second group of ferrites has a cubic crystal structure and a generic theoretical formula $MFeO_3$ (perovskitic structure), where M is a metal in an oxidation state of II or III [Fig. 2.1.2].

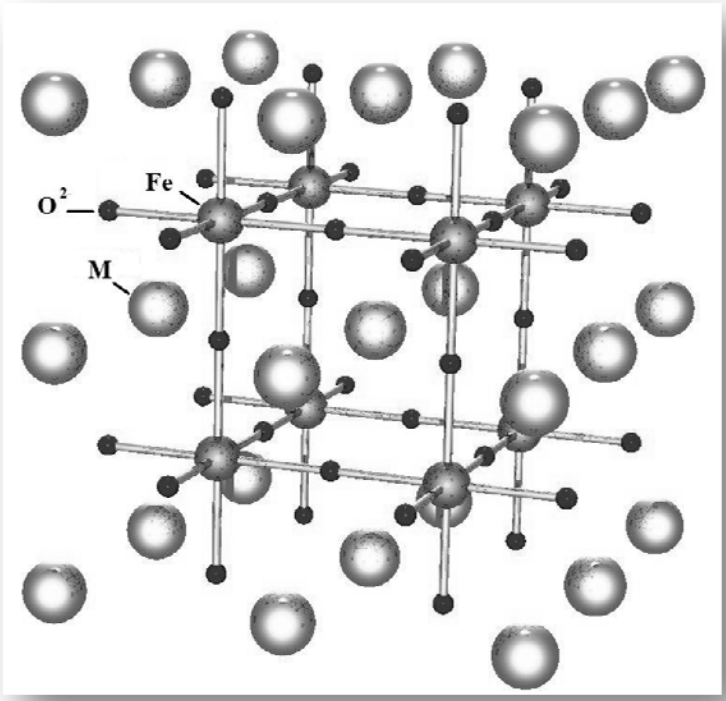

Figure 2.1.2 - *Perovskite cubic structure $MFeO_3$*

In some cases, depending on the radii of the M atoms involved, the FeO_6 octahedra share faces instead of vertices. In this case, the octahedra are grouped into pairs which in turn form chains with one another along the *c* axis of an hexagonal cell [Fig. 2.1.3].[54, 55]

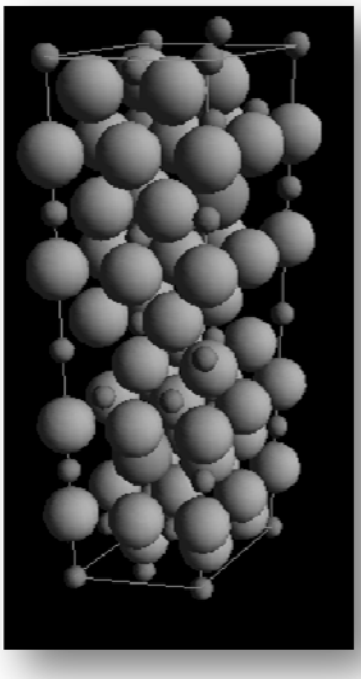

Figure 2.1.3 - *Perovskite hexagonal structure $MFe_{12}O_{19}$*

In the cases where M is a divalent metal, the iron atom in this type of oxide displays as a consequence the, generally rare, IV oxidation state; normally the iron contained in these oxides is not solely present in this state, but is found both in an oxidation state of III or IV, since these compounds have a tendency to display oxygen defects. This second type of ferrite can be considered a sub-class of the so called ferrates having a generic chemical formula $M_{n+1}Fe_nO_{3n+1}$ (where in the case of $MFeO_3$ n is ∞). These oxides are generally characterised by a crystal structure composed by regular or semi-regular FeO_6 octahedra (where the specific shape, regularity and relative position of these octahedra is related to n).[56]

2.2 - Properties and applications of ferrites: state of the art

Ferrites in general are characterised by remarkable thermal and chemical stability[1-6, 8-16] which, when coupled with their numerous other functional properties, make them extremely useful in a wide array of different applications.

As already mentioned, the structure of MFe_2O_4 spinel ferrites[1, 22, 23, 51, 52, 57] determine interesting magnetic properties (ferrimagnetism, antiferromagnetism superparamagnetism) which vary in dependence with the M metal (which in turn influences their structure).[58] Due to these properties, they find applications in a variety of different fields, ranging from electronics (in the field of data storage), to ferrofluid technologies and diagnostic medicine.[39] Spinel ferrites containing Mn, Co, Ni, Zn, Mg, etc. are of great interest for their remarkable magnetic, catalytic, optical, and electrical properties;[59] in particular, ferrites containing cobalt and manganese are employed as supported catalysts for liquid phase aerobic oxidations of α-pinene, β-pinene and limonene[35] and photocatalytic splitting of water to generate hydrogen.[36]

More recently, spinel ferrites have found applications in the development of modern magnetic materials such as smart magnetostrictive materials,[60] modern magnetic data-recording devices,[18]

spintronic devices, film transformers in integrated circuits, power inductors and electromagnetic interference filters.[61] In other fields, such as sensor development, spinel ferrites are employed as gas sensing oxides (combined with other materials in order to optimise performances),[62] or as fluorescence quenchers for the sensing of phosphate groups.[63] These ferrites have also found employment in the field of biology: since it is possible to encase them within a protective layer, allowing to reduce their toxicity, whilst leaving their electrical and magnetic properties unaffected, they can be effective markers for drug delivery and cancer therapy (after suitable functionalisation which enables them to target and bind with the desired cell types).[20, 64] Ferrite nanoparticles are also employed, following incorporation in a suitably functionalised organic matrix, as focal points in microwave-assisted thermal treatment (hyperthermia and thermal ablation) of tumours.[31, 65]

$MFeO_3$ perovskite ferrites (M=La, Sr, Ca, Ba, Mn etc.) can display the capability of diffusing oxygen, although this occurs at high temperatures[66-69] and their efficiency in oxygen diffusion varies with the nature of the M metal.[70] This diffusion process probably takes place by exploiting the oxygen vacancies in the perovskite structure. For these reasons, perovskite ferrites find application in oxygen conducting devices, such as pressure-driven oxygen generators, or in partial oxidation reactors and as electrodes for solid oxide fuel cells (SOFC).[37, 38] Perovskite ferrites also find applications in the field of catalytic photodegradation of organic compounds.[71]

More recently, perovskite ferrites, depending on the M metal in their structure, have found application as piezoelectrics,[72] as catalysts for the combustion of methane[73] and as reduction catalysts for NO and NO_x type oxides.[74] Their interest as components for SOFC remains constant, though currently most research in this field is focused on mixed metal iron ferrites containing f-block elements.

If obtained in nanosized form, both types of ferrites display superparamagnetic properties, which can make them particularly interesting for many of the above mentioned applications.

Mixed metal ferrites containing more than two metal species ($M_xM'_{1-x}Fe_2O_4$ and $M_xM'_{1-x}FeO_3$) are of particular interests as the electronic interaction of the two M and M' species can result in materials with novel or altered properties (e.g. catalytic, thermal response to electromagnetic radiation, magnetism) in comparison to simple M-Fe ferrites.[38, 69, 75-78] Practical utilisations of these types of compounds are too broad to be listed in full (as they effectively span the whole range of ferrite applications, depending on their structure and the metals involved). Notable applications however include substituted perovskites for oxygen conduction, where the inclusion of donor/acceptor metals can stabilise the material in reducing atmosphere, whereas trivalent metals can avoid lattice expansion in response to variations in oxygen nonstoichiometry.[69, 73, 79] In the case of spinels, the properties of mixed metal ferrites most commonly are employed in the field of magnetism (for the development of sensors and diagnostic tools[77, 80] as well as magnetic devices such as microinductors).[17]
Despite being relatively well-known compounds, interest in iron ferrites has not waned in the last years and research regarding ferrites and their applications is currently still thriving.

2.3 - Main features and applications of the synthesised ferrites

In the following paragraphs, the compounds prepared during this Ph.D. thesis will be given a more in-depth description.

2.3.1 - Magnesium spinel $MgFe_2O_4$

This compound is a partially inverse spinel.[81] It displays gas sensing properties[62] which allow for its application (both in pure and Pd-doped form) in LPG (*Liquid Petroleum Gas*) detectors. Unlike the other spinels synthesised in this Ph.D. thesis, this ferrite does not have a transition element as its M metal. The particular electronic structure of this compound gives it an energy gap of 2 eV[82] in the visible range. Due to this gap, which allows for the absorption of low-energy photons (2 eV ca. λ_{ab} 620 nm),[82] $MgFe_2O_4$ is suitable for use as a photocatalyst and has been employed in the decomposition of methylene blue[83] in absence of titania; when instead coupled with titanium oxide, the magnesium spinel has been documented to be photocatalytically active for the degradation of Rhodamine B.[84] Coupled with another photoactive ferrite (specifically the spinel $CaFe_2O_4$), this oxide has been also used in the photooxidation of isopropyl alcohol.[82] Other catalytic applications of this compound include decomposition of N_2O[85] and CO oxidation (in this case the ferrite is coupled with gold nanoparticles).[86] Analogously to the cobalt spinel $CoFe_2O_4$ described in paragraph 2.3.4, this material displays magnetic properties which make it extremely effective as a heating agent in hyperthermia cancer treatment.[87]

2.3.2 - Manganese perovskite $MnFeO_3$

This compound belongs to the $M^{III}Fe^{III}O_3$ class of perovskite ferrites. It is not widely documented in literature[70, 88-90] and, though its properties have been studied,[91-94] only a few applications have been reported: a patent[95] has been deposited regarding the use of this compound for high-temperature oxygen production. Moreover, catalytic CO oxidation over this compound after palladium impregnation has been observed.[96]

2.3.3 - Manganese spinel $MnFe_2O_4$

This spinel, like the cobalt and magnesium compounds, is partially inverse, the degree of inversion being however comparatively much lower (x = 0.20).[59] From a catalytic point of view, this material has been coupled with ZnO in order to achieve photoinduced production of hydrogen from water,[97] used as a supported catalyst for the oxidation of toluene[98] and as a catalyst precursor in the Fischer-Tropsch reaction. Other similar catalytic applications for $MnFe_2O_4$ are also documented.[35, 76, 85, 99, 100] In the medical field, after gold-coating and functionalisation, manganese ferrite is used as a diagnostic tool (in Magnetic Resonance Imaging - MRI) and therapeutic agent (to aid antibody delivery).[33]

2.3.4 - Cobalt spinel $CoFe_2O_4$

This compound displays a partially inverse spinel structure,[59, 101] with the inversion parameter depending on particle size and preparation (specifically the temperatures involved),[101] but normally equal to 0.80 in bulk material. As a compound, it is relatively well known and, as a consequence, many different applications have been already explored. The material has been extensively applied as an heterogeneous catalyst for two-step water splitting,[102, 103] esterification of *p*-cresol[104] and for

the decomposition of toxic organic compounds such as methyl orange,[105] cyclohexane[106] and methylene blue.[107] The magnetic properties (this spinel is a known hard ferrimagnetic material) displayed by the compound due to its spinel structure make it a suitable choice in many fields, such as sensor development[108] and incorporation within polymer films.[109] After suitable functionalisation (both to limit its toxicity and to allow for better interaction with target systems), this compound finds employment in the medical field, where it is both used as a contrast agent in diagnostic medicine and as a targeting tool for cancer treatment.[20, 33, 64]

2.3.5 - Nickel spinel $NiFe_2O_4$

This nickel-iron oxide displays a fully inverse structure (x = 1), meaning that the iron atoms in its structure are equally divided between octahedral and tetrahedral sires. The magnetic and electronic properties of this compound have been widely reported in literature[57-59, 110-114] and make it a viable choice for application in MRI as a contrast agent,[34] in ferrofluids,[115] spintronics,[116] as a microwave-absorbing material[117] and as a gas sensor for Cl_2.[118] This spinel is also employed in a wide variety of catalytic and photocatalytic processes such as total oxidation of propane[119] and toluene,[98] photocatalytic water remediation (combined with silica and titania),[120] decomposition of N_2O[85] and methyl orange,[121] oxidative dehydrogenation of 1-butene to 1,3-butadiene[100] and methane combustion.[122] Aside from the aforementioned use in the field of MRI, this nickel compound is extensively employed in medicine both for drug delivery[123, 124] and for cancer treatment.[64] Anti-bacterial activity has also been evidenced in the oxide and enhanced via tungsten doping.[121, 125] In order to limit cytotoxicity of the compound, particle size control[126] and suitable coatings[121, 123] are requirements to be met.

2.3.6 - Zinc spinel $ZnFe_2O_4$

In full contrast to the nickel spinel discussed in the previous paragraph, the zinc spinel ferrite $ZnFe_2O_4$ normally has a direct structure (x = 0), meaning that the iron atoms in its structure lie only in octahedral sites, whereas zinc atoms occupy tetrahedral sites. This low-cost compound displays electrical and magnetic properties (large specific resistance and magnetic permeability) which make it a useful material for applications in the field of microwave technology and electronics.[127, 128] Like many other ferrites, this compound is highly insulating and prevents (thanks to its high resistivity) the occurrence of eddy currents when an alternating magnetic field is present. This feature makes ferrite nanoparticles invaluable in high-frequency technological applications.[127] The spinel also displays a band gap (at about 2 eV) in the UV-Vis range (the exact gap is dependent on specific particle size)[129, 130] which enables its application in the field of photocatalysis (e.g. in the degradation of acid orange II)[129]. Further catalytic applications include photoelectrochemical water splitting,[131] methylene blue degradation[83] and nitric oxide decomposition.[85]

2.3.7 - Strontium perovskite $SrFeO_3$

This compound belongs to the $M^{II}Fe^{IV}O_3$ class of perovskites. Due to the relative instability of the iron oxidation state (IV), this compound is almost never found displaying the above stoichiometry and would be more correctly described as $SrFeO_{3-\delta}$ (or $SrFe^{IV}_{1-2\delta}Fe^{III}_{2\delta}O_{3-\delta}$, with $0 < \delta < 0.5$). Numerous stable forms having various values of δ have been documented[132] displaying a progressive distortion of the standard cubic perovskite structure with increasing values of δ. The main applications of this ferrite are related to its ability to become an oxygen conductor at high

temperatures.[70, 90, 132, 133] The two most common contexts in which this perovskite is usually employed are therefore in SOFC construction,[38, 68, 134, 135] where they are employed as electrodes, and in devices for the production and/or concentration of oxygen. Similar applications involve doping with lanthanum and use in the production of hydrogen from water and methane.[136] Studies are currently being carried out on the possibility of using perovskite-type materials (including $SrFeO_3$) as materials for hydrogen storage.[137] The reactivity this ferrite shows towards oxygen also makes it useful as a gas sensor.[138] Furthermore, the magnetic properties of this compound[139] enables its use in the field of spintronics.[140]

3 - Wet synthesis routes for ferrites

3.1 - Synthesis of ferrites

Bulk synthesis of ferrites, especially from an industrial point of view, is most commonly carried out through solid-state dry synthesis routes (such as the ceramic method or ball milling). The main advantage of these techniques is that they are relatively simple to implement and (once the protocol has been codified) do not require significant intervention on part of the operator. Also, scaling-up of the protocols is generally quite simple. An inherent limit of solid state reactions is that there is no medium in which the reactants are dissolved, severely limiting the interaction between components. The reaction can only take place either at the interface between the two solid precursors, or through migration of the reactants through a third phase;[141] such processes are therefore usually relatively slow, can lead to non-homogeneous final products and/or require high energies.

Ball milling (or mechanosynthesis) is generally carried out using binary metal oxides (such as hematite and M_xO_y compounds) as starting materials[142-147] although the use of precursor compounds such as carbonates, hydroxides or pure metals is also documented.[132, 148-151] The reactants are placed within a vessel (drum) lined with hard material (such as steel or a ceramic oxide such as zirconia) and containing a ball bearing made of the same material; the drum is placed within the mill and vibrated, causing the ball bearing to grind together the materials contained and causing the solid state reaction to take place. One limit of this technique is that none of the reagents can be harder than the material out of which drum and ball bearing are made; in addition, alloying and other side reactions might take place.[132] It is however a low-temperature approach, that is, safer and more sustainable from an environmental point of view.

The ceramic method involves a direct high-temperature (usually 800°C and above) solid-state reaction in order to prepare the desired structure; normally, metal oxides are employed as precursors,[152-158] although metal carbonates, hydroxides and metallic salts of organic acids are also used.[159] Both pure[152, 155, 156, 158-160] and mixed[153, 154, 157] ferrites can be synthesised with this method. Ball milling is also sometimes employed, following calcination,[155] in order to reduce particle size, since coalescence processes are highly favoured by the high temperatures involved, making the preparation of small particles and the control over their morphology difficult.

3.2 - Wet chemistry routes

Within the framework of nanoparticle synthesis, liquid-phase synthetic routes are generally considered a more promising alternative to the ceramic method and ball milling, as these latter are rather crude and energy-consuming approaches, whereas liquid-phase synthesis allows a finer and more direct control over the reaction pathways on a molecular level during the synthetic process itself.[42]. The most commonly explored routes for ferrite synthesis among wet-chemistry methods are thermal decomposition of organic precursors such as metal carbonyls, metal salts with organic anions (fatty acids, acetylacetone etc.),[161-167] solvo- and hydrothermal synthesis,[168-173] reverse micelle synthesis,[174-177] polyol assisted synthesis,[163, 178] and coprecipitation.[58, 111, 179-181]

An alternative approach is that based on heating the reaction mixture by electromagnetic sources, in this case microwaves (see Par. 1.6). Microwave synthesis displays various advantages over other

methods as it is surfactant free and allows to avoid the use of highly toxic additives and solvents[182], which is an ever-growing concern for modern green chemistry and industry. Another relevant advantage of microwave assisted synthesis is the significant reduction of reaction time for nanoparticle formation, which are typically reduced from days or hours to minutes. The nature of microwave absorption allows for highly homogeneous heating when small vessels are involved, as the entire system can be subjected to direct volumetric irradiation with reduced wall effects.[183] This makes microwave assisted synthesis particularly suited for the synthesis of nanostructured materials, since crystallinity, particle size distribution and uniformity are highly dependent on the initial conditions and on the homogeneity of the reaction.[42, 184-187]

The microwave-assisted non-aqueous sol-gel synthesis method (described in Par. 3.3) makes use of these advantages and has been successfully applied to obtain metal oxides such as MnO, Fe_3O_4, TiO_2 and CeO_2, in addition to spinels such a $Co_{1-x}Zn_xFe_2O_4$ and $Mn/CoFe_2O_4$ and perovskites such as $BaTiO_3$, $BaZrO_3$ and $PbTiO_3$.[184-186, 188] The method allows to rapidly synthesise metal oxides in nanopowder form displaying very small crystallite sizes: this is due to the fact that the high temperatures which are reached locally through microwave irradiation and the speed in which they are reached, allows for very rapid nucleation of the particles and thus for the formation of powders containing small crystallites.

3.3 - Non-aqueous sol-gel synthesis

Traditional sol-gel processes normally imply the hydrolysis and condensation of the precursors (generally alkoxides) in order to form a ceramic oxidic network.[189-191] On the contrary, the nonaqueous sol-gel synthesis we employed involves the reaction of metal halides within an alcoholic liquid phase during microwave irradiation. Generally, benzyl alcohol is chosen as a solvent due to its low toxicity, high boiling point and high loss factor compared to other organic solvents.[42, 184-186] In this environment, the oxygen atoms necessary for the formation of the metal oxide molecules are assumed to come from the solvent.[42] According to the mechanistic investigation carried out by Niederberger and Garnweitner,[186] the steps involved in the synthetic process are [Fig. 3.3.1]: **a)** alkyl halide elimination (alkoxide molecules are assumed to have formed by reaction between the solvent and metal halides), **b)** ether elimination, **c)** condensation of carboxylate groups (ester and/or amide eliminations, depending on the precursors involved), **d)** C-C coupling of benzylic alcohols and alkoxide molecules and **e)** aldol condensation (ketimine condensation can occur with an analogous mechanism).

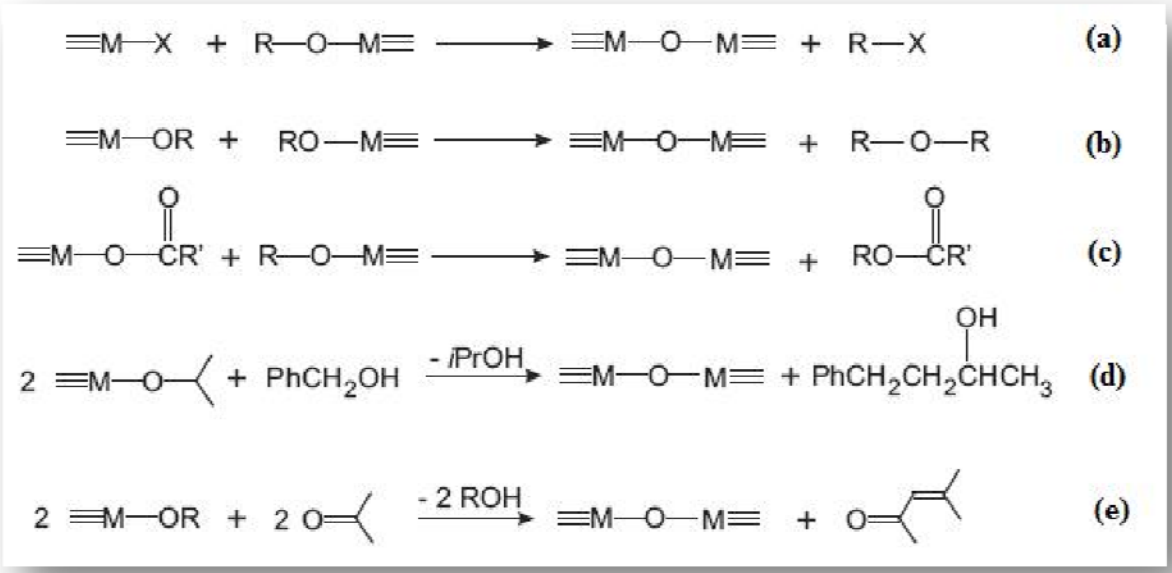

Figure 3.3.1 - *Synthetic steps involved in the nonaqueous sol-gel synthesis of metal oxides*[42]

Nanopowders synthesised through this route often tend to contain residual halide impurities; to avoid this, syntheses involving metal acetate, acetylacetonate or alkoxide precursors were introduced.[42, 184] One disadvantage of this method is the fact that different metallic precursors may display different reaction rates, based not only on the nature and oxidation state of the metal, but also on the counter-ion (an acetylacetonate of a metal may react differently compared to an acetate); this is relevant in syntheses aimed at the preparation of mixed oxides, as precursors must be found that react with a suitable relative speed.

3.4 - Dielectric heating by microwaves

As previously mentioned, heating in nonaqueous sol-gel synthesis can be carried out through microwave irradiation. In order to better understand the processes involved in the microwave-assisted nonaqueous sol-gel process, a more in-depth description of the interactions which take place between microwave radiation and the reaction system is provided. When a dielectric material interacts with the electromagnetic radiation, the energy carried by the radiation is partially dissipated within the material in accordance with equation 3.4.1:

$$P = 2\pi \cdot E^2 \cdot \nu \cdot \varepsilon_0 \cdot \varepsilon'' \qquad (3.4.1)$$

where P is the power dissipated (expressed in $W \cdot m^{-3}$), E is the electrical field strength in the material, ν is the electric field frequency, ε_0 the dielectric constant of vacuum and ε'' the loss factor of the material (the imaginary component of the relative complex permittivity of the material).[192]

Assuming the sample to be heated is small[193] and compositionally homogeneous, and that microwave irradiation is uniform, it can be assumed that the same amount of power per volume unit will be absorbed by the sample.

Disregarding the greater speed in which the material is heated, this uniformity represents one of the main aspects in which microwave heating differs from conventional heating (that is, heating by placing the material in a hot environment): in conventional heating [Fig. 3.4.1-a] the heat is

transmitted from the environment, so that the bulk of the material remains at a lower temperature for a longer time compared to the edges. In the case of microwave heating [Fig. 3.4.1-b], the entire sample is instead heated simultaneously, but contact with the environment, which is at a lower temperature, cools down the areas closest to the edges.

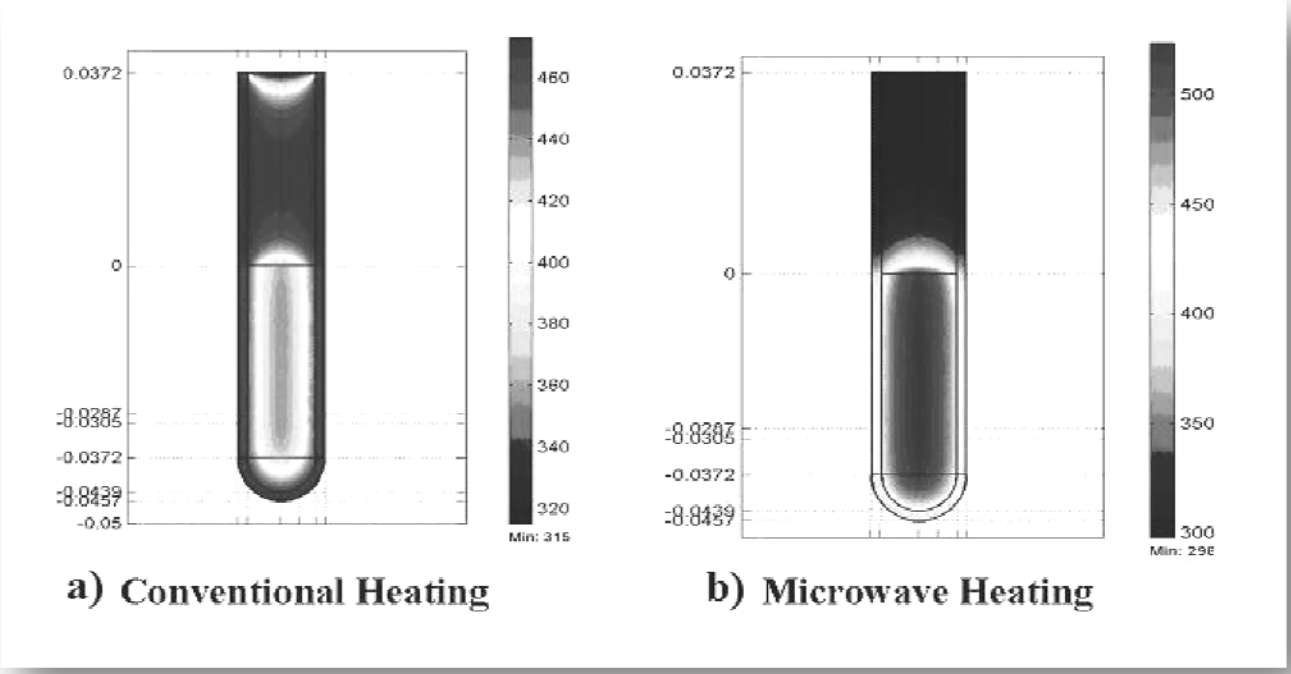

Figure 3.4.1 - *Heat distribution in a uniform sample heated by conventional means (a) and microwave heating (b)*

In the field of chemistry, there has been evidence that chemical transformations carried out at the same measured temperature, by using either conventional or microwave heating, lead to different results in terms of yield and/or selectivity.[183, 187, 194-199] This fact, combined with the fact that dielectric heating by microwaves has in many cases shown to significantly reduce processing times, enhance product purities and increase yields,[183] has sparked a debate on whether these enhancements were merely the result of improved heating, or were also due to non-thermal effects (selective interactions of the EM field with the reagents/solvent/catalysts). It has been however demonstrated that, at least for homogeneous organic reactions, the enhancements are merely due to thermal effects, and that any non-thermal interactions with the various components are negligible.[200]

In the case of non-homogeneous reactions, as is the case of the suspensions involved in the non-aqueous sol-gel synthesis method here employed, the reaction mixture is not heated uniformly: the presence of discrete separate components allows for a greater amount of energy to be dissipated when the EM radiation interacts with components with a higher loss factor. In particular, molecules containing metals tend to have higher loss factors compared to organic solvents such as benzyl alcohol (despite these solvents being classified as high-absorbing solvents) and thus can benefit from an increased heating.[201, 202] This effect renders possible the rapid nucleation of crystalline oxides, since although the reaction mixture is kept at a relatively low temperature (180-200°C), solid aggregates within the mixture may reach much higher temperatures.[184]

3.5 - Coprecipitation of oxalates

In comparison to other coprecipitation techniques (for example those involving the coprecipitation of hydroxides), coprecipitation of oxalates is particularly advantageous for two reasons: firstly it allows for the formation of precipitates of metals which otherwise display a high solubility (such as Sr); secondly the precipitates formed decompose in a way that allows for the resulting oxides to be very homogeneous in their features (size, purity, crystallinity).[203] This synthesis protocol has been already used to synthesise a number of spinel ferrites (such as $CoFe_2O_4$,[204] $Mg_xCd_{(1-x)}Fe_2O_4$,[205] $Ni_{0.6}Co_{0.4}Fe_yMn_{(2-y)}O_4$,[206] $Ni_{0.6}Zn_{0.4}Fe_{2-y}Nd_yO_4$[207] and $Cu_{(0.5-x)}Mg_xZn_{0.5}Fe_2O_4$).[208]

In the context of this thesis (see chapter **5**), this route has been used both by itself (followed by calcination at high temperature) and coupled with hydrothermal treatment (low temperature, see **3.6**) to synthesise the target compounds from an aqueous solution of the metal salts, oxalic acid and tetraethyl ammonium hydroxide (TENOH), used as a peptising agent.[209]

3.6 - Hydrothermal synthesis

A further approach is based on hydrothermal conditions to enhance nucleation and growth of crystalline materials. This synthesis method takes place in a closed system in the presence of a solvent (in this case water, whereas in solvothermal syntheses other solvents are used) at a temperature generally exceeding the boiling point of the solvent[210] and under high pressure. The high pressures involved cause significant changes in the solvent properties, making it possible for crystalline structures to form at relatively low temperatures.[211]

Normally, these conditions can be achieved by using a common autoclave, which subjects the system to externally generated heat and pressure. The two parameters (temperature and pressure) can be therefore altered independently in order to explore different experimental conditions. A second approach is to use a bomb autoclave [Fig. 3.6.1], in which pressure is generated autogenously in response to external heating. In this case, pressure is directly proportional to temperature. During this thesis, this second set up has been employed.

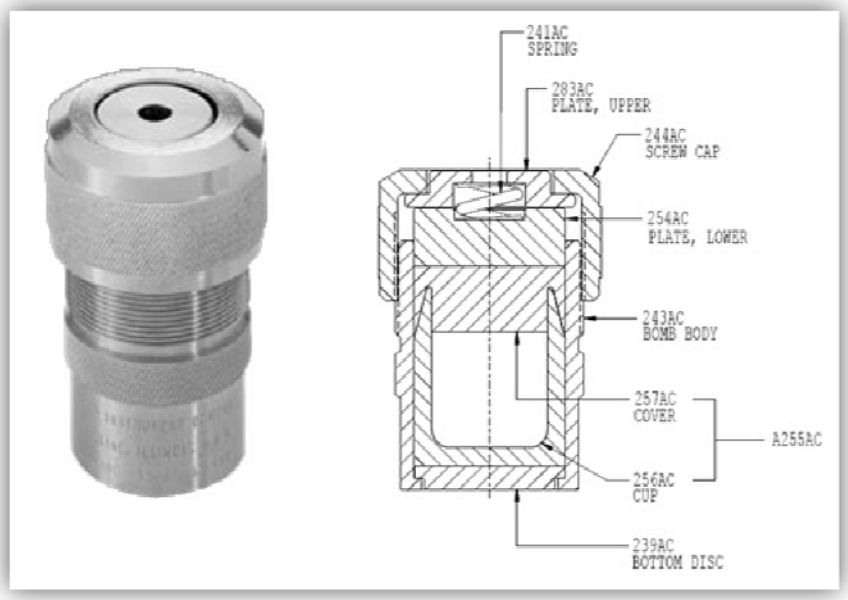

Figure 3.6.1 - *Parr acid digestion bomb*[212]

By heating the reaction mixture in closed system conditions, since the vapour (which forms in response to the elevated temperature) has no escape routes, the pressure inside the system is increased (autogenous pressure). The solvent-vapour system is therefore in a point in its relative phase diagram which allows for the simultaneous presence of a gaseous and a liquid phase, despite the temperature being higher than the normal boiling point.

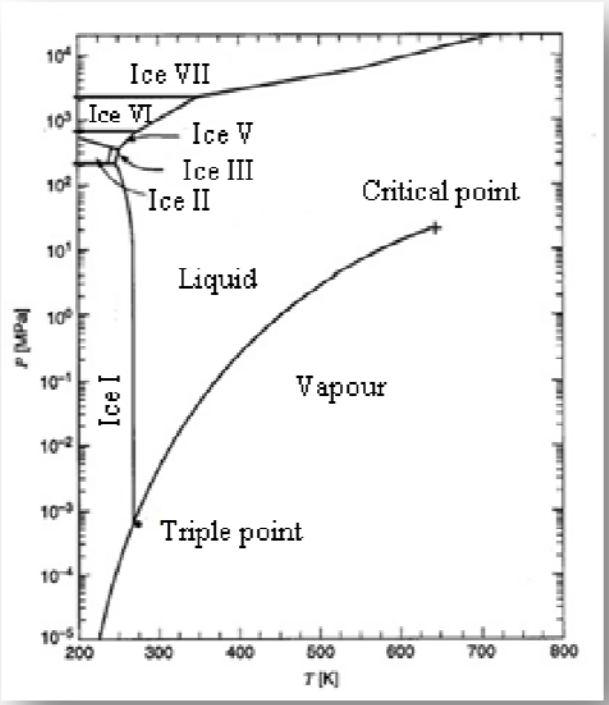

Figure 3.6.2 - *Phase diagram of water*

How the system evolves with increasing temperature is also partly dependant on what volume percentage of the vessel within the bomb autoclave is filled with solvent at room temperature: in the case of water, for example, when the vessel is filled by over 32%, the resulting vapour-liquid meniscus will gradually rise with increasing temperatures as the liquid phase will expand until the whole system is filled. In the (rarer) case, where the vessel is filled by less than 32%, the liquid-vapour meniscus will gradually descend with increased temperature, as the liquid phase will gradually evaporate and disappear. If the vessel is exactly filled by 32% the meniscus will not move and will simply disappear once critical conditions are reached.[141]

In the case of water (although similar considerations hold for other solvents), if both temperature and pressure in the system are greater than their respective critical values (i.e. their values in the critical point, see Figure 3.6.2), the system will be in supercritical conditions; if not it will be in subcritical conditions. Hydro- and solvothermal synthesis processes normally belong to this second category; in this they differ from similar processes where single crystals are obtained hydrothermally from amorphous precursors.[141] In this thesis specifically, no synthesis has been carried out in supercritical conditions, as the highest temperature reached was around 135°C (whereas T_c for water is 374.1°C).

As already anticipated, many of the chemical and physical properties of the liquid phase change significantly at high temperature and pressure: ionic product tends to increase with rising temperature and pressure, whereas viscosity decreases; the dielectric constant of water varies in dependence to the specific operative conditions since it increases with higher pressures, but decreases with rising temperatures.[141, 213] The solvating power of water is therefore significantly increased in comparison to standard conditions: for this reason, the dissolution of compounds (and consequently the formation of products) occurs in hydrothermal conditions whereas in non-hydrothermal conditions it would be unattainable.[211, 214, 215] From the resulting supersaturated solution, crystallisation process that would be impossible in normal conditions can take place, allowing the formation of single- or poly- crystalline products at remarkably low temperatures.[213]

This method has for a long time been considered one of the main routes to obtain crystalline structures without the need for extreme conditions.[169] In the last years, this approach has been employed for the synthesis of mixed oxides in nanocrystalline form.[169, 216] The main advantage of hydrothermal synthesis over conventional wet-chemistry methods is that the chemical reactions take place at relatively low temperatures. While temperatures in the range 400-600°C are normally employed to obtain crystalline compounds, in hydrothermal conditions crystal formation can be observed much earlier (in our case, at temperatures as low as 75°C). Moreover, the hydrothermal approach also allows to tune the resulting particle size by adjusting the treatment temperature and the composition of the reaction medium.[213, 217, 218]

3.7 - Crystallisation process

The purpose of this Ph.D. thesis was to prepare all intended compounds in a crystalline powder form (polycrystalline). A crystal is a solid which displays a high degree of order and where atoms are placed according to a repeated pattern: in a crystal, the constituent atoms are distributed in such a way that a fundamental unit (unit cell) can be identified. This unit cell, repeated sequentially (and ideally *ad infinitum*) along the crystal axes results in the formation of a crystalline domain.[219] Formation of crystals can take place in an extremely wide range of conditions.

In this thesis crystallisation has been induced either through calcination (where the high temperatures allowed the solid compound to reach a high enough energy to form a crystal during subsequent cooling), or from a solution. Formation of crystals from a solution takes place when the solute in a supersaturated mixture is allowed to slowly precipitate. During this step, the crystal grows in an orderly fashion around a central nucleus (crystal seed).[219] If precipitation takes place slowly, a single large crystal will result, if instead the solute precipitates more rapidly, the growth kinetics will be superseded by the crystal seed formation (nucleation) kinetics and a large number of small crystals (powder) will result.

During hydrothermal synthesis, a supersaturated solution can be achieved due to the nonstandard conditions (high pressure and temperature) which the system is subjected to, thus allowing the solubilisation of normally insoluble compounds.[141] The most diffuse theory regarding formation of ceramic oxide crystals through hydrothermal synthesis[220, 221] describes a two-step mechanism: in the first phase (in-situ transformation) the precursor ions are dissolved in the reaction mixture, due to the conditions in which the reaction takes place, and minute quantities of the target oxide are able to form in the liquid phase. Because of the low solubility, even at high pressure and temperature, of

the final compound, the second phase (precipitation and growth) takes place. In this phase, nucleation centres are formed throughout the system around which crystal growth can take place. Given the small size of the crystallites prepared with this method, it can be assumed that these nucleation centres form quite rapidly compared to the growth process. This difference in kinetics results in the formation of a large number of small crystals, as opposed to a series of larger particles. In our case (see Chapter 4), the speed at which the reaction takes place (observations carried out in transparent vessels have shown the formation of powders after 60-120 minutes, depending on the compound in question) suggests that both nucleation and growth processes have very fast kinetics. Data in literature regarding the use of oxalates in hydrothermal processes is scarce, but based upon the results gathered from the obtained samples, particularly the fact that the resulting powders contain a very small amount of organic residue, it can be hypothesised that the oxalate precipitate is progressively consumed as the reaction progresses and redissolved in order to replenish the metal ions which are removed from the solution in order for the final oxide to be formed. Due to the synthetic conditions employed during this thesis, only polycrystalline powders were obtained, as the preparation of single crystals would have created additional difficulties and was beyond the scope of this research.

3.8 - Experiments performed

In this Ph.D thesis, synthesis experiments were carried out with the aim to obtain the spinel ferrites $MgFe_2O_4$, $MnFe_2O_4$, $CoFe_2O_4$, $NiFe_2O_4$, $ZnFe_2O_4$, $CaFe_2O_4$, $BaFe_2O_4$ and $SrFe_2O_4$, and the perovskite ferrites $MgFeO_3$, $CaFeO_3$, $NiFeO_3$, $MnFeO_3$, $CoFeO_3$, $ZnFeO_3$, $BaFeO_3$ and $SrFeO_3$. Furthermore, the mixed ferrite syntheses with the objective of achieving ceramic oxides containing three metal species were also performed. These syntheses were carried out employing i) the non aqueous sol-gel synthesis method, ii) coprecipitation of oxalates and iii) hydrothermal synthesis, and by varying the experimental parameters (temperature, reaction time, additives such as peptising agents, precursor nature and nominal precursor ratio precursors), with the aim of studying how each of these parameters influences the nature and properties of the final product. Not all of the targeted compounds could be achieved, as extensively described in the following chapters.

4 - Results and discussion

In this chapter, the results of the syntheses performed in this thesis will be presented and discussed. Firstly, general considerations common to all compounds synthesised with a single given method will be presented. These introductory paragraphs will be followed by more in-depth descriptions of the analysis results relative to the different ferrite types and their discussion.

4.1 - General considerations

Synthesised compounds underwent a thorough characterisation from the structural, chemical, physical and functional point of view, using a large number of methods.

From a structural point of view, XRPD patterns were initially examined through search and match in order to identify the obtained crystalline phase (or phases) and therefore make a preliminary evaluation regarding the purity of the synthesised compounds. Patterns displaying only a single phase were, in a second stage, further analysed through Rietveld refinement to gather further information on their crystal cell and on the crystallite size. Selected samples were further characterised through TEM in order to confirm what was gathered from the refinement and to investigate the morphology of the powders.

From the chemical and physical point of view, ICP-AES was employed to confirm that the bulk molar ratio between the metals in the prepared oxides corresponded to the expected stoichiometry, whereas surface molar ratios and oxidation states of the species of interest, as well as the chemical environments, were investigated through XPS measurements. Microanalysis was used to gain insight on the amount of organic precursors which remained adsorbed on the final compounds. In order to further investigate the chemical environments and oxidation states o the atoms in the prepared ferrites, Mössbauer spectroscopy (for iron atoms specifically), XAS and RIXS were employed. The oxidation states in the materials were further assessed by TPR. TGA-DSC measurements were finally used to study the behaviour of both the final products and their precursors at high temperature (this was particularly useful to gain insight on the calcination process which follows coprecipitation synthesis).

From the functional point of view, catalytic activity in the oxides was studied, through CH_4-TPO. Dielectric measurements were carried out in order to evaluate the electric behaviour of the materials, whereas their magnetic properties were investigated through SQUID.

4.1.1 - Nonaqueous sol-gel synthesis

Nonaqueous sol-gel syntheses (carried out in the work group of Prof. Markus Niederberger - Laboratory for Multifunctional Materials, ETH-Zürich) aimed at the production of the cobalt and manganese spinels ($CoFe_2O_4$ and $MnFe_2O_4$) were successful and yielded powders with pure crystalline phases. Syntheses aimed at the production of the perovskites for the same metals were unsuccessful, producing powders with mixed crystalline phases. The experiments involving barium (see appendices A1.1, A1.2, A2.1 and A2.2) were generally unsuccessful: the use of a solution of metallic barium dissolved in benzyl alcohol ($Ba_{(sol)}$), to give the alcolate, sometimes in combination with small quantities of water, did not bring any relevant results. Synthesis mixtures containing $Ba_{(sol)}$ displayed some tendency towards a rapid increase in viscosity, quickly reaching a gelatinous

appearance, especially the ones containing water (although this occurred even in those mixtures which were maintained anhydrous, albeit at a much slower rate). This process was in all cases reversed during the reaction in the microwave oven, as the resulting mixtures presented themselves, after heating had been applied, as normal solid suspensions in a liquid phase, without any major impact on the final products. Experiments involving strontium were similarly unsuccessful, yielding a mixture of iron oxide and various mixed strontium-iron oxides.

4.1.2 - Coprecipitation of oxalates

This synthetic approach was successfully applied for the preparation of five compounds, namely the cobalt, magnesium, zinc and nickel spinels $CoFe_2O_4$, $MgFe_2O_4$, $ZnFe_2O_4$ and $NiFe_2O_4$, as well as the manganese and strontium perovskites $MnFeO_3$ and $SrFeO_3$. Syntheses aimed at achieving other compounds (such as the cobalt, magnesium and nickel perovskites and the manganese and strontium spinels) were unsuccessful, generally resulting in impure products composed of multiple crystalline and/or amorphous phases.

Compounds prepared through this synthetic route generally display large crystallite sizes (although the specific size is also dependant on the nature of the compound itself) which increase with increasing calcination temperatures. This suggests that coalescence processes (which are thermally favoured) take place in parallel to the transformation from a mixture of metal oxalates to the final ferrite; although it has been observed that calcination plateau time does indeed affect the final crystallite size, the net influence is much weaker as compared to treatment temperature. This is however probably due to the slow ramp employed for calcination as much smaller crystallites sizes were calculated from patterns relative to cobalt and manganese ferrites (see Par. 4.2 and 4.4) calcined during temperature resolved XRD measurements (TPXRD). The much sharper heating ramp involved during these analyses (see Fig. 4.2.4) is probably the cause for this.

In general, the most efficient coprecipitation of oxalates synthetic protocol was found to involve dropwise addition of NaOH for basification and a short aging period (protocol A, see Par. 5.3).

4.1.3 - Hydrothermal synthesis

This method was used to prepare four spinels, namely the cobalt, manganese, zinc and nickel ferrites. Although the net quantities of product obtained were relatively low (a standard synthesis in a 24 ml Teflon vessel resulted in approximately 100 mg of product), a drawback shared with nonaqueous sol-gel synthesis, this method consistently showed yields over 95%, showing that, if scaled up, large quantities of product may be easily prepared with high atom economy. In comparison to the other two routes explored, the main advantages of this synthesis protocol are the low temperatures involved (crystallisation has been observed already at 75°C) and the use of aqueous solvent (which makes the process greener and purification of products and disposal of waste material much easier). Continuing the trend of similarities between this method and the nonaqueous sol-gel route, unsuccessful syntheses (that is to say, syntheses aimed at compounds other than the three spinels mentioned above) generally resulted in products comprised of several different phases and, as a result, unidentifiable; a notable exception is the synthesis attempt aimed at achieving the nickel perovskite $NiFeO_3$ which will be addressed in paragraph 4.5.

Though other previous works in literature have discussed hydrothermal syntheses of spinel compounds for cobalt,[222, 223] zinc,[129, 224] nickel[225] and manganese,[224, 225] the specific method explored in this thesis is particularly notable due to the high quality of the resulting compounds and the low temperatures involved.

Observation of the process by employing a sealed glass vial as a reactor showed that, at 135°C, the reaction took place rapidly, as the brown precursor suspension was rapidly converted into a dark precipitate. The low temperature registered is particularly notable when compared with the decomposition temperatures reported in literature for metal oxalates[226-230] which, in a solid state, and other conditions being equal, take place at over 200°C. This finding indicates that the process requires an aqueous environment. This was further confirmed through TGA-DSC analyses of the dried precursor solids obtained after basification, which revealed that simple thermal treatment was insufficient even for the removal of crystallisation water (which is normally completed at around 200°C),[227, 230] and is therefore far too low for the decomposition of the oxalate precipitates.

Since pure phases were obtained at temperatures below the boiling point of the solvent, in order to study the effect of pressure on the reaction, separate synthetic attempts were carried out under reflux-like conditions (as the temperature was below the boiling point of the solvent involved, the synthesis cannot strictly speaking be considered "under reflux"). Such syntheses took place at 75°C for 24, 4 and 2 hours (thus subjecting the oxalate suspension mixture to the same thermal conditions, but not the same pressure as the lower temperature hydrothermal syntheses). These attempts successfully yielded the spinel phase. The crystalline powders prepared with this route however, compared to their counterparts prepared through the hydrothermal route, displayed a lower yield (60%) and, from the purity point of view, had a higher carbon and hydrogen content (0.81% and 1.22% respectively, compared to 0.24% and 0.37% for sample I-Zn002, see table 4.8.2, page 75), showing that, at these lower temperatures, a higher amount of organic precursors remained adsorbed on the final powder despite purification.

As with coprecipitation, syntheses carried out with this method were optimised collectively, i.e. the optimal synthesis parameters for one compound proved to be suitable for the preparation of the other three spinels as well.

4.2 - Cobalt spinel ferrite $CoFe_2O_4$

The cobalt spinel $CoFe_2O_4$ was the most easily obtained ferrite among the ones investigated during this Ph.D. thesis, being the only one to be prepared through all three synthetic routes. This was not unexpected, as the compound is well known and has been successfully prepared in the past through a wide variety of methods including coprecipitation,[109] sol-gel,[106] solvothermal synthesis[173] and microemulsion.[57]

In the context of nonaqueous sol-gel synthesis, syntheses were found to be particularly successful when the ferrous acetylacetonate precursor was employed. These syntheses displayed the best results when the precursors were reacted for 15 minutes, as longer reaction times resulted in products in which minor impurities (though too small to be identified) were detected. Analogously to what observed for $MnFe_2O_4$ (see Par. 4.4), syntheses carried out with ferric acetylacetonate resulted in low yields; the products thus obtained were impure showing a mixture of the spinel, cobalt oxide and an amorphous phase. Syntheses carried out using ferrous acetate were likewise

unsuccessful, although the products thus obtained showed a prevalence of $CoFe_2O_4$ (though still mixed with minor impurities). Syntheses where ferrous acetylacetonate was reacted with cobalt^{II} acetylacetonate at 200°C for 15 minutes allowed to prepare pure nanosized $CoFe_2O_4$.

In regards to coprecipitation and hydrothermal syntheses, optimal synthesis of this compound did not require any particular improvement beyond the general observations addressed in paragraphs 4.1.2 and 4.1.3 which also apply to all other compounds.

XRPD patterns [Fig. 4.2.1] were collected on all synthesised samples in order to estimate crystallinity and phase purity of the compounds.

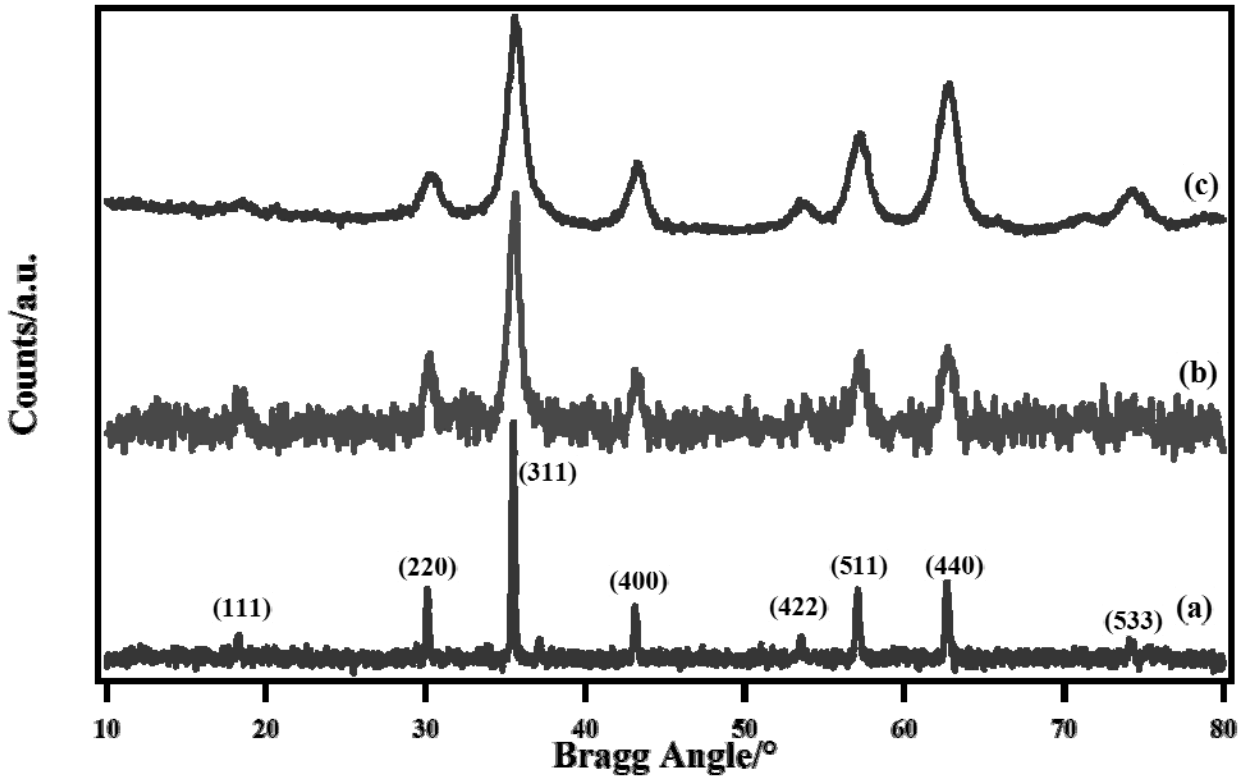

Figure 4.2.1 - *XRPD patterns of notable samples (a) Co017, (b) I-Co001 and (c) S-Co011-4 with main reflections indexed*

The crystallite size was initially estimated by applying the Scherrer formula[231] on the (400) reflection: this reflection was chosen because of its high intensity and the fact that it is well separated from other reflections. A more precise estimation of crystallite size (see table 4.2.1) was obtained by carrying out Rietveld refinement on the patterns. Whilst the resulting crystallite size values were generally higher than those derived from application of the Scherrer formula, this difference has been attributed to errors in determining the correct reflection data (i.e. peak broadening) whilst carrying out the Scherrer analysis (which is inherently less precise). The crystal structure was fitted by making use of the MEEM (Maximum Entropy Electron Maps) model [Fig. 4.2.2] (see Par. 6.1.3).

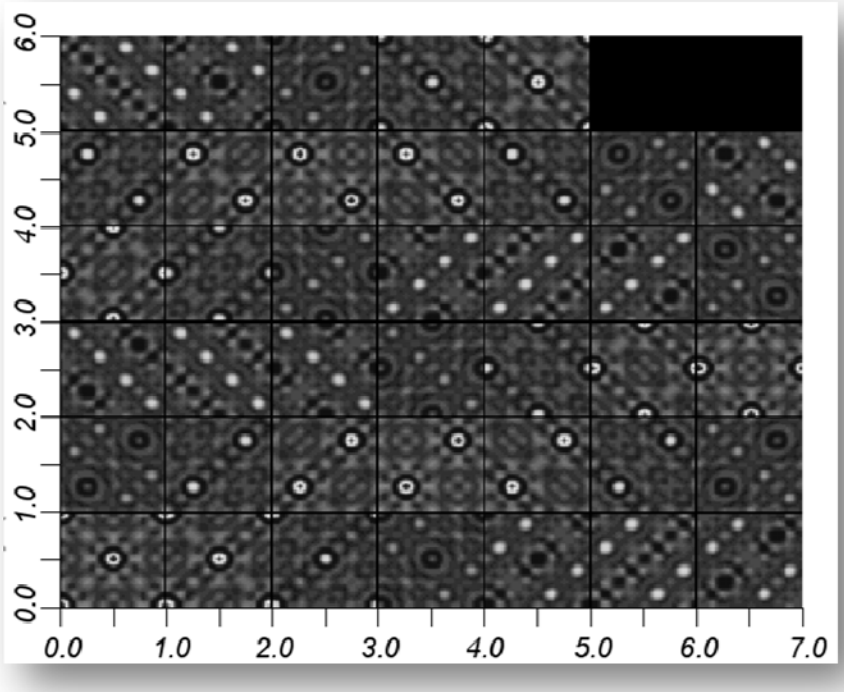

Figure 4.2.2 - *MEEM relative to the XRD pattern obtained from sample S-Co011-4*

The data resulting from the MEEMs was employed in combination with data reported in literature by Wychoff[157] and available on the COD (Crystallography Open Database).[156]

Sample	Method	Treatment temperature and time	Crystallite mean size/nm (from Rietveld)
S-Co010-5	Nonaqueous sol-gel	200°C; 30 minutes	10±2
S-Co011-1	Nonaqueous sol-gel	180°C; 15 minutes	9±2
S-Co011-3	Nonaqueous sol-gel	200°C; 15 minutes	10±2
S-Co011-4	Nonaqueous sol-gel	180°C; 30 minutes	10±2
Co008	Coprecipitation	600°C; 5 hours	23±5
Co007	Coprecipitation	900°C; 2.5 hours	132±10
Co002	Coprecipitation	900°C; 5 hours	185±5
Co011	Coprecipitation	900°C; 5 hours	178±5
Co017	Coprecipitation	900°C; 5 hours	170±5
Co020	Coprecipitation	See Fig. 4.2.4	62±5 (at 900°C)
I-Co001	Hydrothermal	135°C; 24 hours	12±3
I-Co007	Hydrothermal	135°C; 24 hours	17±2
I-Co018-1	Hydrothermal	135°C; 1 hour	/
I-Co018-2	Hydrothermal	135°C; 2 hours	18±3
I-Co018-4	Hydrothermal	135°C; 4 hours	18±1
I-Co019	Hydrothermal	100°C; 24 hours	/
I-Co020	Hydrothermal	75°C; 24 hours	/

Table 4.2.1 - *Crystallite size of significant $CoFe_2O_4$ samples*

Concerning hydrothermal synthesis, all experiments were initially carried out with 24-hour reaction times (regardless of the chosen temperature); experiments aimed at investigating how reaction time influenced the product and how the compound itself evolved during the treatment revealed that the pure crystalline phase formed in as short a time as one hour. This further reinforces the position of

this method as a quick and low-energy route for crystalline powder preparation. Further experiments showed that formation of the oxide can take place at as low temperatures as 75°C, though the high X-ray fluorescence displayed by the compound[232-234] by cobalt and iron resulted in XRPD patterns with high backgrounds. For this reason, though the main spinel reflections were visible, no crystallite size determination was possible. The low crystallite size values found in the other cases suggest that nucleation during hydrothermal synthesis takes place at a far greater speed compared to growth, enabling the formation of smaller particles. Figure 4.2.3 shows a comparison of XRPD patterns relative to samples with different hydrothermal reaction times.

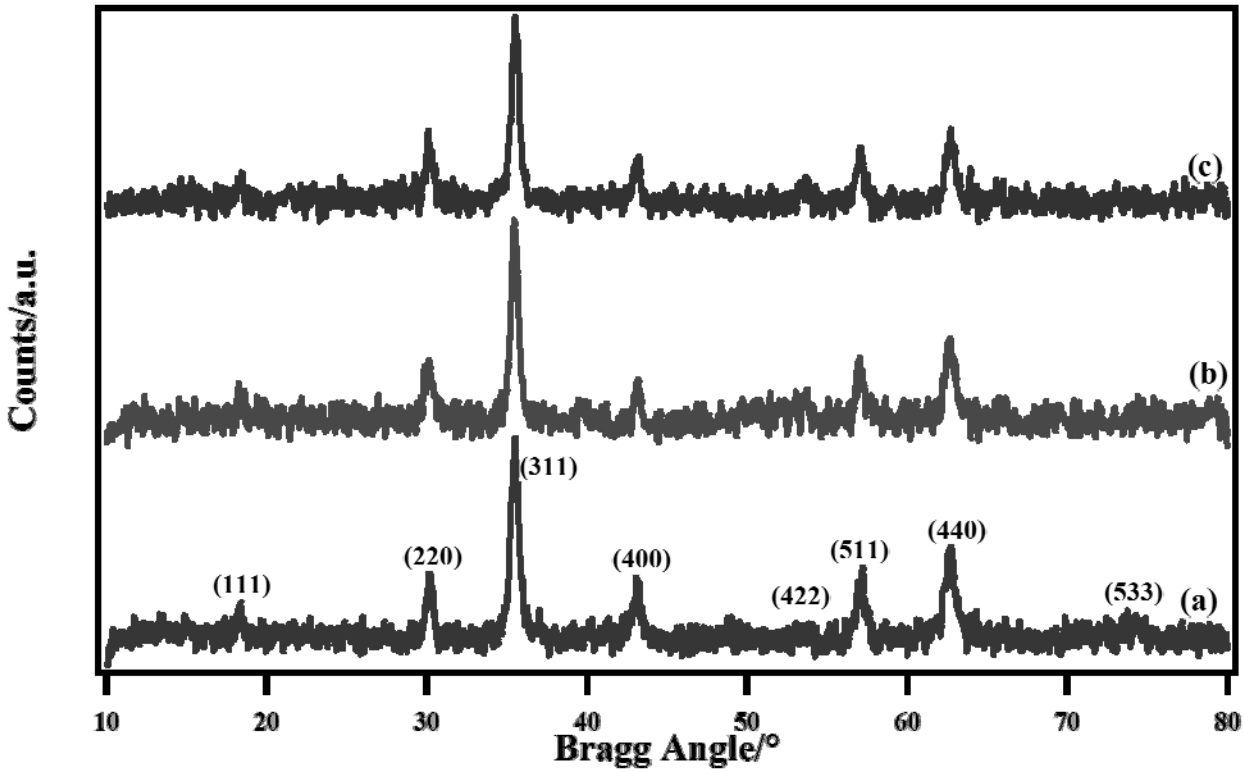

Figure 4.2.3 - *XRPD patterns of sample I-Co018 with reaction times of (a) 1, (b) 2 and (c) 4 hours at 135°C*

A single sample obtained through coprecipitation, prior to calcination, was investigated through XRPD at different temperatures to shed light on how the compound evolved during the calcination process itself. The sample was heated according to the profile shown in figure 4.2.4, with patterns being collected at all plateaux (i.e. every 100°C during heating up to 900°C, and again at 500°C and 40°C during cooling).

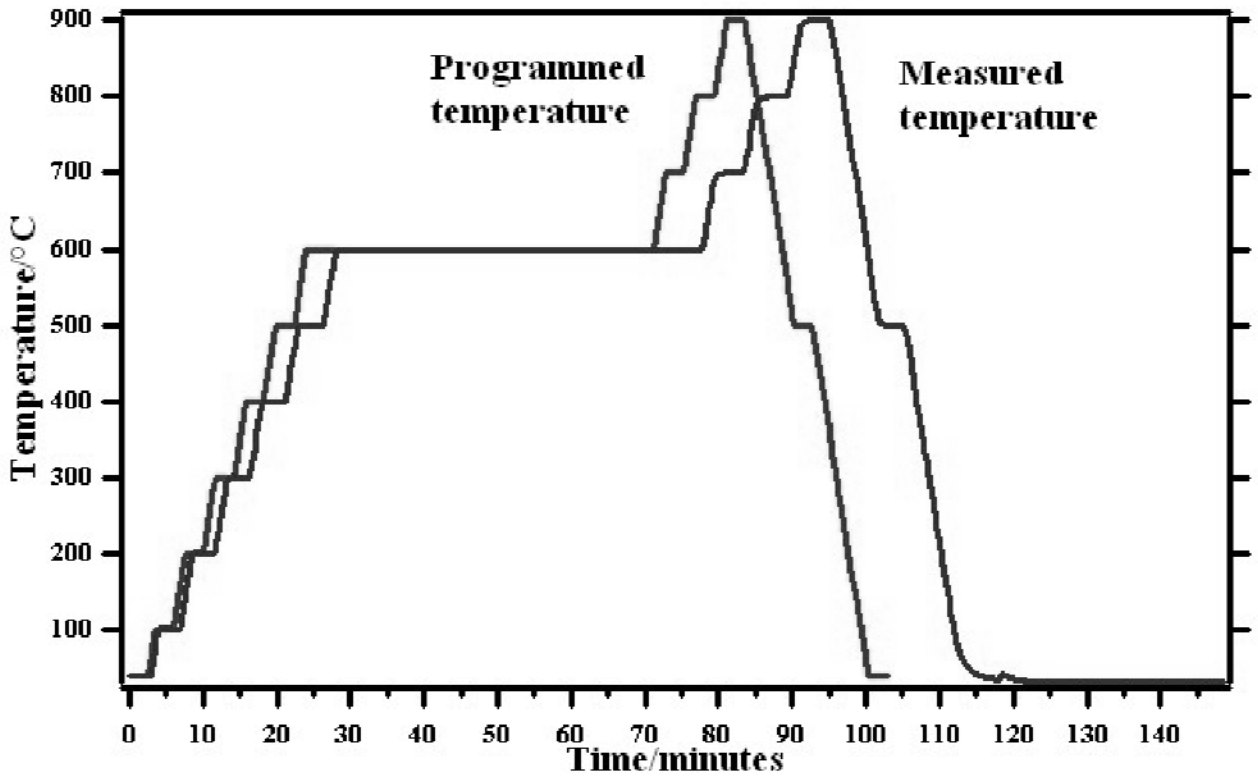

Figure 4.2.4 - *Temperature profiles used for temperature programmed XRD TPXRD*

The resulting patterns [Fig. 4.2.5] showed that, while the reflections typical of the spinel phase, and in particular the (220), (311) and (400) series, were visible already at relatively low temperatures (500-600°C), they became sharp and distinct only when the sample temperature reached 800-900°C. Given that Mössbauer analyses carried out on analogous cobalt ferrite samples calcined at 600°C (not reported) revealed the presence of impure phases, which were absent in samples subjected to higher temperatures, it was concluded that these extra phases were amorphous and were therefore masked by background noise and fluorescence.

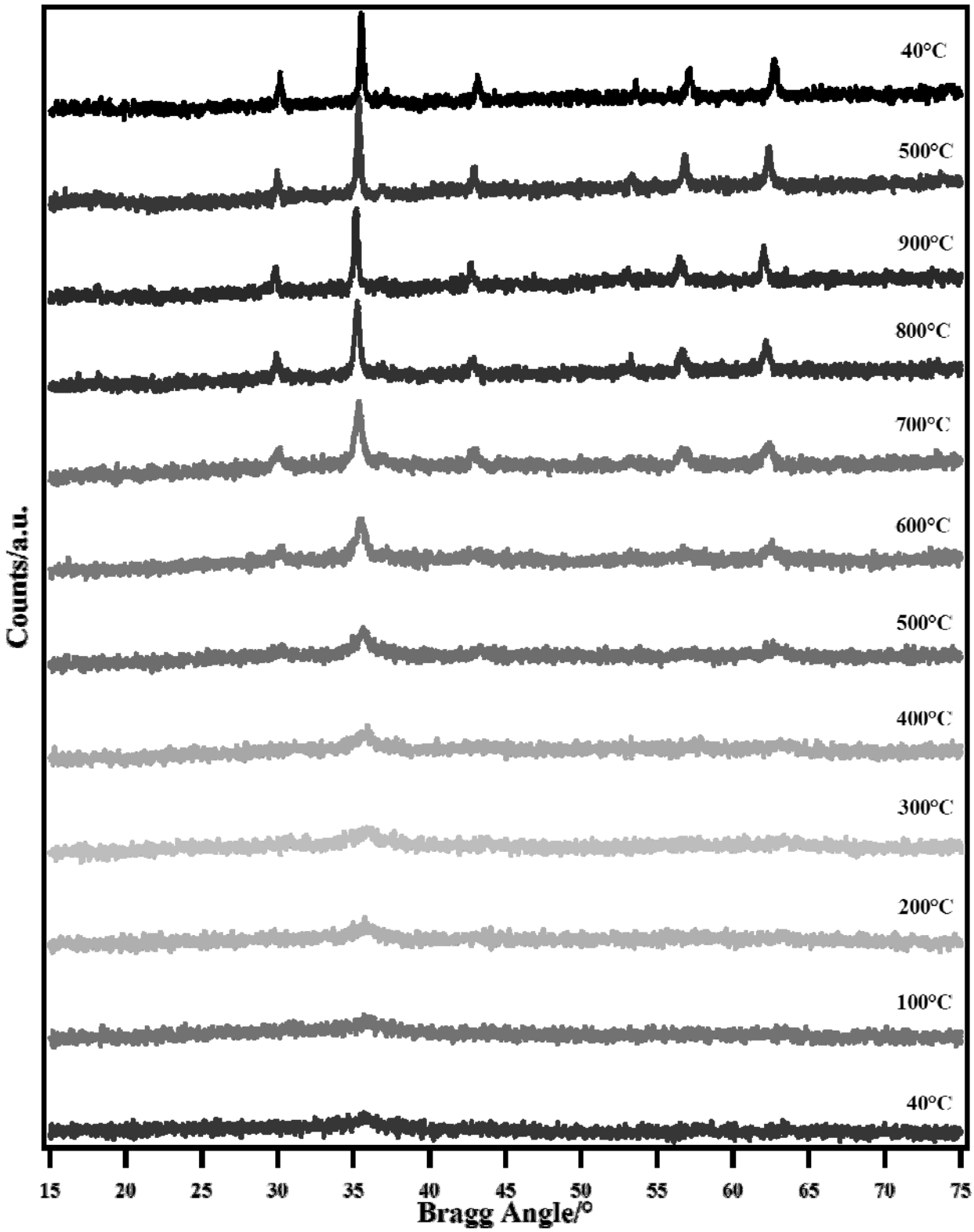

Figure 4.2.5 - *XRPD patterns collected at different temperatures from cobalt ferrite sample Co021*

Samples which were determined through XRD analysis to be pure single-phase products were further investigated; in particular, in order to gain further insight on the morphology of the synthesised particles, transmission electron microscopy was performed on samples S-Co011-3 [Fig. 4.2.6] and Co002 [Fig. 4.2.7]. In the case of the sample synthesised through the nonaqueous sol-gel process, the images show that the ferrite crystallites have a tendency to agglomerate into clusters, although at the higher resolutions [Fig. 4.2.6 - f)] the single crystallites are still visible. Compounds

prepared through coprecipitation show instead evidence of coalescence, confirming the hypotheses regarding the calcination process formulated based on the XRD data. In both cases, the crystallite size thus displayed in the TEM micrographs is compatible with the estimates resulting from XRD analysis. The tendency of the first sample to form the larger aggregates visible at the lowest resolutions [Fig. 4.2.6 - a), b), c)], may at least partly be due to inadequate dispersion of the compound within the liquid phase (ethanol abs.) utilised for the TEM measurements.

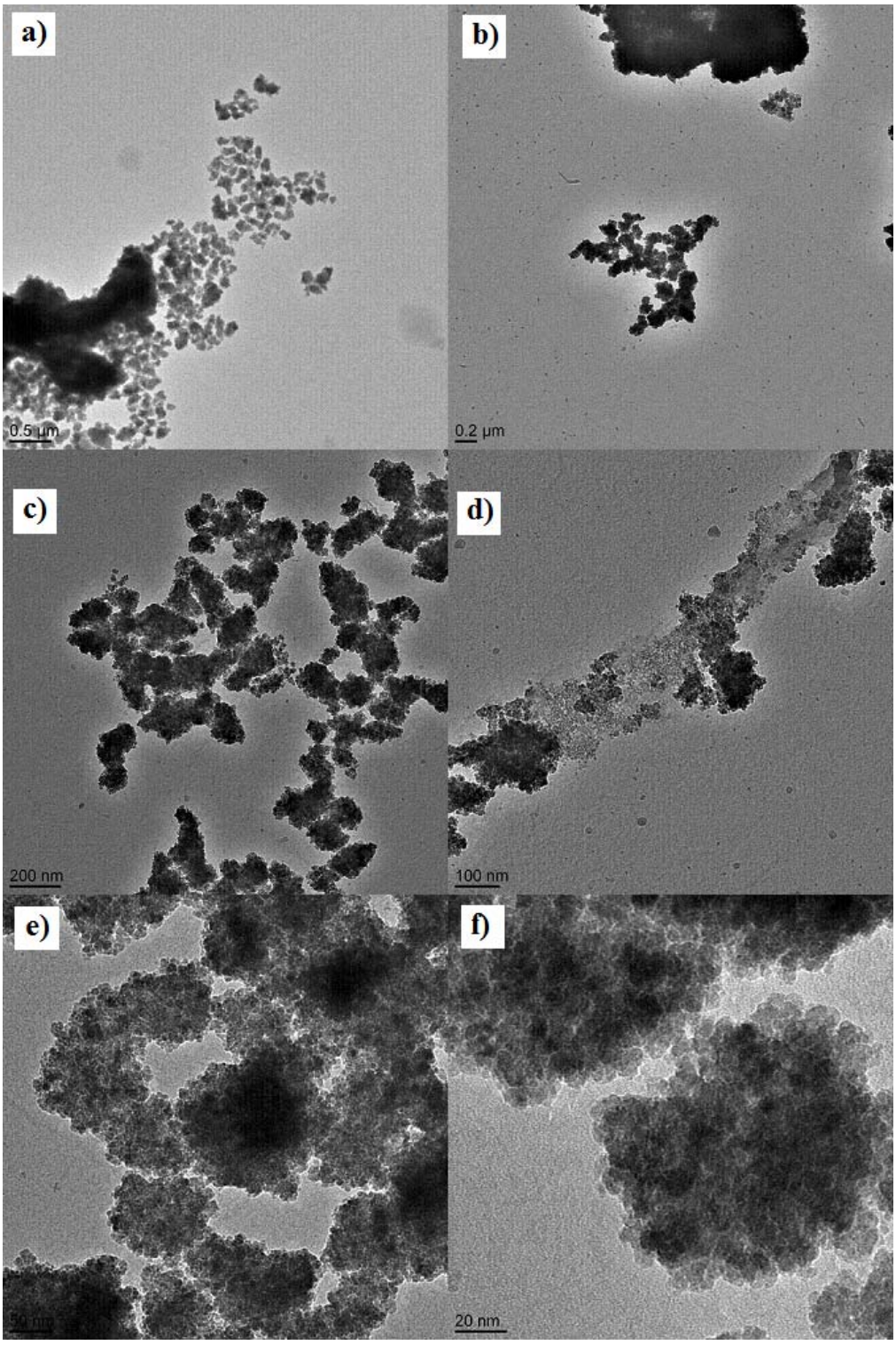

Figure 4.2.6 - *TEM micrographs of sample S-Co011-3 at various resolutions*

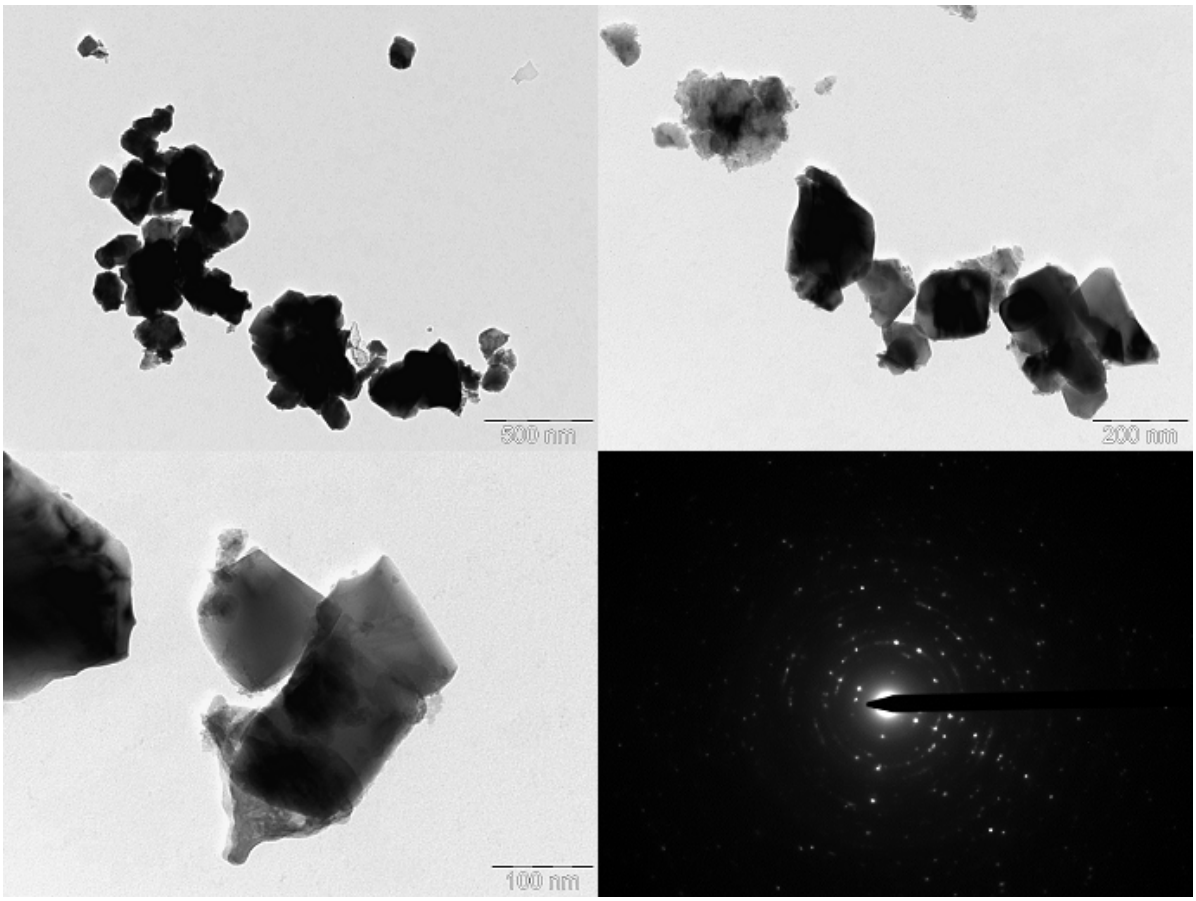

Figure 4.2.7 - *TEM micrographs of sample Co002 at various resolutions*

In order to complement the structural information gained so far with a greater insight on the surface chemical environments of cobalt and iron, as well as the compositional differences with the bulk material, surface composition and oxidation states were analysed through XPS [Fig. 4.2.8]. Unlike other compounds addressed in this thesis, a Mg X-ray source was used for cobalt ferrites: the choice to employ a standard Mg source (rather than the standard Al source employed for all other samples) was made in order to avoid the overlap of Co2p and $FeL_3M_{45}M_{45}$ peaks (both sets falling in the 775-795 eV interval with an Al source) and of the Fe2p and $CoL_2M_{23}M_{45}$ (^1P) peaks (all belonging to the 710-720 eV region).[154]

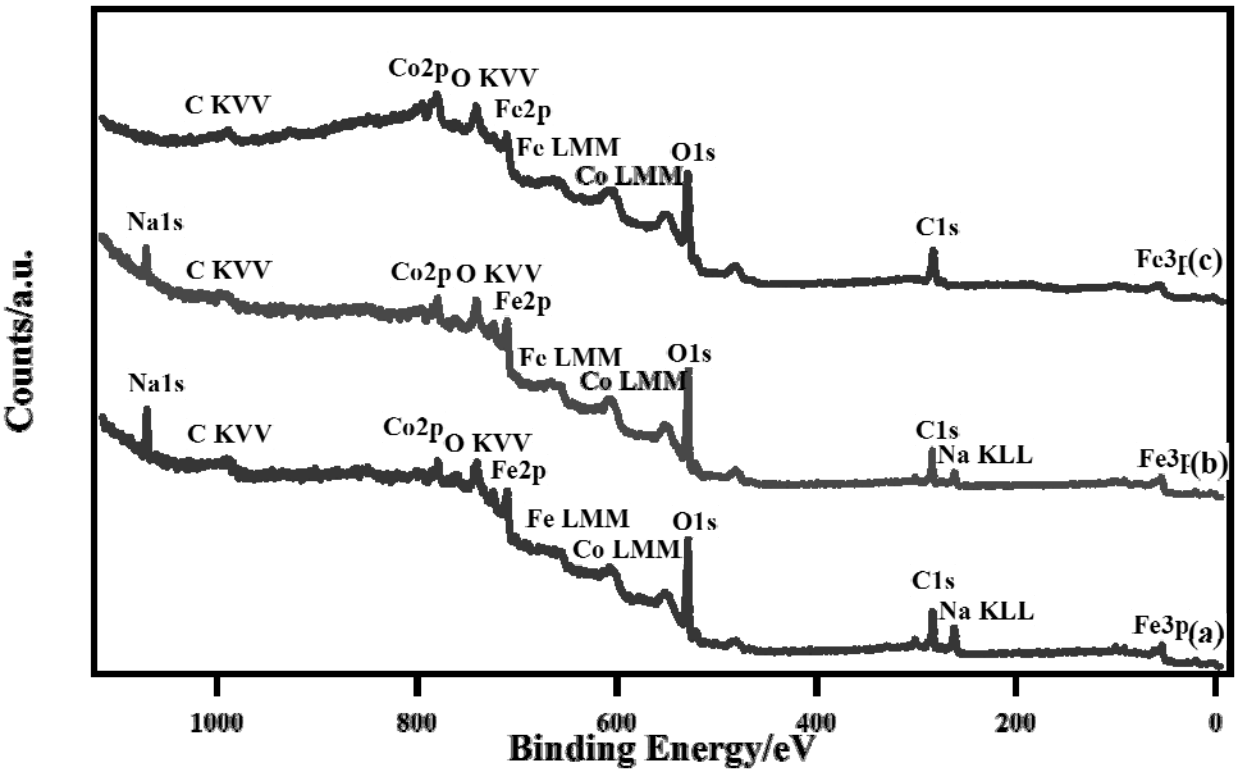

Figure 4.2.8 - *XPS spectra of samples (a) Co017, (b) I-Co001 and (c) S-Co011-4 with main peaks indexed (B.E. values are corrected for charging effects)*

Binding energy values [Tab 4.2.2] and surface composition [Tab. 4.2.3] were in agreement with the data reported in literature for $CoFe_2O_4$.[154, 159, 235, 236]

Sample	Element	Peak	B.E./eV
S-Co011-3	C	1s	284.6
	O	1s	530.0
	Fe	$2p_{3/2}$ and $2p_{1/2}$	710.6 and 723.8
	Co	$2p_{3/2}$ and $2p_{1/2}$	780.2 and 795.3
Co002	C	1s	284.6
	O	1s	530.0
	Fe	$2p_{3/2}$ and $2p_{1/2}$	710.1 and 723.2
	Co	$2p_{3/2}$ and $2p_{1/2}$	780.0 and 795.0
I-Co007	C	1s	284.6
	O	1s	529.4
	Fe	$2p_{3/2}$ and $2p_{1/2}$	710.6 and 723.7
	Co	$2p_{3/2}$ and $2p_{1/2}$	779.4 and 794.8

Table 4.2.2 – *B.E. values, surface and bulk concentrations for $CoFe_2O_4$ samples*

It is notable that the surface Fe/Co ratio very nearly matches the expected bulk ratio of 2, which in turn was also confirmed through ICP-AES analysis. This suggests that metal distribution is uniform throughout this compound, unlike other ferrites such as, for example, the strontium perovskite, where Sr displays a strong tendency to segregate on the surface[237, 238].

Sample	C %	Co %	Fe %	O %	Fe/Co atomic ratio (from XPS)	Fe/Co atomic ratio (from ICP-AES)
Co002	48.2	7.0	14.7	30.1	2.1	2.0
I-Co001	60.1	1.8	3.7	25.3	2.1	2.0
I-Co007	60.7	4.2	8.3	26.7	2.0	1.9
S-Co011-4	58.9	2.0	4.1	35.0	2.1	2.0

Table 4.2.3 - *Surface and bulk elemental concentrations for different $CoFe_2O_4$ samples*

Compounds prepared by coprecipitation and hydrothermal routes display the presence of surface sodium. This has been attributed to residual ions from the basification step in both syntheses (which is absent in the case of nonaqueous sol-gel synthesis). Further optimisation of the purification protocols (such as switching from filtration to centrifugation and introducing a sonication step between the various centrifuge steps) markedly reduced the sodium content.

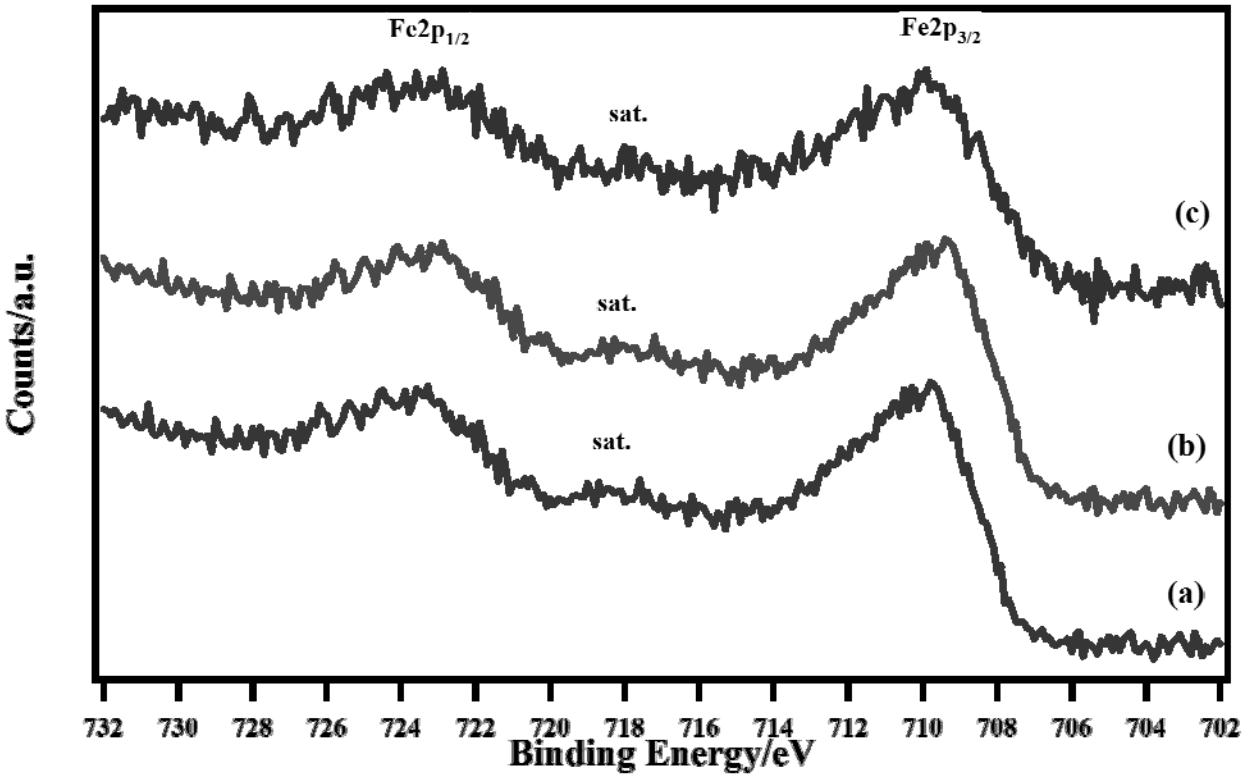

Figure 4.2.9 - *XPS spectra of the Fe2p region for samples (a) Co017, (b) I-Co001 and (c) S-Co011-4 (B.E. values are corrected for charging effects)*

More detailed scans of the Fe2p energy region showed that, in all the samples, the Fe2p peak [Fig. 4.2.9] displayed a satellite ($Fe2p_{3/2}$) peak at a B.E. value 8 eV higher than the main peak, which is consistent with compounds containing iron in a (III) oxidation state and with what expected for this type of compounds.[100, 154, 159, 181, 236, 239, 240] None of the samples [Fig. 4.2.9] displayed a satellite ($Fe2p_{3/2}$) peak at 6 eV higher than the main peak, thus showing that all detectable surface iron is present as Fe^{III}.[240] This is consistent with the data reported in literature[114, 241] and, despite the inversion of the spinel structures, confirms that, even in tetrahedral sites, iron maintains an oxidation state of (III). Mössbauer spectroscopy data (*vide infra*) also confirmed that all iron in the compound exists as Fe^{III}, as is expected for a spinel-type ferrite.

Mössbauer analysis of two samples calcined at 600°C and 900°C (Co008 and Co017 respectively) were carried out in order to gain further insight on the oxidation states and site geometry of iron in the materials. The spectra revealed that the cobalt ferrite is a partially inverse spinel where the inversion parameter γ is dependent on the heat treatment parameters (such as time, temperature and ramp).

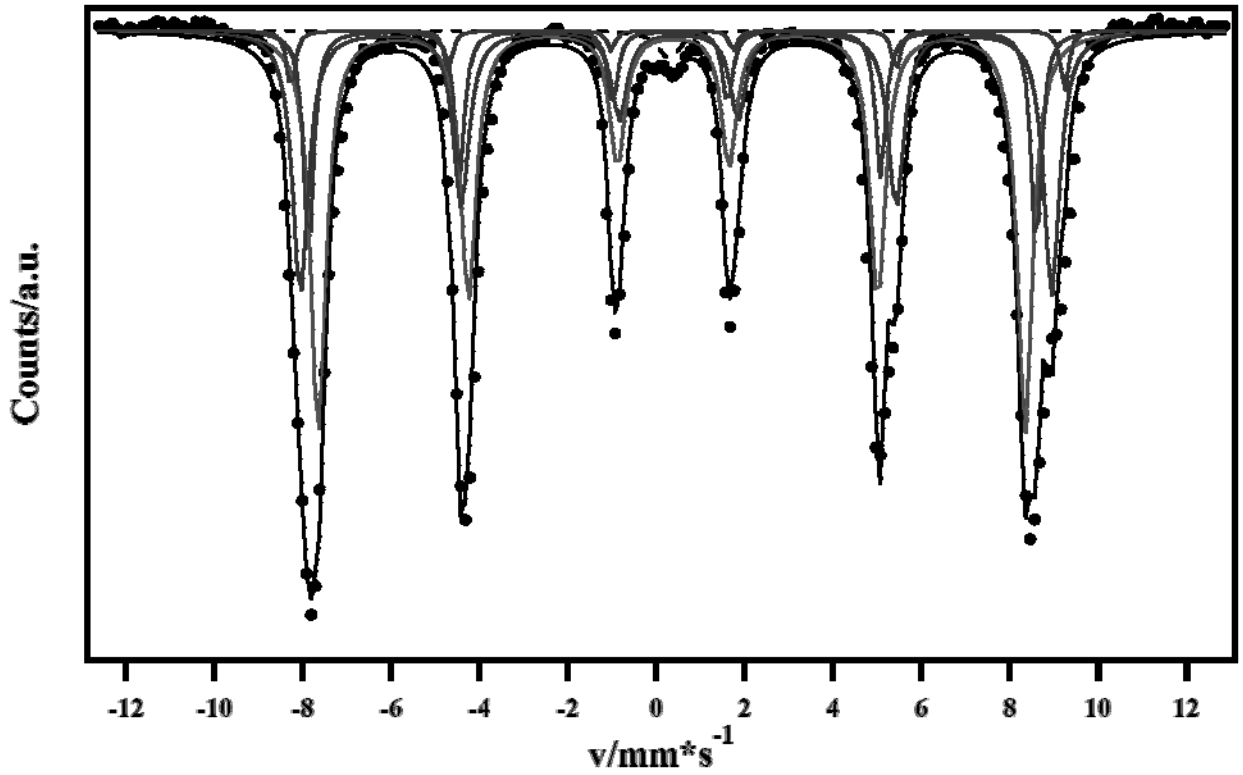

Figure 4.2.10 –*Mössbauer spectrum relative to sample Co008 collected at 14 K*

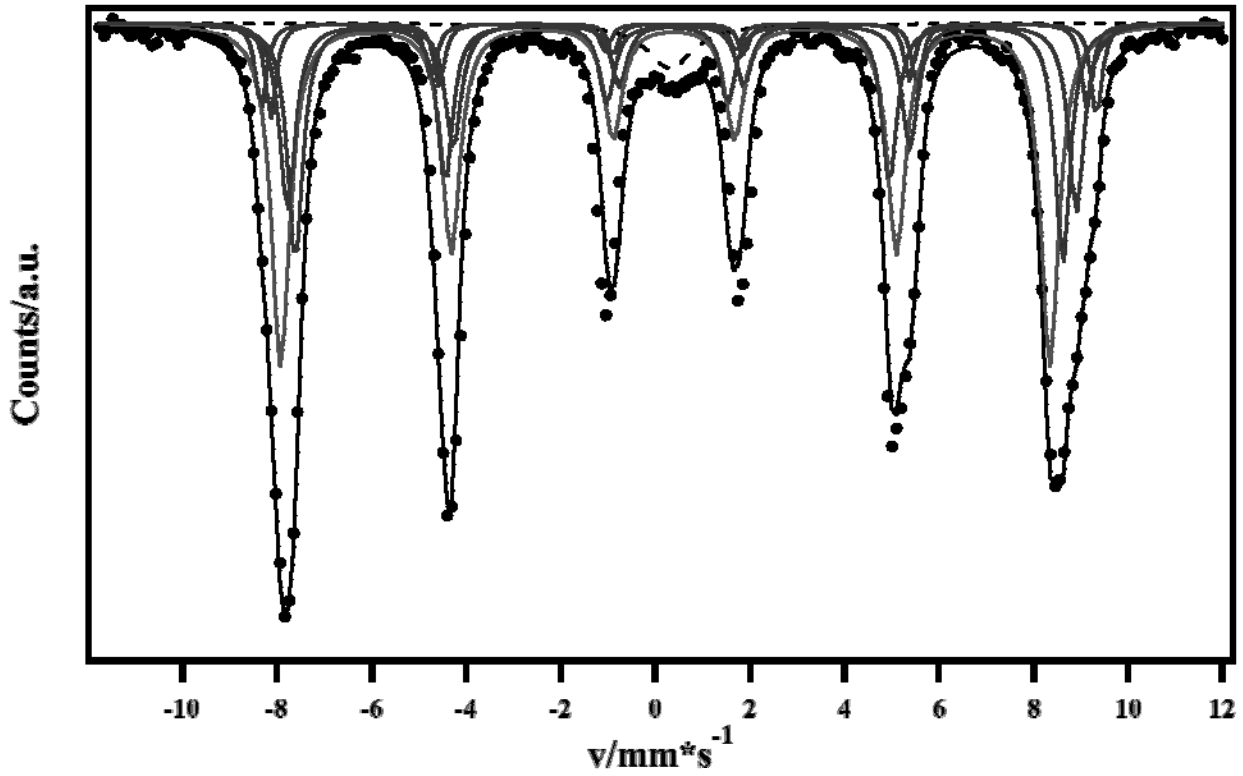

Figure 4.2.11 –*Mössbauer spectrum relative to sample Co017 collected at 14 K*

The 14 K spectra relative to the two samples [Fig. 4.2.10 and 4.2.11] were very similar to each other and consisted of an intense magnetic pattern combined with a small paramagnetic signal (1-2% of the total area) due to impurities. Both the magnetic patterns in the spectra were fitted by using two sextets in order to estimate γ. A degree of inversion equal to 0.92 was calculated for Co008, while a γ of 0.81 was estimated for Co017. The method employed in order to calculate the occupancy of Co^{2+} is described more in detail in section [6.3.3].
For Co008 *x* is equal to 0.05 and the formula can therefore be written as $(Co_{0.05}Fe_{0.95})[Co_{0.95}Fe_{1.05}]O_4$. For Co017 *x* is equal to 0.11, which leads to $(Co_{0.11}Fe_{0.89})[Co_{0.89}Fe_{1.11}]O_4$. By applying a binomial distribution, a B site with three subcomponents was calculated for Co008 (intensity ratios among the components 0.61:0.32:0.08), while for Co017 a B site with four subcomponents was calculated (intensity ratios among the components 0.28:0.40:0.23:0.07).

As mentioned in Chapter 2, ferrites in general, and spinel ferrites in particular, [7, 242] are widely known for displaying evident and important magnetic properties. Having confirmed through XRD and Mössbauer spectroscopy that the cobalt ferrites obtained were indeed spinels, and in order to gain greater insight on this aspect of the synthesised materials, magnetic induction measurements were performed. Hysteresis loops are reported in figures 4.2.12-4.2.13. Partially inverse and fully inverse mixed spinels in general display ferrimagnetic properties and are widely used as soft magnetic materials.[7] The cobalt spinel $CoFe_2O_4$ however is an exception to this rule,[242] behaving as a hard magnetic material.
The analysed cobalt spinels (one obtained through coprecipitation, the other through hydrothermal synthesis) yielded hysteresis cycles which are fully compatible with this premise, as a high magnetic field is required to close the hysteresis loop, showing that the oxide reaches saturation slowly (i.e. is difficult to magnetise) and displays a high magnetic inertia.

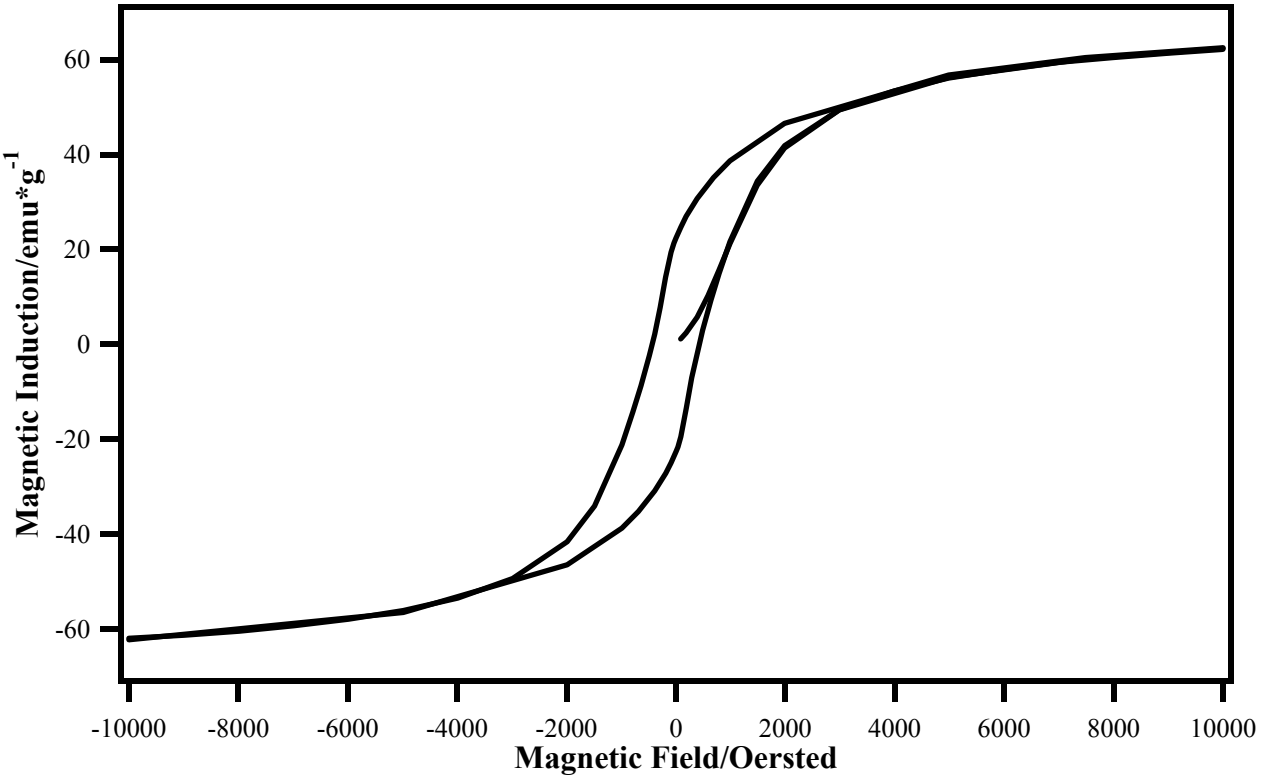

Figure 4.2.12 – *Room temperature hysteresis loop relative to sample Co017*

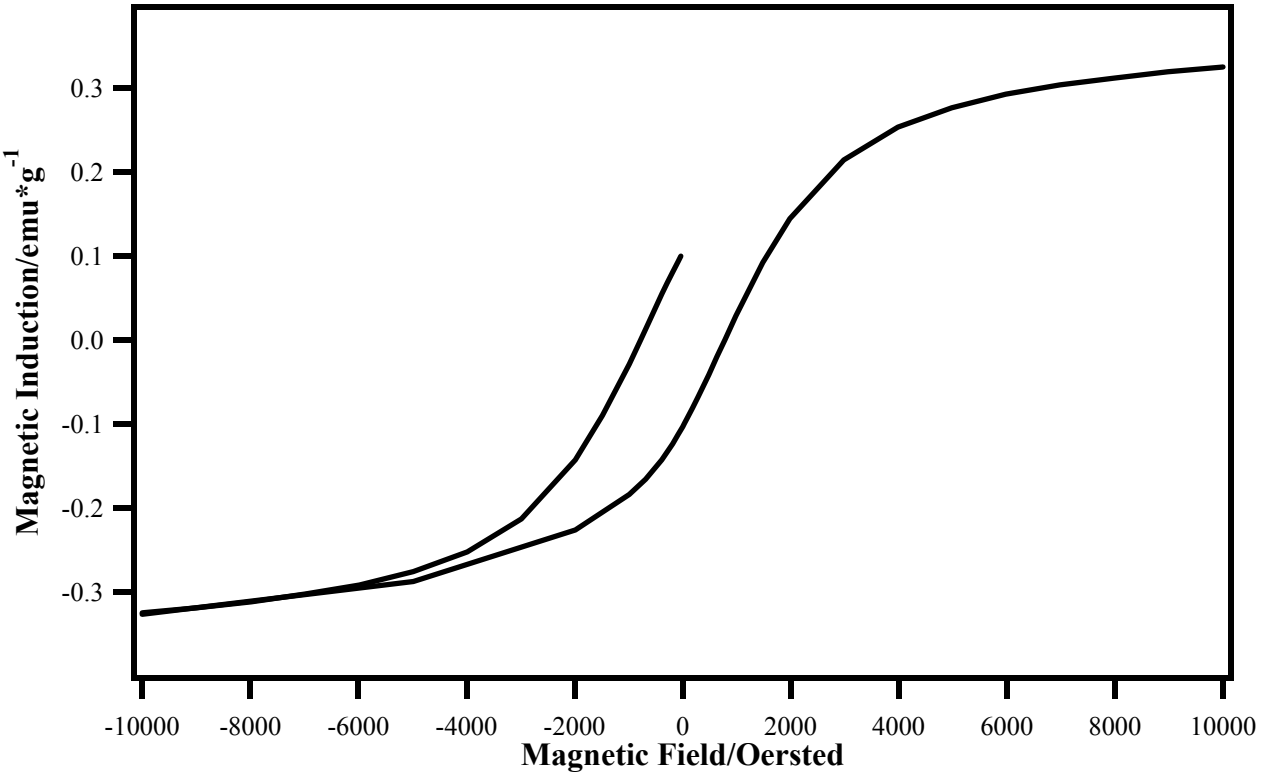

Figure 4.2.13 – *Room temperature hysteresis loop relative to sample I-Co007*

When comparing the loops relative to the two cobalt compounds [Fig. 4.2.12 and 4.2.13], it is very noticeable that the spinel obtained through hydrothermal synthesis shows a saturation magnetisation value which is two orders of magnitude smaller than its counterpart obtained through coprecipitation. This is probably due to the smaller size of the nanoparticles synthesised through hydrothermal synthesis (cfr. Tab. 4.2.1), as the lowering of saturation magnetisation with decreasing particle size has been documented in literature.[243] The two oxides however reach saturation with the same speed. The measured values for the coprecipitated sample are compatible with the data in literature.[60, 75]

In order to look into the chemical environments of the metals in the oxides, EXAFS measurements were carried out on sample S-Co011-3 [Fig. 4.2.14 and 4.2.15] using cobalt^{II} acetylacetonate as a reference for cobalt yielded a spectrum in agreement with expectations for a cobalt spinel, further confirming the data collected through previous investigations. In the case of the Fe edge spectrum, the low resolution is due to the proximity between the Co and Fe K edges (7709 and 7112 keV respectively), which forced to cut off the spectrum prematurely to eliminate the extra edge

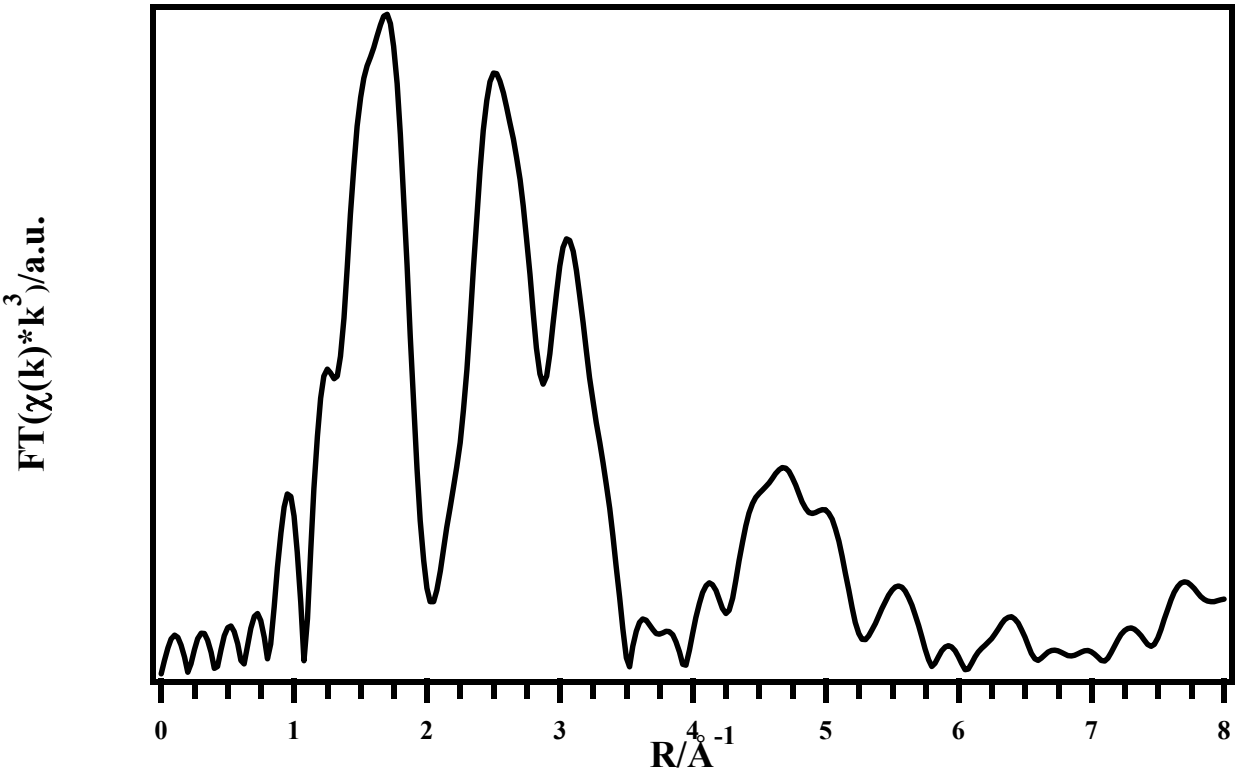

Figure 4.2.14 - *EXAFS spectrum (Co edge; Fourier transform) of sample S-Co011-3*

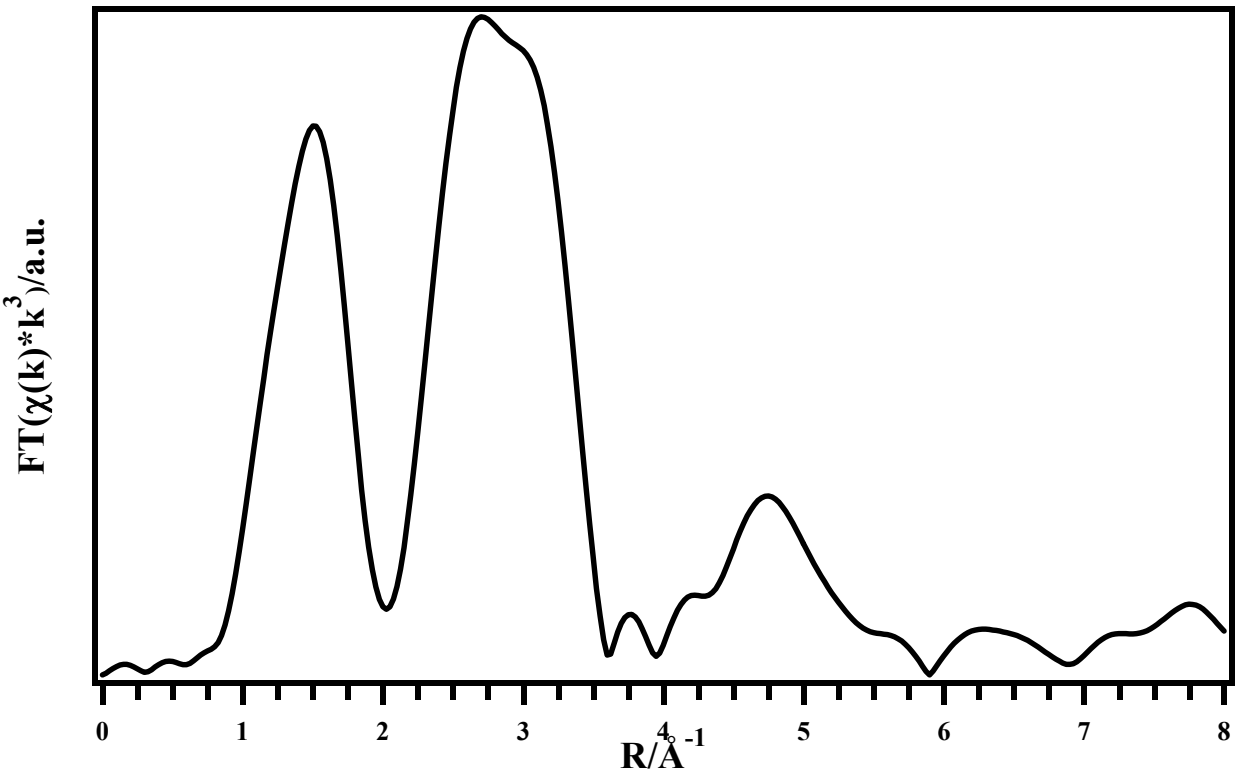

Figure 4.2.15 - *EXAFS spectrum (Fe edge; Fourier transform) of sample S-Co011-3*

Micro-Raman spectroscopy was employed to gain insight on the vibrational energy states within the compounds, as well as to assess the compositional uniformity throughout the powders.[244] Measurements were carried out on samples I-Co007 and Co017 yielded a similar response for both compounds [Fig. 4.2.16]. The two spectra display all the peaks which are characteristic of a cobalt

spinel,[245-247] with all main documented Raman-active phonon modes present.[248, 249] The minor differences between the spectra relative to the two samples can be attributed to differing particle size[246] [Tab. 4.2.1]. The Micro-Raman allowed to collect several spectra in different points on each sample, all of which yielded similar results, confirming the uniformity of the powder composition throughout the samples.

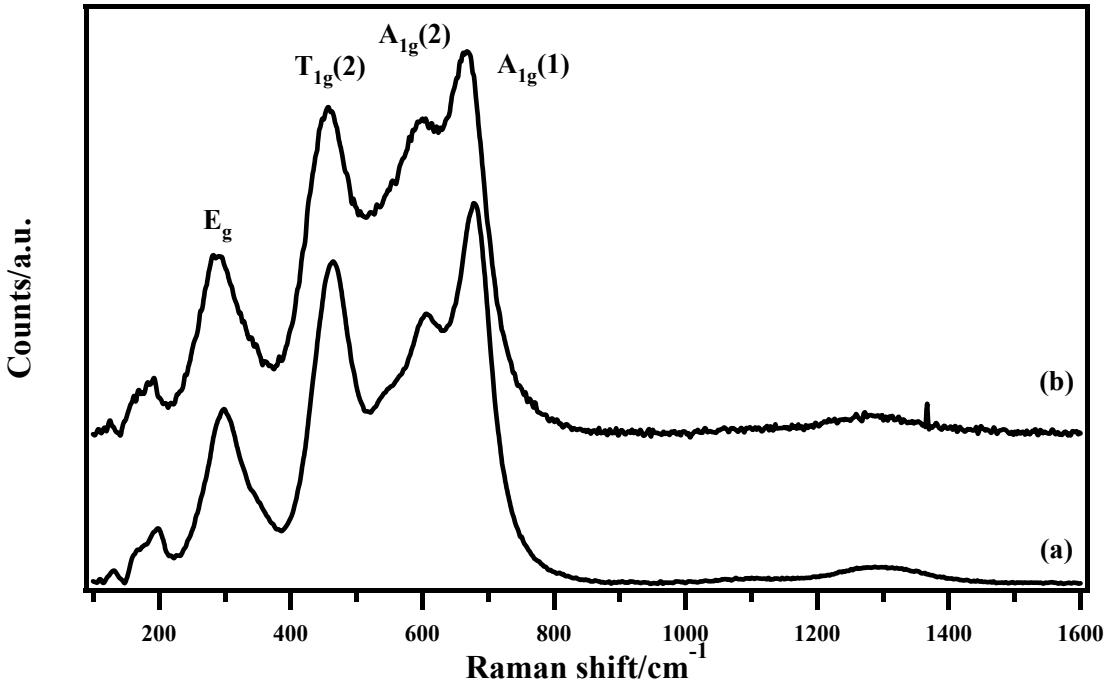

Figure 4.2.16 - *Room temperature micro-Raman spectra of samples (a) Co017 and (b) I-Co007*

In view of possible applications of these compounds in the field of catalysis and in order to assess their behaviour and stability under reducing conditions, as well as on their oxidation states of the component metals, TPR measurements were performed on sample Co017 [Fig 4.2.17].

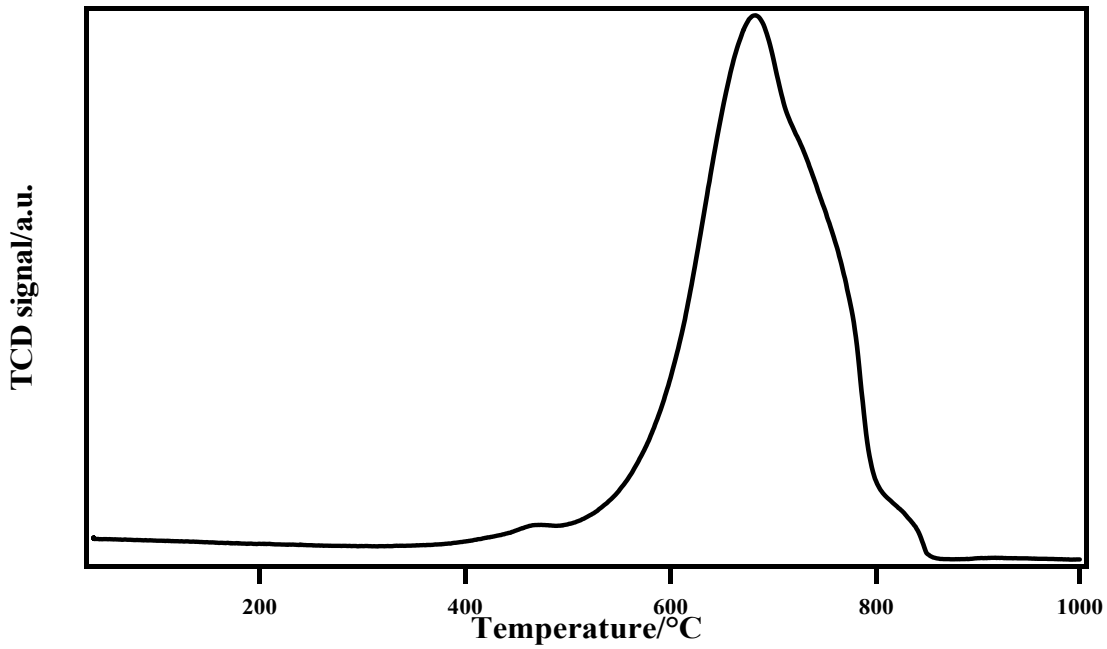

Figure 4.2.17 - *TPR analysis of sample Co017*

The results show that the compound is completely reduced at around 900°C. The hydrogen consumption measured (3.64 mol H_2 consumed per sample mol) are compatible with the reduction of both metals in $Co^{II}Fe^{III}{}_2O_4$ to an oxidation state of zero. Peak shape and positions are compatible with literature data.[119, 250]

Since coalescence phenomena were revealed to have a profound effect on the final product structural characteristics, TGA-DSC analysis was employed to investigate compound evolution during calcination (for coprecipitation) and to estimate the amount of residual organic moieties (for hydrothermal synthesis). The results obtained from these studies were similar, regardless of the nature of the tested compound (as all compounds underwent similar dehydration processes, followed by decomposition of the organic component), and will therefore be discussed in Par. 4.7 together with the results relative to the other compounds.

4.3 - Magnesium spinel ferrites $MgFe_2O_4$

Only coprecipitation synthesis afforded this type of ferrite, whereas both hydrothermal synthesis and nonaqueous sol-gel synthesis resulted in unidentifiable mixed or amorphous compounds (see Appendix 2).

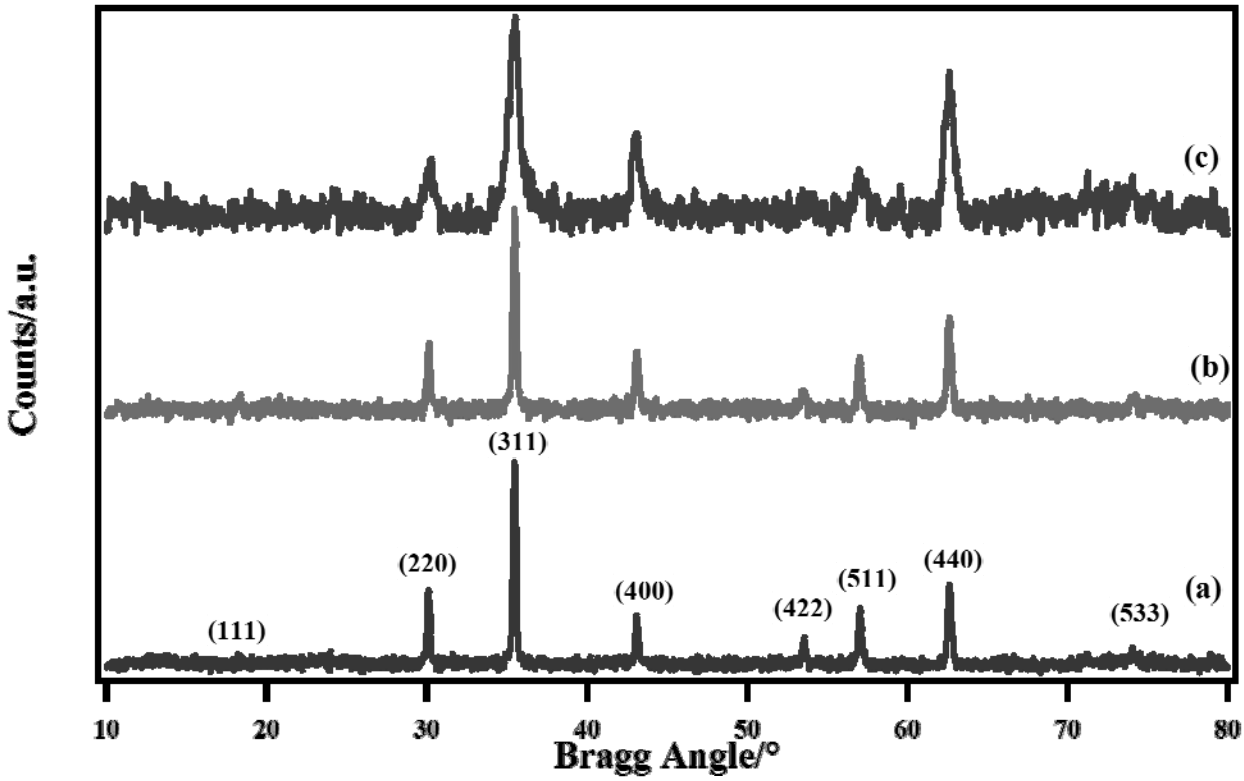

Figure 4.3.1 - *XRPD patterns of samples (a) Mg002, (b) Mg006-a and (c) Mg007 with main reflections indexed*

XRD analysis [Fig. 4.3.1] carried out on significant samples showed a crystalline structure similar to $CoFe_2O_4$, which is consistent with both compounds displaying a spinel structure. Subsequent Rietveld refinement was carried out based upon the information published by Barth et al.[156, 251] The fitted data revealed that this compound shows the same trends in response to treatment time and temperature as the cobalt spinel described above; i.e. crystallite size increases with increasing treatment temperature and with longer calcination times [Tab. 4.3.1].

In comparison to the other ferrites investigated during this Ph.D. thesis, magnesium ferrite crystallites tend to be smaller (nearly 50% in size) at a given set of calcination parameters.

Sample	Method	Treatment temperature and time	Crystallite mean size/nm (from Rietveld)
Mg002	Coprecipitation	900°C; 5 hours	85±5
Mg006-a	Coprecipitation	900°C; 1.5 hours	66±5
Mg007	Coprecipitation	600°C	14±5

Table 4.3.1 - *Crystallite mean size from main samples*

Similarly to other compounds, variations in aging times, basification speed and peptising agent amount did not lead to significant changes in the final product. Concerning the role of the Fe/Mg molar ratio, ICP-AES analyses carried out on the samples to obtain information on the bulk stoichiometry revealed that the magnesium spinel $MgFe_2O_4$, displays a higher Mg content than what expected from the stoichiometry (experimental Fe/Mg molar ratio is 1.54, rather than the expected 2). This finding was ascribed to the formation of a secondary $Mg_{1.55}Fe_{1.6}O_4$ phase whose XRD pattern was not distinguishable from the $MgFe_2O_4$ phase due to their great similitude (both structures belonging to the Fd-3m cubic group and having comparable *a* parameters).[252]

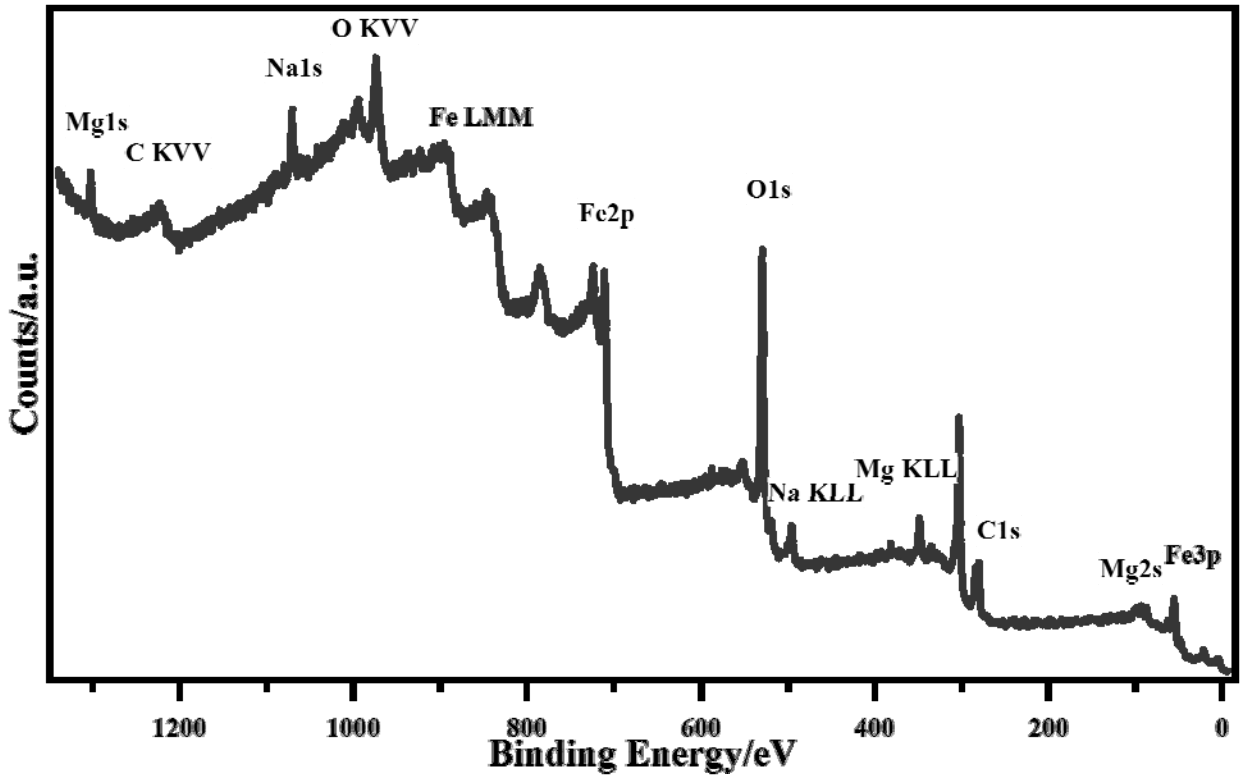

Figure 4.3.2 - *XPS survey spectrum of sample) Mg002 with main peaks indexed (B.E. values are corrected for charging effects)*

XPS analyses carried out on the compound [Fig. 4.3.2] yielded data in agreement with literature concerning general B.E. values [Tab. 4.3.2]. Surface concentrations display a higher Mg content than expected; this is however in agreement with the higher Mg content measured through ICP and has been attributed to the presence of the secondary magnesium ferrite phase.

Sample	C %	Mg %	Fe %	O %	Fe/Mg atomic ratio (from XPS)	Fe/Mg atomic ratio (from ICP-AES)
Mg002	56.2	5.7	8.4	29.6	1.4	1.5
	Element		**Peak**			**B.E./eV**
	C		1s			284.6
	O		1s			529.6
	Fe		$2p_{3/2}$ and $2p_{1/2}$			710.4 and 723.5
	Mg		2s and 1s			87.7 and 1302.4

Table 4.3.2 – *B.E. values, surface and bulk concentrations for $MgFe_2O_4$ sample Mg002*

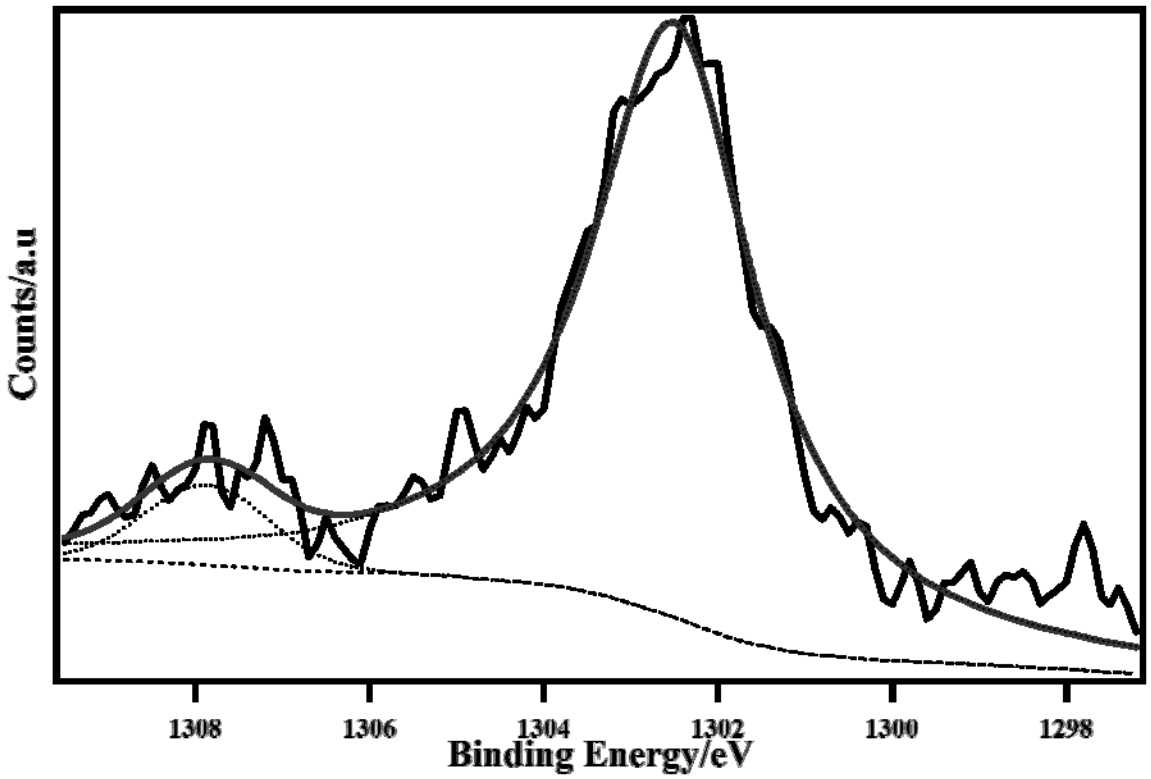

Figure 4.3.3 – *Deconvolution of the Mg1s peak for sample Mg002*
(B.E. values are corrected for charging effects)

The Mg1s peak [Fig. 4.3.3] was fitted with three components (1302.4 eV, 1303.3 eV and 1307.8 eV). The two lower energy peaks were assigned to magnesium in tetrahedral (1302.4 eV) and octahedral (1303.3 eV) sites within the ferrite crystal lattice.[240, 253] This is indicative of a partial inversion of the spinel, which in turn is consistent with the data present in literature.[254] The lower binding energy associated with Mg in tetrahedral sites is due to the lower number of oxygen atoms surrounding the sites.[240, 255] The highest-energy peak was attributed to a plasmon.[154]

4.4 - Manganese ferrites $MnFe_2O_4$ and $MnFeO_3$

Manganese ferrites were, as previously mentioned, successfully synthesised as single-phase crystalline powders both in the perovskite form $MnFeO_3$ (through coprecipitation) and in the spinel form $MnFe_2O_4$ (through nonaqueous sol-gel synthesis and hydrothermal synthesis). Among the compounds explored during this Ph.D. thesis, this is the only type of ferrite which was successfully prepared in both forms; the fact that the product type is dependent on the choice of synthesis protocol is both notable and interesting, as it allows the operator to tune his activity based upon the desired final form of this product.

When using the nonaqueous sol-gel protocol, the synthesis of the manganese spinel $MnFe_2O_4$ was found to be particularly successful when the ferric acetylacetonate precursor was employed. This precursor however, presented the drawback of giving products in the form of very fine powders, which turned out to be very difficult to separate from the synthesis mixture, leading to very low yields (< 20%).

Initial synthetic attempts carried out with short reaction times and low-speed centrifugation were thus unsuccessful. Syntheses carried out with ferrous acetylacetonate and ferrous acetate yielded a greater quantity of product, but such precipitates were always impure (displaying the presence of compounds such as MnO) or were partially amorphous, as was evidenced by the fact that the baseline in the XRD patterns relative to those samples displayed a broad Gaussian-like peak instead of being linear. Further attempts to prepare the product were carried out using higher temperatures and longer reaction times. These syntheses allowed to prepare pure nanosized $MnFe_2O_4$, with the best products being obtained by reacting ferric acetylacetonate and manganese^{II} acetate at 200°C for 45 minutes.

As was the case with previously addressed compounds, the crystallite size of compounds prepared through coprecipitation was revealed to be sensitive to both calcination time and temperature, with temperature being the preponderant factor. In comparison to cobalt and magnesium ferrites, the difference in size between samples calcined at 600 and 900°C (70 and 129 nm respectively) was not as highly significant.

Concerning hydrothermal synthesis, the protocol was found to be sensitive to the nominal ratio between oxalic acid and the metals: when acid was added in excess of stoichiometry (i.e., the acid nominal concentration was higher than the sum of the nominal concentration of manganese and one and a half times the nominal concentration of iron as described in the empirical equation 4.4.1), numerous unidentified reflections appeared in the resulting XRD patterns, indicating the formation of one or more undesired secondary phases.

$$[Acid]_0 = [Fe^{3+}]_0 * 1.5 + [Mn^{2+}]_0 \qquad (4.4.1)$$

This phenomenon did not occur in the coprecipitation syntheses, probably due to the fact that the calcination step allowed any organic by-products resulting from the excess acid to decompose to carbon dioxide and be eliminated.

Based upon the collected XRPD patterns, crystallite size was initially estimated by applying the Scherrer formula on the (400) reflection of the spinel ferrite [Fig. 4.4.1] or the (222) reflection of

the perovskite [Fig 4.4.2]. In both cases, the reflection was chosen because of its intensity and the fact that it was well separated from other reflections.

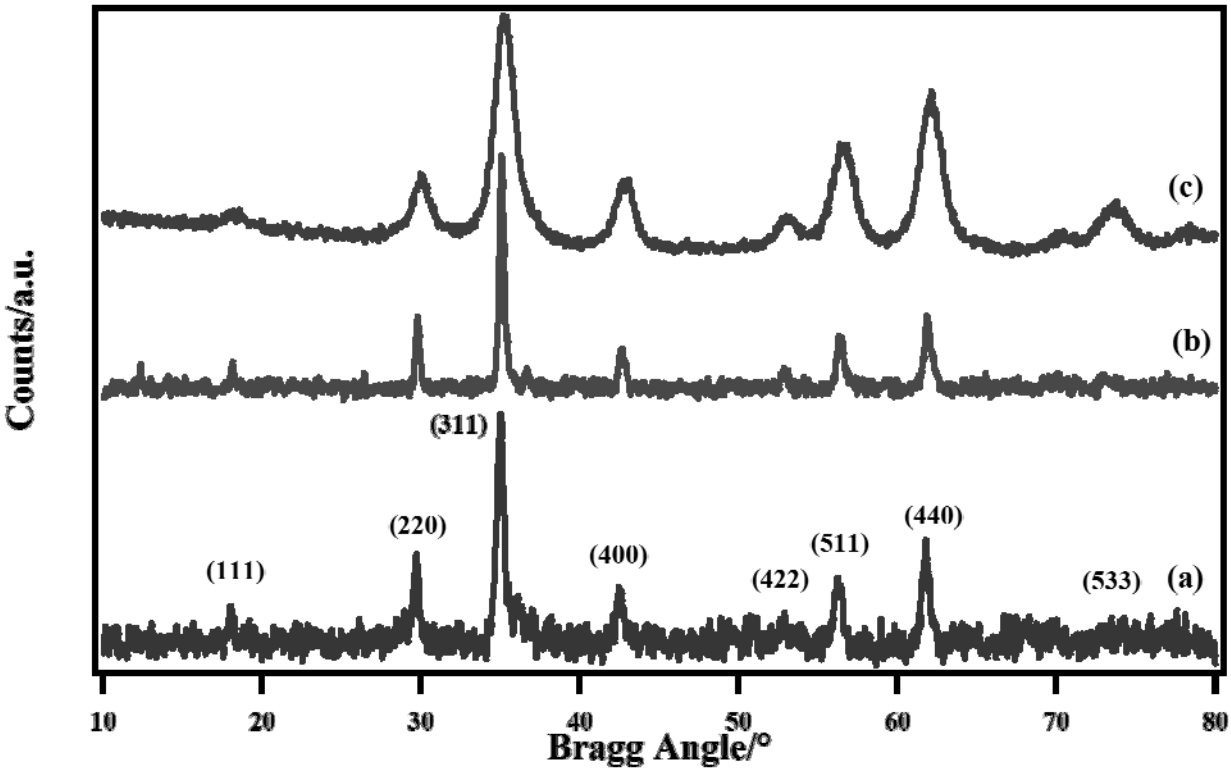

Figure 4.4.1 - *XRPD patterns of spinel samples (a) I-Mn002, (b) I-Mn007 and (c) S-Mn007-3 with main reflections indexed*

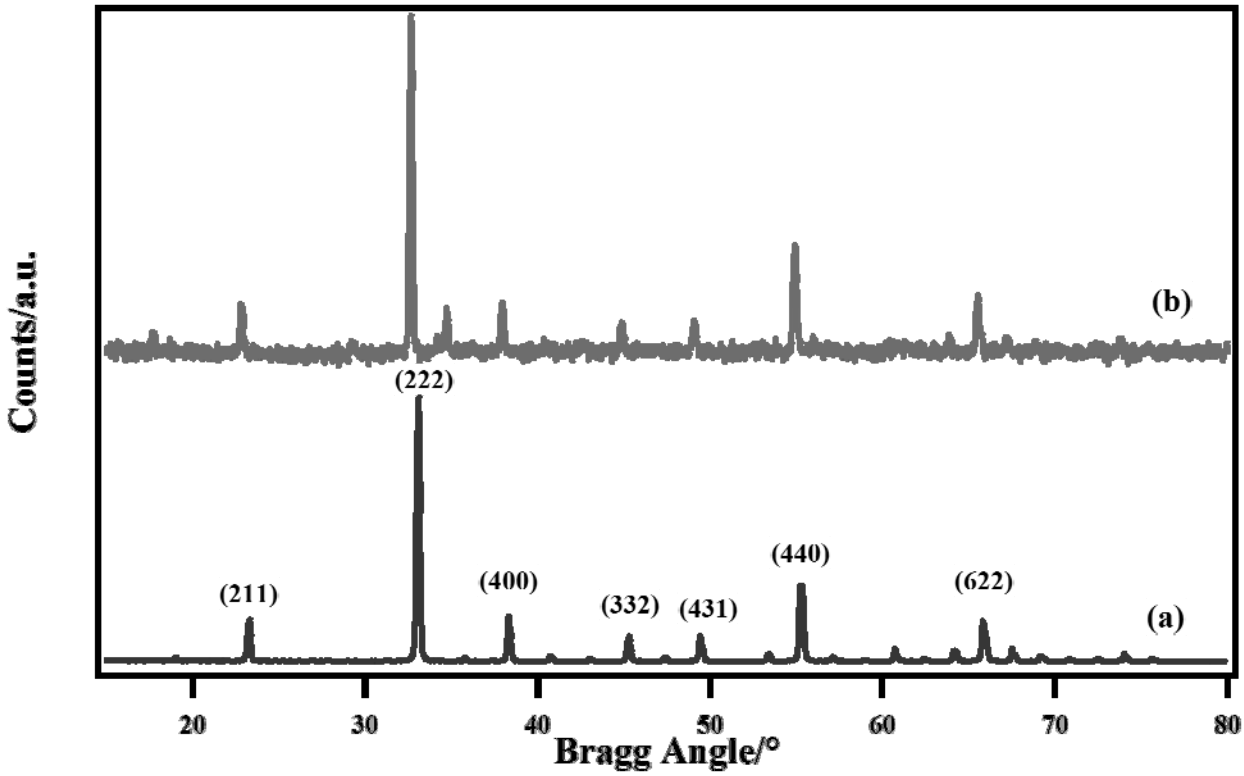

Figure 4.4.2 - *XRPD patterns of perovskite samples (a) Mn001 and (b) Mn0011 with main reflections indexed*

In a later stage, Rietveld refinement carried out through the use of the MAUD program on samples [Tab 4.4.1] yielded a slightly higher value for crystallite size than that obtained through the Scherrer formula; this difference can probably be attributed to errors in determining the correct reflection data whilst carrying out the Scherrer analysis (which is inherently less precise).

Sample	Method	Found structure	Treatment temperature and time	Crystallite mean size/nm (from Rietveld)
S-Mn004-1	Nonaqueous sol-gel	$MnFe_2O_4$	200°C; 30 minutes	8±2
S-Mn005-1	Nonaqueous sol-gel	$MnFe_2O_4$	180°C; 15 minutes	8±2
S-Mn005-2	Nonaqueous sol-gel	$MnFe_2O_4$	180°C; 15 minutes	8±2
S-Mn006-1	Nonaqueous sol-gel	$MnFe_2O_4$	180°C; 15 minutes	8±2
S-Mn006-2	Nonaqueous sol-gel	$MnFe_2O_4$	180°C; 15 minutes	8±2
S-Mn006-6	Nonaqueous sol-gel	$MnFe_2O_4$	200°C; 25 minutes	9±2
S-Mn007-3	Nonaqueous sol-gel	$MnFe_2O_4$	200°C; 45 minutes	9±2
Mn008	Coprecipitation	$MnFeO_3$	600°C; 5 hours	70±5
Mn006-b	Coprecipitation	$MnFeO_3$	900°C; 2.5 hours	115±5
Mn001	Coprecipitation	$MnFeO_3$	900°C; 5 hours	129±5
Mn011	Coprecipitation	$MnFeO_3$	900°C; 5 hours	133±5
Mn020	Coprecipitation	$MnFeO_3$	900°C; 5 hours	140±5
Mn020-b	Coprecipitation	$MnFeO_3$	See Fig. 4.2.4	68±1 (at 900°C)
I-Mn002	Hydrothermal	$MnFe_2O_4$	135°C; 24 hours	20±4
I-Mn007	Hydrothermal	$MnFe_2O_4$	135°C; 24 hours	39±4
I-Mn012-2	Hydrothermal	$MnFe_2O_4$	135°C; 2 hours	33±1
I-Mn012-4	Hydrothermal	$MnFe_2O_4$	135°C; 4 hours	24±1
I-Mn013	Hydrothermal	$MnFe_2O_4$	100°C; 24 hours	36±2
I.Mn014	Hydrothermal	$MnFe_2O_4$	75°C; 24 hours	35±2

Table 4.4.1 - *Crystallite size of significant $MnFeO_3$ and $MnFe_2O_4$ samples*

Rietveld refinement for crystal structure resolution was carried out by utilizing the MEEM model and the Genetic refinement model, using as a starting point the data published in literature by Pauling[155] and by Montoro[256] for the perovskite and the spinel respectively, allowing for a good fitting of the patterns to be achieved.

Like in the case of the cobalt spinel, hydrothermal syntheses were carried out with different reaction times. The resulting products [Fig 4.4.3] revealed that formation of the manganese spinel occurs under hydrothermal conditions with a reaction time as short as 2 hours, without significant changes in crystallite characteristics, showing that the reaction has already reached completion by that time.

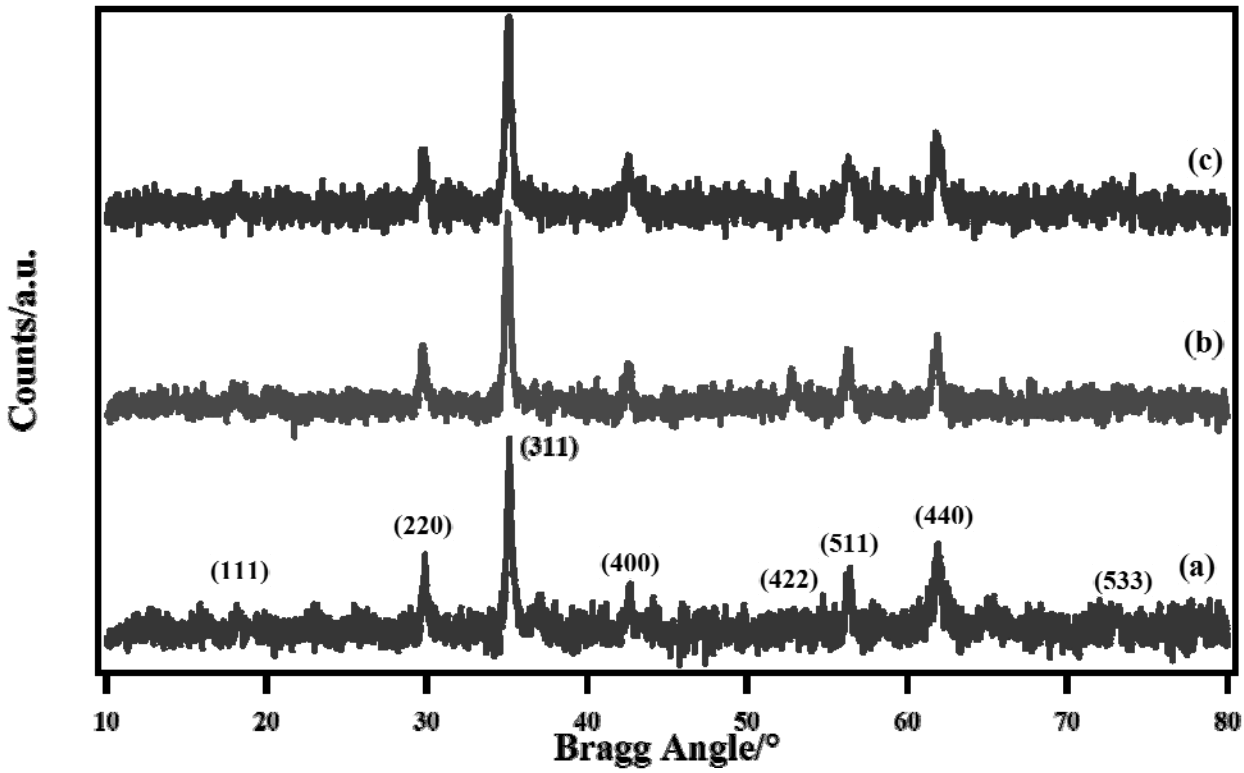

Figure 4.4.3 - *XRPD patterns of sample I-Mn012 with reaction times of (a) 1, (b) 2 and (c) 4 hours at 135°C*

Analogously to what was done with the cobalt spinel, TPXRD patterns were collected from an uncalcined manganese perovskite sample obtained through coprecipitation. The temperature profile program employed was the same which was used for the cobalt sample [Fig 4.2.4]. The gathered data [Fig 4.4.4] shows that, whilst a perovskite phase was clearly visible from 600°C onwards, extra reflections could be spotted, which however gradually disappeared with rising temperature, vanishing completely at 900°C. These reflections were compatible with a manganese spinel phase, indicating that probably the two phases (spinel and perovskite) form simultaneously, and the spinel is then gradually converted to a perovskite. Given the different Fe/Mn ratios in the two phases, a third undetected Mn-rich phase (probably MnO and/or the spinel-like Mn_3O_4) can be inferred which is converted to perovskite together with the spinel. Concerning crystallite sizes, the sample yielded results similar to the cobalt spinel investigated through TPXRD (see Par. 4.2), as the patterns evidence much smaller crystallites (roughly half the size) compared to perovskite samples calcined normally. As was the case for the cobalt spinels, this result was ascribed to the sharper heating ramp employed [Fig 4.2.4].

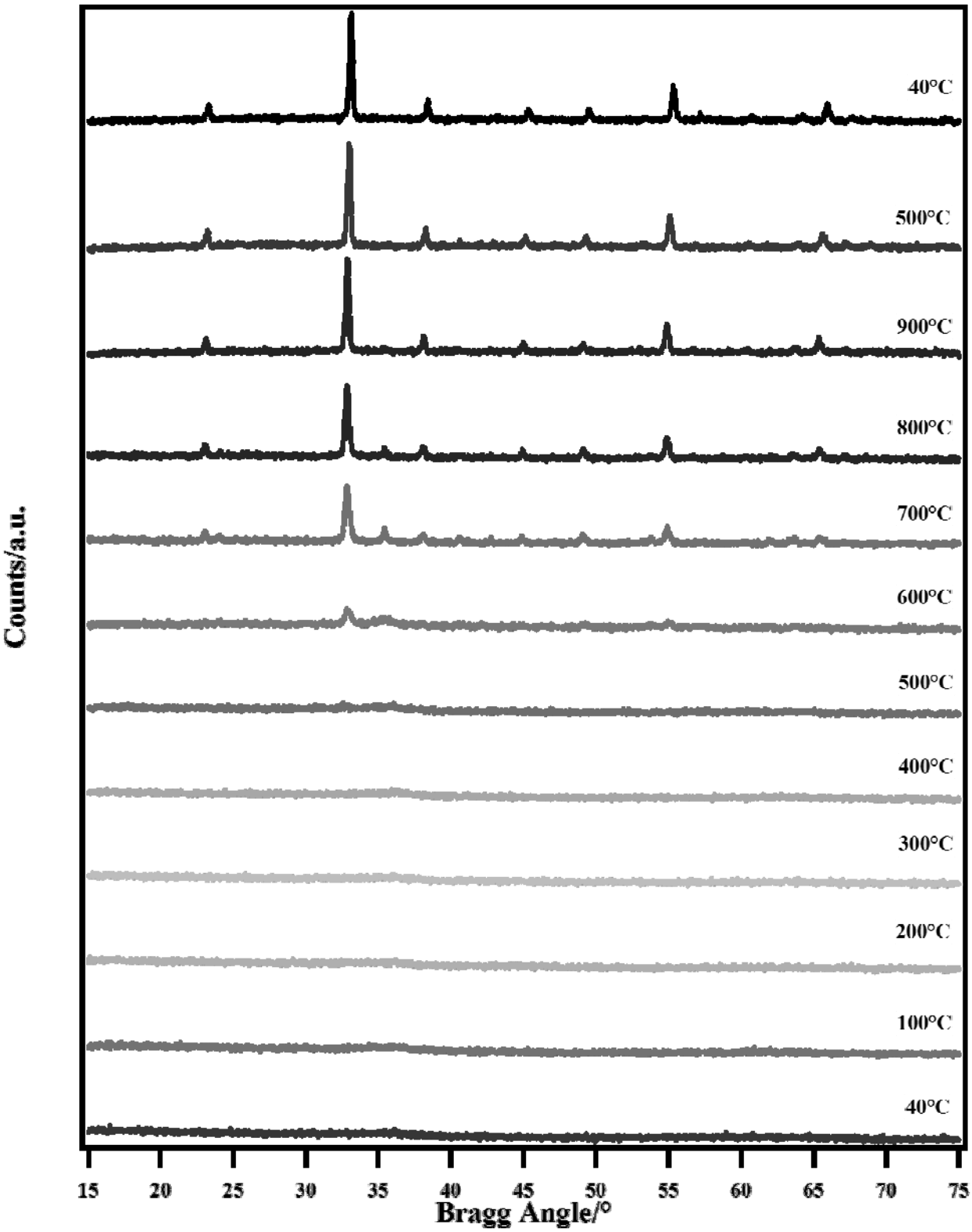

Figure 4.4.4 - *XRPD patterns collected at different temperatures from manganese ferrite sample Mn020-b*

The presence of these extra phases in consistent with the preliminary data gathered from Mössbauer analysis on samples with low treatment temperatures which detected multiple phases in a $MnFeO_3$ sample calcined at 600°C.

In order to confirm the data on crystallite size obtained through XRPD pattern refinement and to gain further insight on the morphology of the compound, transmission electron microscopy was

performed on samples S-Mn007-3 [Fig. 4.4.5] and Mn001 [Fig 4.4.6]. Similarly to with the images gathered from cobalt spinels, the sample synthesised through the nonaqueous sol-gel process displayed crystallites with a tendency to agglomerate into clusters, even though the single crystallites are still visible at the higher resolutions [Fig. 4.4.5 - f)]. Both in the case of ferrites prepared through nonaqueous sol-gel synthesis and coprecipitation, the crystallite size displayed is consistent with the estimates resulting from XRD analysis (9 and 129 nm respectively). Like in the case of cobalt, the larger clusters were visible at the lowest resolutions [Fig. 4.4.5 - a)]: these were proven to be due to non optimal dispersion of the compound within the liquid, as further dilution of the suspension allowed for single particles to become visible [Fig. 4.4.5 - b)-f)]. Particles obtained through coprecipitation are much larger (by roughly 2000%), but in agreement with the data resulting from XRD.

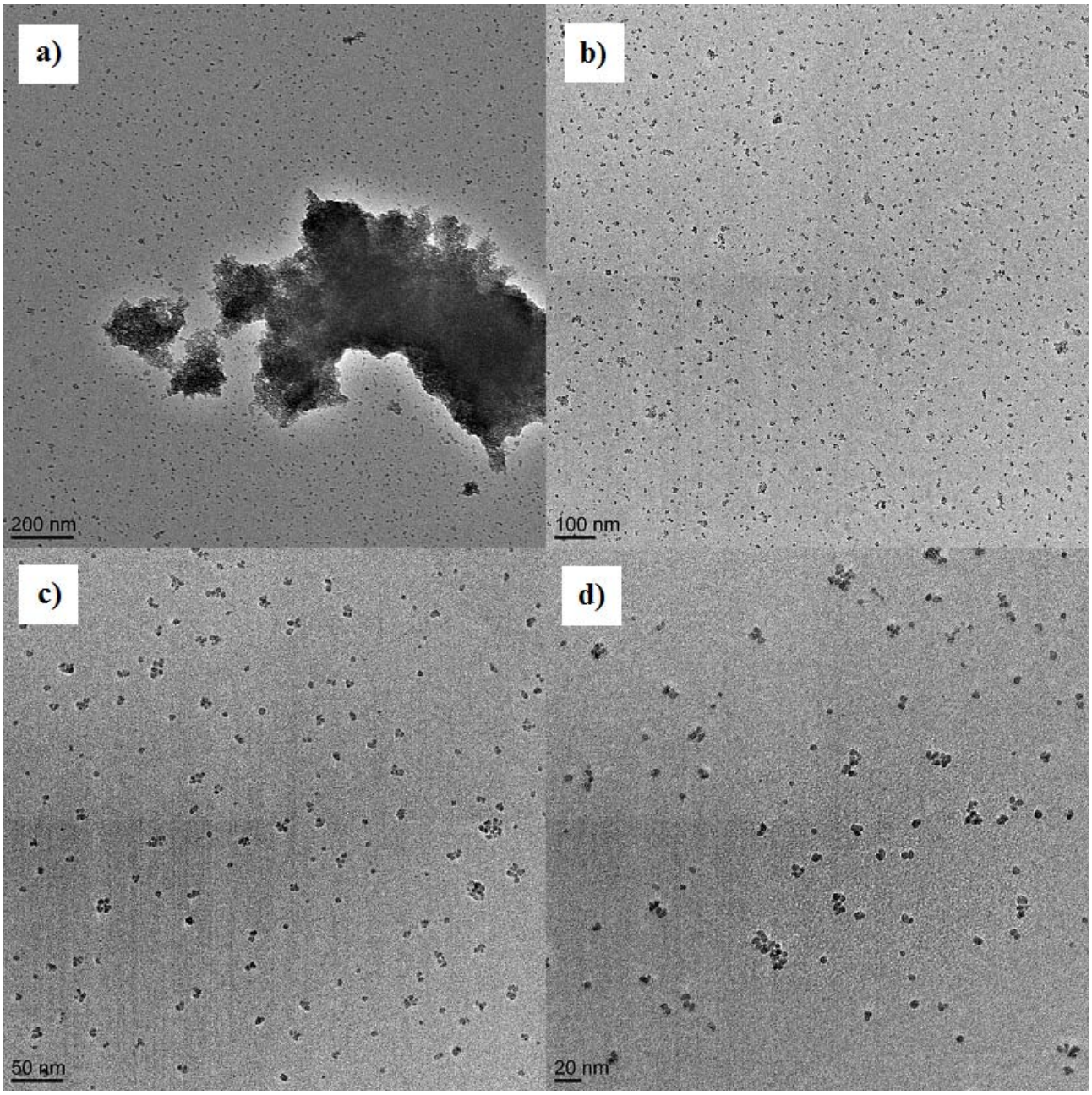

Figure 4.4.5 - *TEM micrographs of sample S-Mn007-3 at various resolutions*

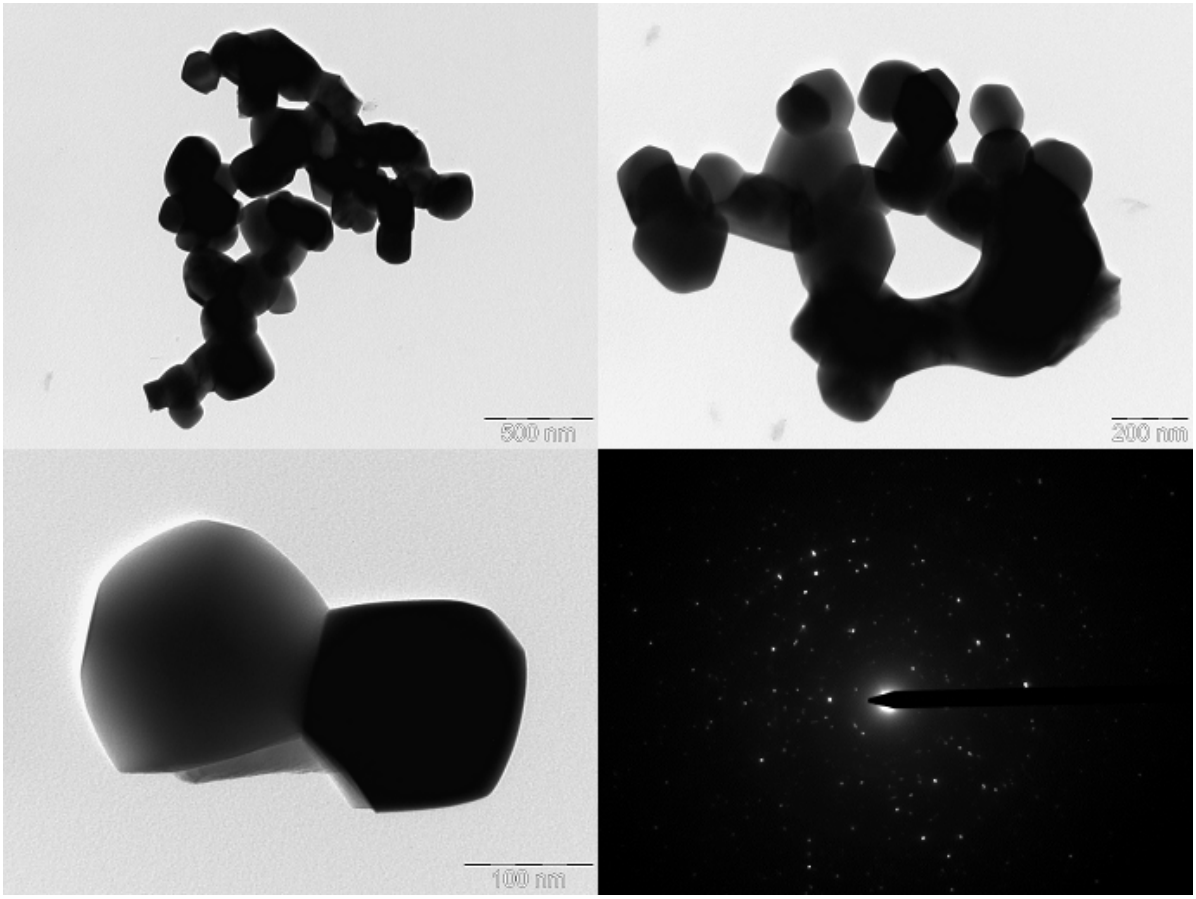

Figure 4.4.6 - *TEM micrographs of sample Mn001 at various resolutions*

Similarly to the magnesium and cobalt samples, XPS analyses were carried out on significant samples [Fig 4.4.7]

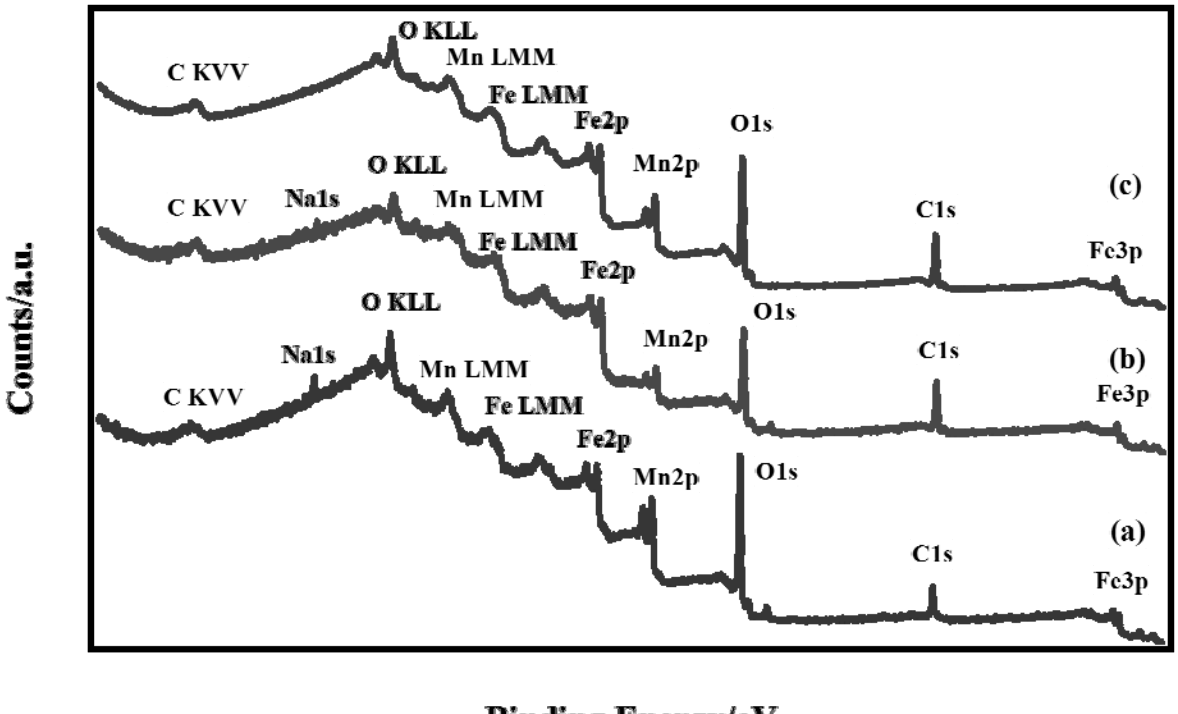

Figure 4.4.7 - *XPS spectra of samples (a) Mn015, (b) I-Mn002 and (c) S-Mn030-4 with main peaks indexed (B.E. values are corrected for charging effects)*

Binding energy values [Tab. 4.4.2] were in agreement with literature data for these types of compounds.[152, 154, 159, 181, 239]

Sample	Compound	Element	Peak	B.E./eV
S-Mn030-3	$MnFe_2O_4$	C	1s	284.6
		O	1s	529.5
		Fe	$2p_{3/2}$ and $2p_{1/2}$	710.5 and 723.6
		Mn	$2p_{3/2}$ and $2p_{1/2}$	640.9 and 652.7
Mn015	$MnFeO_3$	C	1s	284.6
		O	1s	529.3
		Fe	$2p_{3/2}$ and $2p_{1/2}$	710.1 and 723.1
		Mn	$2p_{3/2}$ and $2p_{1/2}$	640.3 and 651.3
I-Mn007	$MnFe_2O_4$	C	1s	284.6
		O	1s	529.3
		Fe	$2p_{3/2}$ and $2p_{1/2}$	710.5 and 723.5
		Mn	$2p_{3/2}$ and $2p_{1/2}$	641.0 and 652.8

Sample	C%	O%	Fe%	Mn%	Fe/Mn atomic ratio (XPS)	Fe/Mn atomic ratio (ICP-AES)
Mn015	48.7	37.1	7.1	7.1	1.1	1.0
I-Mn007	73.6	18.7	5.0	2.7	2.0	1.9

Table 4.4.2 – *B.E. values and surface and bulk atomic concentrations for significant manganese ferrite samples*

As was the case for cobalt ferrites, more detailed scans in the Fe2p energy region showed that in all the samples (both spinel and perovskite), the Fe2p peak [Fig. 4.4.8] displayed a satellite ($Fe2p_{3/2}$) peak at a B.E. value 8 eV higher than the main peak, which is consistent with compounds containing iron in a (III) oxidation state and in agreement with expectations for the synthesised compounds. Although the perovskite $MnFeO_3$ could conceivably contain iron in an oxidation state of IV, a $Mn^{III}Fe^{III}O_3$ type ferrite was considered more likely; this was further confirmed by Mössbauer spectroscopy (*vide infra*).[154, 159, 181, 236, 239, 240] The main difference in the iron peaks between the two types of ferrite is that the perovskite peaks have a lower B.E. by about 0.5 eV. The Fe^{II} satellite ($Fe2p_{3/2}$) peak at 6 eV higher than the main peak is absent in all samples, showing that all surface iron detected is Fe^{III}.[240] This is in agreement with the data reported in literature.[114, 241]

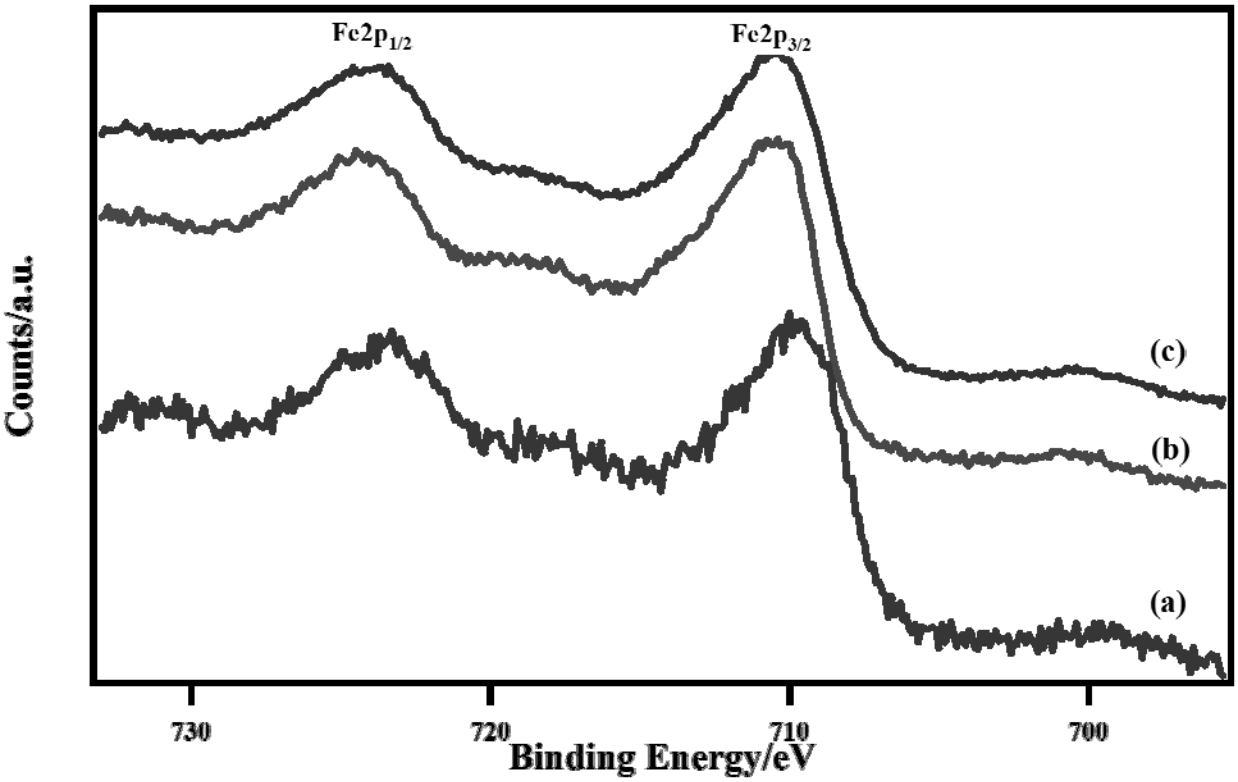

Figure 4.4.8 - *XPS spectra of the Fe2p region for samples (a) Mn015, (b) I-Mn007 and (c) S-Mn030-3 (B.E. values are corrected for charging effects)*

The Mn2p peaks relative to samples resulting from coprecipitation [Fig. 4.4.9] and hydrothermal synthesis [Fig. 4.4.10] were fitted with two pairs of peaks separated by 11 eV (the typical $Mn_{3/2}$-$Mn_{1/2}$ distance)[154] [Tab. 4.4.5]; two peaks, at 640.3 and 641.9 eV, were attributed to $Mn2p_{3/2}$ and the remaining two, at 651.3 and 652.9 eV, to $Mn2p_{1/2}$. For each component, the lowest energy peak was attributed to Mn^{II}, and the highest energy peak to Mn^{IV}.[239] In the case of hydrothermal synthesis, the co-presence of surface manganese in these two oxidation states is consistent with reported data on $MnFe_2O_4$.[99, 239]

Sample	Peak B.E./eV	Region	Attribution
Mn015	640.3	$2p_{3/2}$	Mn^{II}
	641.9	$2p_{3/2}$	Mn^{IV}
	651.3	$2p_{1/2}$	Mn^{II}
	652.9	$2p_{1/2}$	Mn^{IV}
I.Mn007	640.1	$2p_{3/2}$	Mn^{II}
	641.8	$2p_{3/2}$	Mn^{IV}
	651.2	$2p_{1/2}$	Mn^{II}
	652.9	$2p_{1/2}$	Mn^{IV}

Table 4.4.5 – *Peak positions and attributions for the Mn2p peak deconvolution (B.E. values corrected for surface charging)*

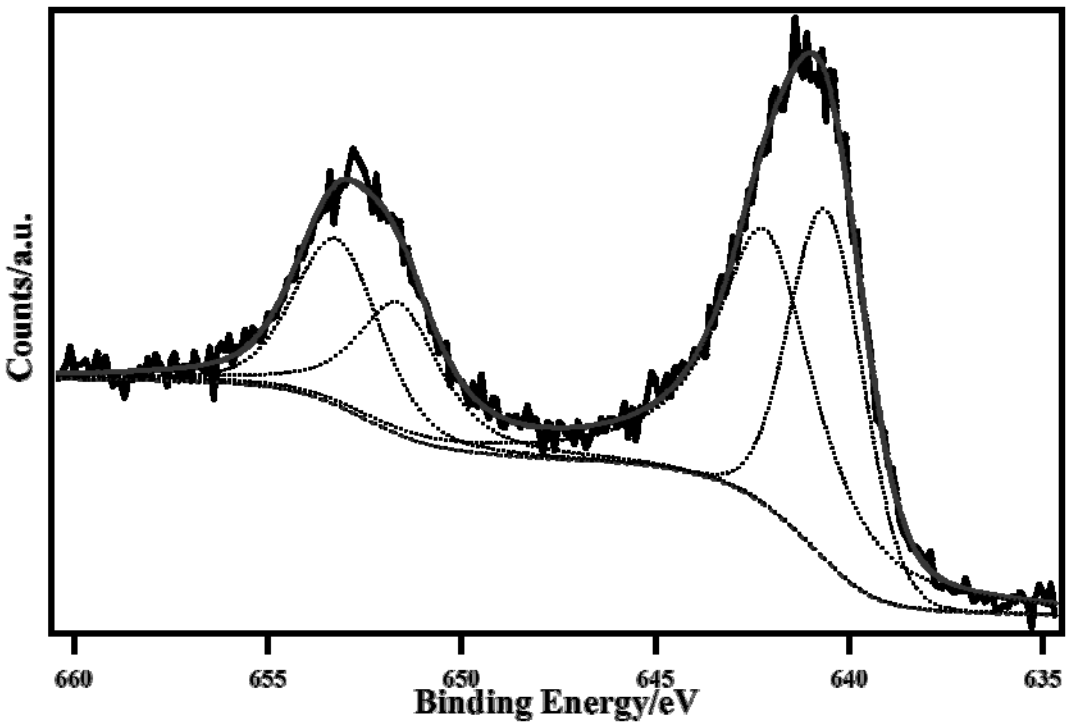

Figure 4.4.9 – *Deconvolution of the Mn2p peak for sample Mn015 (B.E. values are corrected for charging effects*

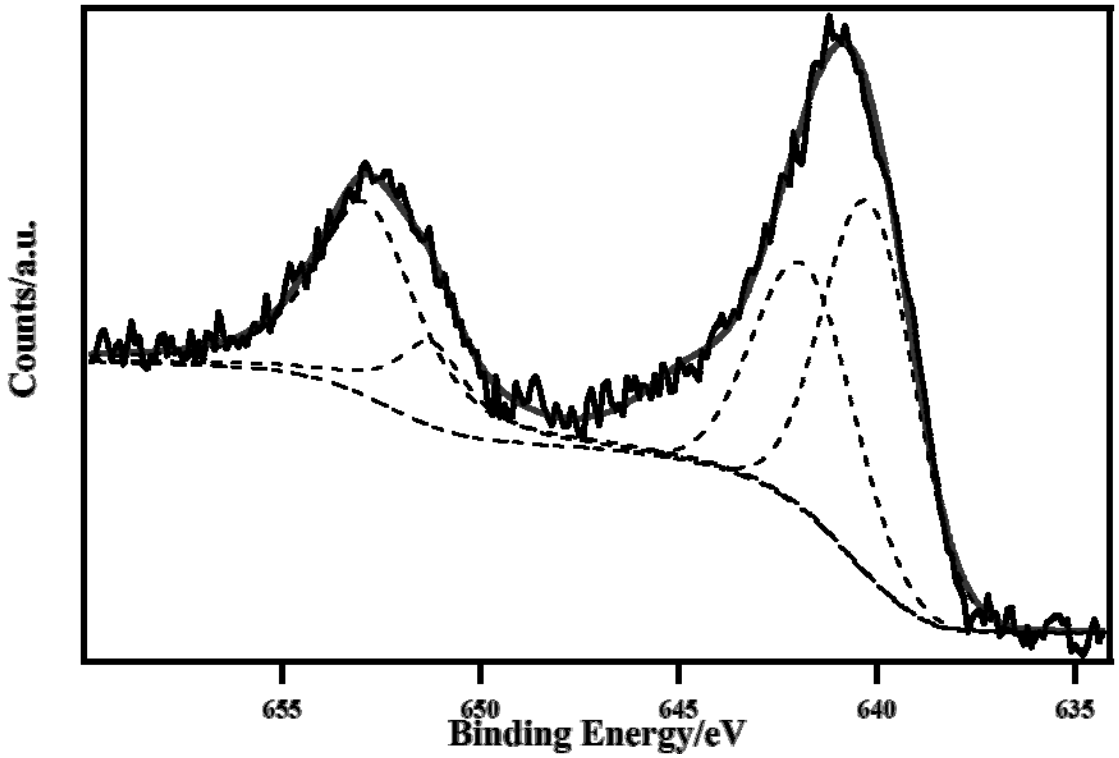

Figure 4.4.10 – *Deconvolution of the Mn2p peak in I-Mn007 (B.E. values corrected for charging effects)*

The fact that manganese in an oxidation state of (II) and (IV), but not (III) was detected on the surface of the perovskite sample is notable: Mössbauer spectroscopy (*vide infra*), carried out to investigate the iron content in the oxide, only revealed the presence of Fe^{III}, indicating that the compound is a $Mn^{III}Fe^{III}O_3$ perovskite. These results indicate that manganese on the surface is present in different states probably due to the inherent defectivity of the surface itself.

In order to study the site geometry and oxidation states of the iron atoms in the perovskite, Mössbauer analyses [Fig. 4.4.11] were carried out. The RT spectrum of sample Mn001 consists of a strong doublet centred in the region of Fe^{III} (velocity values around 0.35 mm/s). The best fitting was obtained by using two Fe^{III} components, indicating the presence of two non-equivalent ferric sites, as reported by Banks et al.[91, 94]

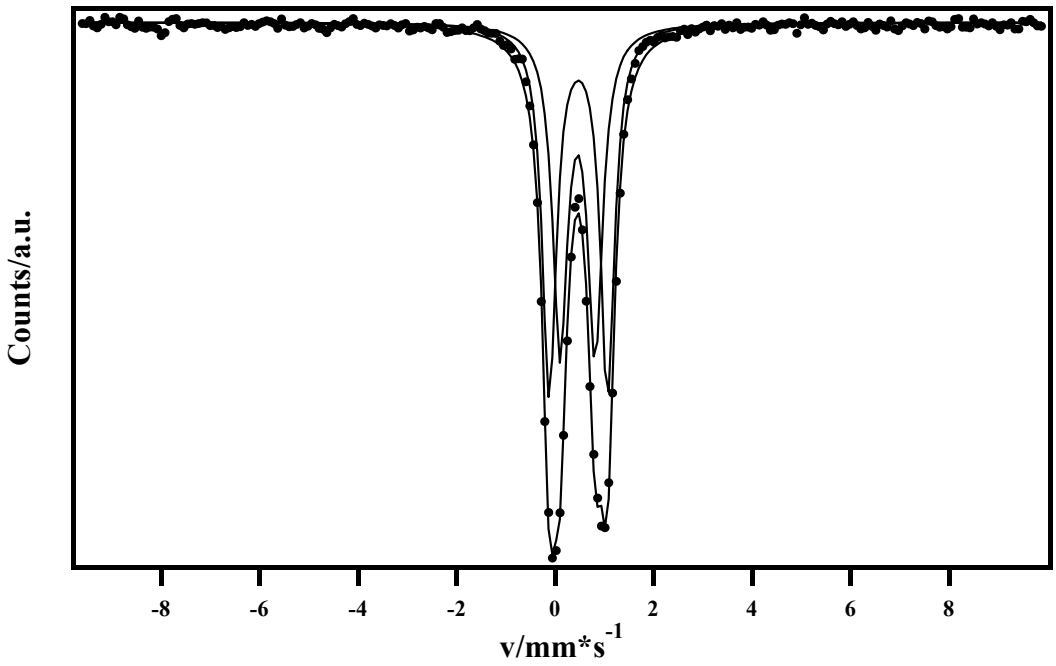

Figure 4.4.11 - Room temperature Mössbauer spectrum of sample Mn001

To assess the magnetic behaviour of the two different types of manganese ferrite (i.e. the perovskite and the spinel) the compounds were investigated through magnetic induction and susceptibility measurements. Compared to the cobalt samples (see figures 4.2.12 and 4.2.13), the manganese spinel [Fig. 4.4.12] displays an extremely fast response, as an external field of less than 2000 Oersted is sufficient to close the hysteresis loop, and inversion of the induction is equally rapid.

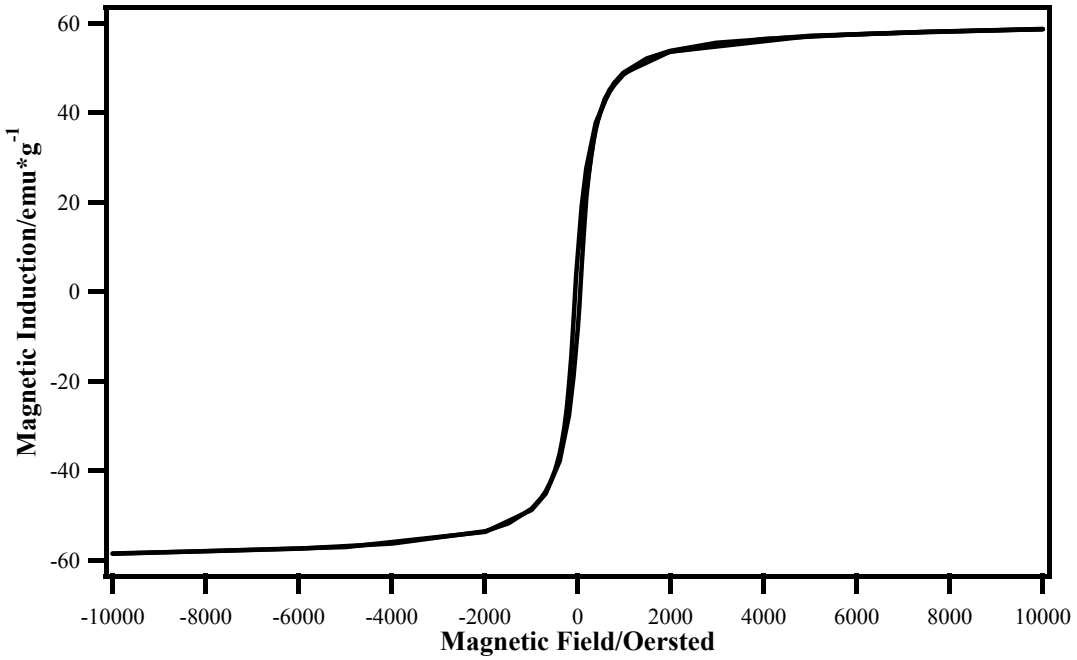

Figure 4.4.12 – *Room temperature hysteresis loop relative to $MnFe_2O_4$ sample I-Mn008*

This shows that the manganese ferrite is a much softer magnetic material than its cobalt analogue; this is consistent with typical spinel ferrite behaviour.
At room temperature, the manganese perovskite displayed a linear response to the external magnetic field [Fig. 4.4.13], and did not appear to reach saturation, showing paramagnetic behaviour. This is consistent with the results obtained through Mössbauer spectroscopy reported above, which did not report significant magnetic behaviour at such temperatures.

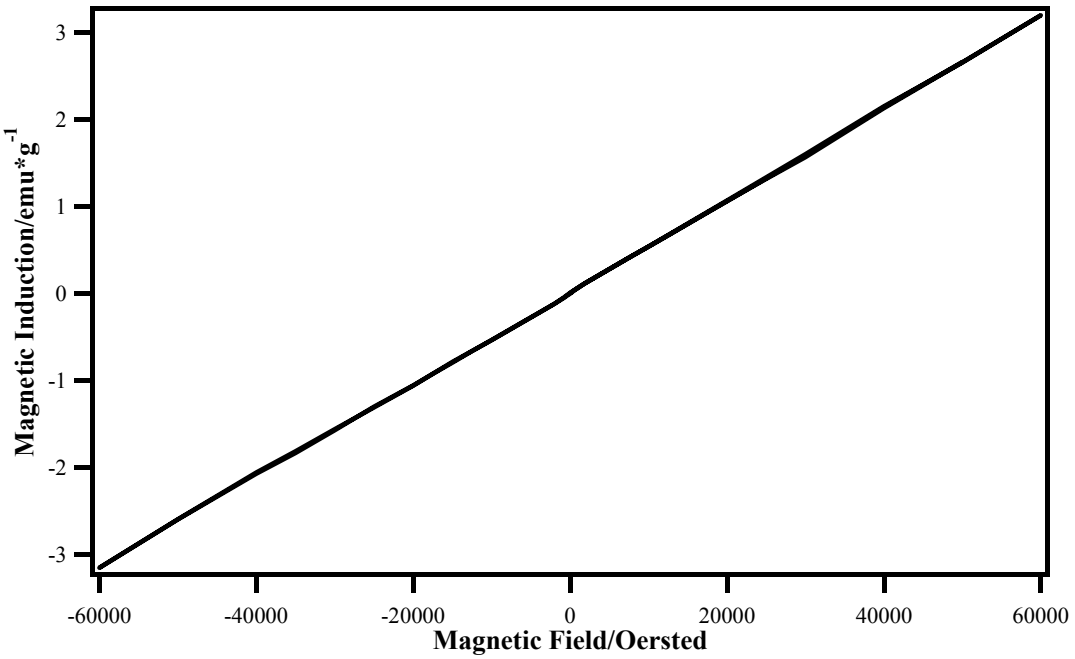

Figure 4.4.13 – *Room temperature induction measurement relative to $MnFeO_3$ sample Mn021*

The hysteresis curve only became visible when measurements were performed at low temperature (i.e. 2.5 K) [Fig. 4.4.14]. In such extreme conditions, the behaviour of the ferrite was typical of a hard magnetic material (high saturation and coercivity).

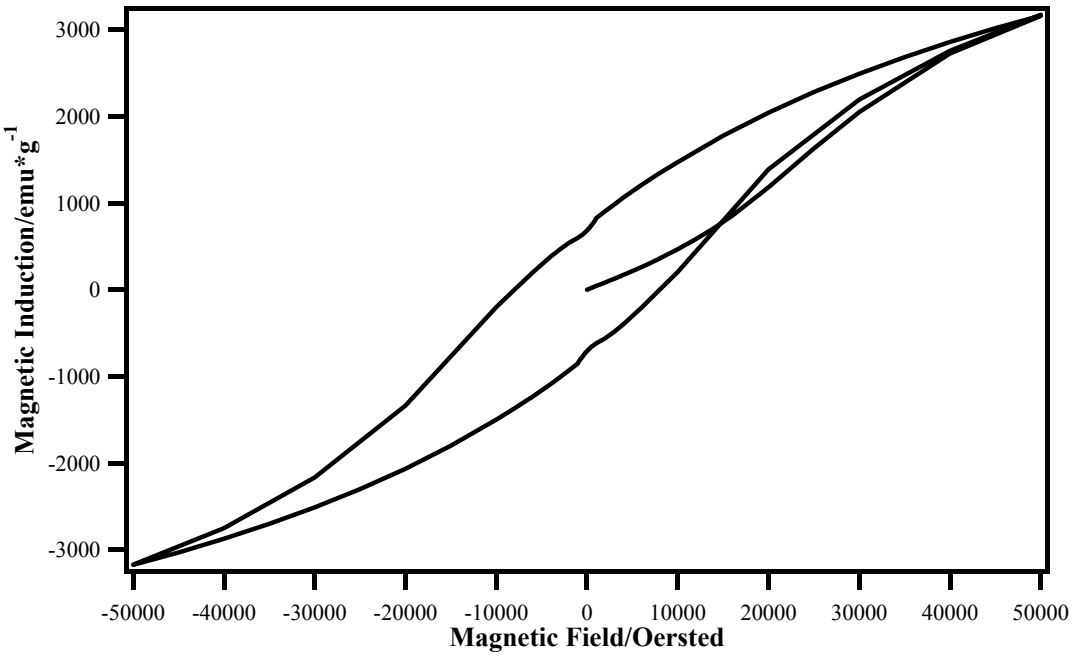

Figure 4.4.14 – *Low temperature induction measurement relative to $MnFeO_3$ sample Mn021*

Susceptibility measurements performed on this system [Fig. 4.4.15] were in agreement with the data reported in literature for this compound,[92, 94, 257] displaying a Néel temperature of 35 K.

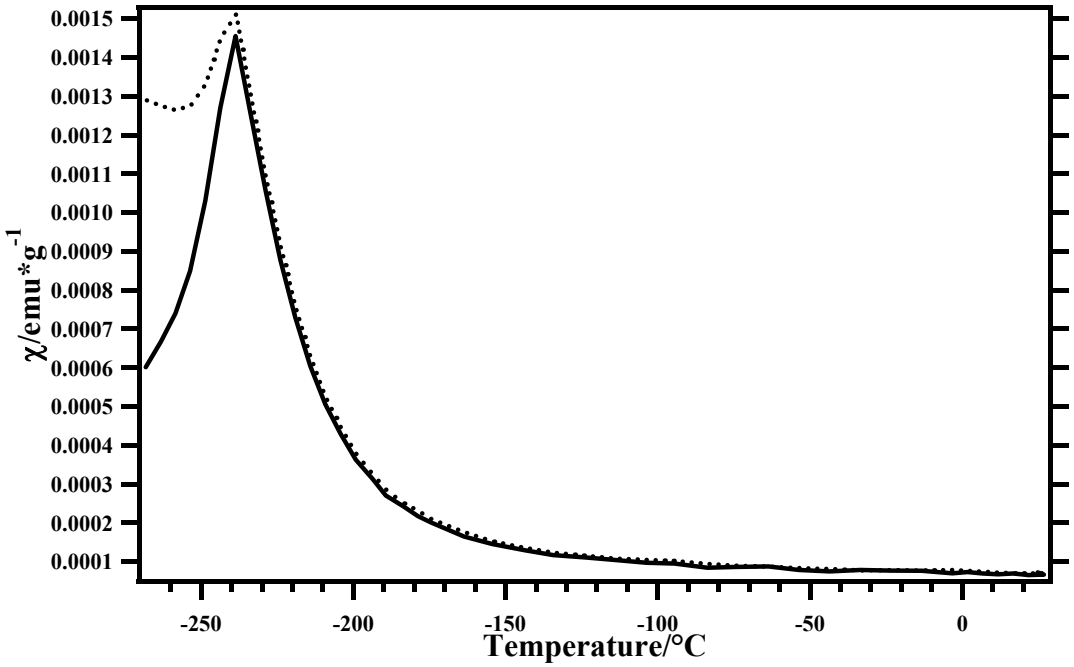

Figure 4.4.15 – *Room Susceptibility measurements (emu/mol vs. K) relative to sample Mn021 (the continuous line is relative to Zero Fill Cool; the dotted line to Fill Cool)*

As with the cobalt spinel (See Par. 4.2) EXAFS analyses [Fig. 4.4.16 and 4.4.17] carried out on sample S-Mn007-3 yielded results in agreement with expectations for a manganese spinel, confirming the structural data gained through XRD. In particular, the Fe edge spectrum [Fig. 4.4.17] is very similar to its counterpart obtained from the cobalt sample [Fig 4.2.15] showing that the iron in the two compounds has a similar chemical environment (which is expected as both are partially inverse spinels). The Mn edge spectrum used manganese^{II} acetate as a reference.

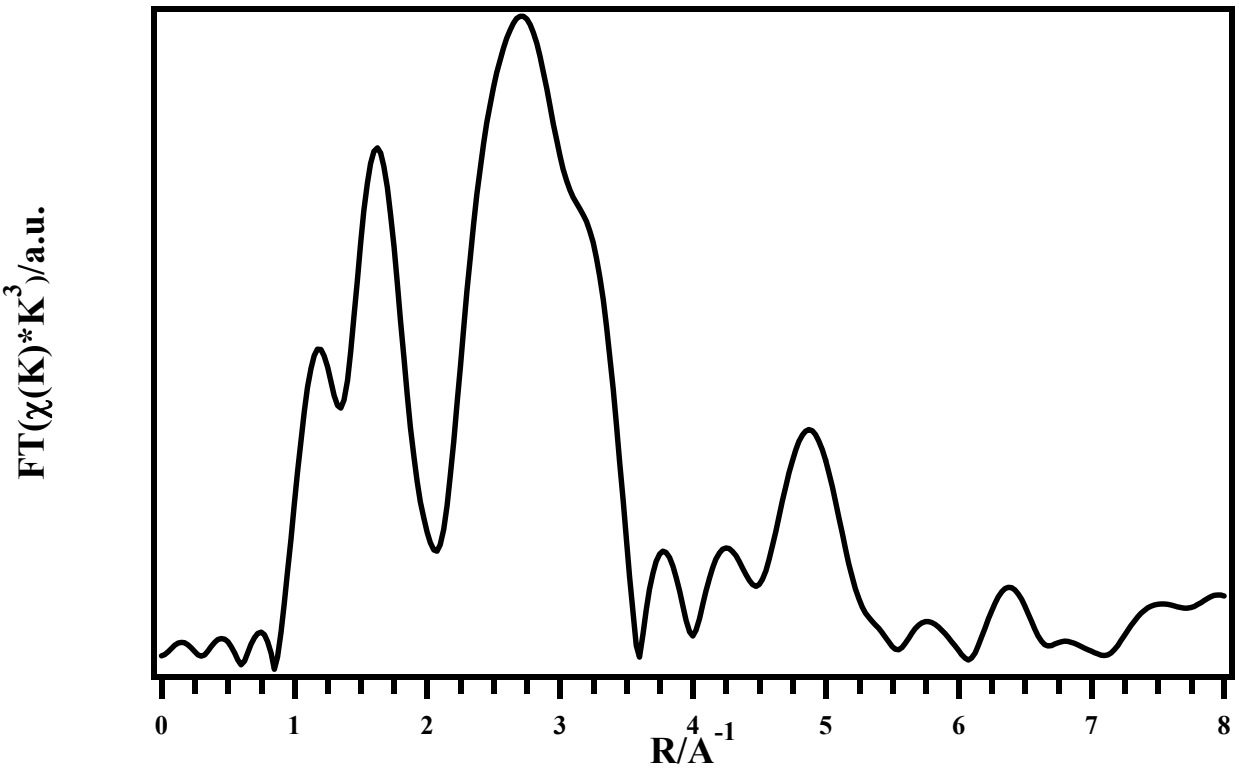

Figure 4.4.16 - *EXAFS spectrum (Mn edge; Fourier transform) of sample S-Mn007-3*

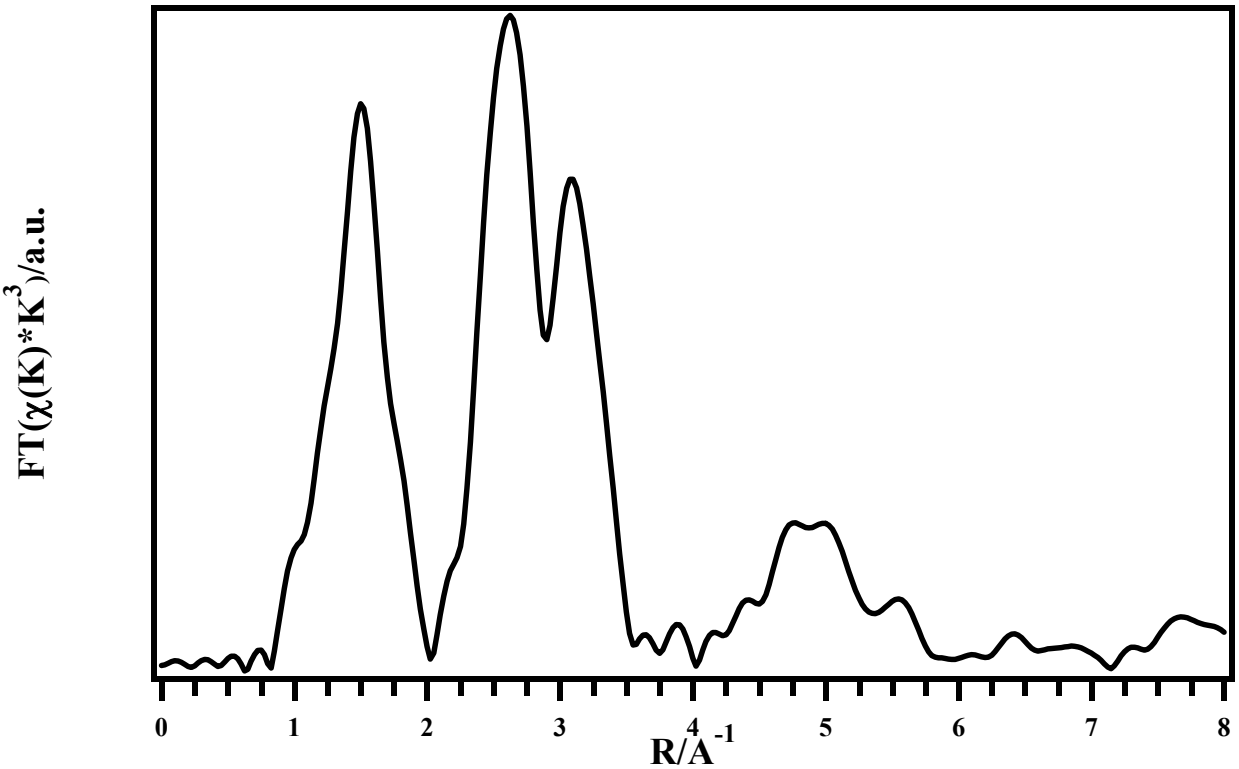

Figure 4.4.17 - *EXAFS spectrum (Fe edge; Fourier transform) of sample S-Mn007-3*

Micro-Raman spectroscopy analyses yielded very different results for the manganese spinel I-Mn008 [Fig. 4.4.18] and the perovskite Mn021 [Fig. 4.4.19]: this has to be expected due the different structure of the two compounds. The shape of the spectrum yielded by the manganese spinel is in agreement with data published by Varshney et al.[258] and Herranz et al.[239] The main

modes expected for a manganese spinel ferrite are visible and were reported in figure 4.4.18.[258, 259] No data was found as a reference for the manganese perovskite, preventing a thorough interpretation of the Raman data to be performed. As with the other compounds investigated with this technique, several measurements carried out in different parts of the powder sample allowed to confirm that the obtained oxides are compositionally uniform, as non significant changes were detected between spectra collected from different portions of the powders.

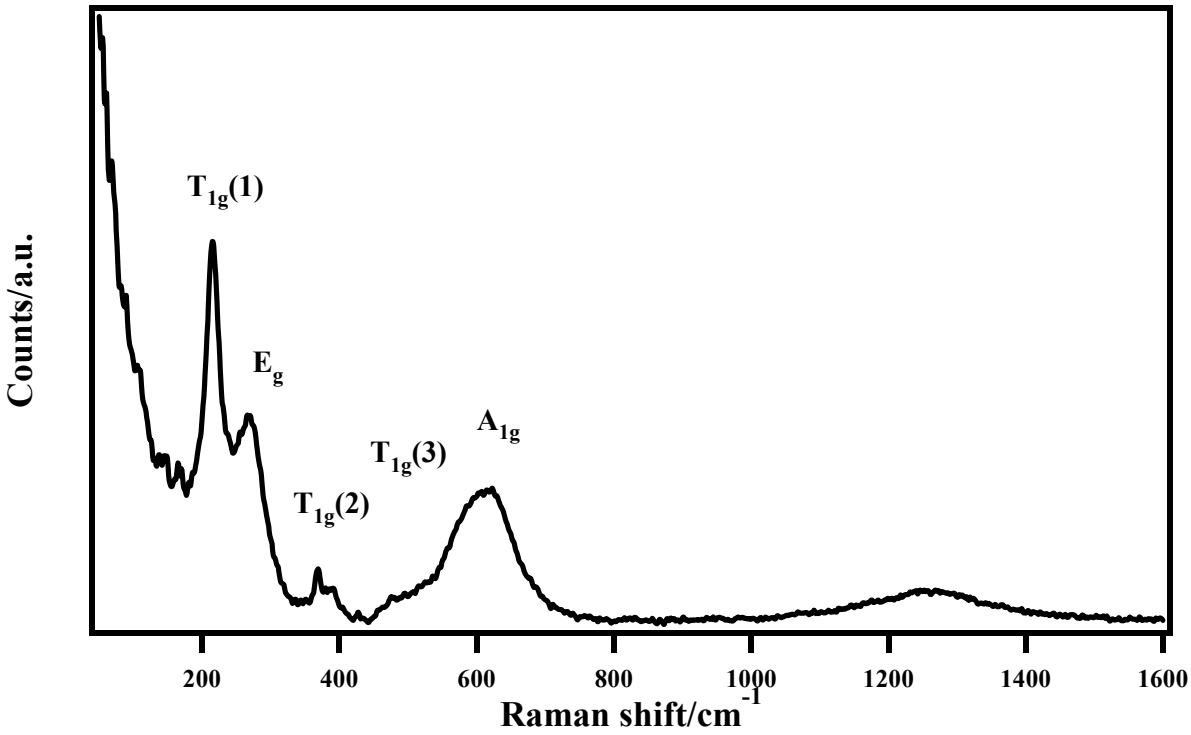

Figure 4.4.18 - *Room temperature micro-Raman spectrum of sample I-Mn008*

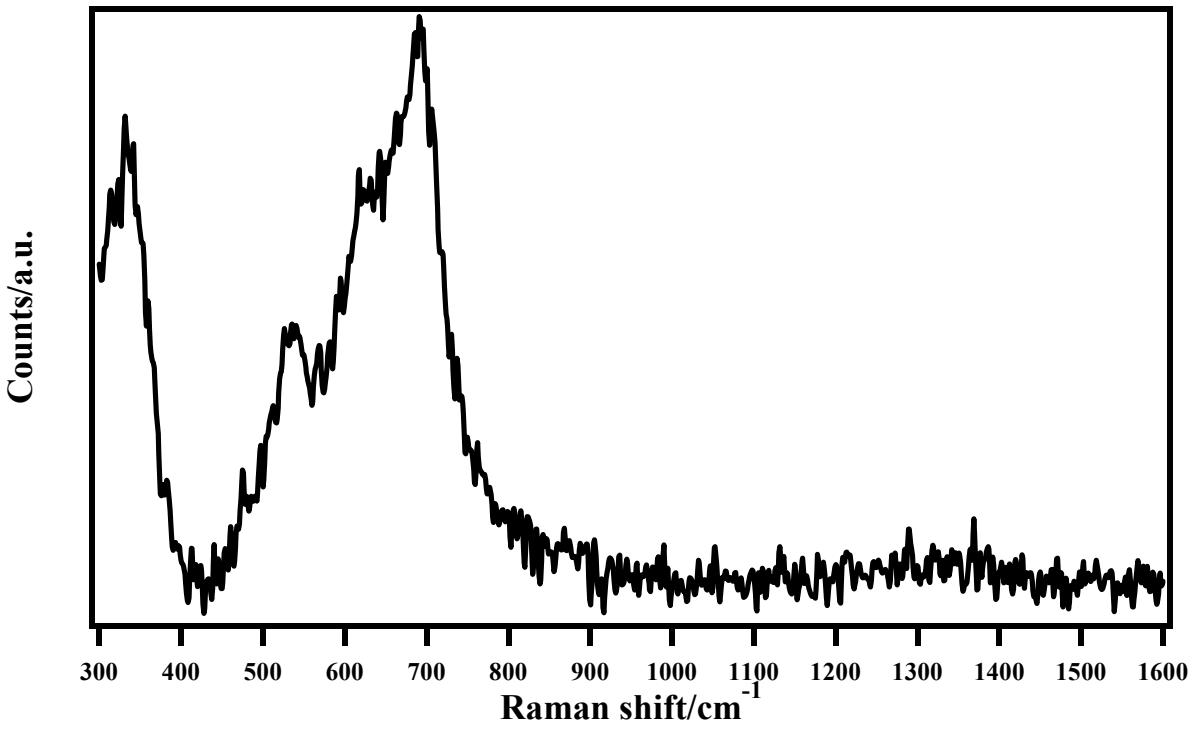

Figure 4.4.19 - *Room temperature micro-Raman spectrum of sample Mn021*

Analogously to what was observed for the cobalt spinel (see Par. 4.2) TPR analyses were carried out on the manganese perovskite Mn001 [Fig. 4.4.20]. Unlike in the case of cobalt, the two peaks are distinct and reduction of the compound is not complete (as the higher temperature peak is cut off). This is also confirmed by the hydrogen consumption measured (1.28 mol H_2 consumed per sample mol), which suggests that the reduction of iron is incomplete. The shape and position of the lower temperature peak (relative to the reduction of manganese) is compatible with data in literature.[88, 89]

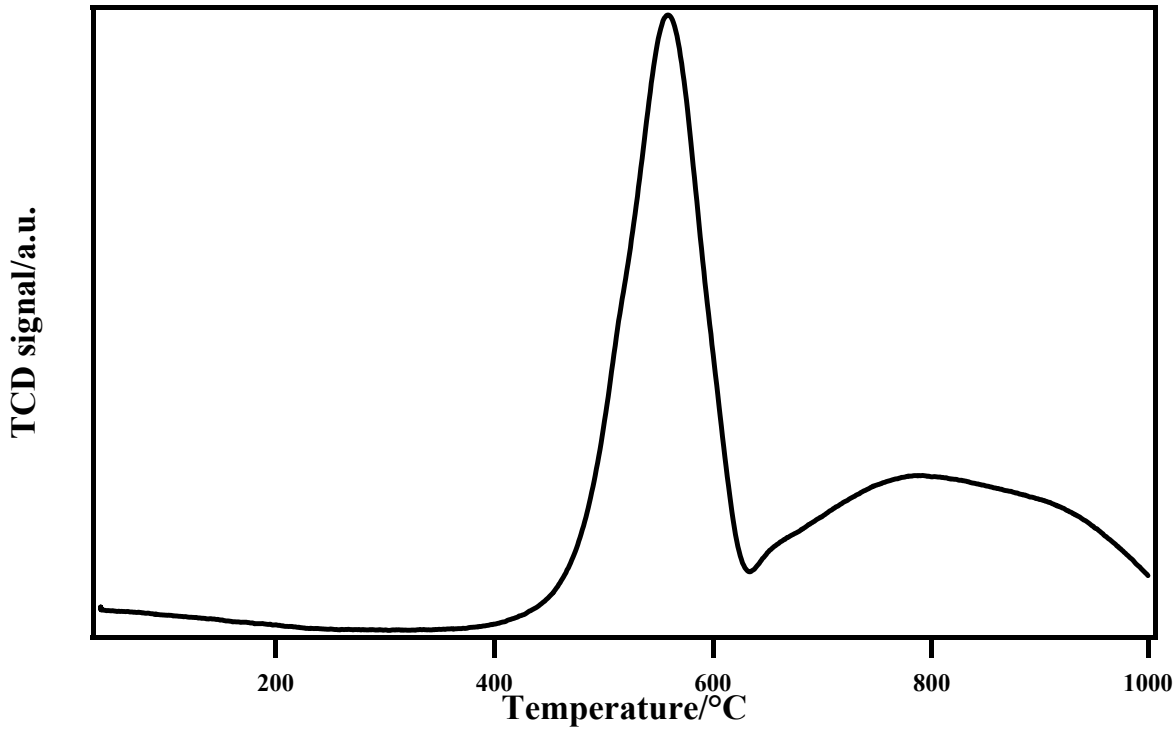

Figure 4.4.20 - *TPR analysis of sample Mn001*

TGA-DSC analyses carried out on samples resulting from coprecipitation and hydrothermal synthesis will be discussed in Par. 4.7 together with the results relative to the other compounds.

4.5 - Nickel spinel ferrite $NiFe_2O_4$

This nickel compound was successfully synthesised though coprecipitation of oxalates and hydrothermal synthesis.

Synthesis of the spinel through coprecipitation is expected to be, like other explored compounds, most sensitive to treatment temperature, whereas treatment time, aging of the suspension, peptising agent amount and basification protocol are not expected to be particularly influential.

Compounds synthesised through hydrothermal protocol were notable in that it was initially thought that the correct parameters for synthesis of the spinel required a 1:1 Fe:Ni nominal ratio. This was due to the fact that XRD patterns of the resulting powders showed extra reflections in samples having a 2:1 ratio, whereas the 1:1 samples appeared pure. By correlating the results from ICP analyses relative to both samples prepared with a 1:1 and a 2:1 Fe:Ni ratio with XRD analyses, it was concluded that the unidentified peaks were due to the excessive amount of precursor oxalic acid (similarly to what had happened with manganese - see Par. 4.4) and were thus eliminated by

adjusting the precursor molar ratios accordingly. By contrast, the apparently pure patterns relative to samples having a 1:1 Fe:Ni nominal molar ratio contained multiple crystalline phases, with very similar crystal cell parameters (*vide infra*).

Rietveld refinement was carried out on the obtained XRPD patterns [Fig. 4.5.1 and 4.5.2] based upon the data published in literature by Wyckoff[157] and Kremnović.[260]

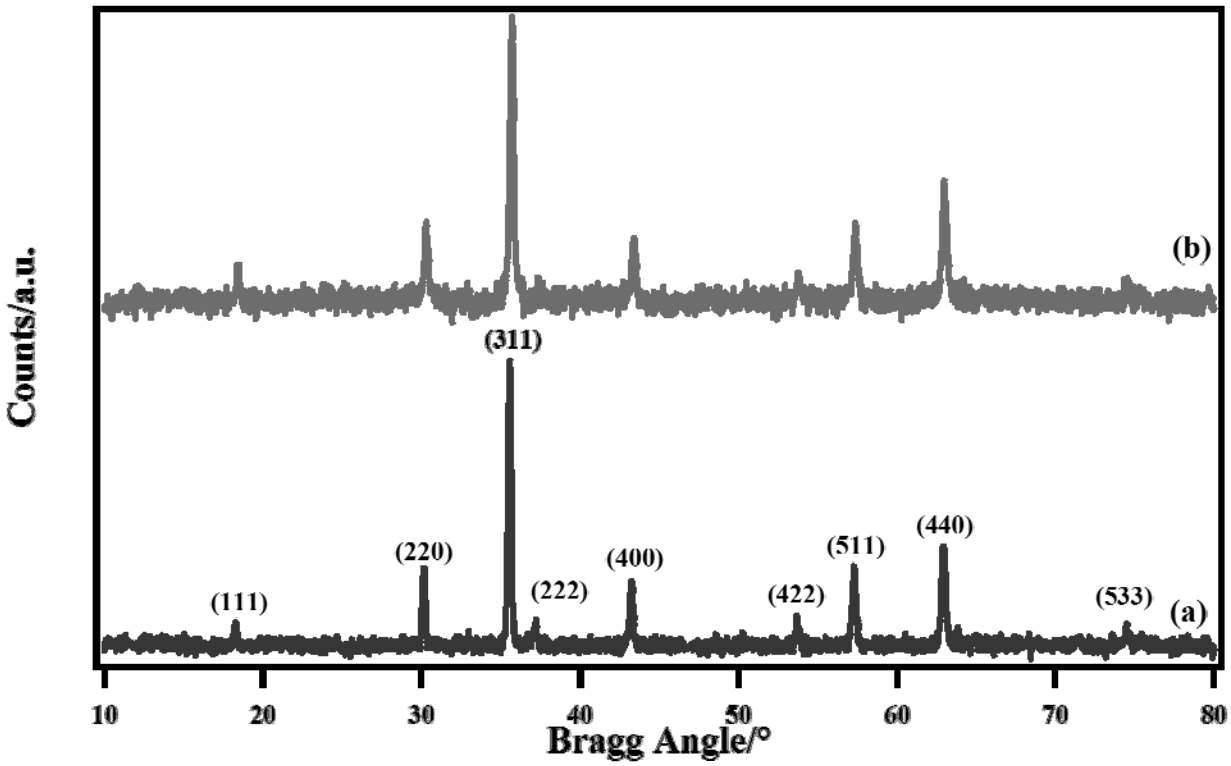

Figure 4.5.1 - *XRPD patterns of spinel samples (a) Ni002 and (b) I-Ni007 with main reflections indexed*

As can be seen in figure 4.5.2, pattern **a)**, relative to the sample having 1:1 Fe:Ni nominal ratio, is seemingly identical to pattern **c)**, relative to pure $NiFe_2O_4$, whereas pattern **b)**, resulting from a sample identical to **c)**, but prepared with a Fe:Ni:acid nominal molar ratio of 2:1:4.5 shows numerous extra reflections.

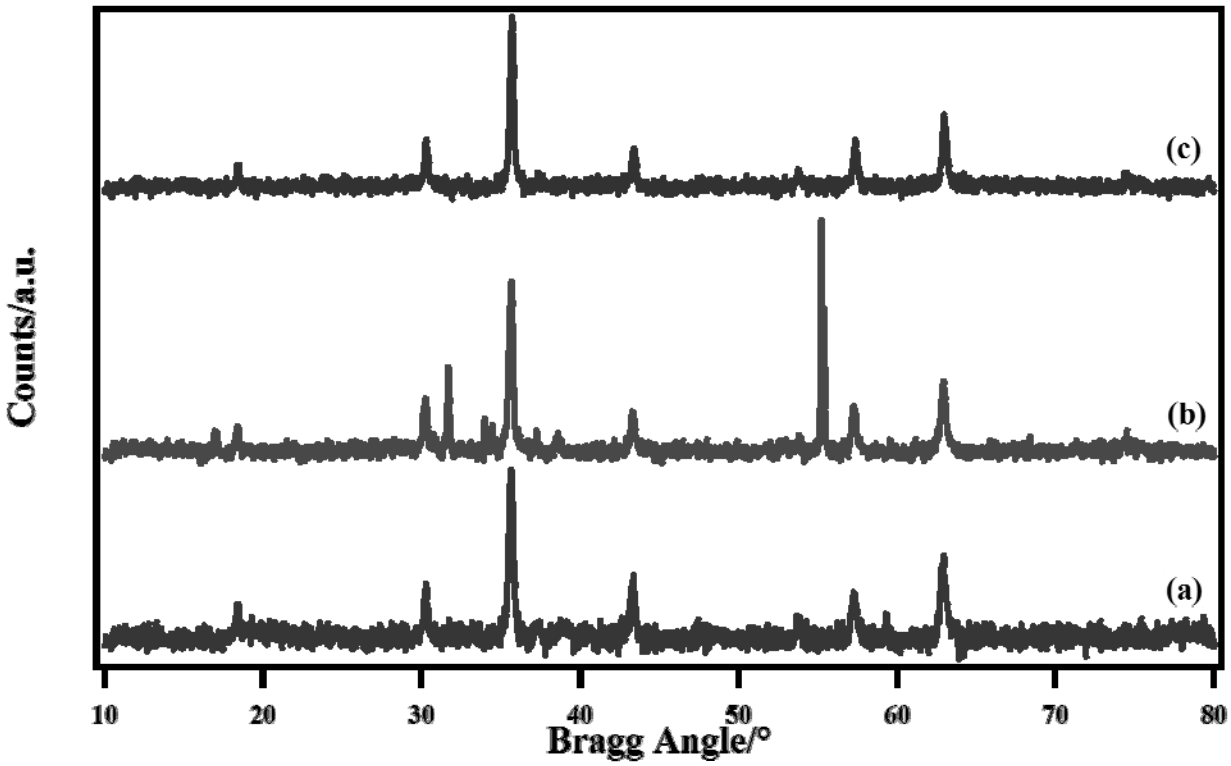

Figure 4.5.2 - *XRPD patterns of samples (a) I-Ni001, (b) I-Ni002 and (c) I-Ni007*

Analysis of the data present in literature[252, 261] lead to the conclusion that the first pattern was comprised of multiple phases, one of them being the desired spinel, and the others being nickel-rich phases such as $Ni_{1.43}Fe_{1.7}O_4$ or NiO. These species were initially undetected as $Ni_{1.43}Fe_{1.7}O_4$ had the same crystal cell and space group, as well as a very similar *a* parameter, and NiO had a pattern which could be masked by the spinel like the latter (i.e. the main reflections of NiO fall in correspondence with secondary reflections of the spinel phase). Crystallite size was calculated through Rietveld refinement [Tab 4.5.1] and showed that, like with the manganese and cobalt spinels, hydrothermal synthesis resulted in smaller crystallites.

Sample	Found structure	Method	Treatment temperature and time	Crystallite average size/nm
Ni002	$NiFe_2O_4$	Coprecipitation	135°C; 24 hours	132±5
Ni004	$NiFe_2O_4$	Coprecipitation	135°C; 24 hours	117±5
I-Ni001	$Ni_{1.43}Fe_{1.7}O_4$, NiO and $NiFe_2O_4$	Hydrothermal	135°C; 24 hours	20±5
I-Ni002	Unidentified mixed product	Hydrothermal	135°C; 24 hours	45±3
I-Ni007	$NiFe_2O_4$	Hydrothermal	135°C; 24 hours	47±2
I-Ni011-2	$NiFe_2O_4$	Hydrothermal	135°C; 2 hours	10±1
I-Ni011-4	$NiFe_2O_4$	Hydrothermal	135°C; 4 hours	34±1
I-Ni012	$NiFe_2O_4$	Hydrothermal	100°C; 24 hours	20±1
I-Ni013	$NiFe_2O_4$	Hydrothermal	75°C; 24 hours	8±5

Table 4.5.1 – *Average crystallite size by compound and synthesis*

Hydrothermal syntheses were also carried out at different reaction times, to investigate if it was possible to prepare the compound in a shorter amount of time (as was shown to be feasible with $CoFe_2O_4$ and $MnFe_2O_4$). The XRD patterns collected from the resulting samples [Fig. 4.5.3]

showed that, although it is possible to employ reaction times shorter than 24 hours, a reaction time of at least 4 hours is required for a pure crystalline product to be isolated, though some evidence of crystallisation is detectable already after 2 hours. The steep increase in crystallite size between the samples treated for 2 and 4 hours (10 and 34 nm respectively) suggests that crystal growth was still taking place when the first treatment (two hours) was completed. Furthermore it has been highlighted that single-phase crystalline products were detected at temperatures as low as 75°C. This result is particularly notable as it is, to the best of our knowledge, the lowest temperature reported in literature for the hydrothermal synthesis of spinel ferrites. Though other low-temperature hydrothermal syntheses have been reported, treatment temperatures fall in the 100-120°C range[21, 222, 224, 262] or higher and generally require longer reaction times such as 12-24 hours.

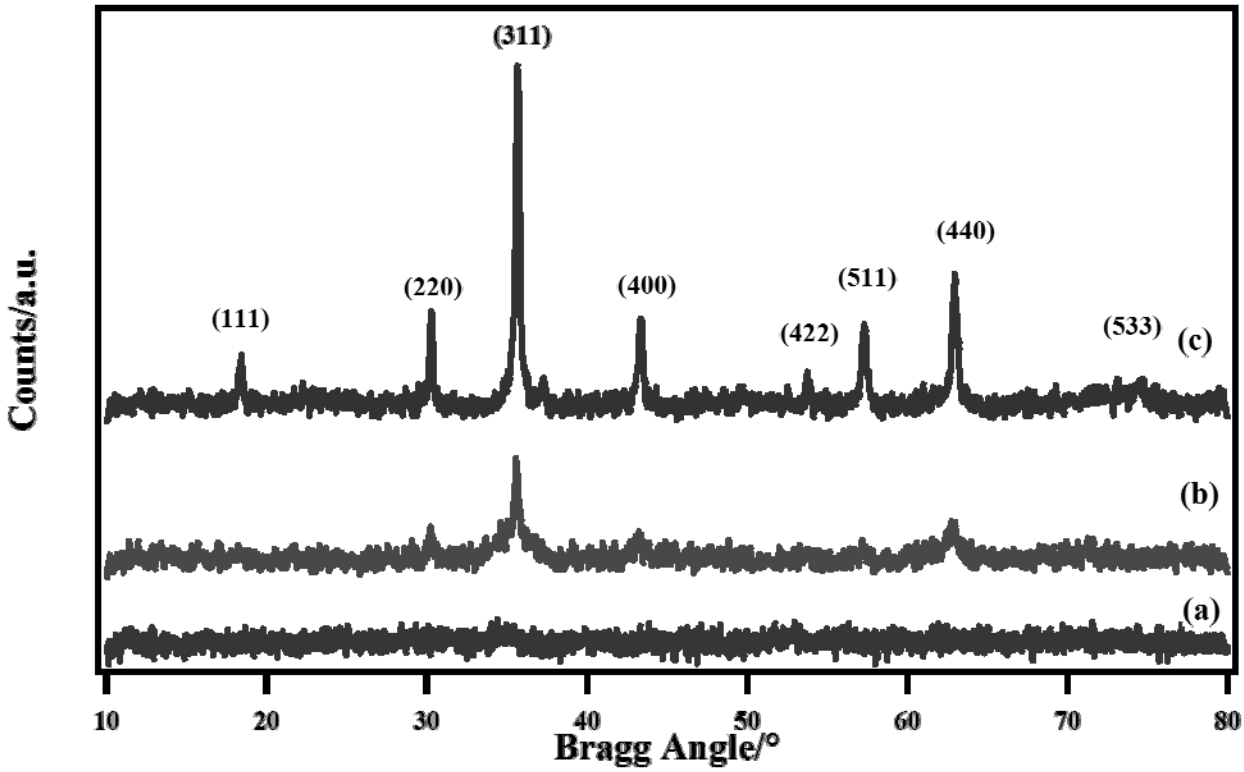

Figure 4.5.3 - *XRPD patterns of sample I-Ni011 with reaction times of (a) 1, (b) 2 and (c) 4 hours at 135°C*

XPS analyses [Fig. 4.5.4] carried out on salient samples revealed that, as with other compounds, elimination of sodium was difficult and could not be completely achieved.

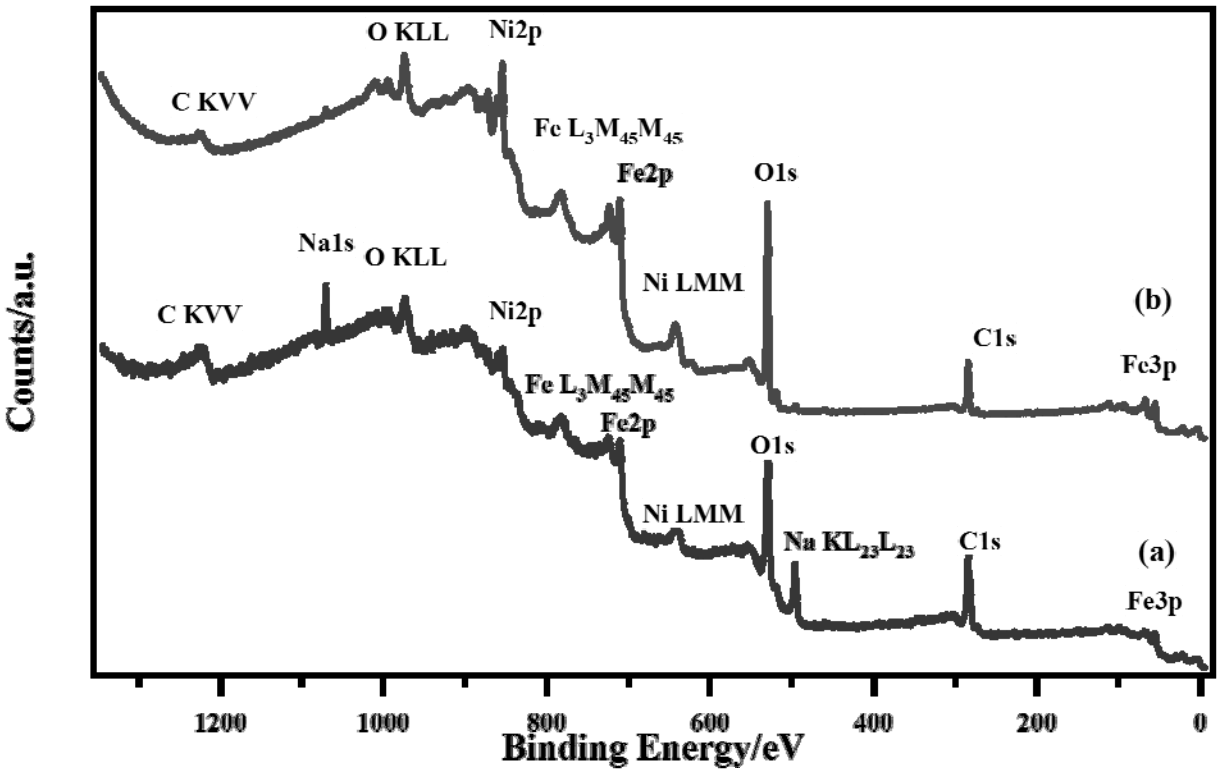

Figure 4.5.4 - *XPS survey spectra of samples (a) Ni002 and (b) I-Ni007 with main peaks indexed (B.E. values are corrected for charging effects)*

Binding energy values [Tab 4.5.2] were in agreement with the data found in literature[152, 154, 159, 235, 240, 253] and surface concentrations were close to expected bulk stoichiometry.

Compound	Element	Peak	B.E./eV
Ni002	C	1s	284.6
	O	1s	529.5
	Fe	$2p_{3/2}$ and $2p_{1/2}$	709.9 and 723.0
	Ni	$2p_{3/2}$ and $2p_{1/2}$	854.6 and 871.9
I-Ni007	C	1s	284.6
	O	1s	529.7
	Fe	$2p_{3/2}$ and $2p_{1/2}$	709.2 and 722.3
	Ni	$2p_{3/2}$ and $2p_{1/2}$	854.9 and 872.6

Compound	C %	M %	Fe %	O %	Fe/M atomic ratio (from XPS)	Fe/M atomic ratio (from ICP-AES)
Ni002	64.7	2.3	4.1	21.4	1.8	1.9
I-Ni007	64.8	3.5	7.1	24.5	2.0	2.1

Table 4.5.2 – *B.E., surface and bulk concentration values for the main peaks in nickel ferrite samples*

As with the other examined ferrites, the iron 2p XPS peaks [Fig. 4.5.5] included the satellite ($Fe2p_{3/2}$) peak at a B.E. value 8 eV higher than the main peak and no peak at 6 eV higher; this is consistent with compounds containing iron in a (III) oxidation state and with the absence of Fe^{II}.[100, 154, 159, 181, 236, 239, 240] This is consistent with the data reported in literature[114, 241] and, despite the inversion of the spinel structure, confirms that even in tetrahedral sites, iron maintains an oxidation state of (III).

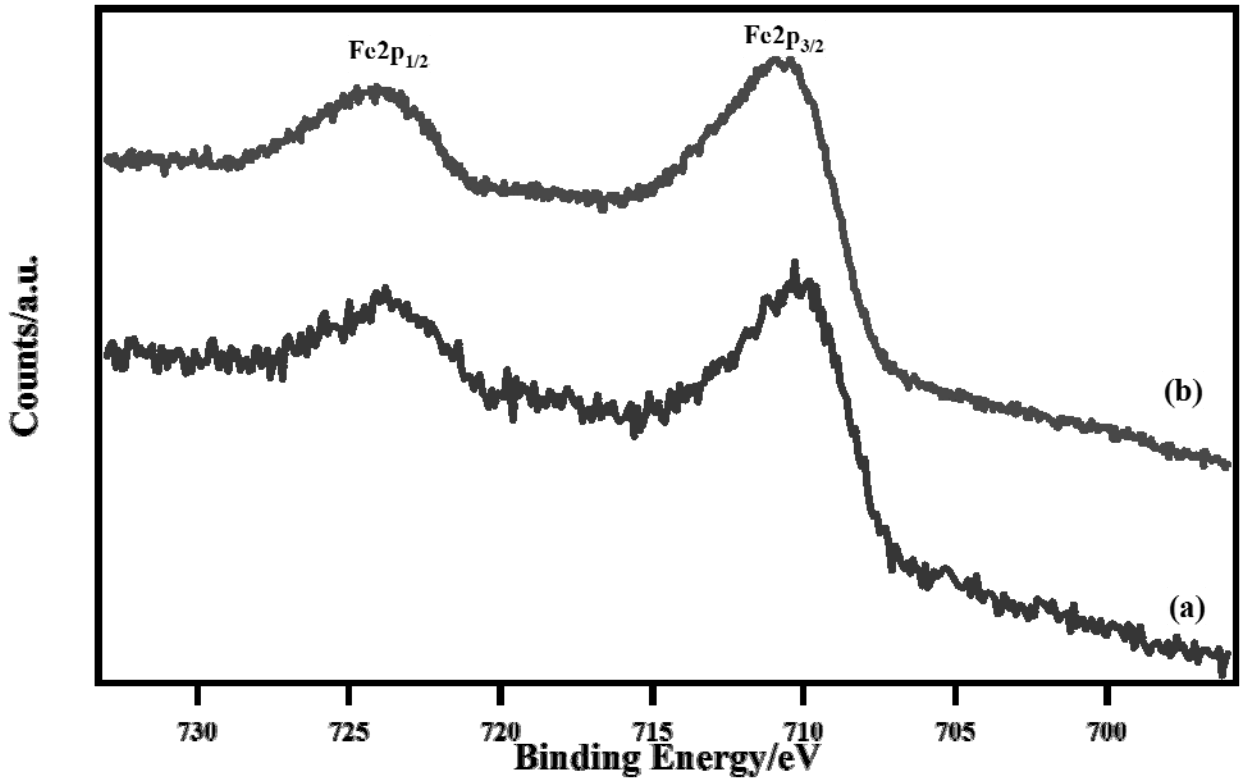

Figure 4.5.5 - *XPS spectra of the Fe2p region for samples (a) Ni002 and (b) I-Ni007 (B.E. values are corrected for charging effects)*

In both the sample resulting from coprecipitation and in the one from hydrothermal synthesis, the Ni2p [Fig. 4.5.6 and 4.5.7] is devoid of the satellite peak at 1.2 eV (the presence of which, combined with a slightly lower binding energy of the main peak, would indicate the presence of surface NiO).[240, 253]

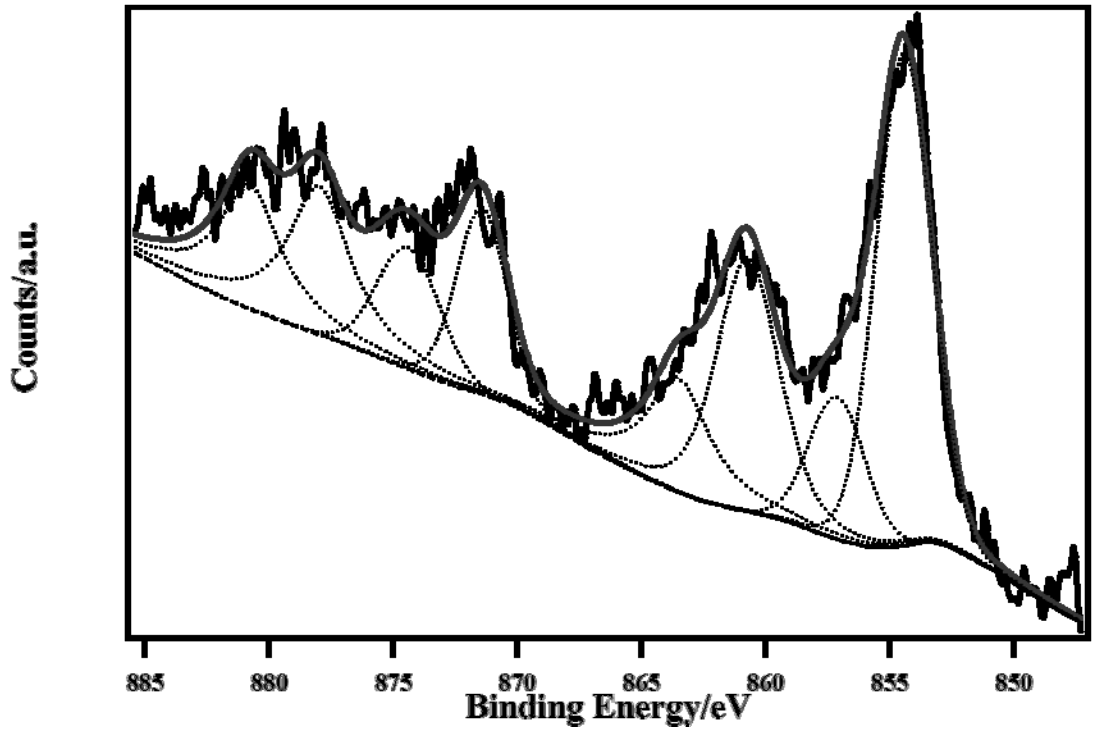

Figure 4.5.6 – *Deconvolution of the Ni2p peak for sample Ni002 (B.E. values are corrected for charging effects)*

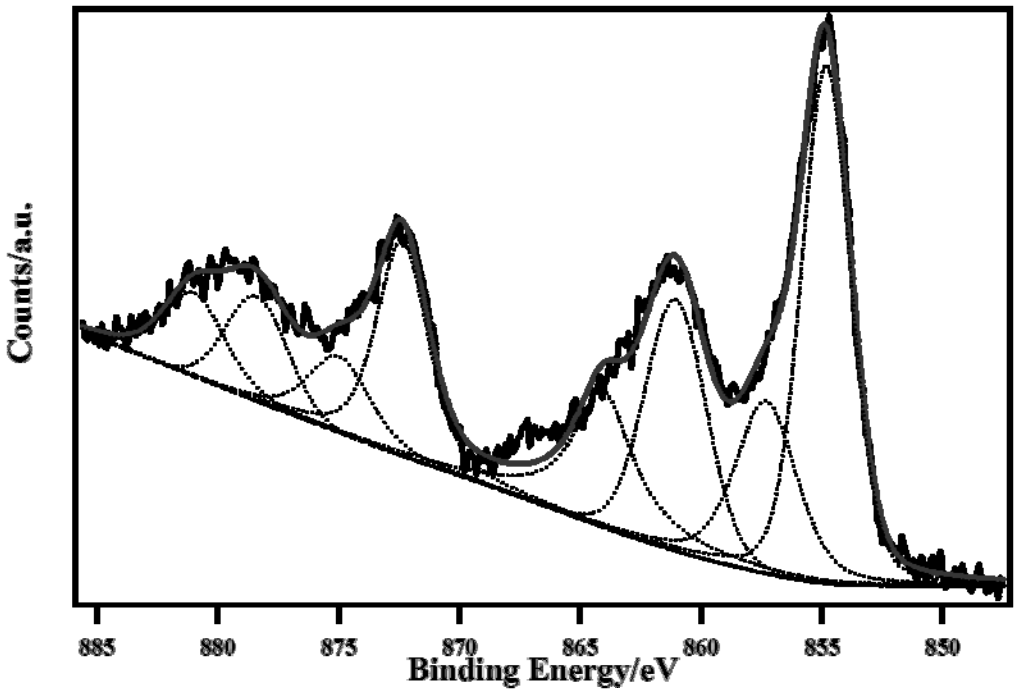

Figure 4.5.7 – *Deconvolution of the Ni2p peak in I-Ni007 (B.E. values corrected for charging effects)*

The spectrum has been fitted with a series of peaks, as reported in table 4.5.3.[114, 241] The presence of substitutional surface Ni^{III} is consistent with a slight excess of surface nickel, as evidenced by quantitative analysis of the peaks [Tab. 4.5.2], especially in the case of the coprecipitated sample.[114, 122, 263] This data, tough Mössbauer analysis (*vide infra*) revealed that the compound was an inverse spinel (i.e. the Ni atoms only occupy octahedral sites), can be attributed to inherent surface defectivity, implying that on the surface the spinel structure is only partially inverse.

Sample	Peak B.E./eV	Region	Attribution
Ni002	854.4	$2p_{3/2}$	Ni^{II} in the spinel lattice (octahedral)
	857.1	$2p_{3/2}$	Ni^{III} in the spinel lattice (tetrahedral)
	860.7	$2p_{3/2}$, sat.	Ni^{II} in the spinel lattice (octahedral)
	863.5	$2p_{3/2}$, sat.	Ni^{III} in the spinel lattice (tetrahedral)
	871.4	$2p_{1/2}$	Ni^{II} in the spinel lattice (octahedral)
	874.4	$2p_{1/2}$	Ni^{III} in the spinel lattice (tetrahedral)
	878.0	$2p_{1/2}$, sat.	Ni^{II} in the spinel lattice (octahedral)
	880.8	$2p_{1/2}$, sat.	Ni^{III} in the spinel lattice (tetrahedral)
I-Ni007	854.8	$2p_{3/2}$	Ni^{II} in the spinel lattice (octahedral)
	857.3	$2p_{3/2}$	Ni^{III} in the spinel lattice (tetrahedral)
	861.1	$2p_{3/2}$, sat.	Ni^{II} in the spinel lattice (octahedral)
	864.0	$2p_{3/2}$, sat.	Ni^{III} in the spinel lattice (tetrahedral)
	872.4	$2p_{1/2}$	Ni^{II} in the spinel lattice (octahedral)
	874.0	$2p_{1/2}$	Ni^{III} in the spinel lattice (tetrahedral)
	878.4	$2p_{1/2}$, sat.	Ni^{II} in the spinel lattice (octahedral)
	881.0	$2p_{1/2}$, sat.	Ni^{III} in the spinel lattice (tetrahedral)

Table 4.5.3 – *Peak positions and attributions for the Ni2p peak deconvolutions (B.E. values corrected for surface charging)*

Studies performed on site occupancy through Mössbauer spectroscopy show that this distribution among different sites occurs only on the surface: as a compound, $NiFe_2O_4$ is a well-known inverse spinel,[59, 122] with Ni^{2+} ions on B sites and Fe^{3+} ion distributed equally among A and B sites (γ:1, see

Par. 6.3.3). The 14 K spectrum of the examined sample [Fig. 4.5.8] consists in an intense sextet and a small doublet centred near the zero value of velocity.

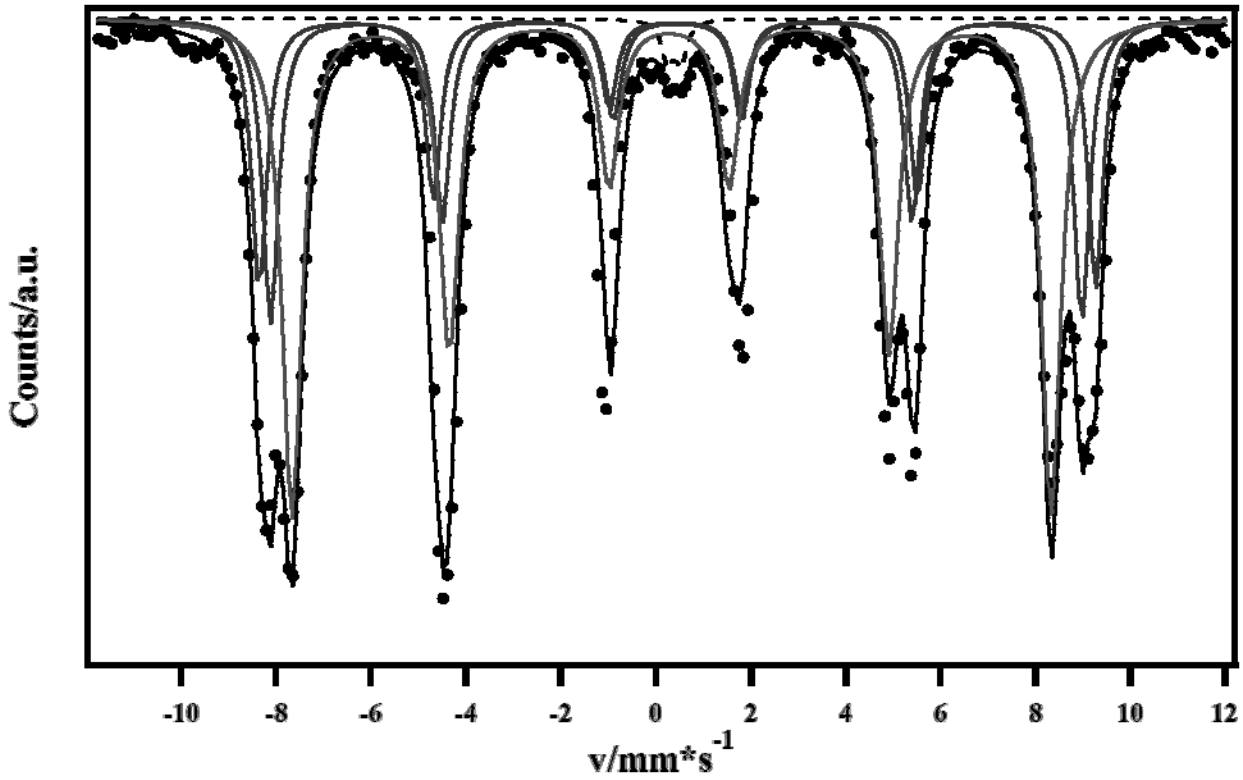

Figure 4.5.8 – *Low-temperature Mössbauer spectrum relative to sample Ni004*

The best fitting was obtained by using a four-component model: one due to a small fraction of paramagnetic or superparamagnetic particles and three belonging to the spinel structure. In accordance with Chinnasamy et al,[264] one sextet has parameters typical of Fe^{3+} in tetrahedral coordination (δ:0.30 mm/s; ε:0.027 mm/s; B:49.6 T), the other two of Fe^{3+} in octahedral coordination (δ:0.43 mm/s; ε:0.022 mm/s; B:54.6T and δ:0.44 mm/s; ε:-0.011 mm/s; B:52.9T).

The calculated ratio between tetrahedral and octahedral sites was very close to one (1.09), confirming that the studied sample had a completely inverse structure. The presence of third site, the parameters of which are attributable to an octahedral site, can be due to Fe^{3+} ions on the surface, as reported by Chinnasamy et al.[264]

As was the case for the cobalt and manganese compounds, Micro-Raman spectra were collected from nickel spinel ferrites synthesised through coprecipitation and hydrothermal synthesis [Fig. 4.5.9]. Results are in agreement with data found in literature for $NiFe_2O_4$,[259, 265, 266] displaying all expected modes for a nickel spinel and thus further confirming the data gathered through XRD, XPS and Mössbauer spectroscopy.[249] Furthermore, the Micro-Raman technique allowed to gain insight on compositional and structural uniformity throughout the synthesised powders: spectra collected for both samples on different portions were identical, confirming the fact that the synthesised powders are compositionally constant.

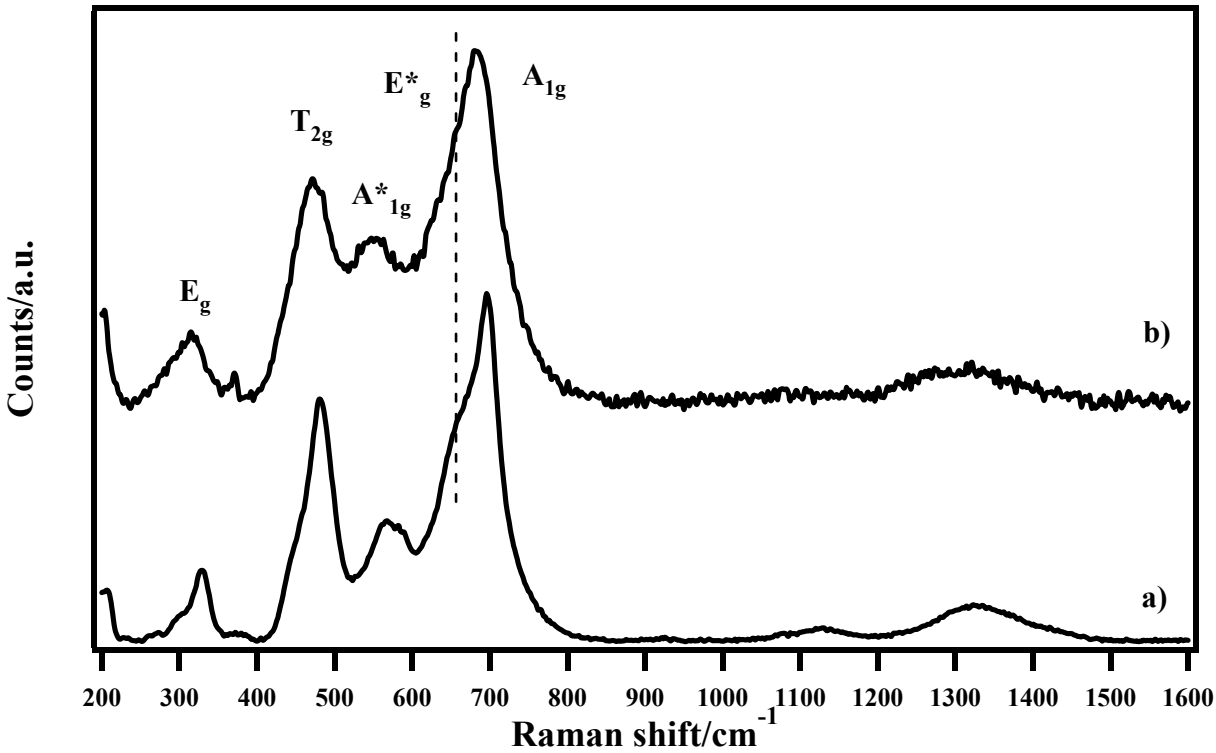

Figure 4.5.9 - *Room temperature micro-Raman spectrum of samples (a) Ni004 and (b) I-Ni007*

Results of DSC-TGA analysis will be discussed in Par. 4.7.

4.6 - Strontium perovskite ferrites $SrFeO_3$

The synthesis of this ferrite was initially addressed in a previous work[237] and only proved successful through coprecipitation. Hydrothermal synthesis yielded mixed phase powders similar to those obtained through the nonaqueous sol-gel method. The strontium ferrite only formed as a single-phase pure powder at 900°C or higher,[237, 238] so the effect of calcination temperature on crystallite size was only evaluated for temperatures higher than the standard treatment temperature used in this Ph.D. thesis.[238] Crystallite sizes resulting from Rietveld refinement performed on the XRD patterns [Fig 4.6.1] are reported in table 4.6.1. As with other ferrites, shorter calcination times produced samples displaying lower crystallite sizes, though the net effect of the "treatment time" synthesis parameter is not especially significant given the slow heating ramp involved.

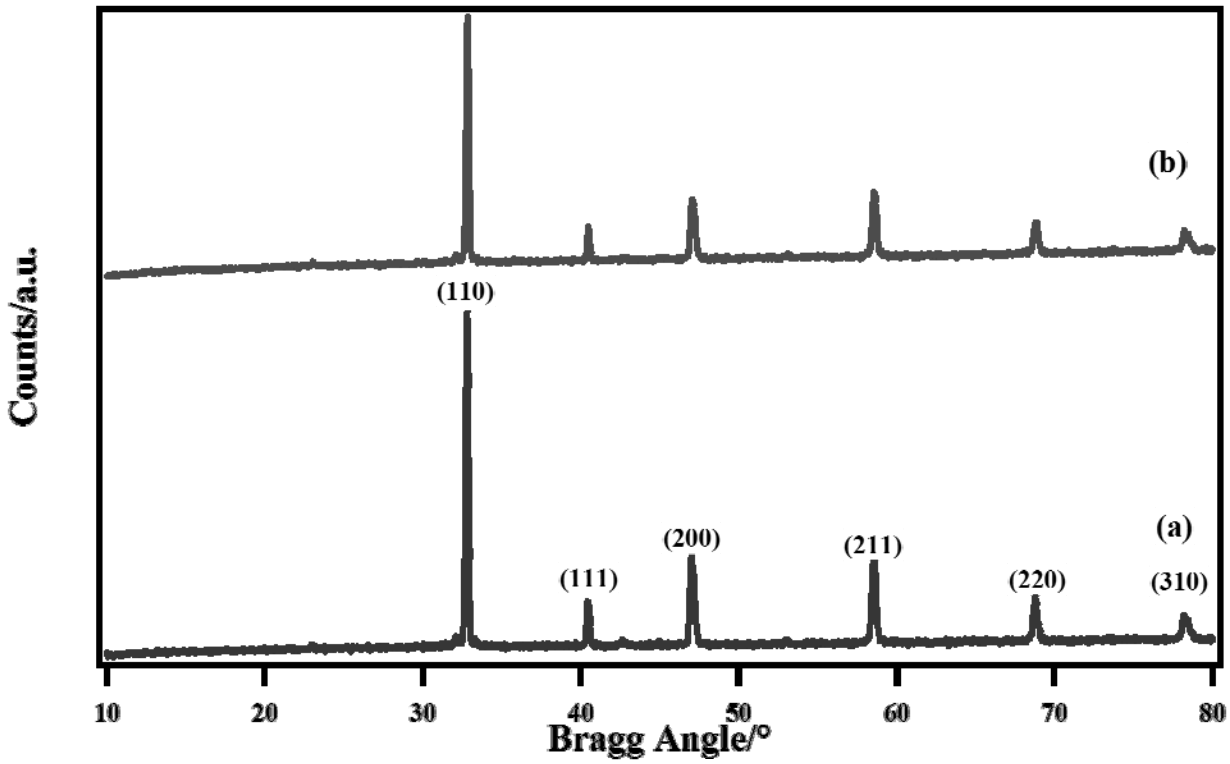

Figure 4.6.1 - *XRPD patterns of strontium perovskite samples (a) Sr001-a and (b) Sr001-b with main reflections indexed*

Sample	Method	Calcination temperature and time	Crystallite mean size/nm
Sr001-a	Coprecipitation	900; 5 hours	184±5
Sr001-b	Coprecipitation	900; 2.5 hours	157±5
Sr002-a	Coprecipitation	900; 1.5 hours	142±5

Table 4.6.1 - *Crystallite size calculated from main samples*

4.7 - Zinc spinel ferrite $ZnFe_2O_4$

This zinc compound was successfully synthesised through coprecipitation of oxalates and hydrothermal synthesis.

Products resulting from coprecipitation syntheses aimed at the preparation of the perovskite $ZnFeO_3$ are notable because, though unsuccessful, they gave as a result a powder made up of two easily identifiable phases: the spinel $ZnFe_2O_4$ and ZnO. By comparison, unsuccessful syntheses for other compounds tended to result in a multitude of crystalline phases (and unidentifiable products).

Hydrothermal syntheses were successful at temperatures as low as 75°C, yielding products with similar crystal structure characteristics as those obtained for cobalt (see Par. 4.2), manganese (see Par. 4.4) and nickel (see Par. 4.5).

Rietveld refinement was carried out on the obtained XRPD patterns [Fig. 4.7.1] based upon the data published in literature by Passerini.[267]

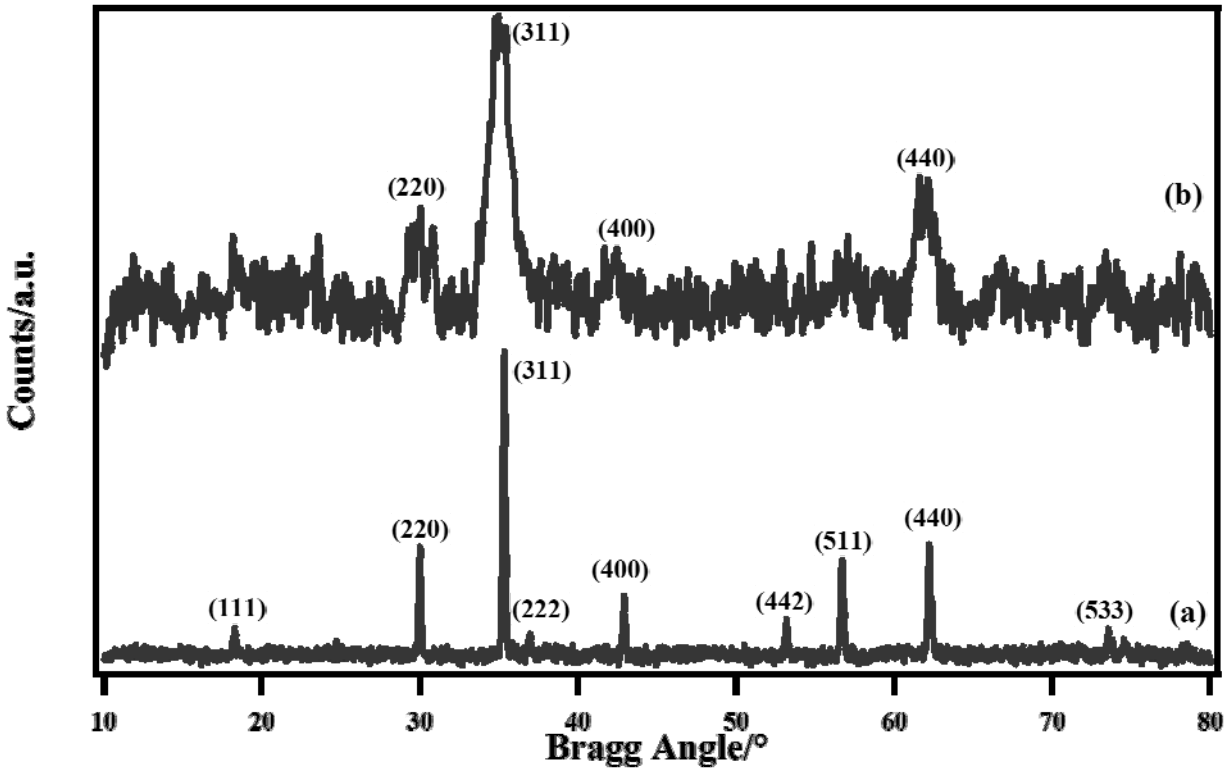

Figure 4.7.1 - *XRPD patterns of spinel samples (a) Zn002 and (b) I-Zn001 with main reflections indexed*

Crystallite size was calculated through Rietveld refinement [Tab 4.7.1] and showed that, like with all other compounds, hydrothermal synthesis resulted in smaller crystallites.

Sample	Found structure	Treatment temperature and time	Crystallite average size/nm
Zn001	$ZnFe_2O_4$ + ZnO	900°C; 5 hours	/
Zn002	$ZnFe_2O_4$	900°C; 5 hours	123±7
I-Zn001	$ZnFe_2O_4$	100°C; 24 hours	5±0.1
I-Zn002	$ZnFe_2O_4$	75°C; 24 hours	4±1
I-Zn003-4	$ZnFe_2O_4$	75°C; 4 hours	4±1

Table 4.7.1 – *Average crystallite size by compound and synthesis*

XPS analyses [Fig. 4.7.2] carried out on salient samples revealed that, as with other compounds, elimination of sodium was difficult and could not be completely achieved.

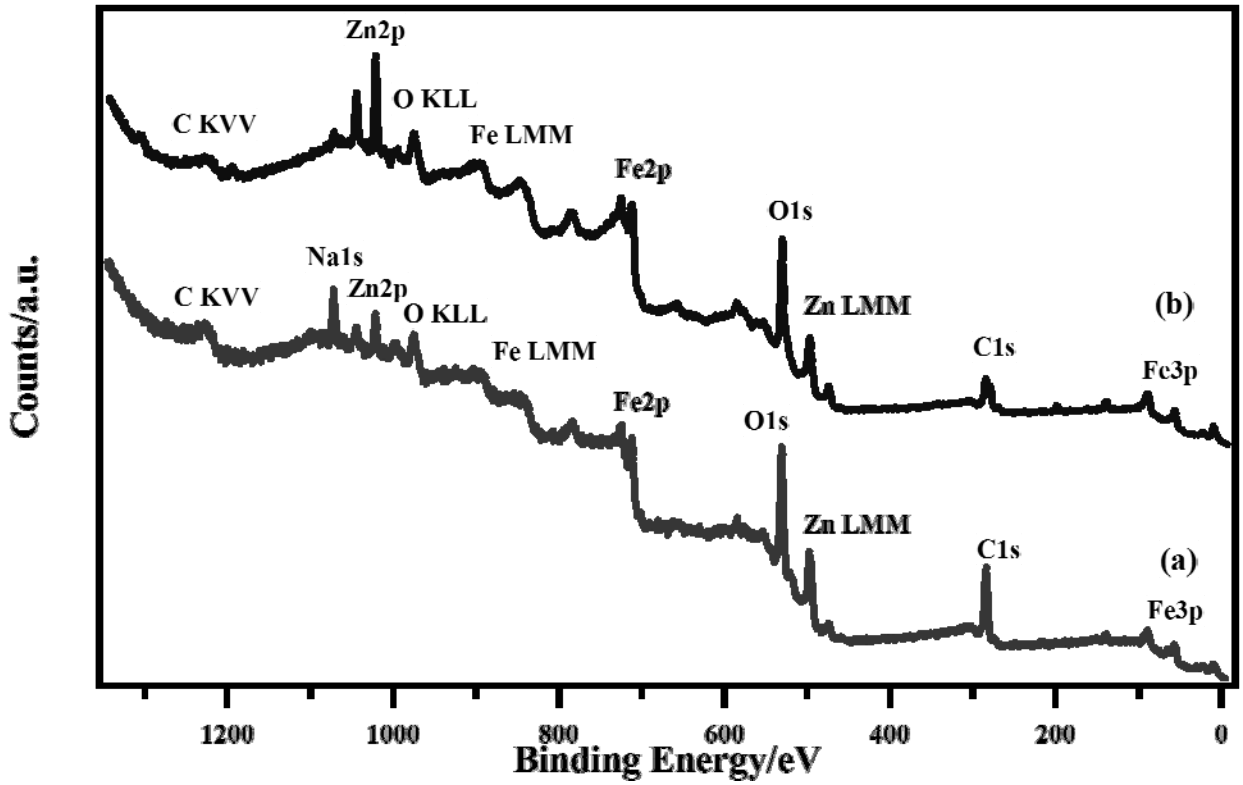

Figure 4.7.2 - *XPS survey spectra of samples (a) Zn002 and (b) I-Zn002 with main peaks indexed (B.E. values are corrected for charging effects)*

Binding energy values [Tab 4.7.2] were in agreement with the data found in literature[100, 127, 131, 154, 159, 268, 269] and, though different from expected bulk stoichiometry, surface concentration values were also in agreement with the data in literature.[100, 127, 131, 268, 269]

Compound	Element	Peak	B.E./eV
Zn002	C	1s	284.6
	O	1s	529.2
	Fe	$2p_{3/2}$ and $2p_{1/2}$	710.8 and 713.9
	Zn	$2p_{3/2}$ and $2p_{1/2}$	1021.6 and 1044.6
I-Zn002	C	1s	284.6
	O	1s	529.5
	Fe	$2p_{3/2}$ and $2p_{1/2}$	710.7 and 723.8
	Zn	$2p_{3/2}$ and $2p_{1/2}$	854.9 and 872.6

Compound	%C	%M	%Fe	%O	Fe/M atomic ratio (from XPS)	Fe/M atomic ratio (from ICP-AES)
Zn002	50.4	2.7	7.6	34.2	2.8	/
I-Zn002	60.6	2.7	7.3	29.4	2.7	/

Table 4.7.2 – *B.E., surface and bulk concentration values for the main peaks in zinc ferrite samples*

As with the other examined ferrites, the Fe2p XPS peaks [Fig. 4.7.3] display a satellite ($Fe2p_{3/2}$) peak at a B.E. value 8 eV higher than the main peak, whereas no peak at 6 eV higher is present, thus showing that all surface iron is present in an oxidation state of (III).[100, 154, 159, 181, 236, 239, 240] These results are in agreement with literature regarding the compound[100, 127, 131, 268, 269] and with the nature of $ZnFe_2O_4$ as a direct spinel, i.e. having all Fe^{III} in octahedral sites.

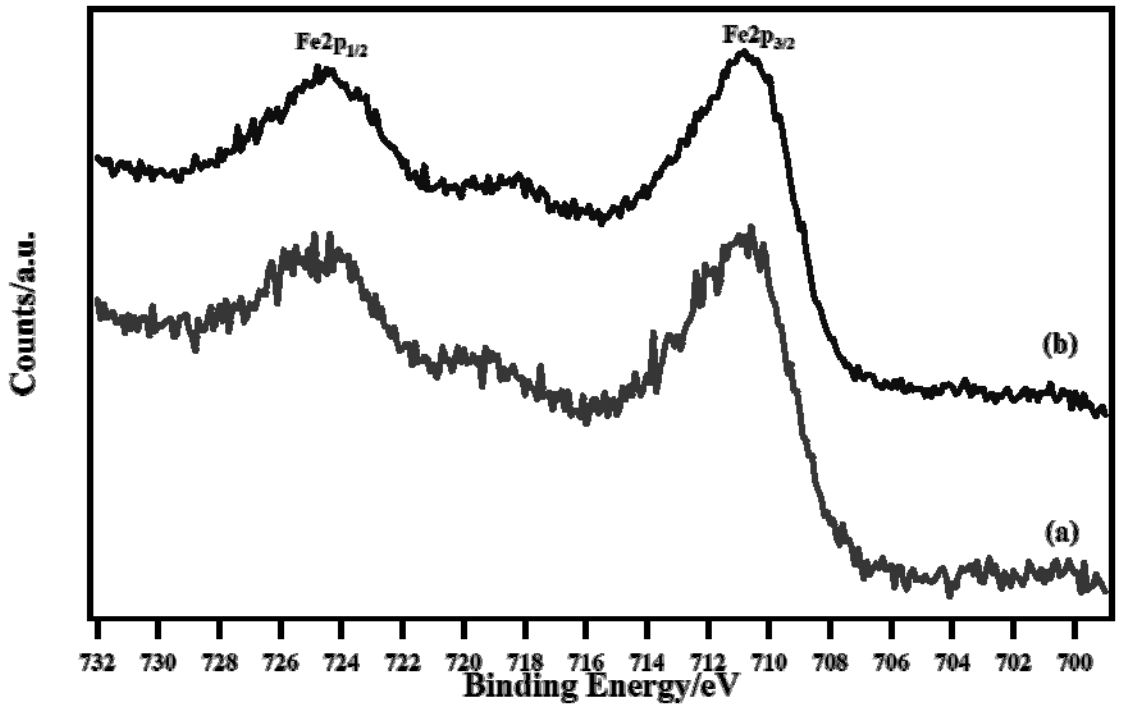

Figure 4.7.3 - *XPS spectra of the Fe2p region for samples (a) Zn002 and (b) I-Zn002 (B.E. values are corrected for charging effects)*

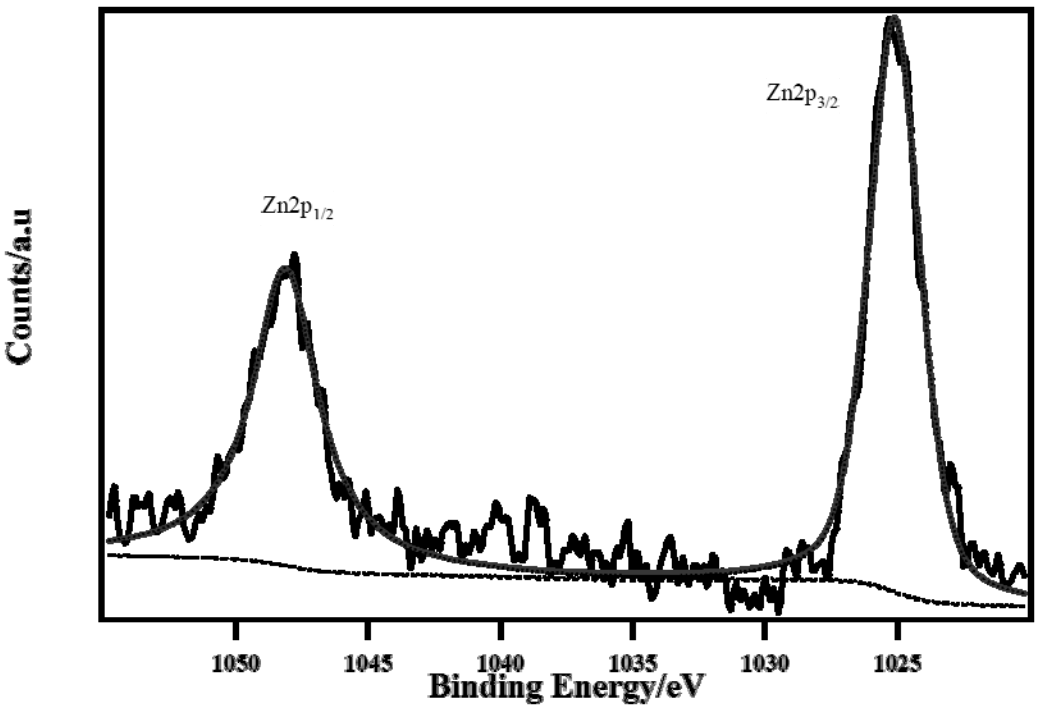

Figure 4.7.4 – *Deconvolution of the Zn2p peak for sample Zn002 (BE values are corrected for charging effects)*

The $Zn2p_{3/2}$ and $Zn2p_{1/2}$ peaks for sample Zn002 [Fig. 4.7.4] were fitted with a single interpolation peak each, showing that all surface zinc is present in the same chemical environment. The same was done for the Zn2p region relative to sample I-Zn002. Both this data and the B.E. values displayed by the peaks are consistent with data present in literature[127, 131, 269] for $ZnFe_2O_4$ and ZnO (if we consider the spinel system as equivalent to a combination of ZnO and Fe_2O_3). The singular chemical environment is also consistent with the zinc ferrite being a normal spinel.[270] Results of Mössbauer spectroscopic analysis confirmed this conclusion, as they also suggested a normal spinel structure (i.e. *x* equal to 0). The 14 K Mossbauer spectrum of zinc spinel ferrite sample Zn002 [Fig. 4.7.5] did not show the presence of magnetic ordering.

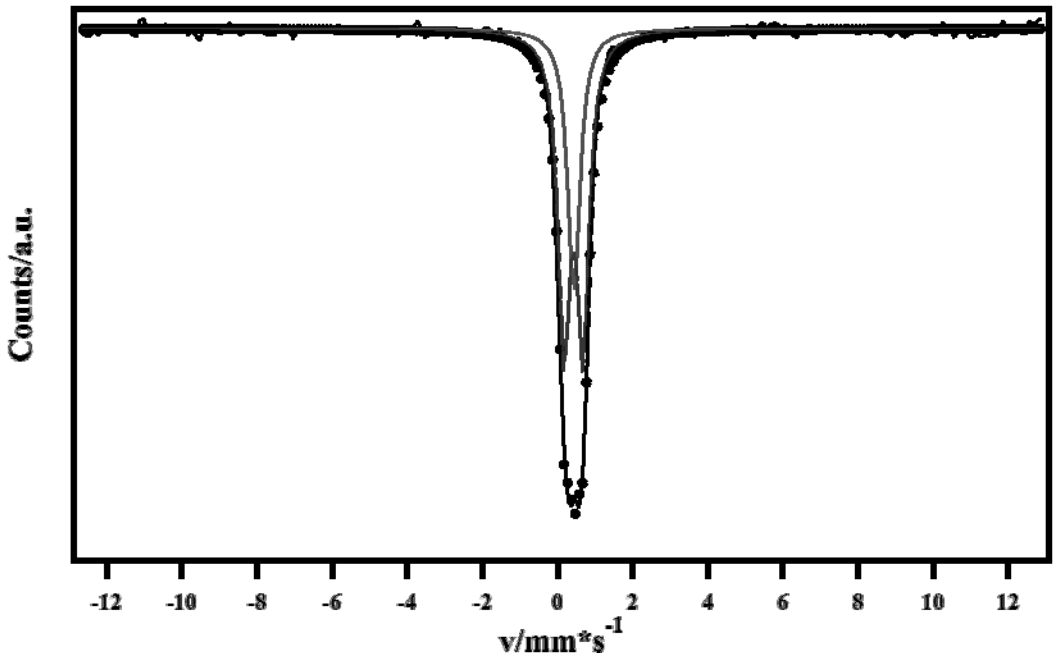

Figure 4.7.5 - *Mössbauer spectrum relative to sample Zn002 measured at 14 K*

The best fitting was obtained by using a two-component model, composed of a singlet (δ:0.43 mm/s) and a doublet (δ:0.42 mm/s, Δ:0.51 mm/s) with an area ratio 1:2. Pannaparayil et al.[271] have showed that $ZnFe_2O_4$ presents a magnetic transition below 13 K.
Micro-Raman analyses of the spinel [Fig. 4.7.6] yielded results in agreement with literature,[258, 272] both in the case of coprecipitated and hydrothermally synthesised samples, further confirming that a spinel zinc ferrite has been synthesised. The main modes for this compound[273] are all visible in both spectra. As with the other ferrites, spectra collected for both samples in different points yielded identical results, confirming the compositional uniformity throughout the powder.

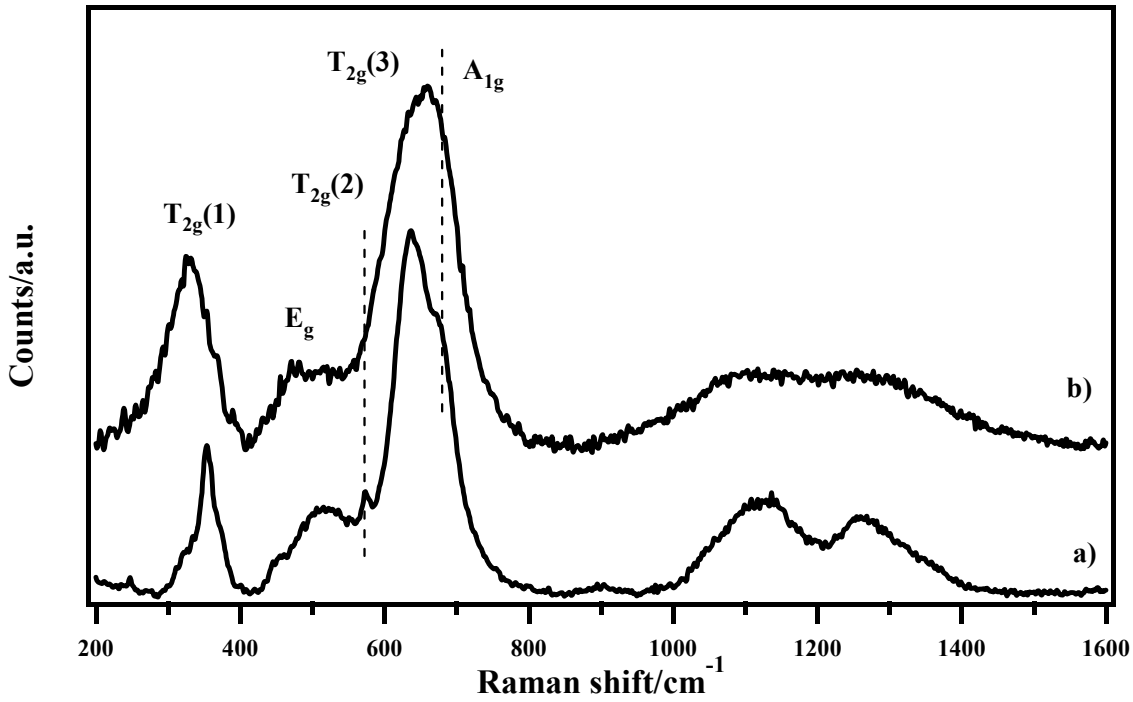

Figure 4.7.6 - *Room temperature micro-Raman spectrum of samples (a) Zn002 and (b) I-Zn002*

Results of DSC-TGA analysis will be discussed in Par. 4.8.

4.8 - Other analyses and results

The data yielded by some of the characterisations carried out on the materials can be more suitably discussed collectively, as opposed to divided by material type. The data in question will be discussed in this paragraph.

Since ferrites, and especially perovskite ferrites, have commonly found applications (see Par. 2.2) in devices where their dielectric properties are exploited, functional characterisation of our compounds from this point of view was necessary. In order to gain further insight on the functional properties of the synthesised compounds, as well as to explore possible applicative avenues, Broadband Electric Spectroscopy was employed. Specifically, Broadband Electric Spectroscopy was employed to assess the electrical responses of the nickel and cobalt spinels obtained through coprecipitation, as well as the manganese perovskite. For each investigated compound, the loss tangent (tanδ), the real component of permittivity (ε') and the logarithm of conductivity (σ) will be plotted in the following figures [Fig. 4.8.1-4.8.3].

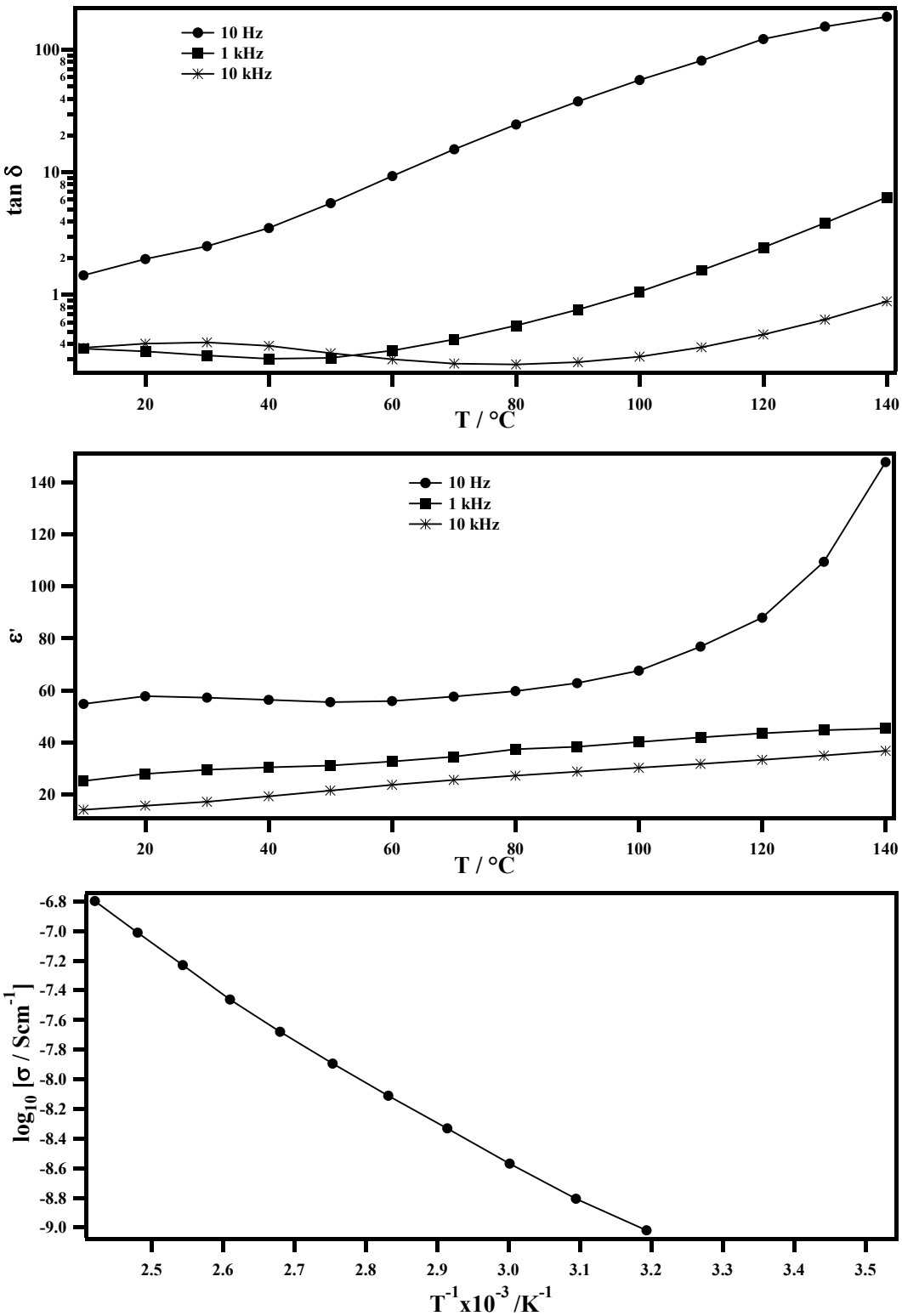

Figure 4.8.1 - *Loss tangent (tanδ), real permittivity (ε') and conductivity (σ) plots for sample Co017*

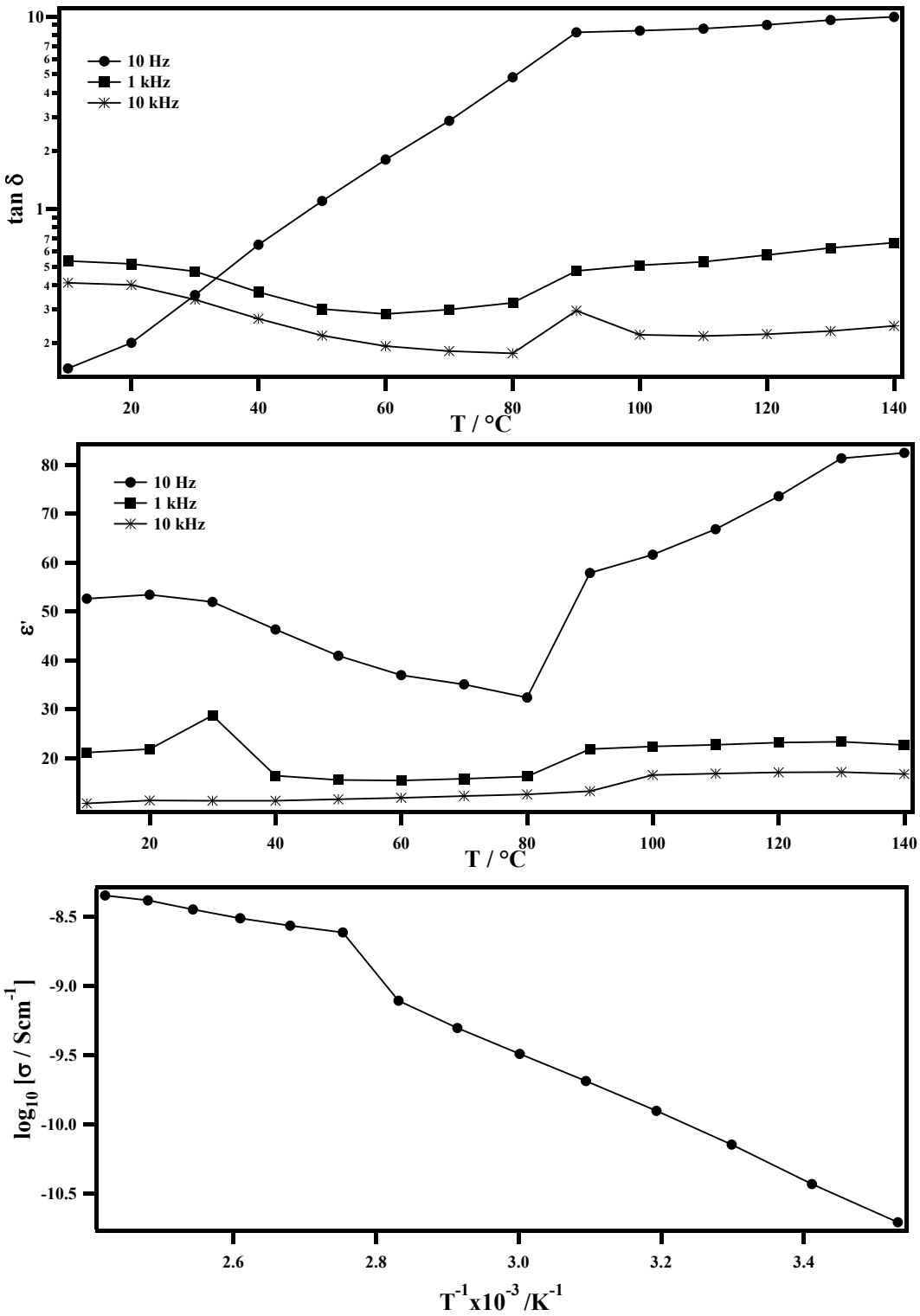

Figure 4.8.2 - *Loss tangent (tanδ), real permittivity (ε') and conductivity (σ) plots for sample Ni004*

The cobalt and nickel spinels [Fig. 4.8.1 and 4.8.2 respectively] displayed good insulating behaviour (as evidenced by the low permittivity); however at higher temperatures (30 and 90°C) relaxations were pointed out, as displayed by the shifts in the two graphs where the real component of permittivity (ε‘) is plotted. These relaxations are also visible in the logarithmic plots of conductivity (σ) and the loss tangent (tan δ) and are compatible with the presence, within the layered spinel structures, of intercalation water. These intercalated molecules make the materials interesting for applications as cathodes in lithium ion batteries, as it is reasonable to assume that,

with a suitable treatment, it might be possible to intercalate lithium ions rather than water molecules. Though the general insulating behaviour displayed by the compounds is in agreement with the data present in literature,[248] the presence of intercalated water is a novel feature which is probably a consequence of the employed synthesis route (i.e. coprecipitation of oxalates).

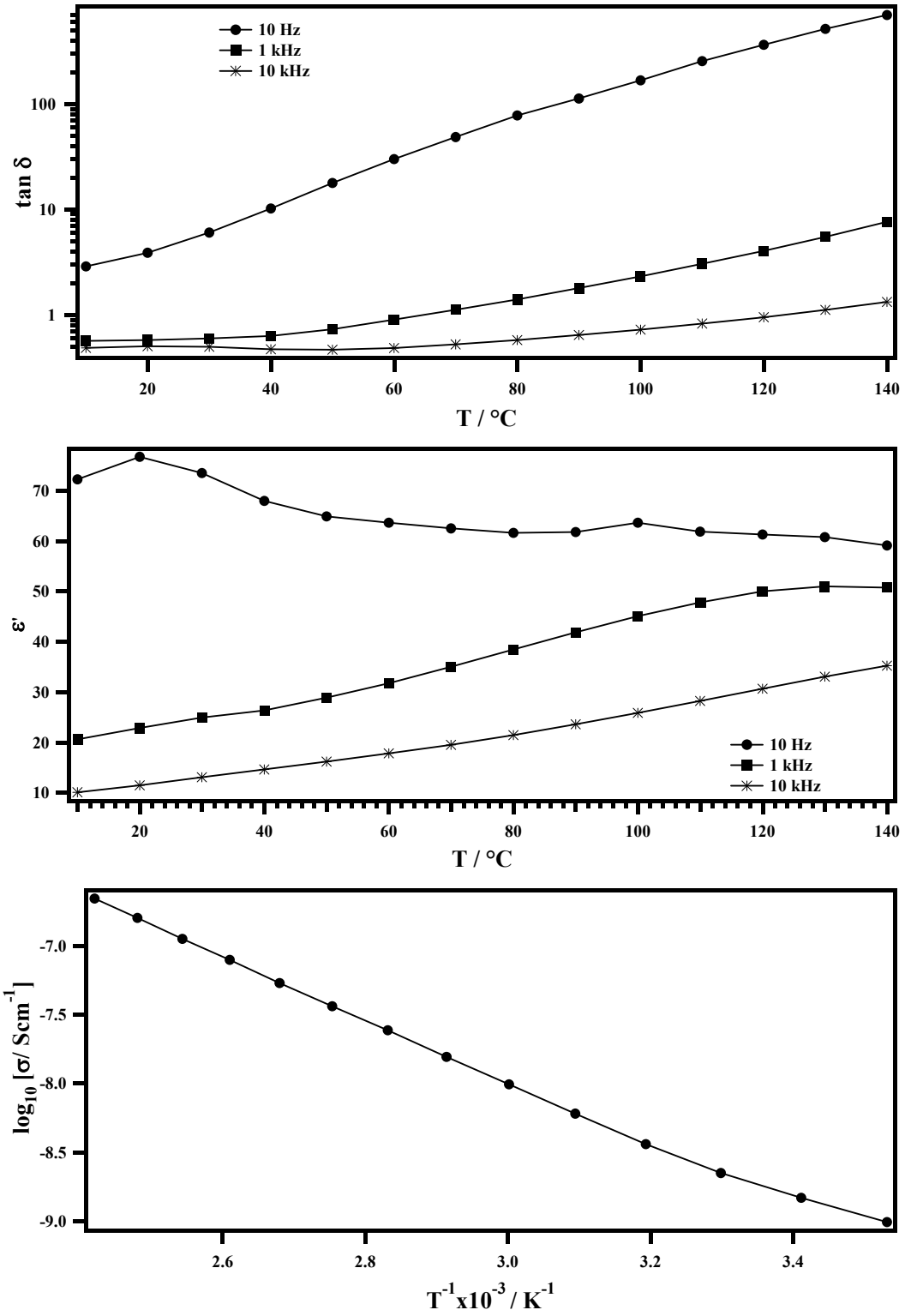

Figure 4.8.3 - *Loss tangent (tanδ), real permittivity (ε') and conductivity (σ) plots for sample Mn015*

By contrast, the manganese perovskite [Fig. 4.8.3] displayed a higher conductivity, and relaxations around 100°C. This behaviour is compatible with ionic conduction, which (as mentioned in Par.

2.2) is a known characteristic of perovskite ferrites.[66-69] These results make it reasonable to assume that the compound may display some degree of oxygen defectivity, which would act as a suitable conduit for conduction of oxygen ions.

Considering the extensive data present in literature[82, 83, 85, 98, 100, 102, 274] regarding the catalytic application of mixed metal ferrites, tests were carried out on the synthesised samples to investigate these possible applications of the compounds. Temperature programmed oxidation of methane (CH_4-TPO) was employed [Tab 4.8.1] to evaluate possible catalytic activity in the synthesised materials. Experiments were both carried out on a pure sample and on a mixture of the sample and SiC powder (in order to limit temperature spikes and formation of local hot spots). Tests performed on Co011 and Mn011 reveal that both materials are highly active in this reaction. The determined onset temperatures for Co011 and Mn011 of 507 °C and 559°C in the first and 523°C and 551°C in the second experiment, respectively, meaning a lowering of at least about 300°C in comparison to the uncatalysed reaction (857°C, empty cell). It should be emphasised that there is only a slight change in the onset temperatures between the first and second cycles, indicating good short-term catalyst stability. Concerning hydrothermally synthesised materials, samples I-Mn003 and I-Co004 showed high activities. Onset temperatures of 490°C and 510°C for the manganese containing sample in the first and second run reveal a lowering of the onset temperature of about 350°C if compared to the empty cell with 857°C (uncatalysed reaction). However, a slide activity loss was detected. Sample I-Co004 showed a much higher activity in the first run (onset temperature of 400°C) but this value was increased to 521°C for the second experiment. Nevertheless, the cobalt as well as the manganese spinel ferrite are highly active. Loss of activity is probably caused by sintering occurring among nanoparticles. According to activity tests described for ferrites in literature[275], results are comparable to published values.

Sample	Onset/°C (first cycle)	Onset/°C (Second cycle)
Blank (empty cell)	855	855
Mn011 (pure)	524	543
Co011 (pure)	683	515
Mn011 (diluted with SiC)	559	551
Co011 (diluted with SiC)	507	523
I-Co004 (diluted with SiC)	400	521
I-Mn003 (diluted with SiC)	490	510
I-Ni003 (diluted with SiC)	357	505

Table 4.8.1 – *CH_4-TPO test results*

As it was revealed by TEM, XRD and TPXRD that the calcination process had a profound influence on the structural and compositional characteristics of the final materials, analyses were carried out to unravel the processes which took place during this step. Moreover, in the case of hydrothermally prepared powders, thermal analyses would allow to investigate compound stability and evaluate the presence of residual organic components. For these reasons, TGA-DSC was employed both on the solids obtained after basification (but prior to calcination) [Fig. 4.8.4] in the coprecipitation synthesis and on the crystalline ferrite powders prepared through hydrothermal synthesis.

The results were similar for samples prepared with the same protocol. In the case of coprecipitation

synthesis, the samples display similar weight loss curves, with minor differences which can be attributed to the differing M metals involved in the reaction.

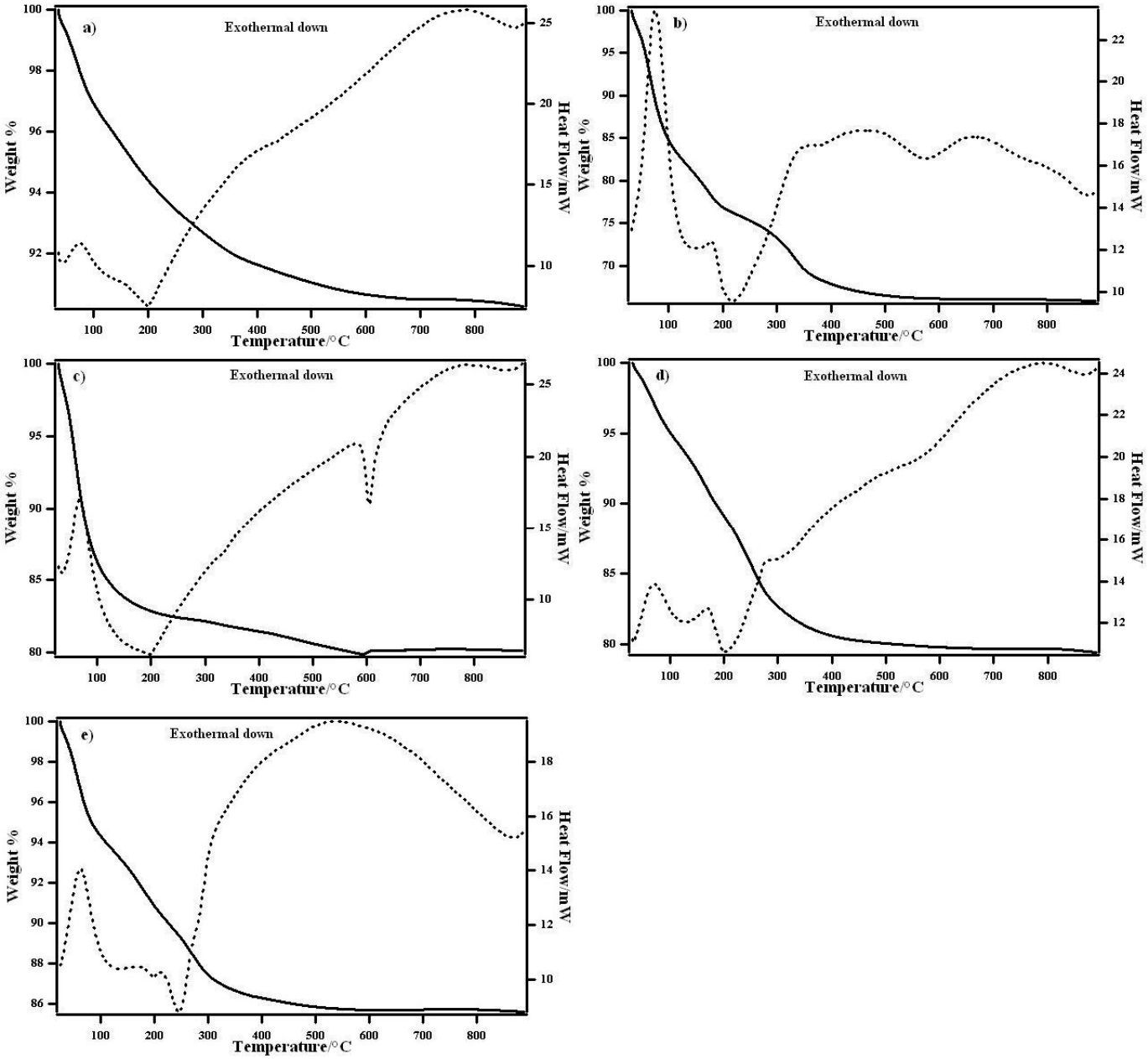

Figure 4.8.4 – *TGA-DSC graphs showing weight loss (line) and heat flow (dashes) for the analysed samples a) Co024, b) Mg018, c)Mn021, d) Ni007 and e) Zn003*

The endothermic peak displayed in all samples at 80°C can be ascribed to the evaporation of residual adsorbed water. Comparison of the curves with the data reported in literature regarding the decomposition of oxalates in air[226-230] show that the exothermal doublet at 200-250°C is relative to the decomposition of ferric oxalate (in some cases overlapping with the decomposition of the metal oxalate). In all cases, the decomposition of the salts to oxides (following a transformation from hydrated salts, to anhydrous salts and finally to oxides)[228] is completed by 370°C (with the specific temperature depending on the M metal). Further thermal reactions taking place in the precursor can be ascribed to the formation of the final bimetallic ferrite from the single oxides.

In the case of hydrothermal synthesis, weight loss was minimal (less than 4%), indicating that most

of the compound obtained was a pure ceramic oxide (and thus impervious to thermal decomposition) [Fig 4.8.5 and 4.8.6]. The detected weight loss can be attributed to several components: initially, (a) residual physisorbed water is lost, successively (b) crystallisation water is eliminated. Further weight losses (c), (d), accounting for approximately 2% weight, can be attributed to the decomposition of residual adsorbed organic residuals (probably on the surface of the powder).

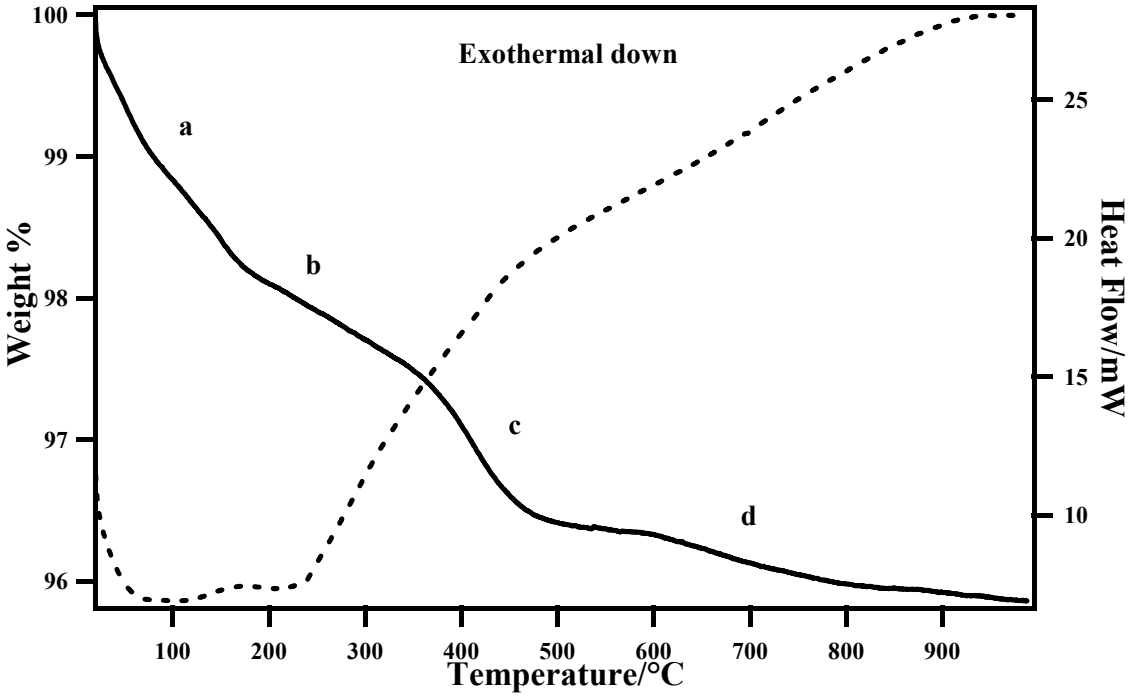

Figure 4.8.5 – *TGA-DSC graphs showing weight loss (line) and heat flow (dashes) for sample I-Co017*

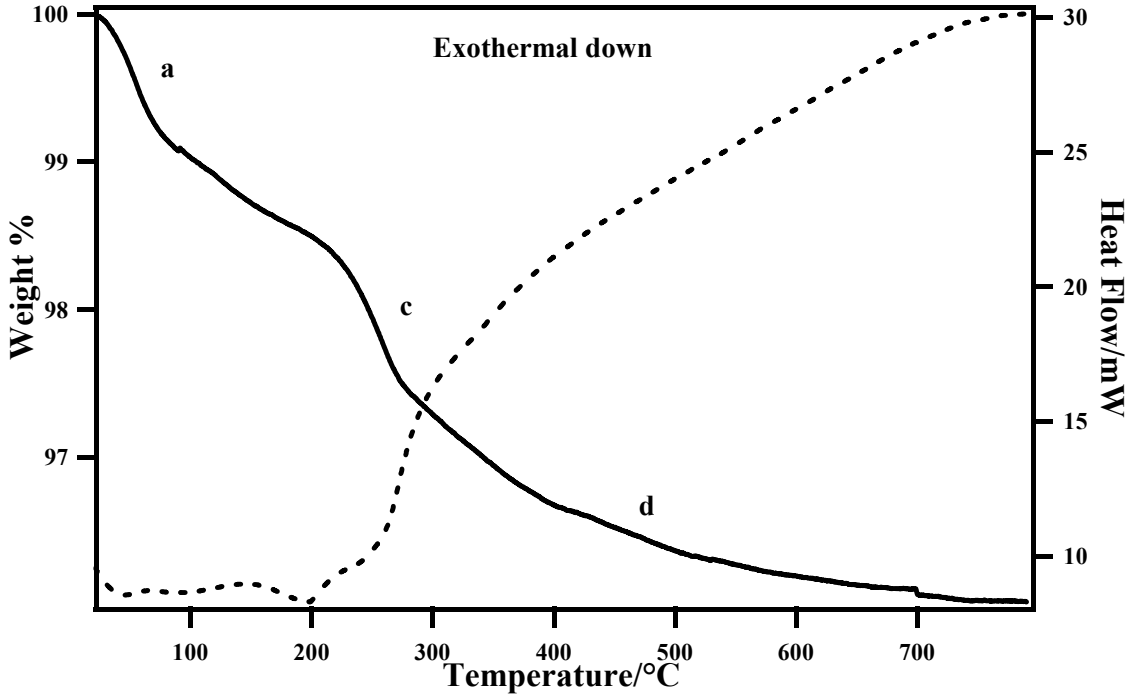

Figure 4.8.6 – *TGA-DSC graphs showing weight loss (line) and heat flow (dashes) for sample I-Ni010*

The TGA data collected from hydrothermally prepared samples is consistent with the results from microanalysis tests [Tab. 4.8.2], which show that only a very small amount of organic material is

present in the final product, thus accounting for the small entity of the weight loss. This proves the purity of the obtained materials.

Sample	Content	Expected C%	Expected H%	Found C%	Found H%
I-Co017	$CoFe_2O_4$	0.00	0.00	0.25	0.35
I-Mn011	$MnFe_2O_4$	0.00	0.00	0.13	0.20
I-Ni010	$NiFe_2O_4$	0.00	0.00	0.70	0.43
I-Zn002	$ZnFe_2O_4$	0.00	0.00	0.24	0.37
R-Zn001	$ZnFe_2O_4$	0.00	0.00	0.81	1.22

Table 4.8.2 - *Microanalysis results for spinel ferrite samples*

Given that coprecipitation synthesis requires a calcination step, during which presumably all organic components are eliminated as CO_2, no microanalysis tests were carried out on coprecipitated samples.

4.9 – Mixed metal ferrites

Through the same protocol applied for the single metal ferrites, mixed ferrites containing iron and two further transition metals were synthesised for the cobalt-magnesium and cobalt-manganese metal couples in spinel form. The cobalt-manganese perovskite was also obtained. Samples were investigated through XRD, XPS and ICP-AES. In particular, ICP-AES analysis allowed to confirm that $M_{0.5}M'_{0.5}Fe_2O_4$ and $M_{0.5}M'_{0.5}FeO_3$ were successfully synthesized.

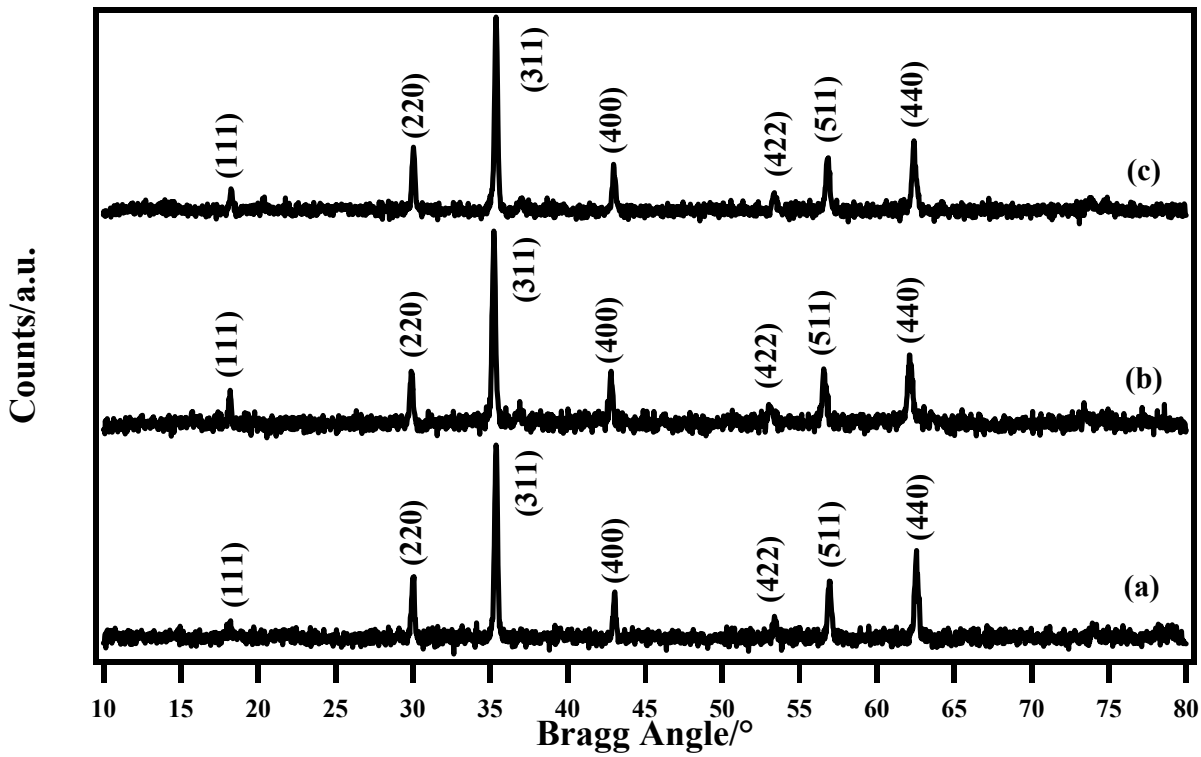

Figure 4.9.1 – *XRD patterns of samples a) CoMg-S; b) CoMn-P and c) CoMn-S with main reflections indexed*

Comparing the results of Rietveld refinement with those relative to non-mixed ferrites prepared with the same method (Par 4.2-4.7), these ferrites show average crystallite sizes [Tab. 4.9.1] in the

same order of magnitude. It is notable that all three patterns show a structure which is typical of spinel-type oxides ($M^{II}M'_2{}^{III}O_4$), even in the case of sample CoMn-P [Fig. 4.9.1-c] where a perovskite-type structure ($MFeO_3$) would have been expected. Among the three compounds, only the cobalt-manganese spinel [Fig. 4.9.1-b] was successfully fitted with a $Co_{0.5}Mn_{0.5}Fe_2O_4$ structure. The cobalt-magnesium spinel [Fig. 4.9.1--a] was fitted as a two-phase crystalline compound consisting of a 1:1 mixture of $MgFe_2O_4$ and $CoFe_2O_4$ (reflections are overlapped as the two phases have identical unit cells and similar cell parameters). The presence of a spinel phase in the third compound [Fig. 4.9.1-c] was attributed to the coexistence of two phases in a 1:3 molar ratio: a $CoFe_2O_4$ spinel and an second manganese oxide phase (γ-Mn_3O_4) which crystallises with very similar crystal cell parameters (cubic Fd-3m a=8.42 Å).[276] The simultaneous presence of these two phases would explain the atomic ratios measured through ICP-AES (see below). Due to the extreme similarities between the two structures, like in the case of the cobalt-magnesium spinel [Fig. 4.9.1-a] it is impossible in the pattern [Fig. 4.9.1-c] to make a distinction between reflections relative to each phase. This indicates that, whilst a mixed-metal perovskite was not successfully obtained, the coprecipitation of oxalates route afforded a mixed crystalline oxide with good stoichiometric control.

Sample	**Obtained compound**	**Crystalline phase(s)**	**Crystallite average size/nm**
CoMg-S	$Co_{0.5}Mg_{0.5}Fe_2O_4$	$CoFe_2O_4$ $MgFe_2O_4$	179±10 107±10
CoMn-S	$Co_{0.5}Mn_{0.5}Fe_2O_4$	$Co_{0.5}Mn_{0.5}Fe_2O_4$	275±10
CoMn-P	$Co_{0.5}Mn_{0.5}FeO_3$	$CoFe_2O_4$	178±5

Table 4.9.1 – *Crystallite size calculated for the synthesized samples*

It is to be noted that the mixed cobalt-manganese phase in sample CoMn-S showed considerably larger crystallites compared to the cobalt phases in samples CoMg-S and CoMn-P. Also, the crystallite size calculated for the mixed Co-Mn is greater than the average crystallite sizes estimated for single-metal manganese and iron ferrites ($CoFe_2O_4$ and $MnFeO_3$) synthesised using the same protocol (Par 4.2 and 4.4). By contrast, the magnesium spinel phase and the cobalt spinel phase in samples CoMg-S and CoMn-P display crystallites with sizes comparable to their single-metal iron ferrite counterparts (Par 4.2-4.4). This data evidences that the coalescence phenomena that take place during the calcination take place at a higher speed for the mixed metal phase compared to the single metal ferrite phases. This is in agreement with the hypothesis of two distinct ceramic oxide phases in both CoMg-S and CoMn-P.

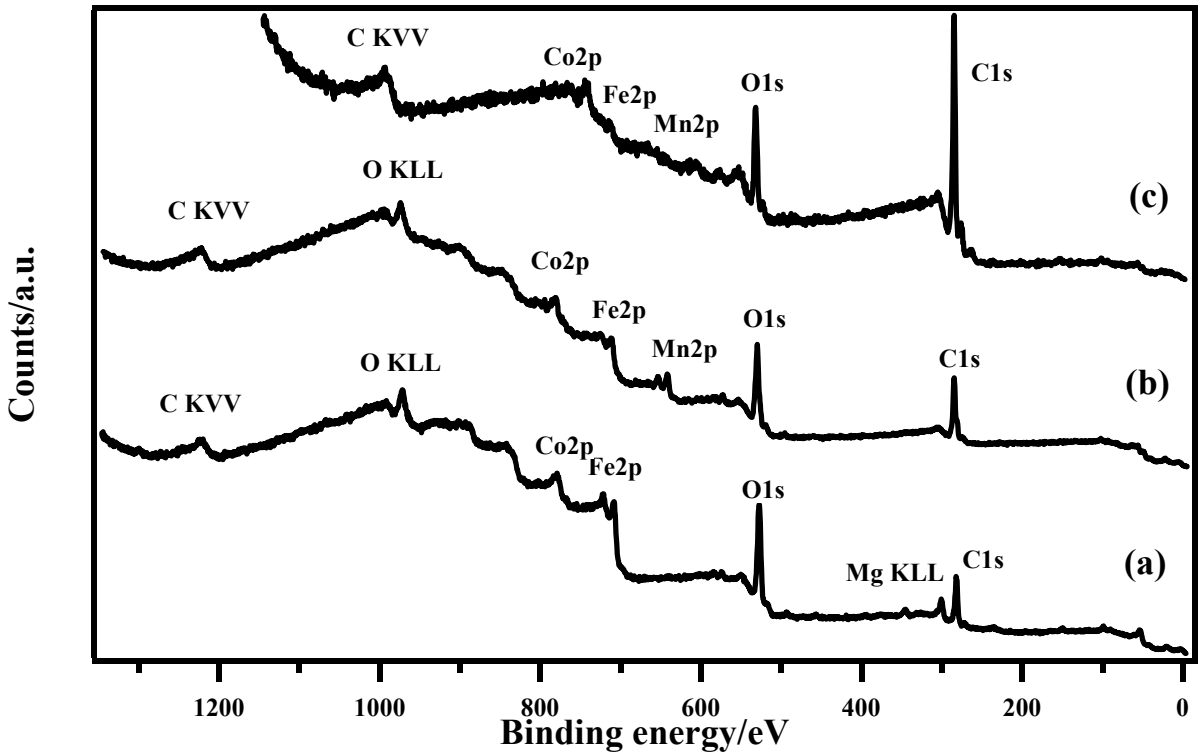

Figure 4.9.2 – *XPS surveys of samples a) CoMg-S; b) CoMn-P and c) CoMn-S (B.E. values are corrected for surface charging)*

XPS analysis [Fig. 4.9.2] carried out on the samples (after correcting for surface charging) showed B.E. (Binding Energy) values [Table 4.9.2] in agreement with the data found in literature for single metal iron ferrites. In particular, B.E. values Fe2p and the 2p transition of the bivalent transition metals (cobalt, manganese and manganese) reported in table 4.9.2 are those typical of spinel iron ferrites containing these elements.[152, 154, 159, 181, 236, 239, 240, 253, 277]

Surface Fe/M ratios [see table 4.9.2], obtained from XPS, were in agreement (within a 10% range) with the bulk material stoichiometry, and with the data present in literature regarding surface concentration trends for cobalt[100, 181, 236] and manganese ferrites.[278] The fact that Fe/Mg ratio is slightly lower on the surface compared to the bulk material is also consistent with normal behaviour for magnesium spinel ferrites.[100, 240] The high carbon content on the materials is presumably due to both adventitious carbon since, given the calcination temperature employed (900°C) the presence of residual organic moieties from the reagents is highly unlikely. In the case of the magnesium spinel, a significant secondary peak with a B.E. of 288.0 eV is visible in the C 1s region, probably due to metallic carbonates, which also contribute to the high surface carbon concentration.

Sample	Element	XPS Peak	Binding Energy/eV	Surface atomic %	Fe/M/M' ratio (XPS)	Fe/M/M' ratio (ICP)	Fe/M/M' ratio (theoretical)
CoMg-S	C	C1s	284.6	64.2	2.0/1.5/0.5	2.00/0.45/0.70	2.00/0.50/0.50
	O	O1s	529.8	27.5			
	Fe	$Fe2p_{3/2}$ and $Fe2p_{1/2}$	710.7 and 723.8	4.2			
	Co	$Co2p_{3/2}$ and $Co2p_{1/2}$	780.3 and 795.3	3.1			
	Mg	Mg1s	1303	1.1			
CoMn-P	C	C1s	284.6	73.0	1.0/0.9/0.6	1.00/0.45/0.50	1.00/0.50/0.50
	O	O1s	529.8	20.1			
	Fe	$Fe2p_{3/2}$ and $Fe2p_{1/2}$	710.5 and 723.6	2.7			
	Co	$Co2p_{3/2}$ and $Co2p_{1/2}$	779.9 and 794.9	2.5			
	Mn	$Mn2p_{3/2}$ and $Mn2p_{1/2}$	641.5 and 652.5	1.7			
CoMn-S	C	C1s	284.6	91.0%	2.0/0.5/0.5	2.00/0.45/0.46	2.00/0.50/0.50
	O	O1s	529.9	7.5			
	Fe	$Fe2p_{3/2}$ and $Fe2p_{1/2}$	710.5 and 723.8	0.5			
	Co	$Co2p_{3/2}$ and $Co2p_{1/2}$	779.8 and 794.8	0.1			
	Mn	$Mn2p_{3/2}$ and $Mn2p_{1/2}$	641.0 and 652.0	0.1			

Table 4.9.2 – *B.E. values, surface and bulk concentrations for mixed ferrites*

Due to peak overlap (regardless of the source used there is significant overlap between the 2p and Auger peaks relative to Co, Fe and M higher resolution spectra of the B.E. regions relative to these peaks did not provide significant further information.

The bulk atomic ratios between the metals obtained through ICP-AES [Tab. 4.9.2] show that the mixed metal ferrites have been obtained with the desired stoichiometry, proving that the chosen synthetic route affords an excellent stoichiometric control. The fact that the stoichiometric ratio between the metals in the final crystalline oxides has been set through the coprecipitation synthesis protocol, simply by adjusting the nominal ratios of the metal precursors, makes this method a powerful tool for the preparation of mixed metal ceramic oxides.

5 - Experimental

In this chapter the various synthetic protocols (nonaqueous sol-gel, coprecipitation and hydrothermal synthesis), as well as the post-synthesis treatment protocols will be described. Samples were labelled according to the following code: compounds prepared by nonaqueous sol-gel synthesis display an S- prefix, compounds obtained by coprecipitation have no prefix, sample names resulting from hydrothermal synthesis are prefaced by I- and samples prepared under reflux are prefaced by R-.

5.1 - Chemicals

The chemicals used during this Ph.D. thesis are summarised in table 5.1.1.

Chemical	Purity	Supplier
Benzyl alcohol	99.8%	Sigma-Aldrich (Milan, Italy)
Ammonium hydroxide	30-33% NH_3 solution in water	Sigma-Aldrich (Milan, Italy)
$Iron^{III}$ acetylacetonate	99.9%	Sigma-Aldrich (Milan, Italy)
$Iron^{II}$ acetylacetonate	99.9%	Sigma-Aldrich (Milan, Italy)
$Iron^{II}$ acetate	99.995%	Sigma-Aldrich (Milan, Italy)
$Manganese^{II}$ acetate	98%	Sigma-Aldrich (Milan, Italy)
$Cobalt^{II}$ acetylacetonate		Sigma-Aldrich (Milan, Italy)
$Cobalt^{II}$ acetate	99.995%	Sigma-Aldrich (Milan, Italy)
Barium	Pure metal	Sigma-Aldrich (Milan, Italy)
Calcium	Pure metal	Sigma-Aldrich (Milan, Italy)
Strontium	Pure metal	Sigma-Aldrich (Milan, Italy)
Magnesium	Pure metal	Sigma-Aldrich (Milan, Italy)
Tetraethyl ammonium hydroxide	20% (v/v) in water	Sigma-Aldrich (Milan, Italy)
Sodium hydroxide		Sigma-Aldrich (Milan, Italy)
Magnesium nitrate hexahydrate		Sigma-Aldrich (Milan, Italy)
Magnesium sulphate	99%	Sigma-Aldrich (Milan, Italy)
$Nickel^{II}$ chloride hexahydrate		Sigma-Aldrich (Milan, Italy)
Strontium nitrate		Sigma-Aldrich (Milan, Italy)
Strontium carbonate		Sigma-Aldrich (Milan, Italy)
$Zinc^{II}$ acetylacetonate		Sigma-Aldrich (Milan, Italy)
$Zinc^{II}$ nitrate hydrate		Sigma-Aldrich (Milan, Italy)
$Iron^{III}$ chloride hexahydrate		Sigma-Aldrich (Milan, Italy)
Barium acetate	99%	Sigma-Aldrich (Milan, Italy)
Oxalic acid dihydrate		AnalytiCals-Carlo Erba (Val de Reuil, France)
$Manganese^{II}$ acetate dihydrate		AnalytiCals-Carlo Erba (Val de Reuil, France)
Calcium nitrate		AnalytiCals-Carlo Erba (Val de Reuil, France)
$Cobalt^{II}$ chloride hexahydrate		AnalytiCals-Carlo Erba (Val de Reuil, France)
$Iron^{III}$ nitrate nonahydrate		Merck (Dramstadt, Germany)
Barium chloride dihydrate		Riedel de Haën (Selze-Hannover, Germany)

Table 5.1.1 - *Reagents used during the Ph.D. Thesis*

All the above reagents, with the exception of barium acetate, were used without further purification. Barium acetate was used after purging the residual air in the packaging through successive applications of vacuum and argon.

5.2 - Nonaqueous sol-gel synthesis protocol

Within a glove box, stoichiometric amounts of the precursor compounds (see tables 5.5.1; 5.7.1; 5.9.1; A1.1.1; A1.1.2; A1.2.1) were placed into a 908035 Discover (CEM) glass vial with a magnetic stirrer. 5 ml benzyl alcohol were added and the vial was sealed with a 908140 Discover (CEM) cap. The resulting mixture was vigorously stirred in order to partially dissolve the precursor compounds in the solvent and suspend the rest.

The suspension was then heated through the use of a Discover-S microwave heater Mod.908860 (CEM Microwave Technology Ltd.) equipped with an Explorer-12 Hybrid autosampler (CEM Microwave Technology Ltd.) and operating on the Synergy program (v. 1.43 - CEM Microwave Technology Ltd.) [Fig. 5.2.1].

Fig. 5.2.1 - *Discover-S microwave heater (CEM Microwave Technology Ltd.)*

The resulting suspension was centrifuged with a Vaudaux-Eppendorf miniSpin centrifuge for one hour at 13.4 kRPM. The solid phase was separated by decantation, suspended in 4 ml of an ethanol/ethyl ether (50% v/v) mixture and centrifuged a second time for 30 minutes at 13.4kRPM. This procedure was repeated twice using 4 ml ethanol/ethyl ether mixture again and finally 2 ml ethyl ether.

The isolated solid phase was dried in open air in a Memmert oven at 60°C for one hour. The resulting solid agglomerates were crushed in an agate mortar prior to analysis. A scheme of the synthetic process is sketched in Fig. 5.5.2.

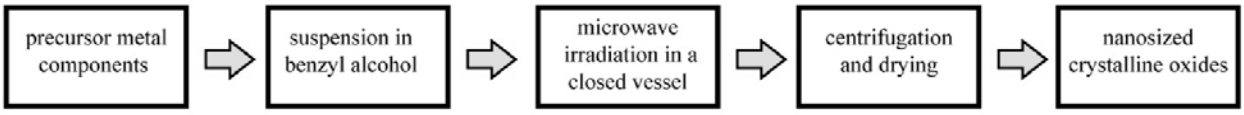

Fig. 5.2.2 - *Reaction scheme for nonaqueous sol-gel synthesis*

Different syntheses were carried out by varying the net amount of used precursor, the nature of the precursors (both for the iron precursor and the bivalent metal precursor), the reported temperature and the time the system was kept at the aforementioned temperature and the presence or absence of

water in the system. It must be noted that, although the instrument allowed to set the temperature for the reaction mixture, the nature of heating by microwave irradiation implies that much higher temperatures might be reached locally (see Par. 3.4) since compounds containing iron are characterised by a higher loss factor than benzyl alcohol (indeed thus allowing the achievement of a higher local temperature and therefore enhancing the formation of the metal oxide particles). The instrument measures temperature by means of a vertically focused IR sensor, which provides a punctual reading (which is then averaged due to stirring in the vessel). The equipment is however unable to monitor local temperature spikes and thus, while it can be assumed that reactions occurring at higher temperatures received more irradiation and thus higher temperatures were reached, the value of these temperatures and the local temperature profiles are unknown. The temperature values reported in the tables relative to these syntheses [Tab 5.5.1; 5.7.1; 5.9.1; A1.1.1; A1.1.2; A1.2.1] are thus indicative only of the average temperature of the reaction mixture.

5.3 - Coprecipitation of oxalates synthesis protocol

In a typical synthesis, stoichiometric amounts of the precursor compounds were dissolved in 50 ml deionised water; in a further batch, oxalic acid dihydrate was dissolved in 50 ml deionised water. The two solutions were mixed and TENOH was added to the solution as a peptising agent.[209] At room temperature, the pH of the solution (monitored with a pH-meter) was raised in accordance to the basification protocol (see below); the resulting precipitate was then isolated and dried in an oven in air at 90°C for 5 hours. The solid thus obtained was ground in an agate mortar and calcined (see table 5.3.1) in air.

Several different protocols were employed to increase the pH: this was done in order to investigate how this important step in the synthesis influenced the structural and compositional features of the final powders. The four protocols used are described below:

- Protocol A: basification a 2 M NaOH solution was used as basification agent and its addition was carried out under stirring. The solution was slowly added dropwise until pH 12 was reached, upon which the resulting suspension was stirred for 45 minutes. The suspension was further aged for 20 minutes before purification.
- Protocol B: as with protocol A, basification was carried out with 2 M NaOH, slowly under stirring. Unlike protocol A, upon reaching pH 12 the suspension was stirred for 3 hours and then aged for 18 hours.
- Protocol C: basification was carried out with a 2 M NaOH solution. The hydroxide was added quickly and in a single step to the reaction mixture without stirring. The resulting suspension was aged for 65 minutes before purification. The amount of NaOH solution employed was dependent on the Fe/M nominal ratio (20 ml if the ratio was 1, 30 ml if the ratio was 0.5) in order to account for the different iron and oxalic acid content.
- Protocol D: a 30-33% (v/v) aqueous solution of NH_4OH was used. The solution was added very slowly, dropwise until pH 11 was reached. The resulting suspension was stirred for 45 minutes and the further aged for 20 minutes before purification.

The different calcination protocols employed are based on a sequence which assumes a linear heating ramp, followed by a plateau, where the sample is maintained at a constant temperature for a given time, and finally a cooling step [Fig. 5.3.1].

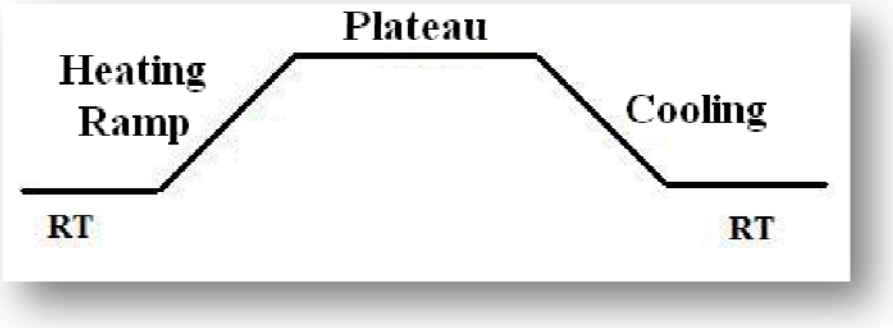

Fig. 5.3.1 - *Calcination scheme*

The specific parameters for the various protocols are summarised in the table below:

Protocol	Heating ramp (from RT)	Plateau	Plateau duration	Cooling
1	1.5 hours	400°C	5 hours	3 hours
2	2 hours	600°C	5 hours	3 hours
3	3 hours	900°C	1.5 hours	4 hours
4	3 hours	900°C	2.5 hours	4 hours
5	3 hours	900°C	3.5 hours	4 hours
6	3 hours	900°C	5 hours	4 hours
7	4 hours	1100°C	5 hours	4 hours

Table 5.3.1 - *Calcination protocols*

The solid fraction in the suspension was isolated through one of two methods:

- filtration over A Büchner funnel: using a blue-band filter (pores < 2 μm) and washing 6 times with deionised water
- centrifugation: 5-minute cycles at 10 kRPM in a HERMLE Z366 (Hermle Labortechnik, Germany) centrifuge to isolate the solid fraction followed by washing 4 times with deionised water. After adding each portion of deionised water and before centrifugation, the vials were sonicated for 15 minutes at 40 kHz using a Sonica Ultrasonic Cleaner (SOLTEC, Italy) Mod. 2200.

The second method (centrifugation) was employed once it was evidenced that simple filtration was less efficient in eliminating residual ions (mainly Na^+ ions resulting from the basification step) from the final product).

The reaction scheme for this synthesis protocol is reported in figure 5.3.2.

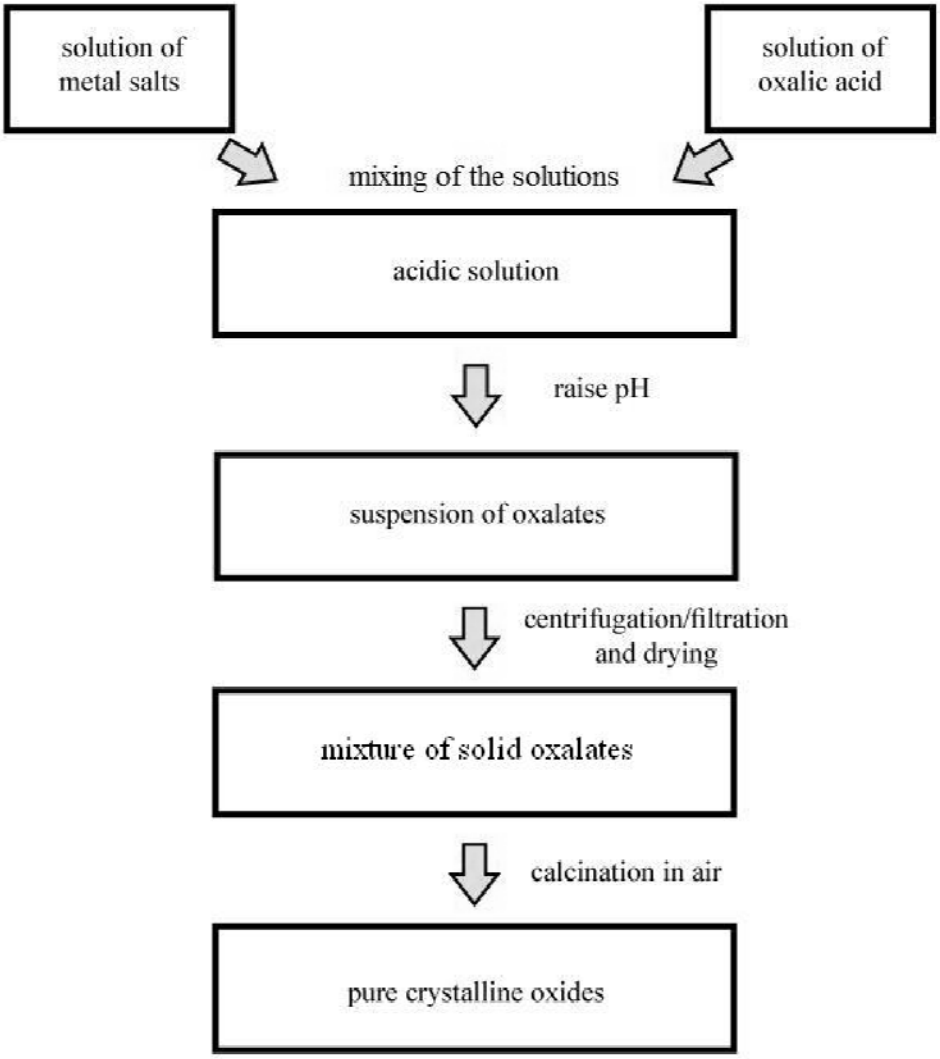

Fig. 5.3.2 - *Flow chart of the synthesis based on coprecipitation of oxalates*

Different syntheses were carried out by changing the nature of the metal precursors, the Fe/M nominal ratio, the Fe/oxalic acid nominal ratio, the purification method, the basification and calcination protocols, as reported in the following paragraphs (5.5-5.11) and in the corresponding tables.

5.4 - Hydrothermal synthesis protocol

In a typical synthesis, stoichiometric amounts of the precursor metal salts and oxalic acid were dissolved in 10 ml deionised water in a 23 ml Teflon liner. 0.2 ml (0.14 mmol) TENOH, acting as a peptising agent,[209] were added to the solution. The pH of the solution was adjusted to the desired value, either using a 10 M NaOH aqueous solution or a 30-33% v/v NH_4OH aqueous solution at room temperature. The liner was then sealed and placed in a 23 ml stainless steel Parr reactor (4745 General Purpose Acid-Digestion Bomb - Parr Instrument Company) [Fig. 5.4.1], heated at 135°C for 24 hours and left to cool down to room temperature. The resulting solid powders were isolated by centrifugation using the same protocol as with coprecipitation of oxalates (see Par. 5.3).

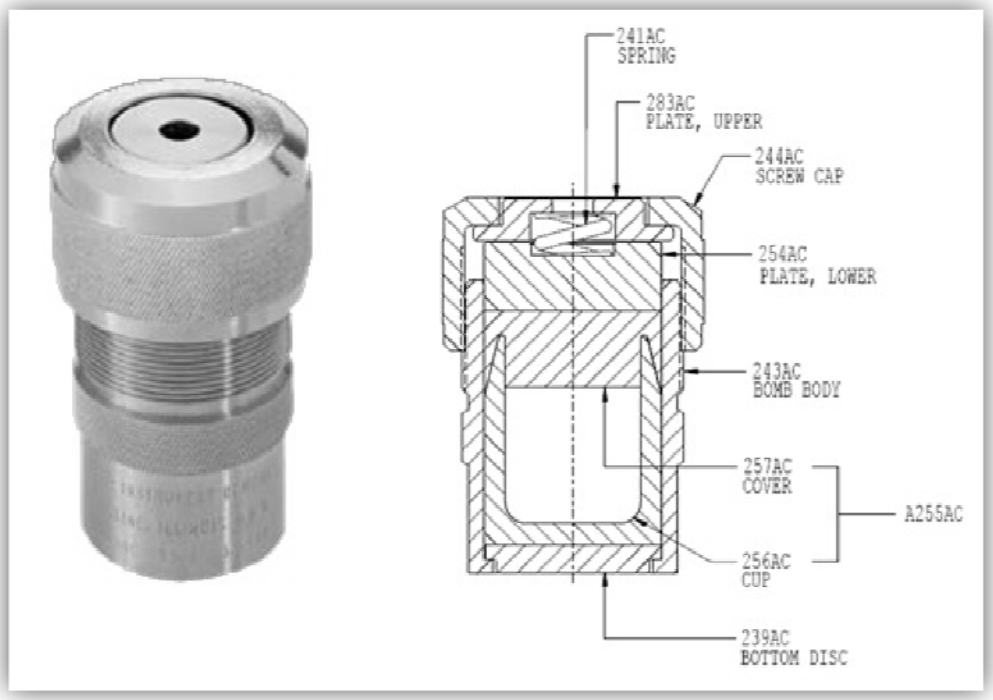

Figure 5.4.1 - *Acid digestion bomb and its components*[212]

The reaction scheme for this synthesis protocol is reported in figure 5.4.2.

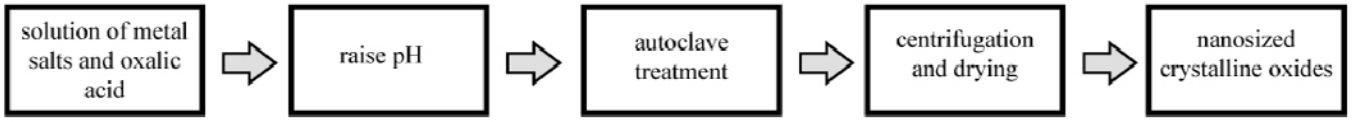

Fig. 5.4.2 - *Reaction scheme for hydrothermal synthesis*

Different syntheses were carried out by changing the Fe/M ratio, the Fe/oxalic acid ratio, the treatment temperature, the treatment time and basification agent, as reported in sections 5.5-5.11. Syntheses were also carried out in a sealed glass vial (rather than in an acid digestion bomb) in order to gather visual data on the process steps and evolution. A similar synthetic route was applied for the zinc ferrite (Par. 5.10), substituting hydrothermal treatment with reflux in open air. Operationally, the syntheses were in all other aspects identical to hydrothermal syntheses.

In the following sections, the synthesis of the different ferrites by using the three synthesis methods described above will be described more in depth, by addressing the specific synthetic protocols used for each ferrite.

5.5 - Syntheses of cobalt ferrites

In a typical synthesis of **$CoFe_2O_4$** by nonaqueous sol-gel route, stoichiometric amounts of $Fe(CH_3COCHCOCH_3)_2$ (254 mg, 1.00 mmol) and $Co(CH_3COCHCOCH_3)_2$ (130 mg, 0.50 mmol) were suspended in 5 ml benzyl alcohol under inert atmosphere in a glove box. The vial containing the suspension was sealed and placed in a microwave heater. The suspension was heated up to 180°C for 30 minutes. The resulting suspension was then isolated through centrifugation as described in the above section. The isolated solid was then dried in an oven at 60°C in open air for one hour and crushed into powder in an agate mortar.

Attempts to synthesise the cobalt perovskite **$CoFeO_3$** by this method have been unsuccessful, resulting in either an amorphous product with traces of crystalline CoO or in a mixed product composed primarily of cobalt spinel.

Different syntheses were carried out by varying the net amount of precursor used, the nature of the iron precursor, the reported temperature and the time the system was kept at said temperature as reported in the table below.

Experiment	Reagent 1	Quantity/mmol	Reagent 2	Quantity/mmol	Treatment temperature/°C	Treatment time/min
S-Co010 - 1	Fe^{III}acac	1.00	Co^{II}acac	0.50	180	15
S-Co010 - 2	Fe^{III}acac	1.00	Co^{II}OAc	0.50	180	15
S-Co010 - 3	Fe^{III}acac	1.00	Co^{II}acac	0.50	200	15
S-Co010 - 4	Fe^{III}acac	1.00	Co^{II}acac	0.50	180	30
S-Co010 - 5	Fe^{III}acac	1.00	Co^{II}acac	0.50	200	30
S-Co010 - 6	Fe^{III}acac	1.00	Co^{II}acac	0.50	180	45
S-Co010 - 7	Fe^{III}acac	1.00	Co^{II}acac	0.50	200	45
S-Co011 - 1	Fe^{II}acac	1.01	Co^{II}acac	0.50	180	15
S-Co011 - 3	Fe^{II}acac	1.00	Co^{II}acac	0.50	200	15
S-Co011 - 4	Fe^{II}acac	1.00	Co^{II}acac	0.50	180	30
S-Co011 - 5	Fe^{II}acac	1.00	Co^{II}acac	0.50	200	30
S-Co012 - 1	Fe^{II}OAc	1.00	Co^{II}acac	0.50	180	15
S-Co012 - 2	Fe^{II}OAc	1.00	Co^{II}acac	0.50	200	15
S-Co012 - 3	Fe^{II}OAc	1.00	Co^{II}acac	0.50	180	30
S-Co012 - 4	Fe^{II}OAc	1.00	Co^{II}acac	0.50	200	30

Table 5.5.1 - *Experimental parameters for the syntheses of $CoFe_2O_4$ via nonaqueous sol-gel synthesis*

In a typical synthesis of **$CoFe_2O_4$** by coprecipitation of oxalates, stoichiometric amounts of $CoCl_2 \cdot 6H_2O$ (1.243 g, 5.22 mmol) and $FeCl_3 \cdot 6H_2O$ (2.872 g, 10.45 mmol) were dissolved in 50 ml deionised water. Separately, oxalic acid dihydrate (2.960 g, 23.50 mmol) was dissolved in 50 ml deionised water. After the obtainment of two clear mixtures, the two solutions were mixed and 2 ml TENOH were added. The pH was raised to 12 by adding dropwise a 2 M NaOH aqueous solution under vigorous stirring. The resulting light brown suspension was stirred for further 45 minutes and left to age for further 20 minutes. The mixture was then filtered over a Büchner funnel and washed

five times with deionised water. The filtered solid was dried in open air in an oven for 5 hours at 90°C. The dried product was ground in an agate mortar and calcined in air at 900°C for 5 hours.

Syntheses through this route aimed at obtaining the perovskite **$CoFeO_3$** were unsuccessful, resulting in the formation of powders displaying either amorphous components or a multitude of crystalline phases (mainly the spinel $CoFe_2O_4$).

Several syntheses were carried out by changing the nominal ratio between reagents, the basification protocol, the amount of TENOH employed, the purification method and the calcination protocol, as reported in table 5.5.2.

Sample	Nominal Fe/M/acid molar ratio	TENOH/ ml	Basification protocol	Purification method	Calcination temperature (protocol number)
Co001	1/1/3	2	A	Filtration	900°C (6)
Co002	2/1/4.5	2	A	Filtration	900°C (6)
Co003	1/1/3	2	B	Filtration	900°C (6)
Co004	2/1/4.5	2	B	Filtration	900°C (6)
Co005	2/1/4.5	2	A	Filtration	900°C (6)
Co006	2/1/4.5	2	B	Filtration	1100°C (7)
Co007-a	2/1/4.5	2	A	Filtration	900°C (3)
Co007-b	2/1/4.5	2	A	Filtration	900°C (4)
Co008	2/1/4.5	2	B	Filtration	600°C (2)
Co009	2/1/4.5	2	A	Filtration	400°C (1)
Co010	1/1/3	2	A	Filtration	600° (2)
Co011	2/1/4.5	2	A	Filtration	900°C (6)
Co012	2/1/4.5	8	A	Filtration	900°C (6)
Co013	2/1/4.5	2	C	Filtration	900°C (6)
Co015	2/1/4.5	2	A	Filtration	900°C (6)
Co016	2/1/4.5	2	A	Filtration	900°C (6)
Co017	2/1/4.5	2	A	Centrifugation	900°C (6)
Co018	2/1/4.5	2	A	Centrifugation	900°C (6)
Co020	2/1/4.5	2	D	Centrifugation	900°C (6)
Co021	2/1/4.5	2	A	Centrifugation	900°C (6)
Co022	2/1/4.5	2	A	Centrifugation	900°C (6)
Co023	2/1/4.5	2	A	Centrifugation	900°C (6)
Co024	2/1/4.5	2	A	Centrifugation	900°C (6)

Table 5.5.2 – *Experimental parameters for the syntheses of $CoFe_2O_4$ via coprecipitation of oxalates*

For a standard synthesis of the cobalt spinel **$CoFe_2O_4$** through the hydrothermal route, stoichiometric amounts of $CoCl_2 \cdot 6H_2O$ (0.124 g, $5.22 \cdot 10^{-1}$ mmol), $FeCl_3 \cdot 6H_2O$ (0.287 g, $10.45 \cdot 10^{-1}$ mmol) and oxalic acid dihydrate (0.296 g, $2.35 \cdot 10^{-1}$ mmol) were dissolved in 10 ml deionised water in a 23 ml Teflon liner, 0.2 ml TENOH were then added to this solution. The pH was raised to 12 with a 10 M NaOH aqueous solution under vigorous stirring. The light brown suspension thus obtained was sealed in a 23 ml Teflon liner inside the acid digestion bomb and treated at 135°C for 24 hours. The bomb was cooled at room temperature for 1.5 hours before opening. The black powder produced after this treatment was isolated by centrifugation (10 kRPM, 5 minutes) and

washed with deionised water. The dark grey product was then dried in open air in an oven for 5 hours at 90°C.

Syntheses aimed at producing the cobalt perovskite **$CoFeO_3$** (I-Co002, I-Co003) were unsuccessful, resulting in generally amorphous powders.

Several syntheses were performed by varying the nominal Fe/M/acid molar ratio, basification agent, treatment temperature, treatment time, pH of the suspension and the vessel in which the reaction was carried out [Tab 5.5.3].

Sample	Nominal Fe/M/acid molar ratio	Final pH	Basification agent	Treatment time/hours	Treatment vessel	Treatment temperature/°C
I-Co001	2/1/4.5	12	NaOH	24	Bomb	135
I-Co002	1/1/3	12	NaOH	24	Bomb	135
I-Co003	2/1/4.5	12	NaOH	24	Bomb	135
I-Co004	2/1/4.5	12	NaOH	24	Bomb	135
I-Co005	2/1/4.5	12	NaOH	24	Bomb	135
I-Co006	2/1/4.5	12	NaOH	24	Bomb	160
I-Co007	2/1/4.5	12	NaOH	24	Bomb	135
I-Co008	2/1/4.5	12	NaOH	24	Vial	135
I-Co009	2/1/4.5	7	NaOH	24	Bomb	135
I-Co010	2/1/4.5	10	NaOH	24	Bomb	135
I-Co011	2/1/4.5	12	NH_4OH	24	Bomb	135
I-Co012	2/1/3	12	NaOH	2	Vial	135
I-Co013	2/1/3	12	NaOH	24	Vial	135
I-Co015	2/1/3	9	NaOH	24	Bomb	135
I-Co016	2/1/3	12	NH_4OH	24	Bomb	135
I-Co017	2/1/3	9	NaOH	24	Bomb	135
I-Co018-1	2/1/3	9	NaOH	1	Bomb	135
I-Co018-2	2/1/3	9	NaOH	2	Bomb	135
I-Co018-4	2/1/3	9	NaOH	4	Bomb	135
I-Co018-6	2/1/3	9	NaOH	6	Bomb	135
I-Co019	2/1/3	9	NaOH	24	Bomb	100
I-Co020	2/1/3	9	NaOH	24	Bomb	75

Table 5.5.3 – *Experimental parameters for the syntheses of $CoFe_2O_4$ via hydrothermal method*

5.6 - Syntheses of magnesium ferrites

No syntheses were performed to obtain magnesium ferrites though nonaqueous-sol gel, due to the difficulties encountered in obtaining a suitable magnesium precursor: although attempts were made to react metallic magnesium with benzyl alcohol in order to produce a magnesium benzyl alkoxide solution, they were unsuccessful, as only turbid solutions (thus with unknown concentration) were produced.

In standard synthesis of **$MgFe_2O_4$** by coprecipitation of oxalates, $Mg(NO_3)_2 \cdot 6H_2O$ (1.340 g, 5.22 mmol) and $FeCl_3 \cdot 6H_2O$ (2.872g, 10.45 mmol) were dissolved in 50 ml deionised water. Separately, oxalic acid dihydrate was dissolved in an equal quantity of deionised water. Having achieved complete solubilisation, the two mixtures were combined and 2 ml TENOH were added to the resulting solution. The pH was raised to 12 by slowly pouring a 2 M NaOH aqueous solution under

vigorous stirring. The brick red suspension was kept under stirring for 45 minutes, afterwards it was aged for further 20 minutes in order to allow partial phase separation. The brick red solid phase was isolated by filtration on a Büchner funnel, washed five times with deionised water and dried in air at 90°C for 5 hours. The resulting solid was ground in an agate mortar and calcined at 900°C for 5 hours.

Syntheses carried out with this method and aimed at the preparation of the magnesium perovskite **$MgFeO_3$** were unsuccessful and generally yielded amorphous or impure powders, mainly consisting of $Mg_xFe_yO_4$ spinels.

Several syntheses were carried out by altering nominal ratio between reagents, basification protocol, TENOH amount, purification method and calcination protocol, as reported in table 5.6.1.

Sample	Nominal Fe/M/acid molar ratio	TENOH/ ml	Basification protocol	Purification method	Calcination temperature (protocol number)
Mg001	1/1/3	2	A	Filtration	900°C (6)
Mg002	2/1/4.5	2	A	Filtration	900°C (6)
Mg003	1/1/3	2	B	Filtration	900°C (6)
Mg004	2/1/4.5	2	B	Filtration	900°C (6)
Mg006-a	2/1/4.5	2	A	Filtration	900°C (3)
Mg006-b	2/1/4.5	2	A	Filtration	900°C (5)
Mg007	2/1/4.5	2	A	Filtration	600°C (2)
Mg008	2/1/4.5	2	A	Filtration	900°C (6)
Mg009	1/1/3	2	A	Filtration	600°C (2)
Mg010	2/1/4.5	2	A	Filtration	900°C (6)
Mg011	2/1/4.5	8	A	Filtration	900°C (6)
Mg012	2/1/4.5	2	C	Filtration	900°C (6)
Mg013	2/1/4.5	2	A	Filtration	900°C (6)
Mg014	2/1/4.5	2	A	Filtration	900°C (6)
Mg015	2/1/4.5	2	A	Filtration	900°C (6)
Mg016	2/1/4.5	2	A	Centrifugation	900°C (6)
Mg017	2/1/4.5	2	D	Centrifugation	900°C (6)
Mg018	2/1/4.5	2	A	Centrifugation	900°C (6)

Table 5.6.1 – *Experimental parameters for the syntheses of $MgFe_2O_4$ via coprecipitation of oxalates*

Attempts made to obtain the magnesium spinel or the magnesium perovskite via hydrothermal synthesis were unsuccessful, yielding mainly amorphous powders. The synthesis procedure was analogous to that used for the hydrothermal synthesis of $CoFe_2O_4$ (see Par. 5.5), with magnesium sulphate as the precursor magnesium salt (as the use of $Mg(NO_3)_2 \cdot 6H_2O$ would have been unwise due to possible explosion risks). The syntheses are reported in table 5.6.2.

Sample	Nominal Fe/M/acid molar ratio	Final pH	Basification agent	Treatment time/hours	Treatment vessel	Treatment temperature/°C
I-Mg001	2/1/4.5	12	NaOH	24	Bomb	135
I-Mg002	1/1/3	12	NaOH	24	Bomb	135
I-Mg004	2/1/4.5	12	NaOH	24	Bomb	160

Table 5.6.2 – *Experimental parameters for the syntheses of magnesium ferrites via hydrothermal method*

5.7 - Syntheses of manganese ferrites

For a typical nonaqueous sol-gel synthesis of the spinel ferrite **$MnFe_2O_4$**, stoichiometric amounts of $Fe(CH_3COCHCOCH_3)_3$ (355 mg, 1.01 mmol) and $Mn(OOCCH_3)_2$ (86 mg, 0.50 mmol) were suspended in 5 ml benzyl alcohol under inert atmosphere in a glove box. The vial containing the suspension was sealed and placed in a microwave heater. The suspension was heated up to 200°C for 45 minutes. The resulting suspension was then isolated through centrifugation as described in the above section. The isolated dark grey solid was then dried in and oven at 60°C in open air for one hour and crushed into powder in an agate mortar.

Different syntheses were carried out by varying the net amount of precursor used, the nature of the precursors (both for the iron precursor and the manganese precursor), the nominal treatment temperature and the time the system was kept at said temperature, as reported in the table below.

Experiment	Reagent 1	Quantity/mmol	Reagent 2	Quantity/mmol	Treatment Temperature/°C	Treatment Time/min
S-Mn003-1	Fe^{III}acac	1.00	Mn^{II}acac	0.52	180	5
S-Mn003-2	Fe^{III}acac	1.00	Mn^{II}OAc	0.53	180	5
S-Mn003-3	Fe^{II}OAc	1.00	Mn^{II}acac	0.50	180	5
S-Mn003-4	Fe^{II}OAc	1.00	Mn^{II}OAc	0.50	180	5
S-Mn004-1	Fe^{III}acac	1.00	Mn^{II}acac	0.50	200	10
S-Mn004-2	Fe^{III}acac	1.00	Mn^{II}OAc	0.51	200	10
S-Mn004-3	Fe^{II}OAc	1.01	Mn^{II}acac	0.50	200	10
S-Mn004-4	Fe^{II}OAc	1.00	Mn^{II}OAc	0.51	200	10
S-Mn005-1	Fe^{III}acac	1.00	Mn^{II}acac	0.51	180	15
S-Mn005-2	Fe^{III}acac	0.97	Mn^{II}OAc	0.50	180	15
S-Mn005-3	Fe^{III}acac	1.00	Mn^{II}acac	0.50	200	15
S-Mn005-4	Fe^{III}acac	1.00	Mn^{II}OAc	0.51	200	15
S-Mn006-1	Fe^{III}acac	1.00	Mn^{II}acac	0.50	180	15
S-Mn006-2	Fe^{III}acac	1.00	Mn^{II}OAc	0.50	180	15
S-Mn006-3	Fe^{III}acac	1.00	Mn^{II}acac	0.50	200	15
S-Mn006-4	Fe^{III}acac	1.00	Mn^{II}OAc	0.50	200	15
S-Mn006-5	Fe^{III}acac	1.00	Mn^{II}acac	0.50	200	25
S-Mn006-6	Fe^{III}acac	1.00	Mn^{II}OAc	0.50	200	25
S-Mn007-1	Fe^{II}acac	1.00	Mn^{II}acac	0.50	180	15
S-Mn007-2	Fe^{II}acac	1.01	Mn^{II}OAc	0.51	180	15
S-Mn007-3	Fe^{III}acac	1.01	Mn^{II}OAc	0.50	200	45
S-Mn008-1	Fe^{II}acac	1.01	Mn^{II}acac	0.50	200	15
S-Mn008-2	Fe^{II}acac	1.00	Mn^{II}OAc	0.50	200	15
S-Mn008-3	Fe^{III}acac	1.00	Mn^{II}acac	0.50	200	45

Table 5.7.1 - *Experimental parameters for the nonaqueous sol-gel syntheses of $MnFe_2O_4$*

Syntheses by using this method and aimed at obtaining the perovskite **$MnFeO_3$** were unsuccessful: the products obtained were generally impure and/or partially amorphous, with the main crystalline phase present being the spinel ferrite $MnFe_2O_4$.

Unlike in the case for the perovskite, attempts to synthesise the spinel **$MnFe_2O_4$** via coprecipitation of oxalates were unsuccessful and generally yielded mainly amorphous powders.

To synthesise the perovskite **$MnFeO_3$**, oxalic acid dihydrate (1.975g, 15.67 mmol) was dissolved in 50 ml deionised water, $Mn(OAc)_2 \cdot H_2O$ (1.092g, 5.22 mmol) and $FeCl_3 \cdot 6H_2O$ (1.412 g, 5.22 mmol) were dissolved in further 50 ml deionised water. After combining the two solutions, 2 ml TENOH were added and the resulting mixture was brought to pH 12 under vigorous stirring by adding dropwise 2 M aqueous NaOH. After stirring the obtained suspension for 45 minutes and aging it for further 20, the brick red solid was isolated by filtering it on a Büchner funnel and washing it with water. After drying (5 hours in an open air oven at 90°C), the brick red product was ground in an agate mortar and calcined at 900°C for 5 hours in air.

Several syntheses were carried out by altering nominal ratio between reagents, basification protocol, TENOH amount, purification method and calcination protocol, as reported in table 5.7.2.

Sample	Nominal Fe/M/acid molar ratio	TENOH/ ml	Basification protocol	Purification method	Calcination temperature (protocol number)
Mn001	1/1/3	2	A	Filtration	900°C (6)
Mn002	2/1/4.5	2	A	Filtration	900°C (6)
Mn003	1/1/3	2	B	Filtration	900°C (6)
Mn004	2/1/4.5	2	B	Filtration	900°C (6)
Mn005	1/1/3	2	A	Filtration	900°C (6)
Mn006-a	1/1/3	2	A	Filtration	900°C (3)
Mn006-b	1/1/3	2	A	Filtration	900°C (4)
Mn006-c	1/1/3	2	A	Filtration	900°C (5)
Mn007	2/1/4.5	2	B	Filtration	1100°C (7)
Mn008	1/1/3	2	B	Filtration	600°C (2)
Mn009	1/1/3	2	A	Filtration	400°C (1)
Mn010	2/1/4.5	2	A	Filtration	600° (2)
Mn011	1/1/3	2	A	Filtration	900°C (6)
Mn012	1/1/3	8	A	Filtration	900°C (6)
Mn013	1/1/3	2	C	Filtration	900°C (6)
Mn014	1/1/3	2	A	Filtration	900°C (6)
Mn015	1/1/3	2	A	Filtration	900°C (6)
Mn016	2/1/4.5	2	A	Filtration	900°C (6)
Mn017	1/1/3	2	A	Filtration	900°C (6)
Mn018	1/1/3	2	D	Centrifugation	900°C (6)
Mn019	1/1/3	2	A	Filtration	900°C (6)
Mn020	1/1/3	2	A	Centrifugation	900°C (6)
Mn021	1/1/3	2	A	Filtration	900°C (6)

Table 5.7.2 – *Experimental parameters for the syntheses of manganese ferrites via coprecipitation of oxalates*

The manganese spinel **$MnFe_2O_4$** was synthesised through hydrothermal synthesis by dissolving in 10 ml deionised water $Mn(OAc)_2 \cdot 2H_2O$ (0.109 g, $5.22 \cdot 10^{-1}$ mmol) $FeCl_3 \cdot 6H_2O$ (0.287 g, 1.05 mmol) and oxalic acid dihydrate (1.98 g, 1.57 mmol) in a Teflon liner. Under vigorous stirring, 0.2 ml of TENOH, followed by 1 ml 10 M aqueous NaOH were added. The resulting suspension was sealed in a 23 ml acid digestion bomb and treated at 135°C for 24 hours. The bomb was cooled at room temperature for 1.5 hours before opening. The resulting black powder was separated by centrifugation (10 kRPM, 5 minutes) and washed with deionised water. The product was then dried in open air in an oven for 5 hours at 90°C.

Syntheses with this route, having the aim of producing the manganese perovskite **$MnFeO_3$** (I-Mn001), were unsuccessful, resulting in mixed-phase powders, with the main phase being the spinel $MnFe_2O_4$.

Syntheses were carried out by varying the nominal Fe/M/acid molar ratio, basification agent, treatment temperature and treatment time [Tab 5.7.3].

Sample	Nominal Fe/M/acid molar ratio	Basification agent	Treatment time/hours	Treatment temperature/°C
I-Mn001	1/1/3	NaOH	24	135
I-Mn002	2/1/4.5	NaOH	24	135
I-Mn003	1/1/3	NaOH	24	135
I-Mn004	1/1/3	NaOH	24	135
I-Mn005	2/1/4.5	NaOH	24	160
I-Mn006	2/1/4.5	NaOH	24	135
I-Mn007	2/1/4.5	NaOH	24	135
I-Mn008	2/1/3	NaOH	24	135
I-Mn009	2/1/3	NaOH	24	135
I-Mn010	2/1/3	NH_4OH	24	135
I-Mn011	2/1/3	NaOH	24	135
I-Mn012-1	2/1/3	NaOH	1	135
I-Mn012-2	2/1/3	NaOH	2	135
I-Mn012-4	2/1/3	NaOH	4	135
I-Mn013	2/1/3	NaOH	24	100
I-Mn014	2/1/3	NaOH	24	75

Table 5.7.3 – *Experimental parameters for the syntheses of $MnFe_2O_4$ via hydrothermal method*

5.8 – Syntheses of nickel ferrites

For the synthesis of the nickel spinel **$NiFe_2O_4$** via coprecipitation of oxalates, $NiCl_2 \cdot 6H_2O$ (1.242 g, 5.22 mmol) and $FeCl_3 \cdot 6H_2O$ (2.872g, 10.45 mmol) were dissolved in 50 ml deionised water while, in an equal amount of the same solvent, oxalic acid dihydrate (2.960 g, 23.50 mmol) was dissolved. The two solutions were mixed after being separately stirred for 30 minutes (the nickel salts do not fully dissolve) and 2 ml TENOH were added. By slowly adding 2 M aqueous NaOH under vigorous stirring, the pH was raised to 12. The stirring was maintained for 45 minutes and then the brown suspension was aged for further 20 minutes. The solid phase was isolated by filtration over a Büchner funnel and washed several times with deionised water to remove residual ions. The brick red product obtained was then dried in a ventilated oven for 5 hours at 90°C, ground to a powder and calcined in air at 900°C for 5 hours.

Syntheses aimed at the synthesis of the perovskite **$NiFeO_3$** generally resulted in mixed-phase powders, with the main phase identified as a nickel spinel ferrite.

Different syntheses were carried out by changing the nominal ratio of the precursors, the purification method and the basification protocol [Tab. 5.8.1].

Sample	Nominal Fe/M/acid molar ratio	TENOH/ ml	Basification protocol	Purification method	Calcination temperature (protocol number)
Ni001	1/1/3	2	A	Filtration	900°C (6)
Ni002	2/1/4.5	2	A	Filtration	900°C (6)
Ni003	2/1/4.5	2	A	Filtration	900°C (6)
Ni004	2/1/4.5	2	A	Centrifugation	900°C (6)
Ni005	2/1/4.5	2	D	Centrifugation	900°C (6)
Ni006	2/1/4.5	2	A	Centrifugation	900°C (6)
Ni007	2/1/4.5	2	A	Centrifugation	900°C (6)

Table 5.8.1 – *Experimental parameters for the syntheses of nickel ferrites via coprecipitation of oxalates*

The synthesis of the nickel spinel **$NiFe_2O_4$** via hydrothermal route was carried out by dissolving in 10 ml deionised water (within a 23 ml Teflon liner) $NiCl_2 \cdot 6H_2O$ (0.124 g, $5.22 \cdot 10^{-1}$ mmol), $FeCl_3 \cdot 6H_2O$ (0.287 g, 1.05 mmol) and oxalic acid dihydrate (0.296 g, 2.35 mmol). Under vigorous stirring, 0.2 ml TENOH and 1 ml 10 M aqueous NaOH were poured into the resulting suspension. The liner was sealed in a 23 ml Parr acid digestion bomb and kept for 24 hours at 135°C. After cooling at room temperature, the resulting dark red powder was isolated by centrifugation at 10 kRPM for 5 minutes followed by washing with deionised water. The final product was dried in an open air oven at 90°C for 5 hours.

Syntheses with the purpose of producing the perovskite $NiFeO_3$ via hydrothermal route were unsuccessful, yielding a product that was initially thought of as a pure $NiFe_2O_4$ phase, but was later identified as a mixture of crystalline phases with a high Ni content (see Par. 4.5).

Several syntheses were carried out by changing treatment temperature, stoichiometric ratios between precursors and basification agent [Tab. 5.8.2].

Sample	Nominal Fe/M/acid molar ratio	Basification agent	Treatment time/hours	Treatment temperature/°C
I-Ni001	1/1/3	NaOH	24	135
I-Ni002	2/1/4.5	NaOH	24	135
I-Ni003	1/1/3	NaOH	24	135
I-Ni004	1/1/3	NaOH	24	135
I-Ni005	1/1/3	NaOH	24	160
I-Ni006	2/1/4.5	NaOH	24	160
I-Ni007	2/1/3	NaOH	24	135
I-Ni008	2/1/3	NaOH	24	135
I-Ni009	2/1/3	NH_4OH	24	135
I-Ni010	2/1/3	NaOH	24	135
I-Ni011-1	2/1/3	NaOH	1	135
I-Ni011-2	2/1/3	NaOH	2	135
I-Ni011-4	2/1/3	NaOH	4	135
I-Ni012	2/1/3	NaOH	24	100
I-Ni013	2/1/3	NaOH	24	75

Table 5.8.2 – *Experimental parameters for the syntheses of $NiFe_2O_4$ via hydrothermal method*

5.9 - Syntheses of strontium ferrites

In order to obtain a suitable metal precursor for the nonaqueous sol-gel synthesis of strontium ferrites, 1.017 g of metallic strontium were reacted with 50 ml benzyl alcohol while maintaining the system at 100°C under constant stirring for 4 days under inert atmosphere in order to obtain a 0.231 M strontium benzyl alkoxide solution ($Sr_{(OBz)}$). For the synthesis of the spinel ferrite **$SrFe_2O_4$**, stoichiometric amounts of $Fe(C_5H_7O_2)_2$ (254 mg, 1.00 mmol) were suspended in 2.14 ml benzyl alcohol and 2.16 ml of $Sr_{(OBz)}$ (0.50 mmol) under inert atmosphere in a glove box. The vial containing the suspension was sealed, stirred for 45 minutes to ensure homogenisation of the system and placed in a microwave heater. The suspension was heated up to 200°C for 45 minutes. The resulting suspension was then isolated through centrifugation as described in the above section. The isolated solid was then dried in an oven at 60°C in air for one hour and crushed into powder in an agate mortar.

A similar approach was used to attempt the synthesis of the perovskite ferrite **$SrFeO_3$**, using stoichiometric amounts of $Fe(C_5H_7O_2)_2$ (128 mg, 0.50 mmol) and $Sr_{(OBz)}$ (2.16 ml, 0.50 mmol). Synthetic attempts with this route for both these products were unsuccessful, yielding mixed-phase powders.

Different syntheses were carried out by varying the nature of the iron precursor, the nominal treatment temperature and the time the system was kept at said temperature, as reported in the tables below.

Experiment	Reagent 1	Quantity/mmol	Reagent 2	Quantity/mmol	Temperature/°C	Treatment Time/min
S-Sr035-1	Fe^{III}acac	1.00	$Sr_{(OBz)}$	0.50	180	15
S-Sr035-2	Fe^{III}acac	1.00	$Sr_{(OBz)}$	0.50	180	45
S-Sr035-3	Fe^{III}acac	1.00	$Sr_{(OBz)}$	0.50	200	15
S-Sr035-4	Fe^{III}acac	1.00	$Sr_{(OBz)}$	0.50	200	45
S-Sr035-5	Fe^{II}acac	1.00	$Sr_{(OBz)}$	0.50	180	15
S-Sr035-6	Fe^{II}acac	1.00	$Sr_{(OBz)}$	0.50	180	45
S-Sr035-X	Fe^{II}acac	1.00	$Sr_{(OBz)}$	0.50	200	15
S-Sr035-8	Fe^{II}acac	1.00	$Sr_{(OBz)}$	0.50	200	45
S-Sr035-9	Fe^{II}OAc	1.00	$Sr_{(OBz)}$	0.50	180	15
S-Sr035-10	Fe^{II}OAc	1.00	$Sr_{(OBz)}$	0.50	180	45
S-Sr035-7	Fe^{II}acac	1.00	$Sr_{(OBz)}$	0.50	200	15
S-Sr035-11	Fe^{II}OAc	1.00	$Sr_{(OBz)}$	0.50	200	15
S-Sr035-12	Fe^{II}OAc	1.00	$Sr_{(OBz)}$	0.50	200	45

Table 5.9.1 - *Experimental parameters for the nonaqueous sol-gel syntheses of strontium spinel ferrites*

Experiment	Reagent 1	Quantity/mmol	Reagent 2	Quantity/mmol	Temperature°C	Treatment Time/min
S-Sr036 - 1X	Fe^{III}acac	0.50	$Sr_{(OBz)}$	0.67	180	15
S-Sr036 - 2X	Fe^{III}acac	0.50	$Sr_{(OBz)}$	0.67	180	45
S-Sr036 - 1Y	Fe^{III}acac	0.50	$Sr_{(OBz)}$	0.40	180	15
S-Sr036 - 2Y	Fe^{III}acac	0.50	$Sr_{(OBz)}$	0.35	180	45
S-Sr036-1	Fe^{III}acac	0.50	$Sr_{(OBz)}$	0.50	180	15
S-Sr036-2	Fe^{III}acac	0.50	$Sr_{(OBz)}$	0.50	180	45
S-Sr036-3	Fe^{III}acac	0.50	$Sr_{(OBz)}$	0.50	200	15
S-Sr036-4	Fe^{III}acac	0.50	$Sr_{(OBz)}$	0.50	200	45
S-Sr036-5	Fe^{II}acac	0.50	$Sr_{(OBz)}$	0.500	180	15
S-Sr036-6	Fe^{II}acac	0.50	$Sr_{(OBz)}$	0.500	180	45
S-Sr036-7X	Fe^{II}acac	0.50	$Sr_{(OBz)}$	0.500	200	15
S-Sr036-8X	Fe^{II}acac	0.50	$Sr_{(OBz)}$	0.500	200	45
S-Sr036-7	Fe^{II}acac	0.50	$Sr_{(OBz)}$	0.500	200	15
S-Sr036-8	Fe^{II}acac	0.50	$Sr_{(OBz)}$	0.500	200	45

Table 5.9.2 - *Experimental parameters for the nonaqueous sol-gel syntheses of strontium perovskite ferrites*

Syntheses carried out with the aim of obtaining the strontium spinel **$SrFe_2O_4$** via coprecipitation of oxalates were unsuccessful, resulting in mixed-phase products, with the main phases identified as $SrFeO_{3-\delta}$ and $Sr_3Fe_2O_{7-\delta}$.

Strontium perovskite **$SrFeO_{3-\delta}$** was successfully synthesised by this route by dissolving $Sr(NO_3)_2$ (1.105 g, 5.22 mmol) and $Fe(NO_3)_3 \cdot 9H_2O$ (2.110 g, 5.22 mmol) in 50 ml deionised water and, in parallel, oxalic acid dihydrate (1.975 g, 15.67 mmol) in 50 ml deionised water. The two solutions were stirred together and 2 ml TENOH were added to the solution. pH was raised to 12 with the slow addition of NaOH 2 M and stirred for further 45 minutes. After 20 minutes aging, the brown suspension settled down to a noticeable degree and was filtered on a Büchner funnel. Following washing with deionised water to remove ionic residue, the brown solid was dried in air at 90°C for 5 hours and calcined for 5 hours at 900°C in air.

Syntheses were carried out by changing basification and calcination protocol, as well as the amount of peptising agent amount [Tab. 5.9.3].

Sample	Nominal Fe/M/acid molar ratio	TENOH/ ml	Basification protocol	Purification method	Calcination temperature (protocol number)
Sr001-a	1/1/2	2	A	Filtration	900°C (6)
Sr001-b	1/1/2	2	A	Filtration	900°C (4)
Sr002-a	1/1/2	2	A	Filtration	900°C (3)
Sr002-b	1/1/2	2	A	Filtration	900°C (5)
Sr003	1/1/2	2	A	Filtration	900°C (6)
Sr004	1/1/2	8	A	Filtration	900°C (6)
Sr005	1/1/2	2	C	Filtration	900°C (6)

Table 5.9.3 – *Experimental parameters for the syntheses of $SrFeO_{3-\delta}$ via coprecipitation of oxalates*

All syntheses performed to obtain the strontium spinel or the strontium perovskite via hydrothermal synthesis were unsuccessful, yielding mainly amorphous powders. The synthesis procedure was analogous to that used for the hydrothermal synthesis of $CoFe_2O_4$ (see Par. 5.5), with strontium carbonate as the precursor strontium salt. The syntheses are reported in table 5.9.4.

Sample	Nominal Fe/M/acid molar ratio	Final pH	Basification agent	Treatment time/hours	Treatment vessel	Treatment temperature/°C
I-Sr001	1/1/2	12	NaOH	24	Bomb	135
I-Sr002	2/1/3	12	NaOH	24	Bomb	135
I-Sr004	1/1/2	12	NaOH	24	Bomb	160

Table 5.9.4 – *Experimental parameters for the syntheses of strontium ferrites via hydrothermal method*

5.10 – Syntheses of zinc ferrites

For the synthesis of the zinc spinel **$ZnFe_2O_4$** via coprecipitation of oxalates, $Zn(NO_3)\cdot 6H_2O$ (1.554 g, 5.22 mmol) and $FeCl_3\cdot 6H_2O$ (2.872g, 10.45 mmol) were dissolved in 50 ml deionised water. In further 50 ml of deionised water, oxalic acid dihydrate (2.960 g, 23.50 mmol) was dissolved. After mixing the two solutions, 2 ml TENOH were added. By slowly adding 2 M aqueous NaOH under vigorous stirring, the pH was raised to 12. The suspension was stirred for 45 minutes and the resulting brown suspension was then aged for further 20 minutes. The solid phase was isolated with a centrifuge and washed several times with deionised water to remove residual ions. The brick red compound thus obtained was dried in a ventilated oven for 5 hours at 90°C, ground to a powder and calcined in air at 900°C for 5 hours.

Attempts to prepare the perovskite **$ZnFeO_3$** with this method generally resulted in two-phase powders, containing the $ZnFe_2O_4$ spinel and the single metal oxide ZnO.

Syntheses were carried out varying the nominal ratio of the precursors, the purification method and the basification protocol [Tab. 5.10.1].

Sample	Nominal Fe/M/acid molar ratio	TENOH/ ml	Basification protocol	Purification method	Calcination temperature (protocol number)
Zn001	1/1/3	2	A	Centrifugation	900°C (6)
Zn002	2/1/4.5	2	A	Centrifugation	900°C (6)
Zn003	2/1/4.5	2	A	Centrifugation	900°C (6)
Zn004	2/1/4.5	2	A	Centrifugation	900°C (6)

Table 5.10.1 – *Experimental parameters for the syntheses of Zinc ferrites via coprecipitation of oxalates*

The synthesis of the zinc spinel **$ZnFe_2O_4$** via hydrothermal route was carried out by dissolving in 10 ml deionised water (within a 23 ml Teflon liner) $Zn(acac)_2 \cdot H_2O$ (0.138 g, $5.22 \cdot 10^{-1}$ mmol), $FeCl_3 \cdot 6H_2O$ (0.287g, 1.05 mmol) and oxalic acid dihydrate (0.296 g, 2.35 mmol). Under vigorous stirring, 0.2 ml TENOH and 1 ml 10 M aqueous NaOH were poured into the resulting suspension. The liner was sealed in a 23 ml Parr acid digestion bomb and kept for 24 hours at 100°C. After cooling at room temperature, the resulting dark red powder was isolated by centrifugation at 10 kRPM for 5 minutes followed by washing with deionised water. The final product was dried in an open air oven at 90°C for 5 hours.

Syntheses were carried out by changing the treatment temperature, the stoichiometric ratios between precursors and the basification agent [Tab. 5.10.2].

Sample	Nominal Fe/M/acid molar ratio	Basification agent	Treatment time/hours	Treatment temperature/°C
I-Zn001	1/1/3	NaOH	24	100
I-Zn002	2/1/4.5	NaOH	24	75
I-Zn003-1	2/1/4.5	NaOH	1	75
I-Zn003-2	2/1/4.5	NaOH	2	75
I-Zn003-4	2/1/4.5	NaOH	4	75

Table 5.10.2 – *Experimental parameters for the syntheses of $NiFe_2O_4$ via hydrothermal method*

In parallel, synthetic attempts were carried out to prepare the spinel **$ZnFe_2O_4$** via a reflux-like route by dissolving $Zn(acac)_2 \cdot H_2O$ (0.138 g, $5.22 \cdot 10^{-1}$ mmol), $FeCl_3 \cdot 6H_2O$ (0.287g, 1.05 mmol) and oxalic acid dihydrate (0.296 g, 2.35 mmol) in 10 ml deionised water (within a 25 ml round flask). Following this, 0.2 ml TENOH and 1 ml NaOH (10 M in water) were poured into the resulting suspension under vigorous stirring. The flask was fitted with a condenser and kept for 24 hours at 75°C. After cooling at room temperature, the resulting dark red powder was isolated by centrifugation at 10 kRPM for 5 minutes followed by washing four times with deionised water. The final product was dried in an open air oven for 5 hours at 90°C.

Syntheses were carried out by changing the treatment time [Tab. 5.10.3].

Sample	Nominal Fe/M/acid molar ratio	Basification agent	Reflux temperature/°C	Reflux time/hours
R-Zn001	2/1/4.5	NaOH	75	24
R-Zn002-4	2/1/4.5	NaOH	75	4
R-Zn002-2	2/1/4.5	NaOH	75	2

Table 5.10.3 - Experimental parameters, yields and average crystallite sizes for performed $ZnFe_2O_4$ syntheses

5.11 - Syntheses of mixed metal ferrites

Syntheses of mixed metal ferrites (i.e. having two divalent metals rather than one) $M_{0.5}M'_{0.5}Fe_2O_4$ and $M_{0.5}M'_{0.5}FeO_3$ were carried out by coprecipitation by using the same experimental procedure of the protocols described above with the only difference being that, rather than employing 5.223 mmol of the chosen M metal, 2.612 mmol of each divalent metal (M and M') were employed. The same reagents for each metal were used as were chosen for single metal ferrite coprecipitation synthesis. The syntheses are reported in table 5.11.1.

Sample	M and M' metals	Nominal Fe/M/M'/acid molar ratio	TENOH/ml	Basification protocol	Calcination temperature (protocol number)
CoMg-P	Co, Mg	0.5/0.5/1/3	2	A	900°C (6)
CoMg-S	Co, Mg	0.5/0.5/2/4.5	2	A	900°C (6)
CoMn-P	Co, Mn	0.5/0.5/1/3	2	A	900°C (6)
CoMn-S	Co, Mn	0.5/0.5/2/4.5	2	A	900°C (6)
CoSr-P	Co, Sr	0.5/0.5/1/3	2	A	900°C (6)
CoSr-S	Co, Sr	0.5/0.5/2/4.5	2	A	900°C (6)

Table 5.11.1 – *Experimental parameters for the syntheses of mixed metal ferrites via coprecipitation of oxalates*

Further syntheses were carried out aiming at obtaining **calcium** and **barium** ferrites ($BaFeO_3$, $BaFe_2O_4$, $CaFeO_3$ and $CaFe_2O_4$); however they resulted in mixed phase or amorphous products regardless of whether they were performed through nonaqueous sol-gel, coprecipitation of oxalates or the hydrothermal method. These experiments are summarised in the tables reported in Appendix 1.

6 - Characterisation methods

Since the functional features of nanosized materials in general and ferrites in particular are determined by their structural and compositional characteristics, a thorough investigation is necessary to gain a full understanding of the synthesised materials and of the structure-composition-functional properties relationships involved.[279] For this reason, a wide array of different techniques must be employed in order to explore the different analytical pathways available and provide complementary data on the investigated compounds. In this chapter, the various analytical methods employed to characterise the prepared materials [Fig. 6.1] will be described. Furthermore, sample preparation procedures for the analysis techniques (XRD, XPS, TGA-DSC, ICP-AES, Mössbauer spectroscopy etc.), as well as information about the instruments themselves, will be provided.

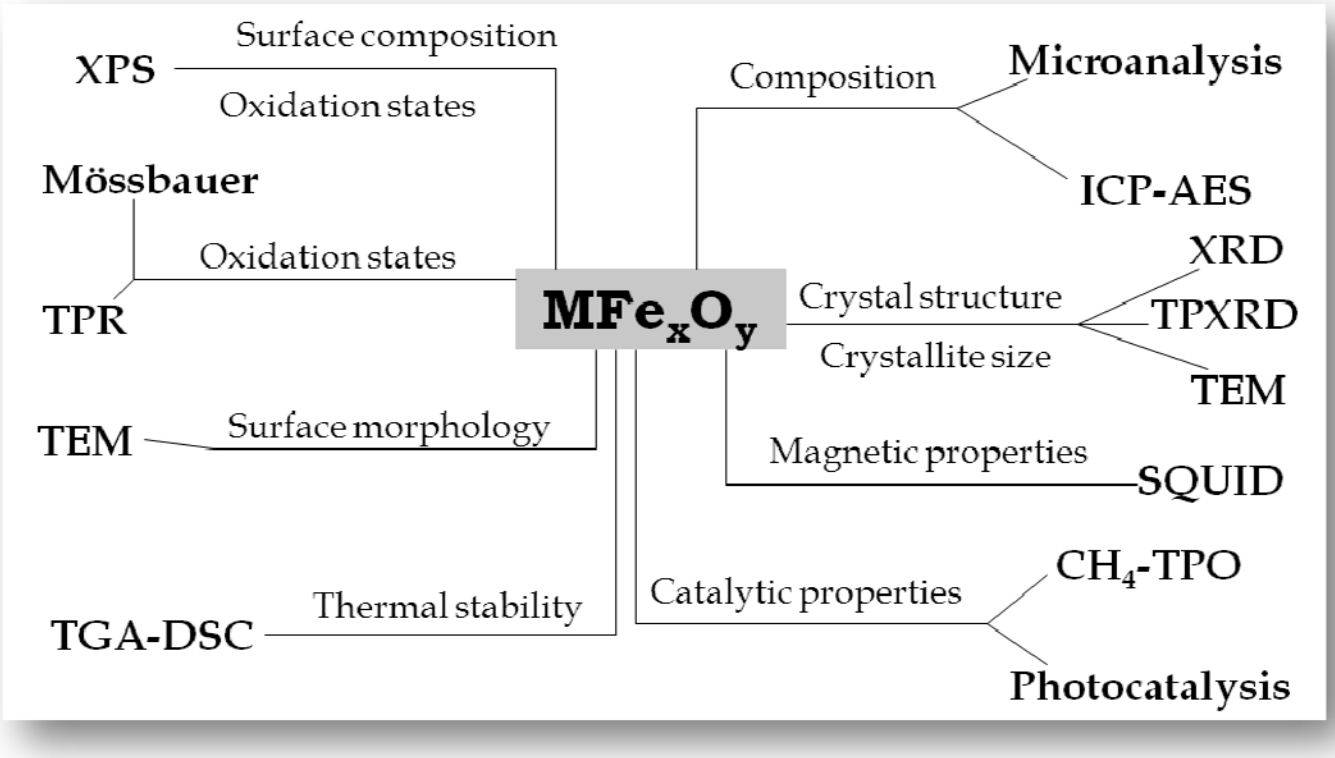

Fig. 6.1 - *Overview of main characterisation techniques employed and their purposes*

6.1 - X-ray diffraction (XRD)

X-ray diffraction[280-285] is a technique which is normally employed to investigate crystalline solids (either single crystals or polycrystalline powders). XRD analysis takes advantage of the diffraction phenomenon, using the electronic clouds of the atoms within the solid as scattering centres. When electromagnetic radiation of suitable wavelength hits a sample, it may display elastic scattering: the radiation wavelength (λ, and consequently its energy) will remain unchanged, whilst its direction will be altered. For simplicity's sake, we can imagine that the incident beam is perfectly coherent (in other words, all photons in the beam, not only have the same wavelength, but also the same phase); after hitting the sample, the electromagnetic field *E* generated by the radiation in a given point ($\bar{r}$) at a given instant (*t*) will be:

$$E(\overline{r},t) = E_0 exp[2\pi i\left(\frac{\overline{k}2\pi}{\lambda} - \nu t + \delta'\right)] \qquad (6.1.1)$$

Where E_0 is the electromagnetic field in the origin point, k is the wave vector, ν is the frequency (in Hertz) and δ' the phase difference with the reference (normally the origin). If we imagine two scattered waves E_1 and E_2, the resulting interference between the two will be:

$$E(\overline{r},t) = E_1(\overline{r},t)[1 + \exp(2\pi i\delta)] \qquad (6.1.2)$$

Where δ is the phase difference between the two waves.

Having defined s_0 the vector which describes the direction of the wave before scattering and s the vector describing the direction of the scattered wave (the two vectors being different in direction and verse, but having equal module), the path difference between two rays scattered by two centres having distance r from each other will be:

$$\overline{r}\cdot\overline{s} - \overline{r}\cdot\overline{s_0} = \overline{r}\cdot(\overline{s} - \overline{s_0}) = \overline{r}\cdot\overline{S} \qquad (6.1.3)$$

If we set the module of s and s_0 as equal to 1/λ, the difference in phase will only depend on r, allows to deduce atomic positions from the interference signal. Although in most cases it is impossible to obtain a coherent radiation source, the above considerations are also valid for non-coherent radiation. This is due to the fact that electromagnetic radiation emitted in a given instant can be considered coherent, although in a macroscopic time interval, phases will be incoherent.

The choice of X-ray radiation for this type of analysis is above all due to the fact that the maximum resolution for an EM-radiation based analysis is given by λ/2. Since the purpose of XRD analysis is to study atomic positions, it is necessary to employ a radiation having wavelength near the Ångstrom range. The most commonly used radiation is CuK_α, having a λ of 1.5406 Å. Furthermore, for scattering phenomena to occur, the incident radiation has to possess a wavelength comparable to the size of the scattering centres, since electronic clouds are in the Å range, the radiation wavelength must be similar.

As far as XRD analysis is concerned, it is acceptable to consider each atom as having a spherical electronic distribution; this is due to the fact that the time frame in which scattering occurs is too long for orbitals to be visible. Since scattering of a beam by a point at a 2θ angle is comparable to reflection by that same point of an incident beam at an angle equal to θ, it is possible to consider

XRD analysis in the same way as common optical microscopy. In optical microscopy, the light beam reflected by the sample is made to diverge and then converge by the glass lenses in order to create an image on the eye of the observer. Unfortunately, there are no physical lenses capable of performing the same task with X radiation; for this reason, the effect of lenses on the radiation is simulated mathematically: the transformation of the detected signal into an image (i.e. the electronic density of the sample) takes place through Fourier transform.

$$\rho(x,y,z) = 1/V \sum_{h=-\infty}^{\infty} \sum_{k=-\infty}^{\infty} \sum_{l=-\infty}^{\infty} \overline{F}(h,k,l) \exp[-2\pi i(hx + ky + lz)] \qquad (6.1.4)$$

In this equation, ρ represents electronic density in a point in space and the complex function F(*h*,*k*,*l*) is the structure factor, i.e. the ratio between the radiation scattered by the sample (in a given point in reciprocal space) and the radiation scattered by a single electron in the origin point.

XRD analysis performs best with solids which have a crystalline structure, this is due to the fact that a crystal, by definition, has a high degree of regularity and the atoms which constitute it are positioned periodically: when the diffraction phenomenon occurs in a solid having these structural features, constructive interference occurs in specific points; by contrast, amorphous structures give a far less resolved signal which is easily confused with background noise. The highest grade of regularity can be obtained when this analysis is performed on a single crystal. Since in this case all crystal cells are oriented in the same direction, constructive interference maxima manifest as dots (ideally, if the crystal was both perfect and infinite, these would be dimensionless mathematical dots). These points, also known by the term reflections, are directly correlated to the atomic positions in reciprocal space [Fig. 6.1.1].

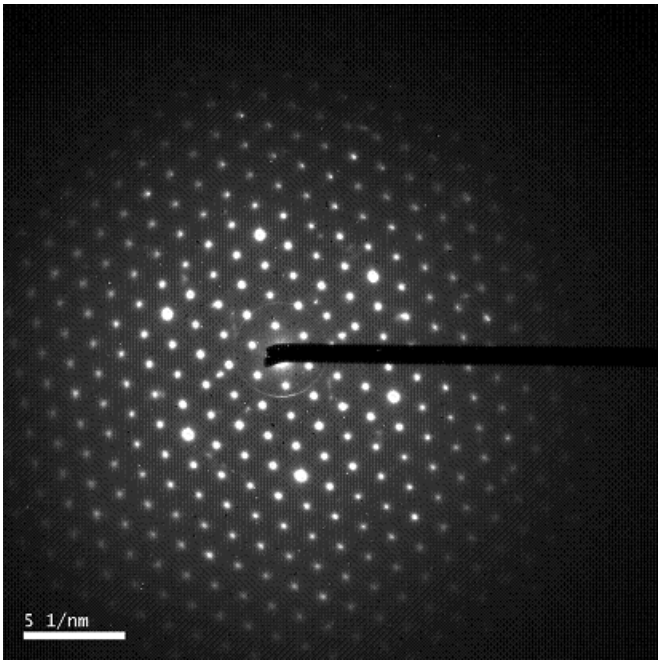

Figure 6.1.1 - *Diffraction pattern of the [1 1 1] axis zone for Mn_2O_3 obtained through SAED*[286]

The reciprocal lattice is a concept which is useful for the task of visualising the signal collected by the diffractometer. It is a lattice where the vectors $\overline{a}, \overline{b}$ and $\overline{c}$ are substitute by three vectors $\overline{a}^*, \overline{b}^*$ and $\overline{c}^*$, each one of which has reciprocal dimensions in respect to its real correspondents and

is perpendicular to the remaining two. In the reverse lattice, the intercepts of a given plane with the crystal cell are expressed as *a/h*, *b/k* and *c/l*, where *h*, *k* and *l* are known as Miller indexes. According to this expression, reflection is only possible under certain conditions (Laue conditions):

$$\frac{\overline{a}}{h} \cdot \overline{S} = 1$$

$$\frac{\overline{b}}{k} \cdot \overline{S} = 1 \qquad (6.1.5)$$

$$\frac{\overline{c}}{l} \cdot \overline{S} = 1$$

In these equations, the *S* vector is known as scattering vector and is equal to the difference between the s_0 and s vectors, having module equal to $1/\lambda$ and direction and verse respectively equal to the beam hitting the crystal plane and to the scattered beam. If we define *d* as the projection of *a/h* along *S* (which is perpendicular to the crystal plane), the module of *S* will be equal to 1/*d* [Fig. 6.1.2].

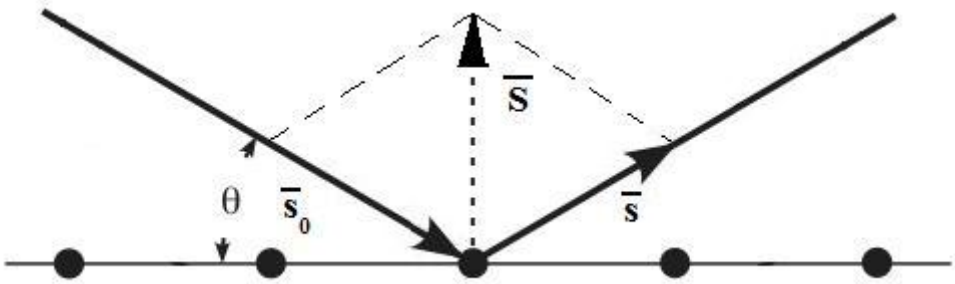

Figure 6.1.2 - *Scheme where the three vectors s_0, s and S are evidenced*

Since, by definition, the module of S is also equal to $2 \cdot \sin\theta/\lambda$, from the above conditions we have:

$$\lambda = 2d \sin\theta \qquad (6.1.6)$$

Equation 6.1.6 is known as Bragg's Law. If we consider sets of parallel planes, we will have $n \cdot \lambda = 2d \cdot \sin\theta$, where n is whole. F(*h*,*k*,*l*) relative to a given set of *h*, *k*, *l* values, is the structure factor generated by the reflection of the incident radiation by a family of equidistant planes (with distance equal to *d*) and having intercepts equal to *a/h*, *b/k* and *c/l*. The θ, *d* and *S*, as well as the *h*, *k* and *l* value sets contain the same information (the first set relative to real space, the second relative to reciprocal space).

Laue conditions can be interpreted from another point of view: if we consider a beam having direction s_0 and deviated by an angle equal to 2θ in the s direction, the *S* vector will always be on the surface of a sphere (Ewald sphere) centred in the scattering centre and having radius equal to $1/\lambda$ (i.e. equal to s_0 and s). By construction, all *S* vectors will have their extremities on the surface of the sphere [Fig. 6.1.3].

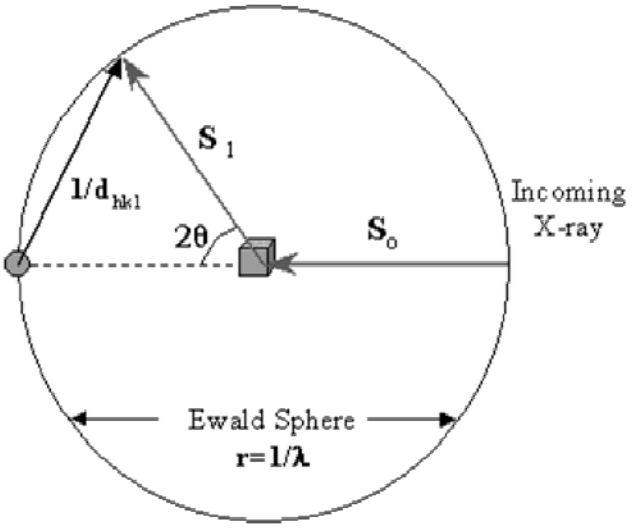

Figure 6.1.3 - *Ewald sphere schematic*

In a crystal, *S* has non arbitrary dimensions, due to the Laue conditions; the fact that *S* must have its extremities on the surface of the Ewald sphere, makes it so that only the points in the reciprocal lattice given by diffraction which fall on the surface are capable of giving a signal. *Tilted crystal* analysis is based upon this phenomenon: by tilting the crystal, the entire lattice is tilted, allowing new points to end up on the surface of the Ewald sphere, and therefore able to give a signal. The number of angles explored is limited, in order to avoid an excessive overlap among points.

Reflections overlapping represent the main problem in X-ray powder diffraction (XRPD): powders can be crystalline and therefore be capable of scattering incident beams exactly like a single crystal. Since crystal cells in a powder are not however oriented in the same way (each grain has a random orientation), reflections relative to all possible crystal orientations are collected simultaneously. The resulting XRPD pattern is therefore not made up of points (as in the case of single crystal patterns) but rather of concentric circles, each one containing all reflections given by the crystal at a given value of 2θ [Fig. 6.1.4].

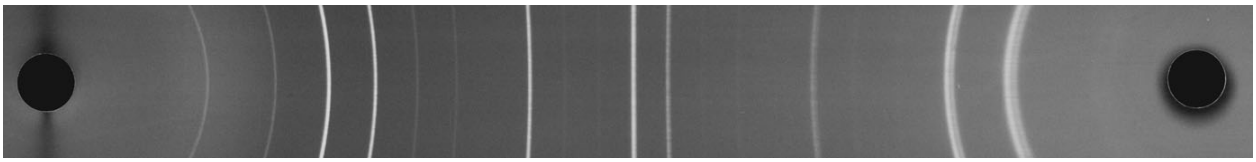

Figure 6.1.4 - *Diffraction pattern collected from $ZnGa_2O_4$ powder.*

This overlap significantly limits the amount of information which can be gathered from the diffraction pattern and makes it basically impossible to resolve the pattern without the aid of specific software.

6.1.1 - The phase problem

The main problem in deducing a crystal structure based upon a diffraction pattern is due to the combination of two factors: the ρ function (see equation 6.1.4) is real: this fact, due to a property of Fourier transforms, implies that both phase and module of its transform (i.e. the structure factor) will be centre symmetric (Friedel conditions). This makes it impossible to directly calculate the phase of F(*h*,*k*,*l*), since what is in fact measured is its square module.

$$I(h,k,l) = |F(h,k,l)|^2 = F(h,k,l) \cdot F^*(h,k,l) \qquad (6.1.1.1)$$

The software normally used to interpret XRD patterns, generally estimates the intensity of a reflection based upon a series of other variables aside from F. Specifically, the calculated intensity in an XRPD pattern is:

$$I_i^{calc} = S_F \sum_{j=1}^{Nphases} \frac{f_j}{V_j^2} \sum_{k=1}^{Nreflections} L_k \left|F_{k,j}\right|^2 S_j(2\theta_i - 2\theta_{k,j}) P_{k,j} A_j + bkg_i \qquad (6.1.1.2)$$

In this equation, I is the reflection intensity, S_F the intensity of the incident beam, V_j the cell volume of the j^{th} phase, f_j its volume fraction, L is the Lorenz polarisation (dependent upon instrumental conditions), F is the structure factor, $S_j(2\theta_i\text{-}2\theta_{k,j})$ is the reflection form function, P is the texture factor (which takes into account the possible preferential orientations within a non-monocrystalline sample), A is the absorption factor and bkg is the estimated background noise (or baseline).

Due to what is described by equations 6.1.1.1 and 6.1.1.2, the phase of F(*h*,*k*,*l*) must be estimated through mathematical calculations , in most cases based upon models which simulate a structure factor which may then be compared to the experimental one. These methods allow for the construction of an approximate electron density map (structure determination phase) which is then improved through successive iterative calculations (refinement phase). Normally these operations are carried out through the use of specific software which, based upon the diffraction pattern and experimental parameters (wavelength, instrument setup, sample properties etc.) simulate the pattern through various algorithms (such as Patterson, direct methods etc.). In this sense, the system tries to solve an equation system where the atomic positions, cell parameters and crystal characteristics represent variables, whereas the pattern points represent equations. The number of variables is significant, therefore, even though an average diffraction pattern contains several hundred if not thousands of points, it is very easy for the program to end up in a "false minimum", i.e. a set of variables other than the best possible. For this reason the programs cannot be fully automatic and often require significant work before a given pattern can be resolved.

6.1.2 - Crystallite size

From an XRPD pattern, it is possible to roughly estimate average crystallite size from the width of the reflections in the pattern, by applying the Scherrer formula.[231]

$$L = K\lambda/\beta cos\theta \qquad (6.1.2.1)$$

In equation 6.1.2.1, L is the mean crystallite size, K is an adimensional constant correlated to the crystal cell shape (specifically, for a cubic crystal cell, as with all compounds synthesised during this Ph.D. thesis, K is equal to 0.94), λ is the instrument wavelength, β is the peak broadening (though the full width at half maximum FWHM, expressed in radians is normally used) of a given reflection and θ is the reflection position (Bragg angle).

The main advantage of the Scherrer equation lies in the extreme ease in its application; it should be noted however, that this method for the estimation of crystallite size makes use of some rather heavy approximations and should not be considered as accurate as a full pattern refinement.

Moreover, it is most accurate when crystallites are relatively small, since in larger crystallites (> 100 nm) reflection shapes are more heavily influenced by other factors.

6.1.3 - Data acquisition and elaboration

For samples obtained via nonaqueous sol-gel synthesis, the obtained powders were investigated by XRD with a PW 1800 Philips X-Ray Diffractometer equipped with a PW 1808 Philips sample changer, allowing batch analysis. The X-ray patterns were collected in the range 10-110° with a λ of 1.5406 Å, a scan step 0.05° (2θ) and a 6 seconds per step acquisition time, with a 0.3 mm recording slit.

For samples analysed through *in situ* TPXRD, data was collected in reflection geometry using a PANalytical Empyrean X-ray diffractometer employing Cu($K_{\alpha1}$+$K_{\alpha2}$) radiation. The diffractometer was equipped with a fixed divergence slit (FDS) optic on the incident beam side and a PIXcel detector with anti-scatter slit on the diffracted beam side. The detector was used in continuous mode with an active length of 3.347°. The implemented X-ray scan program lead to the collection of single scans with 147 s total collection time each with 0.0263° step size in the range 15-75° 2θ at the desired temperatures. The temperature treatment of the samples was performed using an MRI TC-radiation temperature chamber with a Pt heater and a Pt/Rh-thermocouple. The samples were placed in ceramic Al_2O_3 crucibles and heated between room temperature and 1173 K. Data collection was automatically performed using the PANalytical DataCollector software conducting the TC-radiation chamber via a TCPU1 controller.

For all other samples, a Bruker D8 Advance diffractometer, having an angular accuracy of 0.001° and angular resolution better than 0.01°, equipped with a Göbel mirror and employing the CuKα radiation was used. The X-ray patterns were collected in the 10-80° range, with a λ of 1.5406 Å, a 0.03° (2θ) scan step and a 7 seconds per step acquisition time, with a 0.3 mm recording slit. High resolution patterns were acquired in the 10-80° range, with a 0.02° (2θ) scan step and a 14 seconds per step acquisition time, with a 0.3 mm recording slit.

Patterns were analyzed through the use of DICVOL[287] and MAUD[288] programs, after an initial analysis by search-match performed through the use of the X'Pert Highscore v.2.2b program[289] and DIFFRAC.EVA program[290] included in the diffractometer software. Crystallite size was estimated through the Scherrer formula,[231] extrapolating the peak data through the use of the IGOR Pro program.[291] The patterns obtained out through XRD and their subsequent comparison to pre-existing crystal data[156, 289, 290] allowed to determine whether the synthetic procedure was successful. Through the use of the MAUD program, single-phase XRD patterns were further analyzed by performing Rietveld refinement which uses the least squares approach to match the measured pattern with a theoretical line profile, thus allowing to extrapolate data relative to the crystal structure of the sample.[292] In the process of performing the Rietveld refinement, the program made use of algorithms such as the Maximum Entropy Electron Maps (MEEM), an algorithm based on the calculation of an electron distribution map which would result in an XRD pattern that would match the measured one whilst minimizing imperfections due to noise,[158, 293] and the genetic refinement algorithm, based on iteratively creating a "population" of theoretical line profiles by randomly altering the parameters relative to the starting line profile, choosing the one closest to matching the measured pattern and creating a new "generation" from it.

DICVOL91[287] is an indexing program for XRD patterns: based upon the data relative to the reflection positions, it is capable of estimating the most probable crystal cell characteristics, providing not only the space group, but also full crystal cell parameters. For each hypothesis, the program gives a series of values which are useful to evaluate how good the hypothesis is; specifically, for each space group, the program lists the number of indexed reflections, the extra peaks and the missing ones.

MAUD[288] is based upon Rietveld refinement[292] and uses various calculation algorithms together with the least squares method. It allows to solve the crystal structure of a powder, refine said structure and simulate numerous characteristics of a sample (such as sample surface texture).[294]

6.2 - X-ray photoelectron spectroscopy (XPS)

X-ray photoelectron spectroscopy (XPS), otherwise known as Electron Spectroscopy for Chemical Analyses (ESCA), is based upon measuring the kinetic energy of electrons emitted by the surface layers of a sample following irradiation with X-rays.[152] Due to a series of factors, it is necessary for the measurements to be carried out in ultra high vacuum (UHV) conditions, i.e. $\leq 10^{-7}$ Pa: the main reason is that, in order for the kinetic energy measurements to be meaningful, the emitted electrons must undergo as few collisions as possible in their path between the sample and the detector; a secondary reason is that, due to the extreme surface sensitivity of this technique (*vide infra*), a requirement to be met is to minimise the quantity of surface contaminants, such as adsorbed gas (e.g. CO_2), dust, atmospheric contamination or other residuals which may have remained in the analysis chamber from previous analyses. As the name implies, this type of spectroscopy [Fig. 6.2.1] is based upon the photoelectric effect.[295]

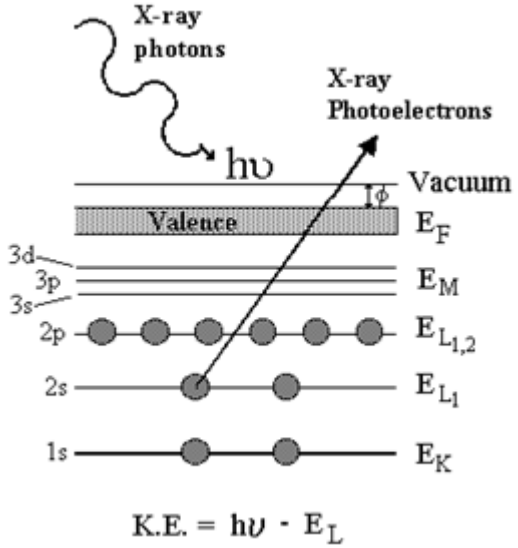

Figure 6.2.1 - *Schematic representation of photoelectric emission*

The photoionisation process can be summarised as:

$$A + h\nu \rightarrow A^{+} + e^{-} \qquad (6.2.1)$$

Where A is a generic atom, h is the Plank constant ($6.626 \cdot 10^{-34}$ J·s) and ν is the frequency (expressed in Hertz) of the incident radiation. The energy conservation principle implies that:

$$E(A) + h\nu = E(A^+) + E(e^-) \quad (6.2.2)$$

Since the energy of the emitted electron E(e^-) only possesses a kinetic component (KE), equation 6.2.2 can be reformulated as:

$$KE = h\nu - [E(A^+) - E(A)] \quad (6.2.3)$$

The term between square brackets is the difference in energy between the ionised atom and the same atom in its unexcited state, which is equal to the binding energy (B.E.) of the electron. This in turn implies that:

$$KE = h\nu - B.E. \quad (6.2.4)$$

Binding energies in solids are normally referenced based upon the Fermi level in the investigated solid. A minor correction is therefore necessary in equation 6.2.4, concerning the introduction of the work function φ_s of the solid:

$$KE = h\nu - B.E. - \phi s \quad (6.2.5)$$

For photoemission to take place, the incident radiation must possess a high enough energy to exceed the electron binding energy.

Each element, and for a given element each different transition, is characterised by binding energies which are specific to the internal energy levels involved. The presence of a peak at a given energy is therefore diagnostic of a certain element on the surface of the analysed sample in a particular chemical environment and oxidation state, whilst the area of the peak is correlated to the atomic concentration of the element in the sampled area. Depending on the chemical environment (or environments) in which a given element is present, the position, shape and broadness (implying the simultaneous presence of the element in different chemical environments) of the relative peaks will be influenced. XPS is therefore a qualitative and semiquantitative analysis technique, capable of detecting nearly all elements (hydrogen and helium are exceptions due to their low cross-sections with respect to X-rays). The X radiation sources most commonly used for this technique are:

- Al K_α radiation, having $h\nu$ equal to 1486.6 eV
- Mg K_α radiation, having $h\nu$ equal to 1253.6 eV

The above considerations imply that, after excitation by the incident X-ray beam [Fig. 6.2.2 a], the substrate will relax in a radiative manner [Fig. 6.2.2 b], and that therefore electronic emission will occur only upon excitation. It is possible however that the sample might undergo non radiative relaxation, with the emission of a secondary electron. This type of emission is known as Auger emission [Fig. 6.2.2 c].

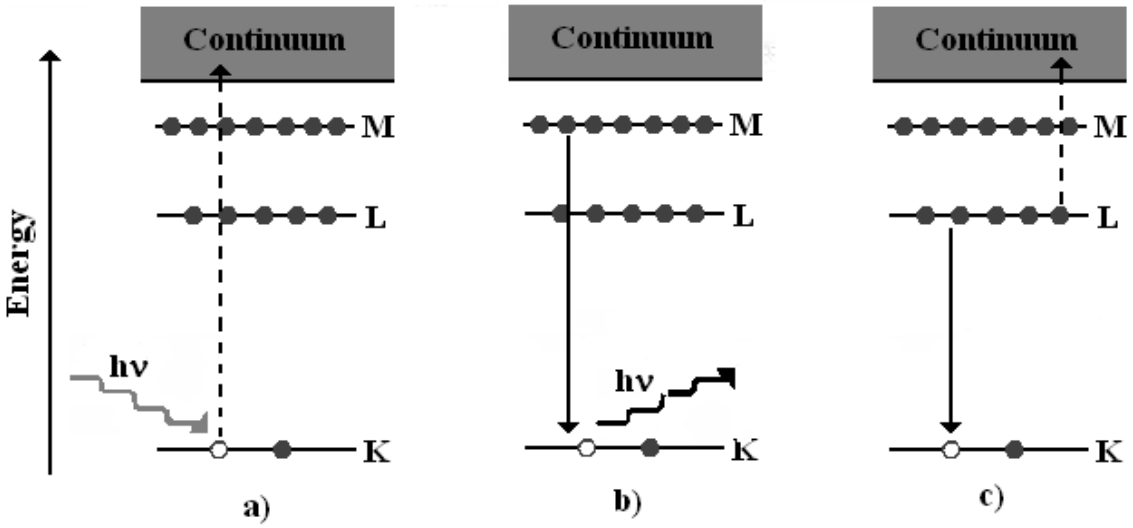

Figure 6.2.2 - *XPS excitation (a), radiative decay (b) and Auger emission (c)*

As a consequence of irradiation and electronic emission, the sample surface tends to acquire a charge, which in turn causes a shift in peak positions by a few eV. In order to counterbalance this effect a twofold approach is employed: i) from the experimental point of view, a device called neutraliser (flood gun) can be used in order to minimise surface charging by irradiating the surface with low energy electrons; ii) during data interpretation, surface charge may be calculated (and therefore compensated) by using a reference. Normally the 1s peak relative to adventitious surface carbon at 284.6 eV[152-154, 159] is used for this purpose.

The instrument [Fig. 6.2.3] consists of an X-ray source, an analysis chamber constantly kept in UHV conditions, an ion gun, an electron gun (i.e. neutraliser), an electron analyser, connected to an electron detector and counter and a computer for data acquisition, storage and elaboration.

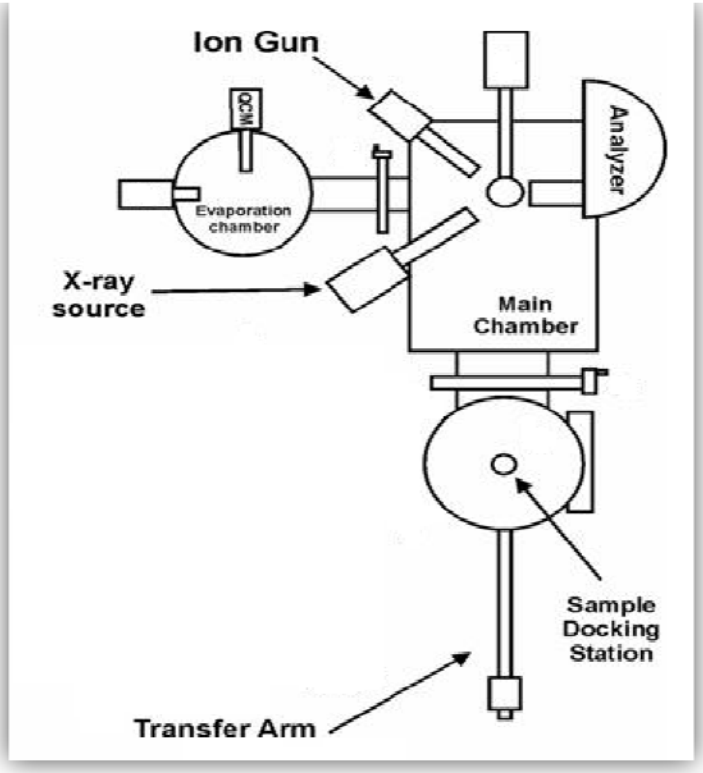

Figure 6.2.3 - *XPS instrument scheme*

Radiation employed during this analysis possesses an energy ranging from 1.5 to 1.2 keV, and is therefore referred to as "soft radiation". This radiation has a penetration power capable of reaching a depth in the 1-10 μm range. However, due to the number of collisions which electrons from deeper layers must undergo before reaching the surface, only atoms from outer surface layers are actually capable of emitting electrons with a sufficient energy to escape the material; photoelectrons emitted by the sample are therefore relative to a surface layer in the 10-50 Å range.

For this reason, XPS is strictly a surface-sensitive analysis and is not suitable when information on bulk material is required. Despite this, it is possible to carry out some form of in-depth analysis (depth profiling), managing to gather important information on the distribution of chemical species within the sample, i.e. how these species are located within the sample at different depths. These special analyses are made possible through the controlled removal (sputtering) of sample layers, which are carried out through bombardment cycles with Ar^+ ions (typically having an energy of 1.5 kV); every erosion cycle is then followed by collection of a spectrum.

In this Ph.D. thesis, only surface spectra were collected, as this technique was employed to determine surface atomic concentrations (to be later compared with bulk concentrations) and to acquire information on the chemical environments of the surface elements, as well as to evaluate the presence of surface contaminants which might have been left over from the synthesis process.

From an experimental point of view, XPS analyses were carried out with a Φ 5600ci Perkin-Elmer spectrometer, using a standard aluminum (Al K_α) source, with an energy of 1486.6 eV operating at 200 W. Compounds containing cobalt were investigated using a standard magnesium (Mg K_α) source with an energy of 1253.6 eV operating at 220 W. The choice to employ a standard Mg source to analyze the cobalt samples (rather than the standard Al source employed for all other

samples) was made in order to avoid the overlap of Co2p and $FeL_3M_{45}M_{45}$ peaks (both sets falling in the 775-795 eV interval with an Al source) and of the Fe2p and $CoL_2M_{23}M_{45}$ (^1P) peaks (all belonging to the 710-720 eV region).[154] The working pressure was $\leq 5 \cdot 10^{-8}$ Pa $\sim 10^{-11}$ torr. The calibration was based on the binding energy (B.E.) of the $Au4f_{7/2}$ line at 83.9 eV with respect to the Fermi level. The standard deviation for the B.E. values was 0.15 eV. The reported B.E. were corrected for the B.E. charging effects, assigning the B.E. value of 284.6 eV to the C1s line of carbon.[152-154, 159] Survey scans were obtained in the 0-1350 eV range (Al source), or 0-1200 eV range (Mg source) (pass energy 58.7 eV, 0.5 eV/step, 25 ms/step). Detailed scans (11.75-29.35 eV pass energy, 0.1 eV/step, 50-150 ms/step) were recorded for relevant regions depending on the sample. The atomic composition, after a Shirley-type background subtraction,[160] was evaluated using sensitivity factors supplied by Perkin-Elmer.[154] Assignment of the peaks was carried out according to literature data. The spectra were analyzed using the IGOR Pro v. 4.01 program, whereas quantitative analysis was performed using the home-made HTIS Lab XPS_AES v. 4.7 program.[296] Fitting of the O1s, C1s Fe2p, Co2p, Mg1s, Mg2s, Mn2p, Ni2p and Sr3d peaks was performed with the XPSPEAK 4.1 freeware program.[297]

6.3 - Mössbauer spectroscopy

Mössbauer spectroscopy is a technique which allows to obtain structural and electronic information on the Mössbauer-active nucleus in the sample through the study of nuclear transitions between the different energy levels of the examined nucleus.

The Mössbauer effect involves the resonant absorption of the γ rays generated when a nucleus, known as *source* nucleus, decays without recoil from an excited state to a lower energy state. The photons are absorbed (again without recoil) by a nucleus which is identical to the source nucleus, which in turn is promoted to an excited state [Fig. 6.3.1]. If, during the decay of the source nucleus, part of the energy is expended in nuclear recoil, the emitted electron would have a lower associated energy, no longer sufficient to induce the same transition in the target nucleus.

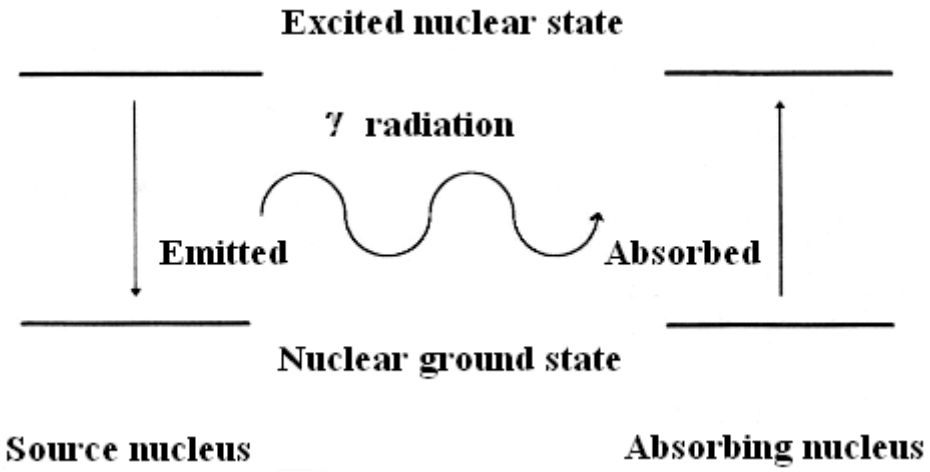

Figure 6.3.1 - *Scheme illustrating the Mössbauer process*

This phenomenon occurs in several elements of the periodic table, but, due to energy intervals being too high, or active nucleus life times (both in the source and in the sample) being too brief or too long, it can only be employed for analytical purposes in determined cases, the most common one

being ^{57}Fe. Due to nuclear recoil, an isolated nucleus is incapable of producing Mössbauer effect, as the phenomenon is only possible when the nucleus is within a crystal lattice: this is due to the fact that recoil energy is transferred to the lattice itself as vibrational energy, which in turn causes a change in the phononic energy in the entire crystal as whole multiples of the fundamental frequency $h\omega$. The process is such that there is conservation, over the entire solid, of both energy and momentum, despite there being a certain fraction of events without recoil, known as *recoil-free fraction* f.

$$f \approx exp\left[-\frac{4\pi\langle\chi^2\rangle}{\lambda^2}\right] \tag{6.3.1}$$

Where λ is the photon wavelength and $<\chi^2>$ is the mean quadratic shift of the nucleus in the direction of the photon.

Since the nuclei in question are not isolated, but rather lie within electromagnetic fields, their nuclear momentums (angular, spin etc.) are capable of interaction with these fields, generating a perturbation in the energy levels of the nuclei themselves. The energy required for there to be resonant absorption is consequently subject to change, and that change provides information regarding the Mössbauer isotope present in the compound. These perturbations are known as *hyperfine nuclear interactions*.

The nature and strength of hyperfine interactions are reflected in the Mössbauer spectrum through the following values (hyperfine interaction parameters): *isomeric shift* (δ), *quadrupole splitting* (ΔE_Q) and *magnetic splitting* (ΔE_M).

Measurements were performed on a conventional constant-acceleration spectrometer, with a room temperature Rh matrix ^{57}Co source (nominal strength 1850 MBq). The hyperfine parameters, isomer shift (δ), quadrupole splitting (Δ), full line width at half maximum (Γ), expressed in mm/s, internal magnetic field (B) expressed in Tesla and percent areas (A), were obtained by means of standard least-squares minimisation techniques. The spectra were fitted with Lorentzian line shapes with the minimum number of components. It was assumed that, in all the spectra, each hyperfine parameter was affected by the same error, postulated as the maximum error over all measurements. A deviance of ± 0.03 mm/s from the obtained value was assigned to δ, Δ and Γ, ± 0.1 T to B and ± 2 % to A. Isomer shift is quoted relative to α-metallic iron at room temperature. The spectra were collected at 298 K (RT) and 12 K. Low-temperature spectra were collected in a ARS® closed circuit cryostat.

6.3.1 - Low temperature measurements

Mössbauer spectra collected at low temperature are a powerful investigation tool for many reasons. First of all, since Mössbauer effect is enhanced as the analysed structure becomes more rigid, the spectrum quality is improved at lower temperatures. This occurs because, as temperature decreases, so does the mean quadratic shift $<\chi^2>$ of the active nucleus and, consequently, the recoil-free fraction f increases (see Fig. 6.3.1). Furthermore, at low temperatures conditions may be met to isolate magnetic phases which are undetectable at higher temperatures due to thermal agitation which causes constant changes in spin orientations.

6.3.2 - Information provided

In this thesis, Mössbauer spectroscopy has been used to study iron atoms within ferrites, Mössbauer spectroscopy allows to define the following properties of iron atoms in a sample:

- Oxidation state: the different electronic configurations in Fe^{IV} ($3d^4$) and Fe^{III} ($3d^5$) stems from the removal of an electron in the 3d orbital. This is reflected in the nucleus charge density generated by the s electrons, causing Fe^{III} to present a higher isomeric shift than Fe^{IV}.
- Quantitative ratio: If multiple oxidation states (or multiple site geometries for a single oxidation state) are present, the quantitative ratio can be estimated by the ratio of the spectral areas. In this calculation it is assumed that both species have the same recoil-free fraction; although this is strictly valid only at absolute zero, at a temperature of 10 K, typical value for low temperature spectra collection, the difference is negligible.
- Site geometry: both isomeric shift δ and quadrupole splitting Δ normally increase when the coordination number increases; it is thus possible to distinguish an octahedral geometry (O_h) having six ligands, from a tetrahedral geometry (T_d) with four ligands.
- Presence of iron oxides: this is possible due to the fact that these compounds (e.g. hematite or magnetite) display specific magnetic behaviour.

6.3.3 – Study of spinel ferrites

Mössbauer spectroscopy was also employed in order to understand the degree of inversion (γ) of the obtained spinels. The magnetic properties of these oxides strongly depend on the type of cations and on their distribution over the two positions. Moreover the dimension of the crystallites can affect the magnetic properties of these spinels ferrite. These pieces of information are easily achieved by performing Mössbauer measurements both at RT and at 14 K. The former experiments were performed in order to underline the eventual presence of superparamagnetic species, while the latter to estimate the Fe distribution over the tetrahedral and octahedral sites. In general, the chosen model consist in an estimation of γ, by using the tetrahedral over the octahedral area ratio, obtained from the 14 K spectrum, and from this value, as suggested by Rusanov et al.,[298] the occupancy of M^{2+} in A sites can be calculated. The 14 K spectra were firstly fitted by using only two components, one belonging to the Fe^{III} in A site the other one to the Fe^{III} in B site. The two sites differs each other for the δ and B values, as underlined by Chinnasamy et al.[264] The sextet with the largest hyperfine field value and the largest centre shift is assigned to the Fe^{3+} ions at the B sites and the sextet with the smallest centre shift is assumed to arise from the Fe^{3+} ions occupying the A sites. Moreover it is evident, especially in the $CoFe_2O_4$ series, that the spectra are broadened and the large linewidths are due to the presence of multiple hyperfine fields at the Fe^{3+} nuclei at A and B sites. While the distribution of subcomponents in the site A can be neglected, the presence of multiple subcomponents in the B site has to be taken in account. As mentioned by Sawatzky et al.,[299] the hyperfine magnetic fields at the B-sites ^{57}Fe nuclei are function of the occupation of the six nearest A sites by Fe^{3+} and M^{2+}. The intensity ratio of the different B-site subcomponent (i.e. subspectra) can be calculated since it is proportional to the ration of the probabilities of the different surroundings. So, by applying the distribution reported in equation 6.3.3.1, the number of subcomponent can be estimated.

$$I(n) = \binom{6}{n}(1-\gamma)^{6-n}\,\gamma^{n} \qquad (6.3.3.1)$$

In the reported formula *I(n)* is the relative intensity of the B sub-spectrum with *n* Fe^{3+} ions in the nearest-neighbour in A sites and γ is the degree of inversion.

6.3.4 - Experiment setup

Mössbauer spectroscopy analyses were performed on a conventional constant-acceleration spectrometer, with a room temperature Rh matrix ^{57}Co source (nominal strength 1850 MBq). The hyperfine parameters, isomer shift (δ), quadrupole splitting (Δ), full line width at half maximum (Γ), expressed in mm/s, internal magnetic field (B) expressed in Tesla and percent areas (A), were obtained by means of standard least-squares minimisation techniques. The spectra were fitted with Lorentzian line shapes with the minimum number of components. It was assumed that, in all the spectra, each hyperfine parameter was affected by the same error, postulated as the maximum error over all measurements. A deviance of ± 0.03 mm/s from the obtained value was assigned to δ, Δ and Γ, ± 0.1 T to B and ± 2 % to A. Isomer shift is quoted relative to α-metallic iron at room temperature. The spectra were collected at 298 K (RT) and 12 K. Low-temperature spectra were collected in an ARS® closed circuit cryostat.

6.4 - Inductively coupled plasma - atomic emission spectroscopy (ICP-AES)

As implied by the full name of the technique (ICP-AES standing for inductively coupled plasma - atomic emission spectroscopy), this analytical method is based upon atomic emission spectroscopy. One of the oldest and most familiar forms of atomic emission spectroscopy is flame testing: the colours produced when placing the salts of certain metals within the flame of a Bunsen burner are an easy method to qualitatively identify elements. With more powerful methods of excitation, the principles behind this technique have been expanded into the broader and more accurate field of emission spectroscopy.[300] Among the three possible emission spectra (continuous, band and line), line spectra are the most informative, as all atoms display their own particular atomic emission spectrum.[300] When more than one element is present, usually it is only necessary to identify the strongest lines, which will always be in definite positions and conclusively determine the presence of a certain element. Since these lines are also the last to disappear as the element is consumed by the analysis, they are also known as "persistent lines" or R.U. lines (from *raies ultimes*). Since quantitative treatment of these spectra is possible and since (except in a few very rare cases) the constituent elements of a sample will produce non-overlapping lines, these methods are extremely powerful tool for quantitative analysis of samples.

This technique is very powerful and precise, this is because of the plasma employed in order to produce excitation in the analysed atoms: due to its high energy content (normally between 7000 and 15000 K) plasma is a very useful excitation source, as it greatly increases the number of excited emitted atoms compared to other sources (such as flame excitation),[300, 301] and allows large numbers of different elements to be studied simultaneously,[301] also atomisation conditions are reproduced with a much greater degree of precision compared to arc and spark spectroscopy. Two types of plasma are normally used in AES: direct current plasma (DCP) and inductively coupled plasma (ICP), the former of which was used in this thesis.

The plasma generation system is comprised of three concentric quartz tubes [Fig. 6.4.1], the central tube carries the sample aerosol in argon to the plasma itself. An auxiliary flow of argon is used to sustain the plasma and is excited by passing through the top section of the tube, around which a metal induction tube is coiled (with a frequency of 4-50 MHz). The helical pattern in which the gas is made to flow helps provide stability and thermally isolates the outside quartz tube.[300]

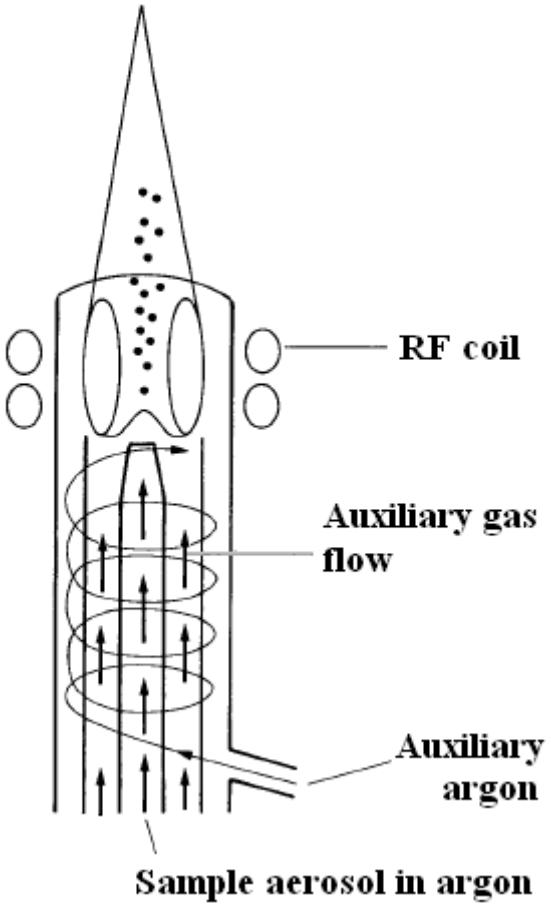

Figure 6.4.1 - *Schematic illustrating the ICP setup*[300]

Once initiated (usually by a spark from a probe) the plasma is self-sustaining, the sample is introduced in the central zone of the plasma (relatively cooler than the rest) by a nebuliser system, which slowly feeds the sample solution into an intense argon flow. The signal generated by the excited atoms is then collected either with a simultaneous multi-element spectrometer (where light emitted from the plasma is split by a grate according to the different atomic emission lines) capable of measuring the emission of several elements at the same time, or with a sequential spectrometer (where each desired emission line is singled out sequentially by using a pair of monochromators).[300]

In this Ph.D. thesis, ICP-AES analysis was used to determine the bulk atomic Fe/M and Fe/M'/M'' (where applicable) ratios. Analyses were carried out with a Spectroflame Modula sequential and simultaneous ICP-AES spectrometer equipped with a capillary cross-flow nebuliser was used (Spectro Analytical, Kleve, Germany). Analytical determinations were performed using a plasma power of 1.2 kW, a radiofrequency generator of 27.12 MHz and an argon gas flow with nebuliser and a coolant set at 1, 0.5 and 14 $l \cdot min^{-1}$, respectively. Sample preparation involved mineralising approx. 100 mg (exactly measured) in 4 ml aqua regia and then diluting the resulting solution to 250 ml with a 2 % wt. HCl solution in bidistilled water.

6.5 - Other methods

6.5.1 - Transmission Electron Microscopy (TEM)

This technique allows direct imaging of the analysed sample, making it particularly useful for the investigation of nanoparticles and, more in general, objects with nanosized features. During a measurement, the sample is irradiated by an electron beam, generated by a thermoionic or field emission gun, and focused by a suitable electromagnetic lens system.[302] The electron beam undergoes scattering and the transmitted wave (which in the case of a thin specimen and high-energy electrons can be considered a forward elastically-scattered wave) goes through an objective lens and a magnification system before hitting the data recording system (usually a charge coupled device device (CCD) or a photographic plate).[302] The electron image which forms is the interference result of the beams scattered at different angles. The ultimate resolution of the images is influenced by aberrations introduced by the lenses.[302] The patterns collected by the detector are then interpreted mathematically into images. In addition to direct images, selected area electron diffraction (SAED) patterns can be recorded to obtain crystallographic information from the imaged regions.

In this thesis, this technique was used to study sample morphology and particle size. In the case of ferrites synthesised through nonaqueous sol-gel synthesis, images were collected on a Philips CM200 instrument using a voltage of 160 kV by the work group of Prof. Markus Niederberger at ETH Zürich, whereas samples synthesized though coprecipitation of oxalates were investigated with an analytical Philips CM12 electron microscope, operated at 120 keV by Dr. Gloria Ischia at the University of Trento.

6.5.2 - Superconducting Quantum Interference Device (SQUID)

The SQUID analytical method is based upon a very sensitive magnetic flux looped detector (i.e. the SQUID itself) which combines both the Josephson tunnelling and the flux quantisation phenomena.[303] The device responds to changes in the magnetic flux within the superconducting loop with a change in voltage, in the case of a dc (direct current) SQUID, or with a change in the amplitude of the oscillating voltage, in the case of RF (Radio Frequency) SQUID. In this thesis, the technique was used to measure the hysteresis loops of the cobalt and manganese spinels as well as the manganese perovskite and to investigate the magnetic behaviour of the manganese perovskite as a function of temperature (thus allowing to detect the transition of the perovskite from a paramagnetic to ferrimagnetic material). Analyses were carried out with a Cryogenic S600 SQUID magnetometer by the work group of Prof. Andrea Caneschi at the University of Firenze.

6.5.3 - X-ray absorption spectroscopy (XAS)

Like XPS analysis (see Par. 6.2), XAS is based upon the absorption of X radiation by the analysed sample. Unlike XPS, this analysis is not directly concerned with the electrons expelled by the sample, but rather with how the absorption coefficient of a given element in the material (equation 6.5.3.1) changes with the energy E of the incident radiation.[304]

$$\mu \approx \frac{\rho Z^4}{AE^3} \qquad (6.5.3.1)$$

where ρ is the sample thickness, Z is the atomic number and A the atomic mass. Due to the fact that μ varies with Z^4, different elements can possess very different absorption coefficients, allowing in many cases to separate the investigation of a sample by its constituent elements.[304] Since different wavelengths must be explored, it is necessary to use an X-ray beam which can be tuned; for this reason, and due to superior source brilliance, XAS spectroscopy is carried out in facilities where synchrotron radiation is available. In EXAFS (Extended X-ray Absorption Fine Structure) μ(E) is measured in proximity of an absorption edge of the element to be studied (the chosen edge depends on the element), in proximity of the edge, absorption (and thus μ) increases dramatically, and a large variation of the μ function can be measured. When a photon is absorbed by the analysed atom, the consequent excitation-relaxation process causes the atom to emit an electron. This electron may interact with the electronic clouds relative to atoms surrounding the emitter as if they were scattering centres and, after scattering, return to the original atom. Due to the fact that absorption depends on the availability of a suitable energy state (i.e. an electron in the absorbing atom with an appropriate energy and momentum),[304, 305] backscattering alter the absorption coefficient in the analysed atom according to equation 6.5.3.2.

$$\chi(k) = \sum_j S_0 \frac{N_j}{kr_j^2} F_j(k) e^{-2\sigma_j^2 k^2} e^{-\frac{2r_j}{\lambda(k)}} \sin\left[2kr_j + \varphi_{ij}(k)\right] \qquad (6.5.3.2)$$

In the above equation, χ is the EXAFS fine-structure function, k is the photoelectron wave number, j is the j^{th} backscattering atom type, S_0 is the amplitude reduction factor, N is the average number of j atoms in a shell of identical atoms, r is their average distance, σ is the man-square displacement and F and φ represent backscattering amplitude and phase shift (which are element specific).[304, 305] The collected spectrum is thus influenced by the oxidation state of the atoms, by the nature of the atoms in proximity to the chosen element and by the nature and geometry of the atomic bonds involved,[304, 305] this technique is therefore a very powerful tool to investigate chemical environments within a sample.

Samples of particular interest were characterised using the DORIS III synchrotron at Deutsches Elektronen-Synchrotron *DESY* (Hamburg) and interpreted by Prof. Matthias Bauer (TU Kaiserslautern).

6.5.4 – Resonant Inelastic X-ray Scattering (RIXS)

As with XAS, this is an analytical method which requires synchrotron light in order to obtain X-rays of the desired frequency and intensity. Unlike XAS, it is an emission spectroscopy, that is to say, the measured signal relies on the electrons generated by the material as a result of the incident beam (a second order process).[306] The term *inelastic* indicates that the final energy state in which the material finds itself after the excitation-relaxation process is different from the initial state (if the two states were identical, we would have elastic scattering).[306] In systems containing transition metals (such as ferrites), this technique is a powerful tool to investigate electronic states of the elements involved, as well as inter-atomic interactions.[306]

Interesting samples were characterised at the European Synchrotron Radiation Facility (ESRF), Grenoble, using line ID 26 (data analysis and interpretation are currently in progress).

6.5.5 - Micro-Raman spectroscopy

Raman spectroscopy is an analytical technique based upon the inelastic scattering of EM radiation, normally in the 50-4000 cm^{-1} range.[244] Due to the low intensity of scattered light relative to the incident beam, monochromatic lasers are the preferred choice as EM sources, in order to boost the collected signal and obtain better spectra. Similarly to IR spectroscopy, this analytical technique is sensitive to the vibrational modes of the analysed molecules, unlike IR however, where the only active modes are those where molecular dipole changes, Raman spectroscopy only modes where there is a change in molecular polarisability are active.[307] This spectroscopic technique is therefore considered complementary to IR spectroscopy, as usually the modes invisible to one analysis will be visible to the other. In Micro-Raman, the Raman spectrometer is coupled with a microscope, allowing systematic measurements to be carried out in different points of the sample, thus affording information on possible compositional gradient and allowing mapping of the sample composition to be performed. In this thesis, measurements were carried out with a Thermo Scientific® DXR Raman Microscope using a 532 laser as an excitation source.

6.5.6 - Temperature Programmed Reduction (TPR)

Temperature-Programmed Reduction (TPR) determines the number of reducible species present on a sample and reveals the temperature at which the reduction of each species occurs. The TPR analysis begins by flowing an analysis gas (typically hydrogen 5 % in an inert carrier gas such as argon) through the sample placed in a quartz reactor. While the gas is flowing, the temperature of the sample is increased linearly with time and the consumption of hydrogen by adsorption/reaction is monitored. A thermal conductivity detector (TCD) is used to measure changes in the thermal conductivity of the gas stream. The TCD signal is then converted to concentration of active gas using a level calibration. Integrating the area under the concentration vs. time (or temperature) yields total gas consumed. TPR measurements were performed with an Autochem II 2010 Micromeritics, equipped with a TCD detector.

In this Ph.D. thesis, TPR was used to investigate the stability of the synthesised metal oxides, as well as to study the oxidation states of the constituent metal species. The investigated samples were further characterised with post-TPR XRPD in order to determine the nature of the reduced compound.

6.5.7 - Broadband Electric Spectroscopy (BES)

The electric response of three ferrites ($CoFe_2O_4$, $MnFeO_3$ and $NiFe_2O_4$) was investigated through BES. In this technique, the measurement separates molecular process on the basis of response time, providing a unique relaxation frequency along with a signature variation with frequency. This allows, among other things, to study dielectric processes such as (in our case) bulk conduction in solids and electrode effects. By performing measurements at different temperatures, relaxation phenomena in the analysed material can be distinguished and characterised.

Measurements were collected over the frequency range from 1 to 10^7 Hz using a Novocontrol Alpha analyzer from 10 to 140°C in 10°C intervals with accuracy better than 0.1°C. The temperature was controlled with a homemade cryostat equipped with a gaseous nitrogen heating-

cooling system. Samples were placed between two gold disk electrodes with a 13 mm diameter and a thickness of approximately 200 μm.

6.5.8 - Temperature Programmed Methane Oxidation (CH_4-TPO)

The catalytic activity of selected samples was tested in the temperature programmed oxidation of methane using a ChemBET 3000 apparatus from Quantachrome Instruments. Therefore, 20 mg of the sample were diluted with SiC powder (200 - 400 mesh, Sigma-Aldrich) in a weight ratio of 1 to 4 and the physical mixture was fixed with quartz wool in a U tube made of quartz glass. After placing the sample cell in the oven, sample was flowed through by a mixture of 4.5 % O_2, 1.5 % CH_4 and 96.0 % He with a total amount of 20 $ml \cdot min^{-1}$. The oven temperature was raised up to 900°C with a ramp of $5°C \cdot min^{-1}$. The composition of the produced gas was analysed using a thermal conductivity detector (TCD), whereas the detector signal was plotted against the sample temperature. The intersection of the tangent with the highest slope and the baseline was defined as onset temperature (detector signal rises if oxidation takes place) and allowed the comparison of different samples. After cooling down the sample, a second heating cycle was performed to test the sample stability.

6.5.9 - Thermogravimetric Analysis (TGA)

A thermogravimetric analysis investigates the change in mass, determined by using a microbalance, of a sample upon heating it at increasing temperature; the sample is subjected to a heating ramp which allows to plot the mass variation as a function of temperature. This analysis is therefore very useful to study thermal decomposition phenomena, oxidation, desorption and vaporisation phenomena. This analysis also allows to identify temperature intervals where the sample is stable and also how these intervals change based upon ambient conditions (i.e. the atmosphere where the reactions take place). Through data analysis, it is also possible to identify the reaction type which occurs in correspondence with each mass variation. In case of reactions occurring simultaneously, by deriving the thermogram curve ($\partial m/\partial T$), which isolates the temperatures where mass loss is fastest, it is possible to separate these overlapping curves.

Measurements were carried out in air with a SDT 2960 apparatus from TA instruments [Fig. 6.5.9.1], capable of measurements both in air and in nitrogen controlled atmosphere. The setup is made up by a horizontal analytical balance, a furnace for temperature control and a gas flow system (in order for the experiment to be able to take place in the desired environment).

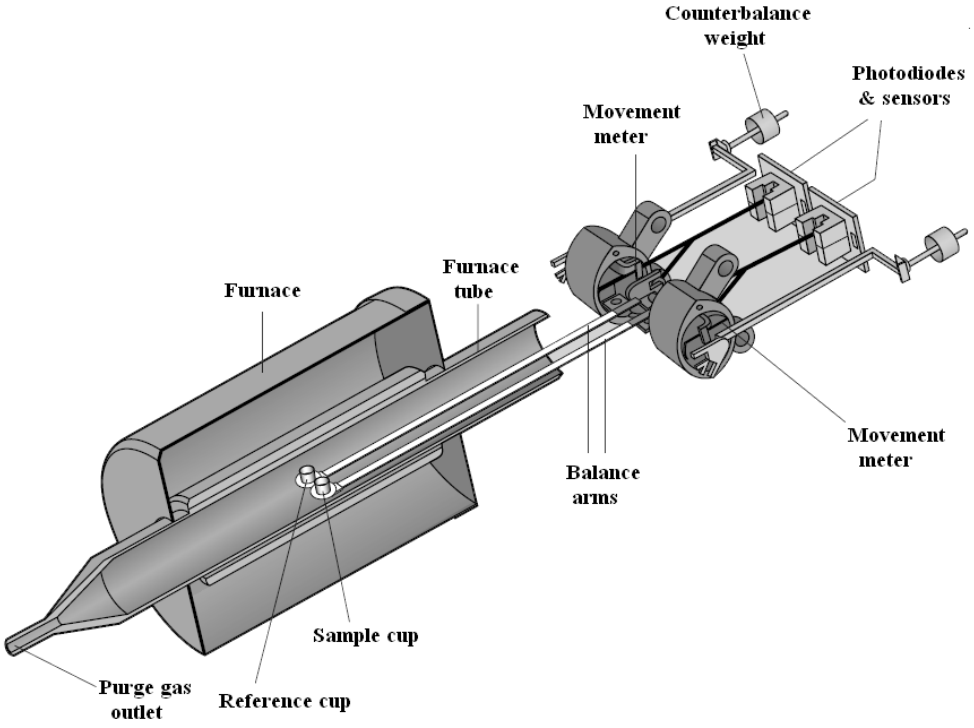

Figure 6.5.9.1 - *SDT 2960 balance components*[308]

The balance is in turn constituted of a pair of parallel ceramic arms (stable at high temperatures): one extremity, inside the furnace, is connected to the sample holder, a thermocouple and a platinum sensor (which constitute the sample temperature registration apparatus), the other extremity, outside of the furnace to avoid temperature expansions, is connected to the weight variations measurement system. Two sample holders are employed; one contains a few milligrams of the sample whereas the other, used as a reference, is empty.

The position of each balance arm is monitored by an optic system made up of an infrared light source and a photodiode, which keeps the arm connected to the filled sample holder arm horizontal and parallel to the other. Any weight change in the sample causes the balance arm to shift from its reference position, and thus changes the amount of light reaching the photosensor, in reaction to this, an electric current (directly proportional to the weight change) is applied in order to bring the arm back to a horizontal position. At the same time, the two thermocouples allow for the corresponding DSC (see Par. 6.5.10) thermogram ($\partial H/\partial T$ versus T) to be collected. Calibration is carried out for temperature, weight and DSC signal; for the first, standard metal samples having known melting points, such as zinc (T_m = 419.60°C) and indium (T_m = 156.53°C)[309] are used; for weight measurements carried out in set conditions (empty and with known mass weights); lastly, DSC signal is measured with empty sample holders and with sapphire standards references.

6.5.10 - Differential Scanning Calorimetry (DSC)

Differential Scanning Calorimetry (DSC) is an analytical method in which the temperature of a sample is compared with that of an inert reference material during a programmed change of temperature. The temperature difference ΔT between the sample and the reference material should be null until a thermal event occurs. When this change is endothermic, the sample temperature lags behind the reference one, while when an exothermic event occurs, it leads the reference

temperature. In the arrangement generally used, the sample and the reference are placed side by side in a heat block which could be either heated or cooled at a constant rate. Two identical thermocouples, placed in each and connected back to back, record the temperature difference. When the sample and the reference have the same temperature, the net output of the thermocouple is zero. As soon as a thermal event takes place in the sample, a temperature difference ΔT is recorded as a net voltage in the thermocouple.[310, 311] The heating/cooling rate is usually in the range 1-50°C.

The resulting thermogram, showing the applied heat flow ($\partial H/\partial T$) versus temperature, will display a peak corresponding to every detected transition. The nature of each transition can be deduced from baseline changes (in the case of a glass transition) or from the peak type. Different setups however might show an exothermal reaction as a positive or negative peak, thus requiring graphs to specify whether they are exothermal-down or -up.

These two analytical techniques (i.e. TGA and DSC) were employed in this Ph.D. thesis in order to study the decomposition pattern of the oxalates, the calcination process of the samples synthesised through coprecipitation of oxalates as well as the behaviour at high temperatures of the samples prepared through hydrothermal synthesis.

6.5.11 - Microanalysis

The elemental analysis technique allows to detect the presence of elements (specifically nitrogen, carbon, hydrogen and sulphur) within a sample and determine their abundance (expressed as weight percentage). During this analysis, an exactly measured quantity of sample is introduced in a quartz tube which is kept at 1020°C and through which a constant flow of oxygen enriched helium is maintained. The part of sample capable of reacting by combustion burns and the resulting gasses, after flowing through a few layers of WO_3 and metallic copper in the primary column, are separated by frontal gas-chromatography through the use of a 2 m *Porapak* QS chromatographic column kept at 190°C. The separated gas components are then analysed with a *Frison EA* 1108 analyser. Analyses were carried out at the Department of Chemical Sciences microanalysis laboratory of the University of Padova. In this thesis, this technique was used to measure the carbon and hydrogen content in the final samples (in mass %), and therefore to estimate the amount of residual organic precursors which remained adsorbed on the oxides after purification.

7 - Conclusions

Iron ferrites of bivalent metals were successfully synthesised through nonaqueous sol-gel synthesis, coprecipitation of oxalates and hydrothermal synthesis [Tab. 7.1]. These three methods allowed the easy and rapid preparation of ceramic oxides, with high yields and purity and without the need for expensive and/or toxic solvents or reagents.

Different synthetic routes resulted in products with different characteristics and structure, in particular nonaqueous sol-gel and hydrothermal synthesis yielded products with a much smaller average crystallite size in comparison to coprecipitation. While not all methods allowed to obtain the same products, comparison between the synthesised compounds provided insight on how both synthesis parameters and choice of synthetic approach can be fine-tuned in order to prepare a material with the desired structural and functional characteristics. In particular, coprecipitation synthesis proved to be, among the routes explored, the only one through which perovskite ferrites could be synthesised. Nonaqueous sol-gel synthesis and hydrothermal synthesis selectively afforded spinel-type ferrites, however these two methods are characterised by the advantage of being far quicker and greener in execution (as no calcination step was required).

Coprecipitation synthesis yielded the highest number of different crystalline compounds as seven different ferrites ($MgFe_2O_4$, $CoFe_2O_4$, $MnFe_2O_4$, $NiFe_2O_4$, $ZnFe_2O_4$, $MnFeO_3$ and $SrFeO_3$) were successfully obtained with this route. Calcination proved to be a crucial step in determining the final qualities of the desired product, as the temperature and time of calcination were both shown to influence the structure of the resulting powder and the particle size. The temperature in particular has a remarkable effect on the resulting oxides, as lower temperatures yield smaller crystallites (revealing that coalescence phenomena take place during calcination) and finer powders; this however comes at the cost of purity: Mössbauer spectroscopy analyses of samples treated at lower temperatures revealed the presence of secondary phases absent in analogous compounds treated at 900°C. The sharpness of the heating ramp also proved to be a significant factor, as TPXRD analyses (employing a 600°/hour ramp) yielded powders with much smaller crystallites.

Nonaqueous sol-gel synthesis only allowed to successfully synthesise two spinels ($CoFe_2O_4$ and $MnFe_2O_4$) despite many different synthetic attempts having been carried out with different metals. It was, among the three explored routes, the one requiring the least amount of time, however it was also the most demanding (in terms of reagent purity, reagent cost and equipment cost). The necessity to find anhydrous precursors which are soluble or at least partially soluble in benzyl alcohol also significantly limited the options available to the operator. It however allows a wide variety of different synthetic permutations to be explored in a very short time, thus being very useful for explorative synthesis.

Hydrothermal synthesis was successfully used to prepare four spinel ferrites (namely $CoFe_2O_4$, $MnFe_2O_4$, $NiFe_2O_4$ and $ZnFe_2O_4$) with extremely high purity and yields. As a synthetic method, it combines a good versatility (it was possible to prepare four different spinels with this route) with reasonable speed, high quality of products and low costs.

The low temperatures (75-135°C) employed in this method make it particularly attractive for possible larger scale applications, where the absence of a calcination step and of complex purification and waste disposal steps would significantly cut down the costs.

As part of the investigation of this last synthetic route, a fourth protocol, involving heating under reflux conditions (rather than hydrothermal conditions) was explored. Whilst it has been possible to synthesise the desired compound ($ZnFe_2O_4$) with this method, and while this route holds some objective advantages over hydrothermal synthesis (as it is cheaper and less complex), preliminary results show that the method affords lower yields and products with a higher amount of impurities (it must be however stressed that this last synthetic protocol has yet to be investigated in depth, let alone optimised).

In general, functional analyses carried out on the different compounds allowed to gain insight on their properties and suggested avenues for possible future applications.

As far as the magnetic and electric properties are concerned, the cobalt spinel displayed hard ferrimagnetic behaviour and, when synthesised through coprecipitation, showed a dielectric response at high temperatures compatible with water intercalation.

The nickel spinel yielded a similar response, making these two materials interesting for possible applications in lithium batteries.

The manganese spinel ferrite displayed ferrimagnetic behaviour typical of most spinel ferrites (that is to say it is a soft magnetic material). Analogously toe the cobalt and nickel spinels, as well as the manganese perovskite, the manganese spinel was also able to serve as an active catalyst for CH_4-TPO, though, similarly to the other tested ferrites, it lacked long-term stability over several catalytic cycles.

Aside from the aforementioned catalytic properties, the magnesium perovskite displayed an interesting magnetic behaviour, undergoing a transition from paramagnetic to hard ferrimagnetic material at 35 K. From a dielectric point of view, BES analyses yielded a response compatible with ionic conduction, suggesting that the material is capable of acting as an O^{2-} conductor.

Sample	Method	Found structure	Treatment temperature and time	Crystallite mean size/nm (from Rietveld)
S-Co010-5	Nonaqueous sol-gel	$CoFe_2O_4$	200°C; 30 minutes	10±2
S-Co011-1	Nonaqueous sol-gel	$CoFe_2O_4$	180°C; 15 minutes	9±2
S-Co011-3	Nonaqueous sol-gel	$CoFe_2O_4$	200°C; 15 minutes	10±2
S-Co011-4	Nonaqueous sol-gel	$CoFe_2O_4$	180°C; 30 minutes	10±2
Co008	Coprecipitation	$CoFe_2O_4$	600°C; 5 hours	23±5
Co007	Coprecipitation	$CoFe_2O_4$	900°C; 2.5 hours	132±10
Co002	Coprecipitation	$CoFe_2O_4$	900°C; 5 hours	185±5
Co011	Coprecipitation	$CoFe_2O_4$	900°C; 5 hours	178±5
Co017	Coprecipitation	$CoFe_2O_4$	900°C; 5 hours	170±5
I-Co001	Hydrothermal	$CoFe_2O_4$	135°C; 24 hours	12±3
I-Co007	Hydrothermal	$CoFe_2O_4$	135°C; 24 hours	17±2
I-Co018-1	Hydrothermal	$CoFe_2O_4$	135°C; 1 hour	/
I-Co018-2	Hydrothermal	$CoFe_2O_4$	135°C; 2 hours	18±3
I-Co018-4	Hydrothermal	$CoFe_2O_4$	135°C; 4 hours	18±1
I-Co019	Hydrothermal	$CoFe_2O_4$	100°C; 24 hours	/
I-Co020	Hydrothermal	$CoFe_2O_4$	75°C; 24 hours	/
Mg002	Coprecipitation	$MgFe_2O_4$	900°C; 5 hours	85±5
Mg006-a	Coprecipitation	$MgFe_2O_4$	900°C; 1.5 hours	66±5
Mg007	Coprecipitation	$MgFe_2O_4$	600°C	14±5
S-Mn004-1	Nonaqueous sol-gel	$MnFe_2O_4$	200°C; 30 minutes	8±2
S-Mn005-1	Nonaqueous sol-gel	$MnFe_2O_4$	180°C; 15 minutes	8±2
S-Mn005-2	Nonaqueous sol-gel	$MnFe_2O_4$	180°C; 15 minutes	8±2
S-Mn006-1	Nonaqueous sol-gel	$MnFe_2O_4$	180°C; 15 minutes	8±2
S-Mn006-2	Nonaqueous sol-gel	$MnFe_2O_4$	180°C; 15 minutes	8±2
S-Mn006-6	Nonaqueous sol-gel	$MnFe_2O_4$	200°C; 25 minutes	9±2
S-Mn007-3	Nonaqueous sol-gel	$MnFe_2O_4$	200°C; 45 minutes	9±2
Mn008	Coprecipitation	$MnFeO_3$	600°C; 5 hours	70±5
Mn006-b	Coprecipitation	$MnFeO_3$	900°C; 2.5 hours	115±5
Mn001	Coprecipitation	$MnFeO_3$	900°C; 5 hours	129±5
Mn011	Coprecipitation	$MnFeO_3$	900°C; 5 hours	133±5
Mn020	Coprecipitation	$MnFeO_3$	900°C; 5 hours	140±5
I-Mn002	Hydrothermal	$MnFe_2O_4$	135°C; 24 hours	20±4
I-Mn007	Hydrothermal	$MnFe_2O_4$	135°C; 24 hours	39±4
I-Mn012-2	Hydrothermal	$MnFe_2O_4$	135°C; 2 hours	33±1
I-Mn012-4	Hydrothermal	$MnFe_2O_4$	135°C; 4 hours	24±1
I-Mn013	Hydrothermal	$MnFe_2O_4$	100°C; 24 hours	36±2
I.Mn014	Hydrothermal	$MnFe_2O_4$	75°C; 24 hours	35±2
Ni002	Coprecipitation	$NiFe_2O_4$	135°C; 24 hours	132±5
Ni004	Coprecipitation	$NiFe_2O_4$	135°C; 24 hours	117±5
I-Ni001	Hydrothermal	$Ni_{1.43}Fe_{1.7}O_4$, NiO and $NiFe_2O_4$	135°C; 24 hours	20±5
I-Ni002	Hydrothermal	Unidentified mixed product	135°C; 24 hours	45±3
I-Ni007	Hydrothermal	$NiFe_2O_4$	135°C; 24 hours	47±2
I-Ni011-2	Hydrothermal	$NiFe_2O_4$	135°C; 2 hours	10±1
I-Ni011-4	Hydrothermal	$NiFe_2O_4$	135°C; 4 hours	34±1
I-Ni012	Hydrothermal	$NiFe_2O_4$	100°C; 24 hours	20±1
I-Ni013	Hydrothermal	$NiFe_2O_4$	75°C; 24 hours	8±5

Sr001-a	Coprecipitation	$SrFeO_3$	900; 5 hours	184±5
Sr001-b	Coprecipitation	$SrFeO_3$	900; 2.5 hours	157±5
Sr002-a	Coprecipitation	$SrFeO_3$	900; 1.5 hours	142±5
Zn001	Coprecipitation	$ZnFe_2O_4$ + ZnO	900°C; 5 hours	/
Zn002	Coprecipitation	$ZnFe_2O_4$	900°C; 5 hours	123±7
I-Zn001	Hydrothermal	$ZnFe_2O_4$	100°C; 24 hours	5±0.1
I-Zn002	Hydrothermal	$ZnFe_2O_4$	75°C; 24 hours	4±1
I-Zn003-4	Hydrothermal	$ZnFe_2O_4$	75°C; 4 hours	4±1

Table 7.1 – *Summary of synthesised and analysed samples*

References

1. N. N. Greenwood and A. Earnshaw, *Chemistry of the Elements, 2nd Ed.*, Pergamon Press, India, 1998.
2. F. A. Cotton and G. Wilkinson, *Advanced Inorganic Chemistry, 5th Ed.*, John Wiley & Sons, New York, 1988.
3. P. A. Cox, *Transition Metal Oxides : Introduction to their Electronic Structure and Properties*, Oxford University Press, Oxford, U.K., 1995.
4. A. F. Holleman and E. Wieberg, *Lehrbuch der Anorganischen Chemie, 101th Ed.*, Walter de Gruyter, New York, 1995.
5. C. N. R. Rao and B. Raveau, *Transition Metal Oxides: Structure, Properties and Synthesis of Ceramic Oxides*, Wiley VCH, Weinheim, 2009.
6. J. Beretka, *Proc. Roy. Aust. Chem. Inst.*, 1970, **37**, 152-155.
7. R. Tilley, *Understanding Solids - The Science of Materials*, J. Wiley & Sons, Chichester, West Sussex, England, 2004.
8. C. McCammon, *Phase Transitions*, 1996, **58**, 1-26.
9. J. P. Jolivet, C. Chaneac, P. Prene, L. Vayssieres and E. Tronc, *J. Phys. IV*, 1997, **7**, C1/573-C571/576.
10. R. G. Kulkarni, *Asian J. Phys.*, 1997, **6**, 204-211.
11. J. P. Jolivet, E. Tronc and C. Chaneac, *Eur. Phys. J.: Appl. Phys.*, 2000, **10**, 167-172.
12. G. R. Lumpkin, *Prog. Nucl. Energy*, 2001, **38**, 447-454.
13. J.-P. Jolivet, E. Tronc and C. Chaneac, *C. R. Chim.*, 2002, **5**, 659-664.
14. A. Weidenkaff, *Adv. Eng. Mater.*, 2004, **6**, 709-714.
15. W. Prellier, M. P. Singh and P. Murugavel, *J. Phys.: Condens. Matter*, 2005, **17**, R803-R832.
16. V. A. M. Brabers, *Handbook of Magnetism and Advanced Magnetic Materials - Ferrimagnetic Insulators (Conference Proceedings)*, John Wiley & Sons Ltd., New York, U.S.A., 2007.
17. N. Varalaxmi and K. V. Sivakumar, *J. Mater. Sci.: Mater. Electron.*, 2011, **22**, 555-560.
18. J. Sun, Z. Wang, Y. Wang, Y. Zhu, T. Shen, L. Pang, K. Wei and F. Li, *Mat. Sci. Eng. B*, 2012, **177**, 269-273.
19. A. Bieńkowski and R. Szewczyk, *Sensor Actuat. A-Phys.*, 2004, **113**, 270-276.
20. V. S. Coker, N. D. Telling, G. van der Laan, R. A. D. Pattrick, C. I. Pearce, E. Arenholz, F. Tuna, R. E. P. Winpenny and J. R. Lloyd, *ACS Nano*, 2009, **3**, 1922-1928.
21. G.-Y. Zhang, Y.-Q. Sun, D.-Z. Gao and Y.-Y. Xu, *Mater. Res. Bull.*, 2010, **45**, 755-760.
22. C. Nordhei, A. L. Ramstad and D. G. Nicholson, *Phys. Chem. Chem. Phys.*, 2008, **10**, 1053-1066.
23. A. C. F. M. Costa, E. Tortella, M. R. Morelli and R. H. G. A. Kiminami, *J. Magn. Magn. Mater.*, 2003, **256**, 174-182.
24. A. Verma, T. C. Goel, R. G. Mendiratta and M. I. Alam, *Mat. Sci. Eng. B*, 1999, **60**, 156-162.
25. X. Wang, L. Wang, I. I. S. Lim, K. Bao, D. Mott, H.-Y. Park, J. Luo, S. Hao and C.-J. Zhong, *J. Nanosci. Nanotechnol.*, 2009, **9**, 3005-3012.
26. A. Franco Júnior and F. C. Silva, *Appl. Phys. Lett.*, 2010, **96**, 172505.
27. K. E. Mooney, J. A. Nelson and M. J. Wagner, *Chem. Mater.*, 2004, **16**, 3155-3161.
28. L. Horng, G. Chern, M. C. Chen, P. C. Kang and D. S. Lee, *J. Magn. Magn. Mater.*, 2004, **270**, 389-396.
29. A. Franco Júnior, E. Celma de Oliveira Lima, M. A. Novak and P. R. Wells Jr, *J. Magn. Magn. Mater.*, 2007, **308**, 198-202.
30. I. H. Gul and A. Maqsood, *J. Alloy. Compd.*, 2008, **465**, 227-231.
31. A. H. Latham and M. E. Williams, *Acc. Chem. Res.*, 2008, **41**, 411-420.
32. T. Dai Lam, L. Van Hong, P. Hoai Linh, H. Thi My Nhung, N. Thi Quy, L. Thien Tai, H. Phuong Thu and N. Xuan Phuc, *Adv. Nat. Sci.: Nanosci. Nanotechnol.*, 2010, **1**, 045013.
33. U. S. Penades, M. I. Garcia and P. J. Gallo, WO2011036191A2, 2011.
34. E. A. Schultz-Sikma, H. M. Joshi, Q. Ma, K. W. MacRenaris, A. L. Eckermann, V. P. Dravid and T. J. Meade, *Chem. Mater.*, 2011, **23**, 2657-2664.
35. L. Menini, M. C. Pereira, L. A. Parreira, J. D. Fabris and E. V. Gusevskaya, *J. Catal.*, 2008, **254**, 355-364.
36. J. R. Scheffe, J. Li and A. W. Weimer, *Int. J. Hydrogen Energ.*, 2010, **35**, 3333-3340.
37. M. Sahibzada, D. Mantzavinos, A. Hartley, W. Morton and I. S. Metcalfe, *Chem. Eng. Res. Des.*, 2000, **78**, 965-970.
38. M. Mori, Y. Hiei and T. Yamamoto, *J. Am. Ceram. Soc.*, 2001, **84**, 781-786.
39. Y. I. Kim, D. Kim and C. S. Lee, *Physica B*, 2003, **337**, 42-51.
40. S. Lorentzou, A. Zygogianni, K. Tousimi, C. Agrafiotis and A. G. Konstandopoulos, *J. Alloy. Compd.*, 2009, **483**, 302-305.
41. H. Yang, J. Yan, Z. Lu, X. Cheng and Y. Tang, *J. Alloy. Compd.*, 2009, **476**, 715-719.
42. M. Niederberger and N. Pinna, *Metal Oxide Nanoparticles in Organic Solvents - Synthesis, Formation, Assembly and Applications*, Springer, New York, 2009.
43. M. Gotic, S. Music, M. Ivanda, M. Soufek and S. Popovic, *J. Mol. Struct.*, 2005, **744-747**, 535-540.

44. G. Taglieri, M. Tersigni, P. L. Villa and C. Mondelli, *Int. J. Inorg. Mater.*, 1999, **1**, 103-110.
45. C. B. Carter and M. G. Norton, *Ceramic Materials - Science and Engineering*, Springer, New York, 2007.
46. X. Zhu, Z. Liu and N. Ming, *J. Mater. Chem.*, 2010, **20**, 4015-4030.
47. A. I. Rykov, Y. T. Pavlukhin and Y. Y. Medikov, *Proc. Indian Acad. Sci. A*, 1989, **55**, 721-731.
48. V. C. B. Pegoretti, P. R. C. Couceiro, C. M. Goncalves, M. d. F. F. Lelis and J. D. Fabris, *J. Alloy. Compd.*, 2010, **505**, 125-129.
49. A. Z. Simoes, F. G. Garcia and C. d. S. Riccardi, *Mater. Chem. Phys.*, 2009, **116**, 305-309.
50. L. Malavasi, C. A. J. Fisher and M. S. Islam, *Chem. Soc. Rev.*, 2010, **39**, 4370-4387.
51. A. M. Gismelseed, K. A. Mohammed, H. M. Widtallah, A. D. Al-Rawas, M. E. Elzain and A. A. Yousif, *J. Phys. Conf. Ser.*, 2010, **217**, 012138.
52. K. P. Thummer, M. C. Chantbar, K. B. Modi, G. J. Baldha and H. H. Joshi, *J. Magn. Magn. Mater.*, 2004, **280**.
53. I. P. Parkin, G. Elwin, M. V. Kuznetsov, Q. A. Pankhurst, Q. T. Bui, G. D. Forster, L. F. Barquìn, K. A.V. and M. Y.G., *J. Mater. Process. Tecnol.*, 2001, **110**, 239-243.
54. R. H. Mitchell, *Perovskites Modern and Ancient*, Almaz Press, Thunder Bay, Canada, 2002.
55. P. Batti, *Caramurgia, Colloquio Nazionale sugli Ossidi Ferrimagnetici Esagonali (Anno VI)*, Parma, 19-20 Giugno, 1975.
56. P. Adler, *J. Solid State Chem.*, 1997, **130**, 129-139.
57. D. S. Mathew and R.-S. Juang, *Chem. Eng. J.*, 2007, **129**, 51-65.
58. J.-C. Lee, D. Caruntu, J.-H. Lee, J.-J. Kim, B. Cushing, V. Golub, S.-H. Cho and C. J. O'Connor, *Funct. Mater.*, 2006, **13**, 447-456.
59. D. Carta, M. F. Casula, A. Falqui, D. Loche, G. Mountjoy, C. Sangregorio and A. Corrias, *J. Phys. Chem. C*, 2009, **113**, 8606-8615.
60. R. C. Kambale, P. A. Shaikh, N. S. Harale, V. A. Bilur, Y. D. Kolekar, C. H. Bhosale and K. Y. Rajpure, *J. Alloy. Compd.*, 2010, **490**, 568-571.
61. J. Wu, N. Li, J. Xu, Y. Jiang, Z.-G. Ye, Z. Xie and L. Zheng, *Appl. Phys. Lett.*, 2011, **99**, 202505-202503.
62. S. Darshane and I. S. Mulla, *Mater. Chem. Phys.*, 2010, **119**, 319-323.
63. I.-B. Kim, M. H. Han, R. L. Phillips, B. Samanta, V. M. Rotello, Z. J. Zhang and U. H. F. Bunz, *Chem. Eur. J.*, 2009, **15**, 449-456.
64. H.-M. Fan, J.-B. Yi, Y. Yang, K.-W. Kho, H.-R. Tan, Z.-X. Shen, J. Ding, X.-W. Sun, M. C. Olivo and Y.-P. Feng, *ACS Nano*, 2009, **3**, 2798-2808.
65. P. Di Barba, F. Dughiero and S. E., *Proceedings of Hes-10 - Heating by Electromagnetic Sources*, Padova, 2010.
66. A. Kovalevsky, V. Kharton, E. Naumovich, F. Marques and J. Frade, *NATO Science Series, II: Mathematics, Physics and Chemistry*, 2004, **123**, 109-122.
67. V. Thangadurai, P. Schmid-Beurmann and W. Weppner, *Mater. Res. Bull.*, 2002, **37**, 599-604.
68. M. V. Patrakeev, I. A. Leonidov, V. L. Kozhevnikov and V. V. Kharton, *Solid State Sci.*, 2004, **6**, 907-913.
69. V. V. Kharton, A. A. Yaremchenko, A. L. Shaula, A. P. Viskup, F. M. B. Marques, J. R. Frade, E. N. Naumovich, J. R. Casanova and I. P. Marozau, *Defect Diffus. Forum*, 2004, **226-228**, 141-159.
70. A. V. Berenov, J. L. MacManus-Driscoll and J. A. Kilner, *Int. J. Inorg. Mater.*, 2001, **3**, 1109-1111.
71. Y. Yang, Y. Jiang, Y. Wang and Y. Sun, *J. Mol. Catal. A: Chem.*, 2007, **270**, 56-60.
72. F. de Lira, M. de Souza Farias, A. de Figueiredo, F. dos Santos Gil, M. dos Santos, B. Malheiros, J. Ferreira, J. Pinheiro, O. Treu-Filho and R. Kondo, *J. Mol. Model.*, 2011, **17**, 1621-1624.
73. T. Tian, M. Zhan, W. Wang and C. Chen, *Catal. Commun.*, 2009, **10**, 513-517.
74. S. Furfori, N. Russo, D. Fino, G. Saracco and V. Specchia, *Chem. Eng. Sci.*, 2010, **65**, 120-127.
75. K. Chandra, S. Singhal and S. Goyal, *Hyperfine Interact.*, 2008, **183**, 75-80.
76. S. B. Han, T. B. Kang, O. S. Joo and K. D. Jung, *Sol. Energy*, 2007, **81**, 623-628.
77. H. Hirazawa, S. Kusamoto, H. Aono, T. Naohara, K. Mori, Y. Hattori, T. Maehara and Y. Watanabe, *J. Alloy. Compd.*, 2008, **461**, 467-473.
78. K. Lazar, T. Mathew, Z. Koppany, J. Megyeri, V. Samuel, S. P. Mirajkar, B. S. Rao and L. Guczi, *Phys. Chem. Chem. Phys.*, 2002, **4**, 3530-3536.
79. L. Nalbandian, A. Evdou and V. Zaspalis, *Int. J. Hydrogen Energ.*, 2009, **34**, 7162-7172.
80. N. Rezlescu, C. Doroftei and P. D. Popa, *Rom. J. Phys.*, 2007, **52**, 353-360.
81. S. M. Antao, I. Hassan and J. B. Parise, *Am. Min.*, 2005, **90**, 219-228.
82. H. G. Kim, P. H. Borse, J. S. Jang, E. D. Jeong, O.-S. Jung, Y. J. Suh and J. S. Lee, *Chem. Commun.*, 2009, 5889-5891.
83. R. Dom, R. Subasri, K. Radha and P. H. Borse, *Solid State Commun.*, 2011, **151**, 470-473.
84. L. Zhang, Y. He, Y. Wu and T. Wu, *Mat. Sci. Eng. B*, 2011, **176**, 1497-1504.
85. N. Russo, D. Fino, G. Saracco and V. Specchia, *Catal. Today*, 2007, **119**, 228-232.
86. C.-J. Jia, Y. Liu, M. Schwickardi, C. Weidenthaler, B. Spliethoff, W. Schmidt and F. Schüth, *Appl. Catal. A-Gen.*, 2010, **386**, 94-100.
87. M. Jeun, S. Bae, A. Tomitaka, Y. Takemura, K. H. Park, S. H. Paek and K.-W. Chung, *Appl. Phys. Lett.*, 2009, **95**, 082501/082501-082501/082503.

88. F. G. Duran, B. P. Barbero, L. E. Cadus, C. Rojas, M. A. Centeno and J. A. Odriozola, *Appl. Catal. B-Environ.*, 2009, **92**, 194-201.
89. I. D. Lick and D. B. Soria, *J. Argent. Chem. Soc.*, 2009, **97**, 102-108.
90. J. Sfeir, S. Vaucher, P. Holtappels, U. Vogt, H. J. Schindler, J. Van herle, E. Suvorova, P. Buffat, D. Perret, N. Xanthopoulos and O. Bucheli, *J. Eur. Ceram. Soc.*, 2005, **25**, 1991-1995.
91. E. Banks, E. Kostiner and G. K. Wertheim, *J. Chem. Phys.*, 1966, **45**, 1189-1191.
92. S. Geller, R. W. Grant, J. A. Cape and G. P. Espinosa, *J. Appl. Phys.*, 1967, **38**, 1457-1458.
93. G. Huo, Z. Gu and M. Qiu, *J. Alloy. Compd.*, 2004, **381**, 317-319.
94. D. Seifu, A. Kebede, F. W. Oliver, E. Hoffman, E. Hammond, C. Wynter, A. Aning, L. Takacs, I. L. Siu, J. C. Walker, G. Tessema and M. S. Seehra, *J. Magn. Magn. Mater.*, 2000, **212**, 178-182.
95. A. Lambert, EP2246305A1, 2010.
96. S. K. Kulshreshtha, S. Sharma, R. Vijayalakshmi and R. Sasikala, *Indian J. Chem. Technol.*, 2004, **11**, 427-433.
97. M. Inoue, N. Hasegawa, R. Uehara, N. Gokon, H. Kaneko and Y. Tamaura, *Sol. Energy*, 2004, **76**, 309-315.
98. M. Florea, M. Alifanti, V. I. Parvulescu, D. Mihaila-Tarabasanu, L. Diamandescu, M. Feder, C. Negrila and L. Frunza, *Catal. Today*, 2009, **141**, 361-366.
99. J. Hu, Lo and G. Chen, *Langmuir*, 2005, **21**, 11173-11179.
100. H. Lee, J. C. Jung, H. Kim, Y.-M. Chung, T. J. Kim, S. J. Lee, S.-H. Oh, Y. S. Kim and I. K. Song, *Catal. Lett.*, 2008, **124**, 364-368.
101. Y. H. Hou, Y. J. Zhao, Z. W. Liu, H. Y. Yu, X. C. Zhong, W. Q. Qiu, D. C. Zeng and L. S. Wen, *J. Phys. D Appl. Phys.*, 2010, **43**, 445003.
102. M. D. Allendorf, R. B. Diver, N. P. Siegel and J. E. Miller, *Energ. Fuel.*, 2008, **22**, 4115-4124.
103. R. S. Gaikwad, S.-Y. Chae, R. S. Mane, S.-H. Han and O.-S. Joo, *Int. J. Electrochem.*, 2011, 729141, 729146 pp.
104. P. P. Hankare, U. B. Sankpal, R. P. Patil, P. D. Lokhande and R. Sasikala, *Mat. Sci. Eng. B*, 2011, **176**, 103-109.
105. N. Li, M. Zheng, X. Chang, G. Ji, H. Lu, L. Xue, L. Pan and J. Cao, *J. Solid State Chem.*, 2011, **184**, 953-958.
106. J. Tong, L. Bo, Z. Li, Z. Lei and C. Xia, *J. Mol. Catal. A: Chem.*, 2009, **307**, 58-63.
107. K. K. Senapati, C. Borgohain, K. C. Sarma and P. Phukan, *J. Mol. Catal. A-Chem.*, 2011, **346**, 111-116.
108. R. W. McCallum, K. W. Dennis, D. C. Jiles, J. E. Snyder and Y. H. Chen, *Low Temp. Phys.*, 2001, **27**, 266-274.
109. N. Frickel, M. Gottlieb and A. M. Schmidt, *Polymer*, 2011, **52**, 1781-1787.
110. H. A. K. M. Akther, M. Seki, T. Kawai and H. Tabata, *J. Appl. Phys.*, 2004, **96**, 1273-1275.
111. A. M. Kumar, M. C. Varma, C. L. Dube, K. H. Rao and S. C. Kashyap, *J. Magn. Magn. Mater.*, 2008, **320**, 1995-2000.
112. K. K. Bharathi, K. Balamurugan, P. N. Santhosh, M. Pattabiraman and G. Markandeyulu, *Phys. Rev. B*, 2008, **77**, 172401.
113. A. S. Albuquerque, J. D. Ardisson, W. A. A. Macedo, J. L. López, R. Paniago and A. I. C. Persiano, *J. Magn. Magn. Mater.*, 2001, **226–230, Part 2**, 1379-1381.
114. A. B. Nawale, N. S. Kanhe, K. R. Patil, S. V. Bhoraskar, V. L. Mathe and A. K. Das, *J. Alloy. Compd.*, 2011, **509**, 4404-4413.
115. M. H. Sousa, E. Hasmonay, J. Depeyrot, F. A. Tourinho, J. C. Bacri, E. Dubois, R. Perzynski and Y. L. Raikher, *J. Magn. Magn. Mater.*, 2002, **242–245, Part 1**, 572-574.
116. M. Foerster, J. M. Rebled, S. Estrade, F. Sanchez, F. Peiro and J. Fontcuberta, *Phys. Rev. B: Condens. Matter Mater. Phys.*, 2011, **84**, 144422/144421-144422/144427.
117. T. Giannakopoulou, L. Kompotiatis, A. Kontogeorgakos and G. Kordas, *J. Magn. Magn. Mater.*, 2002, **246**, 360-365.
118. C. V. Gopal Reddy, S. V. Manorama and V. J. Rao, *Sensor Actuat. B-Chem.*, 1999, **55**, 90-95.
119. A. Urda, A. Herraiz, A. Redey and I.-C. Marcu, *Catal. Commun.*, 2009, **10**, 1651-1655.
120. S. Xu, W. Shangguan, J. Yuan, M. Chen and J. Shi, *Appl. Catal. B-Environ.*, 2007, **71**, 177-184.
121. R. Venkatasubramanian, R. S. Srivastava and R. D. K. Misra, *Mat. Sci. Tech.*, 2008, **24**, 589-595.
122. S. Feng, W. Yang and Z. Wang, *Mat. Sci. Eng. B*, 2011, **176**, 1509-1512.
123. M. R. Phadatare, V. M. Khot, A. B. Salunkhe, N. D. Thorat and S. H. Pawar, *J. Magn. Magn. Mater.*, 2012, **324**, 770-772.
124. S. Rana, A. Gallo, R. S. Srivastava and R. D. K. Misra, *Acta Biomater.*, 2007, **3**, 233-242.
125. B. K. Sunkara and R. D. K. Misra, *Acta Biomater.*, 2008, **4**, 273-283.
126. H. Yin, H. P. Too and G. M. Chow, *Biomaterials*, 2005, **26**, 5818-5826.
127. A. Bardhan, C. K. Ghosh, M. K. Mitra, G. C. Das, S. Mukherjee and K. K. Chattopadhyay, *Solid State Sci.*, 2010, **12**, 839-844.
128. D. Sibera, J. Kaszewski, D. Moszynski, E. Borowiak-Palen, W. Lojkowski and U. Narkiewicz, *Phys. Status Solidi C*, 2010, **7**, 1420-1423.
129. G. Fan, Z. Gu, L. Yang and F. Li, *Chem. Eng. J.*, 2009, **155**, 534-541.

130. J. S. Jang, S. J. Hong, J. S. Lee, P. H. Borse, O.-S. Jung, T. E. Hong, E. D. Jeong, M. S. Won and H. G. Kim, *J. Korean Phys. Soc.*, 2009, **54**, 204-208.
131. A. A. Tahir and K. G. U. Wijayantha, *J. Photochem. Photobiol., A*, 2010, **216**, 119-125.
132. M. W. Schmidt, *Phase formation and structural transformation of strontium ferrite SrFeO3-x*, Australian National University - Ph.D. Thesis, Canberra, Australia, 2001.
133. C. Solis, M. D. Rossell, G. Garcia, A. Figueras, T. G. Van and J. Santiso, *Solid State Ionics*, 2008, **179**, 1996-1999.
134. V. Thangadurai and W. Weppner, *Ionics*, 2002, **8**, 360-371.
135. S. Gangopadhayay, T. Inerbaev, A. m. E. Masunov, D. Altilio and N. Orlovskaya, *ACS Appl. Mater. Interfaces*, 2009, **1**, 1512-1519.
136. A. Evdou, V. Zaspalis and L. Nalbandian, *Fuel*, 2010, **89**, 1265-1273.
137. Q. Wang, Z. Chen, Y. Chen, N. Cheng and Q. Hui, *Ind. Eng. Chem. Res.*, Ahead of Print.
138. M. L. Post, J. J. Tunney, D. Yang, X. Du and D. L. Singleton, *Sensor Actuat. B-Chem.*, 1999, **B59**, 190-194.
139. Y. M. Zhao and P. F. Zhou, *J. Magn. Magn. Mater.*, 2004, **281**, 214-220.
140. D.-Y. Kim, J. S. Kim, B. H. Park, J.-K. Lee, S.-Y. Maeng and S.-J. Yoon, *Integr. Ferroelectr.*, 2004, **67**, 25-30.
141. U. Schubert and N. Hüsing, *Synthesis of inorganic materials, 2nd Ed.*, Wiley-VCH, Weinheim, 2005.
142. D. Braga and F. Grepioni, *Angew. Chem., Int. Ed.*, 2004, **43**, 4002-4011.
143. M. Sorescu, T. Xu, J. D. Burnett and J. A. Aitken, *J. Mater. Sci.*, 2011, **46**, 6709-6717.
144. V. G. Harris, D. J. Fatemi, J. O. Cross, E. E. Carpenter, V. M. Browning, J. P. Kirkland, A. Mohan and G. J. Long, *J. Appl. Phys.*, 2003, **94**, 496-501.
145. T. F. Marinca, I. Chicinas, O. Isnard, V. Pop and F. Popa, *J. Alloy. Compd.*, 2011, **509**, 7931-7936.
146. T. Sritharan, F. Y. C. Boey and A. Srinivas, *J. Mater. Process. Technol*, 2007, **192-193**, 255-258.
147. O. N. C. Uwakweh, R. Mas, C. Morales, P. Vargas, J. Silva, A. Rosa, N. Lopez, R. P. Moyet and Y. Cardona, *J. Mater. Eng. Perform.*, 2011, **20**, 1157-1162.
148. D. Chen and H.-y. Liu, *Mater. Lett.*, 2012, **72**, 95-97.
149. Z. Z. Lazarevic, C. Jovalekic, A. Recnik, V. N. Ivanovski, M. Mitric, M. J. Romcevic, N. Paunovic, B. D. Cekic and N. Z. Romcevic, *J. Alloy. Compd.*, 2011, **509**, 9977-9985.
150. E. Manova, T. Tsoncheva, D. Paneva, M. Popova, N. Velinov, B. Kunev, K. Tenchev and I. Mitov, *J. Solid State Chem.*, 2011, **184**, 1153-1158.
151. R. Sani, A. Beitollahi, Y. V. Maksimov and I. P. Suzdalev, *J. Mater. Sci.*, 2007, **42**, 2126-2131.
152. D. Briggs and M. P. Seah, *Practical Surface Analysis - Volume 1 - Auger and X-ray Photoelectron Spectroscopy, 2nd Ed.*, John Wiley & Sons, New York, 1990.
153. Z. G. Wang, X. T. Zu, S. Zhu and L. M. Wang, *Phys. E.*, 2006, **35**, 199-202.
154. J. F. Moulder, W. F. Stickle, P. E. Sobol and K. D. Bomben, *Handbook of X-Ray Photoelectron Spectroscopy*, Perkin-Elmer Corp., Eden Prarie, Minnesota, 1992.
155. L. Pauling and M. D. Shappel, *Z. Kristallogr. Krist.*, 1930, **75**, 128-142.
156. *COD - Crystallography Open Database,* http://www.crystallography.net/.
157. R. W. G. Wychoff, *Structure of Crystals*, The Chemical Catalogue Company INC, New York, 1931.
158. R. K. Bryan, M. Bansal, W. Folkhard, C. Nave and D. A. Marvin, *Proc. Natl. Acad. Sci. USA*, 1983, **80**, 4728-4731.
159. *NIST XPS Database - Version 3.5*.
160. D. A. Shirley, *Phys. Rev. B*, 1972, **5**, 4709-4713.
161. E. Kang, J. Park, Y. Hwang, M. Kang, J. G. Park and T. Hyeon, *J. Phys. Chem. B*, 2004, **108**, 13932-13935.
162. T. Hyeon, S. S. Lee, J. Park, Y. Chung and H. Bin Na, *J. Am. Chem. Soc.*, 2001, **123**, 12798-12801.
163. G. Schemer, E. Tirosh, T. Livneh and M. G., *J. Phys. Chem. C*, 2007, **111**, 14334-14338.
164. X. L. Jiao, T. He, H. Y. Wang and W. Jiang, *J. Phys. Chem. C*, 2008, **112**, 911-917.
165. N. Z. Bao, L. M. Shen, Y. H. Wang, P. Padhan and A. Gupta, *J. Am. Chem. Soc.*, 2007, **129**, 12374-12375.
166. N. R. Jana, Y. F. Chen and X. G. Peng, *Chem. Mater.*, 2004, **16**, 3931-3935.
167. Q. Song and Z. J. Zhang, *J. Am. Chem. Soc.*, 2004, **126**, 6164-6168.
168. A. Yan, X. Liu, R. Shi, N. Zhang, R. Yi, Y. Li, G. Gao and G. Qiu, *Solid State Commun.*, 2008, **146**, 483-486.
169. D. R. Modeshia and R. I. Walton, *Chem. Soc. Rev.*, 2010, **39**, 4303-4325.
170. W. H. Lin and C. S. Hwang, *J. Mater. Sci.*, 2002, **37**, 1067-1075.
171. X. L. Jiao, D. Chen and Y. Hu, *Mater. Res. Bull.*, 2002, **37**, 1583-1588.
172. N. Pinna, S. Grancharov, P. Beato, P. Bonville, M. Antonietti and M. Niederberger, *Chem. Mater.*, 2005, **17**, 3044-3049.
173. S. Yáñez-Vilar, M. Sánchez-Andújar, C. Gómez-Aguirre, J. Mira, M. A. Señarís-Rodríguez and S. Castro-García, *J. Solid State Chem.*, 2009, **182**, 2685-2690.
174. L. Sichu, L. Limin, V. T. John, C. J. O'Connor and V. G. Harris, *IEEE T. Magn.*, 2001, **37**, 2350-2352.
175. F. Grasset, N. Labhsetwar, D. Li, D. C. Park, N. Saito, H. Haneda, O. Cador, T. Roisnel, S. Mornet, E. Duguet, J. Portier and J. Etourneau, *Langmuir*, 2002, **18**, 8209-8216.

176. S. Sun, H. Zeng, D. B. Robinson, S. Raoux, P. M. Rice, S. X. Wang and G. Li, *J. Am. Chem. Soc.*, 2004, **126**, 273-279.
177. V. L. Calero-DdelC and C. Rinaldi, *J. Magn. Magn. Mater.*, 2007, **314**, 60-67.
178. C. Feldmann, *Polyol-vermittelte Darstellung nanoskaliger Festkörper und multinärer Bismutiodide*, Rhenisch-Westfälischen Technischen Hochschule - Habilitation Thesis, Aachen, Germany, 2002.
179. M. Pal and D. Chakravorty, *Sadhana*, 2003, **28**, 283-297.
180. J. H. Wu, S. P. Ko, H. L. Liu, S. Kim, J. S. Ju and K. Y. Kim, *Mater. Lett.*, 2007, **61**, 3124-3129.
181. S. Zhang, H. Niu, Y. Cai, X. Zhao and Y. Shi, *Chem. Eng. J.*, 2010, **158**, 599-607.
182. B. Nair, *Int. J. Toxicol.*, 2001, **20**, 23-50.
183. C. O. Kappe, D. Dallinger and S. S. Murphree, *Practical Microwave Synthesis for Organic Chemists - Strategies, Instruments, and Protocols*, Wiley-VCH, Weinheim, 2009.
184. I. Bilecka and M. Niederberger, *Nanoscale*, 2010, **2**, 1358-1374.
185. M. Niederberger, *Acc. Chem. Res.*, 2007, **40**, 793-800.
186. M. Niederberger and G. Garnweitner, *Chem. Eur. J.*, 2006, **12**, 7282-7302.
187. S. Mascotto, O. Tsetsgee, K. Müller, C. Maccato, B. Smarsly, D. Brandhuber, E. Tondello and S. Gross, *J. Mater. Chem.*, 2007, **17**, 4387-4399.
188. M. Kubli, L. Luo, I. Bilecka and M. Niederberger, *Chimia*, 2010, **64**, 170-172.
189. L. L. Hench and J. K. West, *Chem. Rev.*, 1990, **90**, 33-72.
190. C. Brinker and G. Scherer, *Sol-Gel Science: The Physics and Chemistry of Sol-Gel Processing*, Academic Press, New York, U.S.A., 1990.
191. C. J. Brinker, Y. Lu, A. Sellinger and H. Fan, *Adv. Mater.*, 1999, **11**, 579-585.
192. G. Roussy and J. A. Pearce, *Foundations and Industrial Applications of Microwaves and Radio Frequency Fields. Physical and Chemical Processes*, J. Wiley & Sons, Chichester, 1995.
193. B. Ondruschka and W. Bonrath, *Chimia*, 2006, **60**, 326-329.
194. C. O. Kappe, *Angew. Chem. Int. Edit.*, 2004, **43**, 6250-6284.
195. L. Perreux and A. Loupy, *Tetrahedron*, 2001, **57**, 9199.
196. L. Perreux and A. Loupy, *Microwaves in Organic Synthesis, 2nd Ed.*, Wiley-VCH, Weinheim, 2006.
197. A. de la Hoz, A. Diaz-Ortiz and A. Moreno, *Chem. Soc. Rev.*, 2005, **34**, 164-178.
198. M. Hosseini, N. Stiasni, V. Barbieri and C. O. Kappe, *J. Org. Chem.*, 2007, **72**, 1417.
199. M. A. Herrero, J. M. Kremsner and C. O. Kappe, *J. Org. Chem.*, 2008, **73**, 36.
200. D. Obermayer, B. Gutmann and C. O. Kappe, *Angew. Chem. Int. Edit.*, 2009, **48**, 8321-8324.
201. D. R. Lide, *CRC Handbook of Chemistry and Physics, 89th Ed. (Internet Version)*, CRC Press/Taylor and Francis, Boca Raton, 2009.
202. G. A. Tompsett, B. Panzarella, W. C. Conner, K. S. Yngvesson, F. Lu, S. L. Suib, K. W. Jones and S. Bennett, *Review of Scientific Instruments*, 2006, **77**, 124101-124110.
203. F. Khairallah, *Magnesium oxide-based nanoscale systems: synthesis, characterization and reactivity study*, Università degli Studi di Padova, Dip. di Scienze Chimiche - Ph.D. Thesis, Padova, 2005.
204. Z. Zhu, X. Li, Q. Zhao, Y. Shi, H. Li and G. Chen, *J. Nanopart. Res.*, 2011, **13**, 2147-2155.
205. A. Gadkari, T. Shinde and P. Vasambekar, *J. Mater. Sci. - Mater. El.*, 2010, **21**, 96-103.
206. S. A. Kanade and V. Puri, *J. Alloy. Compd.*, 2009, **475**, 352-355.
207. T. Shinde, A. Gadkari and P. Vasambekar, *J. Mater. Sci. - Mater. El.*, 2010, **21**, 120-124.
208. D. N. Bhosale, V. M. S. Verenkar, K. S. Rane, P. P. Bakare and S. R. Sawant, *Mater. Chem. Phys.*, 1999, **59**, 57-62.
209. J. Yang, S. Mei and J. M. F. Ferreira, *J. Am. Ceram. Soc.*, 2001, **84**, 1696-1702.
210. G. Demazeau, *J. Mater. Sci.*, 2008, **43**, 2104-2114.
211. H. Hayashi and Y. Hakuta, *Materials*, 2010, **3**, 3794-3817.
212. *Parr Instrument Company*.
213. K. Byrappa and M. Yoshimura, *Handbook of Hydrothermal Technology*, Noyes Publications, Park Ridge, New Jersey, U.S.A, 2001.
214. M. S. Whittingham, J.-D. Guo, R. Chen, T. Chirayil, G. Janauer and P. Zavalij, *Solid State Ionics*, 1995, **75**, 257-268.
215. S. Somiya and R. Roy, *Bull. Mater. Sci.*, 2000, **23**, 453-460.
216. J. Livage, *Materials*, 2010, **3**, 4175-4195.
217. L. Dem'yanets, L. Li and T. Uvarova, *J. Mater. Sci.*, 2006, **41**, 1439-1444.
218. Y. Jin, C. An, K. Tang, L. Huang and G. Shen, *Mater. Lett.*, 2003, **57**, 4267-4270.
219. A. Holden and P. Singer, *Crystals and Crystal Growing*, Anchor Books Doubleday & Company Inc., Garden City, New York, 1971.
220. X. Chen, H. Fan and L. Liu, *J. Cryst. Growth*, 2005, **284**, 434-439.
221. I. MacLaren and C. B. Ponton, *J. Eur. Ceram. Soc.*, 2000, **20**, 1267-1275.
222. Y. Zhang, Y. Liu, C.-L. Fei, Z. Yang, Z.-H. Lu, R. Xiong, D. Yin and J. Shi, *J. Appl. Phys.*, 2010, **108**, 084312/084311-084312/084316.

223. L. Zhao, H. Zhang, Y. Xing, S. Song, S. Yu, W. Shi, X. Guo, J. Yang, Y. Lei and F. Cao, *J. Solid State Chem.*, 2008, **181**, 245-252.
224. L. Chen, Y. Shen and J. Bai, *Mater. Lett.*, 2009, **63**, 1099-1101.
225. G.-H. Ren and Z.-S. Yu, *Diffus. De. B*, 2012, **181-182**, 393-396.
226. D. Broadbent, D. Dollimore and J. Dollimore, *J. Chem. Soc. A*, 1966, 278-281.
227. D. Broadbent, D. Dollimore and J. Dollimore, *J. Chem. Soc. A*, 1967, 451-454.
228. D. Dollimore, D. L. Griffiths and D. Nicholson, *J. Chem. Soc.*, 1963, 2617-2623.
229. D. Dollimore and D. Nicholson, *J. Chem. Soc. A*, 1966, 281-284.
230. D. Dollimore and D. Nicholson, *J. Chem. Soc.*, 1962, 960-965.
231. H. P. Klug and L. E. Alexander, *X-Ray Diffraction Procedures for Polycrystalline and Amorphous Materials*, J. Wiley & Sons, New York, 1954.
232. G. Ceccone, P. Marmorato, J. Ponti, F. Rossi, B. Kaulich, A. Gianocelli, L. Pascolo, M. Salome and M. Kiskinova, *Synchrotron radiation X-ray fluorescence mapping of cobalt ferrite nanoparticles in Balb/3T3 fibroblast cells*, Pacifichem 2010 - International Chemical Congress of Pacific Basin Societies, Honolulu, U.S.A., 2010.
233. W. Dabrowski, J. Fink, T. Fiutowski, H. G. Krane and P. Wiacek, *J. Inst.*, 2012, **7**, P03002/03001-P03002/03021.
234. N. Stroeters, A. Diefenbach and M. A. Benenuto, *Energy dispersive X-ray fluorescence (EDXRF) of a series of copper-based coins of the Kushan emperor Kujula Kadphises*, American Chemical Society, 2012.
235. G. C. Allen and K. R. Hallam, *Appl. Surf. Sci.*, 1996, **93**, 25-30.
236. Z. Zhou, Y. Zhang, Z. Wang, W. Wei, W. Tang, J. Shi and R. Xiong, *Appl. Surf. Sci.*, 2008, **254**, 6972-6975.
237. S. Diodati, *Ferriti di Stronzio Nanostrutturate - Sintesi e Caratterizzazione*, Università degli Studi di Padova, Dip. di Scienze Chimiche, Master Thesis, Padova, 2009.
238. S. Diodati, L. Nodari, M. M. Natile, U. Russo, E. Tondello, L. Lutterotti and S. Gross, *Dalton Trans.*, 2012, **41**, 5517-5525.
239. T. Herranz, S. Rojas, M. Ojeda, F. J. Pérez-Alonso, P. Terreros, K. Pirota and J. L. G. Fierro, *Chem. Mater.*, 2006, **18**, 2364-2375.
240. V. K. Mittal, S. Bera, R. Nithya, M. P. Srinivasan, S. Velmurugan and S. V. Narasimhan, *J. Nucl. Mater.*, 2004, **335**, 302-310.
241. B. Baruwati, R. K. Rana and S. V. Manorama, *J. Appl. Phys.*, 2007, **101**, 014302-014307.
242. J. M. D. Coey, *Magnetism and Magnetic Materials, 1st Ed.*, Cambridge University Press, New York, 2010.
243. W.-W. Wang, *Mater. Chem. Phys.*, 2008, **108**, 227-231.
244. B. Schrader, *Infrared and Raman Spectroscopy - Methods and Applications, 1st Ed.*, VCH, Weinheim, Germany, 1995.
245. S. Ayyappan, S. Mahadevan, P. Chandramohan, M. P. Srinivasan, J. Philip and B. Raj, *J. Phys. Chem. C*, 2010, **114**, 6334-6341.
246. P. Chandramohan, M. P. Srinivasan, S. Velmurugan and S. V. Narasimhan, *J. Solid State Chem.*, 2011, **184**, 89-96.
247. S. W. da Silva, R. C. Pedroza, P. P. C. Sartoratto, D. R. Rezende, S. N. A. V. da, M. A. G. Soler and P. C. Morais, *J. Non-Cryst. Solids*, 2006, **352**, 1602-1606.
248. R. Nongjai, S. Khan, K. Asokan, H. Ahmed and I. Khan, *J. Appl. Phys.*, 2012, **112**, 084321/084321-084321/084328.
249. A. V. Ravindra, P. Padhan and W. Prellier, *Appl. Phys. Lett.*, 2012, **101**, 161902/161901-161902/161904.
250. E. L. Uzunova, I. G. Mitov and D. G. Klissurski, *Bull. Chem. Soc. Jpn.*, 1997, **70**, 1985-1993.
251. T. F. Barth and E. Posnjak, *Z. Kristallogr. Krist.*, 1932, **82**, 325-341.
252. M. C. Blesa, U. Amador, E. Morán, N. Menéndez, J. D. Tornero and J. Rodríguez-Carvajal, *Solid State Ionics*, 1993, **63–65**, 429-436.
253. V. K. Mittal, P. Chandramohan, S. Bera, M. P. Srinivasan, S. Velmurugan and S. V. Narasimhan, *Solid State Commun.*, 2006, **137**, 6-10.
254. M. Gaudon, N. Pailhe, A. Wattiaux and A. Demourgues, *Mater. Res. Bull.*, 2009, **44**, 479-484.
255. V. G. Harris and N. C. Koon, *J. Appl. Phys.*, 1996, **79**, 4561.
256. V. Montoro, *Gazz. Chim. Ital.*, 1938, **68**, 728-733.
257. B. Zhang, G. Tang, Z. Yan, Z. Wang, Q. Yang and J. Cui, *J. Wuhan Univ. Technol., Mater. Sci. Ed.*, 2007, **22**, 514-517.
258. D. Varshney, K. Verma and A. Kumar, *Mater. Chem. Phys.*, 2011, **131**, 413-419.
259. Z. Z. Lazarevic, C. Jovalekic, A. Milutinovic, M. J. Romcevic and N. Z. Romcevic, *Acta Phys. Pol., A*, 2012, **121**, 682-686.
260. A. Kremnović, B. Antić, M. Vučinić-Vasić, P. Colomban, C. Jovalekić, N. Bibić, V. Kahlenberg and M. Leoni, *J. Appl. Cryst.*, 2010, **43**, 699-709.
261. R. W. Cairns and E. Ott, *J. Am. Chem. Soc.*, 1933, **55**, 527-533.
262. S. Gyergyek, M. Drofenik and D. Makovec, *Mater. Chem. Phys.*, 2012, **133**, 515-522.
263. V. Šepelák, S. Indris, P. Heitjans and K. D. Becker, *J. Alloy. Compd.*, 2007, **434-435**, 776-778.

264. C. N. Chinnasamy, A. Narayanasamy, N. Ponpandian, K. Chattopadhyay, K. Shinoda, B. Jeyadevan, K. Tohji, K. Nakatsuka, T. Furubayashi and I. Nakatani, *Phys. Rev. B: Condens. Matter Mater. Phys.*, 2001, **63**, 184108/184101-184108/184106.
265. A. Ahlawat and V. G. Sathe, *J. Raman Spectrosc.*, 2011, **42**, 1087-1094.
266. A. Ahlawat, V. G. Sathe, V. R. Reddy and A. Gupta, *J. Magn. Magn. Mater.*, 2011, **323**, 2049-2054.
267. L. Passerini, *Gazz. Chim. Ital.*, 1930, **60**, 389-399.
268. B. Domenichini, G. Pataut and S. Bourgeois, *Surf. Interface Anal.*, 2002, **34**, 540-544.
269. S. Bera, A. A. M. Prince, S. Velmurugan, P. S. Raghavan, R. Gopalan, G. Panneerselvam and S. V. Narasimhan, *J. Mater. Sci.*, 2001, **36**, 5379-5384.
270. J. Haetge, C. Suchomski and T. Brezesinski, *Inorg. Chem.*, 2010, **49**, 11619-11626.
271. T. Pannaparayil, S. Komarneni, R. Marande and M. Zadarko, *J. Appl. Phys.*, 1990, **67**, 5509-5511.
272. Z. Wang, D. Schiferl, Y. Zhao and H. S. C. O'Neill, *J. Phys. Chem. Solids*, 2003, **64**, 2517-2523.
273. O. Yamashita and T. Ikeda, *J. Appl. Phys.*, 2004, **95**, 1743-1748.
274. M. Yasumichi, *J. Solid State Chem.*, 1996, **126**, 227-234.
275. M. Kantserova and S. Orlik, *Kinetics and Catalysis*, 2007, **48**, 414-429.
276. G. M. Faulring, W. K. Zwicker and W. D. Forgeng, *Am. Min.*, 1960, **45**, 946-959.
277. V. K. Mittal, S. Bera, T. Saravanan, S. Sumathi, R. Krishnan, S. Rangarajan, S. Velmurugan and S. V. Narasimhan, *Thin Solid Films*, 2009, **517**, 1672-1676.
278. N. van Vegten, T. Baidya, F. Krumeich, W. Kleist and A. Baiker, *Appl. Catal. B-Environ.*, 2010, **97**, 398-406.
279. S. Gross, *Sol-gel synthesis of nanocomposite inorganic systems: clusters and thin films*, Università degli Studi di Padova - Ph.D. Thesis, Padova, Italy, 2001.
280. R. E. Dinnebier and S. J. R. Billinge, *Powder Diffraction - Theory and Practice*, Royal Society of Chemistry, Cambridge, 2008.
281. C. Giacovazzo, H. L. Monaco, D. Viterbo, F. Scordari, G. Gilli, G. Zanotti and M. Catti, *Fundamentals of Crystallography*, Oxford University Press Inc., New York, 2002.
282. G. Stout and L. H. Jensen, *X-Ray Structure Determination*, Macmillian Publishing Co. Inc., New York, 1968.
283. B. E. Warren, *X-Ray Diffraction*, Dover, Mineola, 1990.
284. C. Whiston, *X-Ray Methods*, J. Wiley & Sons, London, 1987.
285. M. M. Woolfson, *X-Ray Crystallography*, Cambridge University Press, J. W Arowsmith Ltd., Bristol, 1970.
286. Holger and Klein.
287. Louer, *DICVOL91*, (1992) University of Rennes.
288. L. Lutterotti, *MAUD Program*, (1998) Università degli Studi di Trento, Trento.
289. PANalytical, *X'Pert Highscore v.2.2b*, (2006).
290. Brüker, *Diffrac.Eva*.
291. Wavemetrics, *IGOR Pro*, (1988).
292. H. M. Rietveld, *J. Appl. Cryst.*, 1969, **2**, 65-71.
293. S. F. Gull and G. J. Daniell, *Nature*, 1978, **272**, 686-690.
294. L. Lutterotti, D. Chateigner, S. Ferrari and J. Ricote, *Thin Solid Films*, 2004, **450**, 34-41.
295. A. Einstein, *Ann. Phys*, 1905, **17**, 132-148.
296. H.T.I.S., *XPS_AES*, 4.7 edn., 2006.
297. R. H. W. Kwok, *XPSPEAK*, (1994) University of Hong Kong, Hong Kong.
298. V. Rusanov, V. Gushterov, S. Nikolov and A. X. Trautwein, *Hyperfine Interact.*, 2009, **191**, 67-74.
299. G. A. Sawatzky, d. W. F. Van and A. H. Morrish, *Phys. Rev.*, 1969, **187**, 747-757.
300. A. Vogel, *Vogel's Textbook of Quantitative Chemical Analysis, 5th Ed.*, Longman Group UK ltd., London, UK, 1989.
301. S. E. Manahan, *Quantitative chemical analysis*, Wadsworth Inc., Belmont, California, 1986.
302. Z. L. Wang, in *Characterization of Nanophase Materials, 1st Ed.*, Wiley-VCH, Weinheim, Germany, 2001, pp. 37-80.
303. R. Kleiner, D. Koelle, F. Ludwig and J. Clarke, *Proc. IEEE*, 2004, **92**, 1534-1548.
304. M. Newville, *Fundamentals of XAFS (Unpublished)*, University of Chicago, Chicago, IL, 2004.
305. M. Bauer and H. Bertagnolli, *Bunsen Magazin*, 2007, **9**, 216-231.
306. A. Kotani and S. Shin, *Rev. Mod. Phys.*, 2001, **73**, 203-246.
307. R. L. McCreery, *Raman Spectroscopy for Chemical Analysis*, John Wiley & Sons, New York, 2005.
308. *SDT Catalogue*, TA Instruments.
309. D. R. Lide, *Handbook of Chemistry and Physics, 84th Ed.*, CRC Press, 2004.
310. S.-D. Clas, C. R. Dalton and B. C. Hancock, *Pharm. Sci. Technol. Today*, 1999, **2**, 311-320.
311. M. J. Richardson, *Thermochim. Acta*, 1997, **300**, 15-28.

Appendix 1

This appendix reports the synthetic protocols for experiments that were not successful.

A1.1 Synthesis of barium ferrites

For the nonaqueous sol-gel synthesis of the spinel ferrite **$BaFe_2O_4$**, stoichiometric amounts of Fe^{II} acetylacetonate (254 mg, 1.00 mmol) and Ba acetate (128 mg, 0.50 mmol) were suspended in 5 ml benzyl alcohol under inert atmosphere in a glove box. The vial containing the suspension was sealed and placed in a microwave heater. The suspension was heated up to 180°C for 45 minutes. The resulting suspension was then isolated through centrifugation as described in the above section. The isolated solid was then dried in and oven at 60°C in open air for one hour and crushed into powder in an agate mortar.

A similar approach was utilised to attempt the synthesis of the perovskite ferrite **$BaFeO_3$**, using stoichiometric amounts of Fe^{II} acetylacetonate (128 mg, 0.50 mmol) and Ba acetate (130 mg, 0.50 mmol).

A similar approach required the use of a barium benzyl alkoxide solution in benzyl alcohol ($Ba_{(OBz)}$) in place of the barium acetate. This solution was obtained by placing 1411 mg (10,27 mmol) of metallic barium in 50 ml of benzyl alcohol and dissolving them by applying vigorous stirring at 60°C for three days.

Different syntheses were carried out by varying the net amount of precursor used, the nature of the iron precursor, the reported temperature and the time the system was kept at said temperature and the presence or absence of water (2 drops) in the system as reported in Tables A1.1.1 and A1.1.2.

Experiment	Reagent1	Quantity/mmol	Reagent2	Quantity/mmol	Temperature/°C	Treatment Time/min	H_2O
S-Ba018 - 1	Fe^{III}acac	1.00	Ba(OAc)2	0.50	180	15	No
S-Ba018 - 2	Fe^{III}acac	1.00	Ba(OAc)2	0.50	180	45	No
S-Ba018 - 3	Fe^{III}acac	1.00	Ba(OAc)2	0.50	200	15	No
S-Ba018 - 4	Fe^{III}acac	1.00	Ba(OAc)2	0.50	200	45	No
S-Ba019 - 1	Fe^{II}acac	1.00	Ba(OAc)2	0.51	180	15	No
S-Ba019 - 2	Fe^{II}acac	1.01	Ba(OAc)2	0.50	180	45	No
S-Ba019 - 3	Fe^{II}acac	1.00	Ba(OAc)2	0.50	200	15	No
S-Ba019 - 4	Fe^{II}acac	1.00	Ba(OAc)2	0.51	200	45	No
S-Ba020 - 1	Fe^{II}OAc	1.00	Ba(OAc)2	0.50	180	15	No
S-Ba020 - 2	Fe^{II}OAc	1.00	Ba(OAc)2	0.50	180	45	No
S-Ba020 - 3	Fe^{II}OAc	1.00	Ba(OAc)2	0.50	200	15	No
S-Ba020 - 4	Fe^{II}OAc	1.00	Ba(OAc)2	0.50	200	45	No
S-Ba026 - 1	Fe^{III}acac	1.00	$Ba_{(OBz)}$	0.50	180	15	No
S-Ba026 - 2	Fe^{III}acac	1.00	$Ba_{(OBz)}$	0.50	180	45	No
S-Ba026 - 3	Fe^{III}acac	1.00	$Ba_{(OBz)}$	0.50	200	15	No
S-Ba026 - 4	Fe^{III}acac	1.00	$Ba_{(OBz)}$	0.50	200	45	No
S-Ba026 - 5	Fe^{III}acac	1.00	$Ba_{(OBz)}$	0.50	180	15	Yes
S-Ba026 - 6	Fe^{III}acac	1.00	$Ba_{(OBz)}$	0.50	180	45	Yes
S-Ba026 - 7	Fe^{III}acac	1.00	$Ba_{(OBz)}$	0.50	200	15	Yes
S-Ba026 - 8	Fe^{III}acac	1.00	$Ba_{(OBz)}$	0.50	200	45	Yes
S-Ba027 - 1	Fe^{II}OAc	1.00	$Ba_{(OBz)}$	0.50	200	45	No
S-Ba027 - 2	Fe^{II}OAc	1.00	$Ba_{(OBz)}$	0.50	200	45	Yes
S-Ba027 - 3	Fe^{II}OAc	1.00	$Ba_{(OBz)}$	0.50	200	45	No
S-Ba027 - 4	Fe^{II}OAc	1.00	$Ba_{(OBz)}$	0.50	200	45	Yes
S-Ba028 - 1	Fe^{II}acac	1.00	$Ba_{(OBz)}$	0.50	200	45	No
S-Ba028 - 2	Fe^{II}acac	1.00	$Ba_{(OBz)}$	0.50	200	45	Yes

Table A1.1.1 - *Experimental parameters for the nonaqueous sol-gel syntheses of barium spinel ferrites*

Experiment	Reagent1	Quantity/mmol	Reagent2	Quantity/mmol	Temperature/°C	Treatment Time/min	H_2O
S-Ba021 - 1	Fe^{III}acac	0.50	Ba(OAc)2	0.50	180	15	No
S-Ba021 - 2	Fe^{III}acac	0.50	Ba(OAc)2	0.50	180	45	No
S-Ba021 - 3	Fe^{III}acac	0.50	Ba(OAc)2	0.50	200	15	No
S-Ba021 - 4	Fe^{III}acac	0.50	Ba(OAc)2	0.50	200	45	No
S-Ba022 - 1	Fe^{II}acac	0.50	Ba(OAc)2	0.50	180	15	No
S-Ba022 - 2	Fe^{II}acac	0.50	Ba(OAc)2	0.50	180	45	No
S-Ba022 - 3	Fe^{II}acac	0.50	Ba(OAc)2	0.50	200	15	No
S-Ba022 - 4	Fe^{II}acac	0.50	Ba(OAc)2	0.50	200	45	No
S-Ba022 - 5	Fe^{II}acac	1.01	Ba(OAc)2	1.00	200	15	No
S-Ba022 - 6	Fe^{II}acac	1.00	Ba(OAc)2	1.00	200	45	No
S-Ba023 - 1	Fe^{II}OAc	0.50	Ba(OAc)2	0.50	180	15	No
S-Ba023 - 2	Fe^{II}OAc	0.50	Ba(OAc)2	0.50	180	45	No
S-Ba023 - 3	Fe^{II}OAc	0.50	Ba(OAc)2	0.50	200	15	No
S-Ba023 - 4	Fe^{II}OAc	0.50	Ba(OAc)2	0.50	200	45	No
S-Ba028 - 3	Fe^{II}acac	0.50	$Ba_{(OBz)}$	0.50	200	45	No
S-Ba028 - 4	Fe^{II}acac	0.50	$Ba_{(OBz)}$	0.50	200	45	Yes

Table A1.1.2 - *Experimental parameters for the nonaqueous sol-gel syntheses of barium perovskite ferrites*

The coprecipitation of oxalates method was used to attempt the synthesis of these compounds, but was unsuccessful both in the case of **$BaFeO_3$** and **$BaFe_2O_4$**, as all isolated powders presented a multitude of crystalline phases. The different synthetic parameters employed are summarised in table A1.1.3.

Sample	Fe/M/acid nominal molar ratio	TENOH/ml	Basification protocol	Calcination temperature (protocol number)
Ba001	1/1/3	2	A	900°C (6)
Ba002	2/1/4.5	2	A	900°C (6)
Ba003	1/1/3	2	A	900°C (6)
Ba004	1/1/3	2	B	900°C (6)
Ba005-a	2/1/4.5	2	B	900°C (6)
Ba005-b	2/1/4.5	2	B	1100°C (7)
Ba006-a	2/1/4.5	2	A	600°C (2)
Ba006-b	2/1/4.5	2	A	400°C (1)
Ba007	1/1/3	2	A	600°C (2)

Table A1.1.3 - *Experimental parameters for the syntheses of barium ferrites via coprecipitation of oxalates*

A1.2 - Syntheses of calcium ferrites

Similarly to magnesium ferrites (see Par. 5.6), no syntheses for were carried out for **$CaFeO_3$** and **$CaFe_2O_4$** via nonaqueous sol-gel route, as attempts to prepare a suitable calcium precursor were unsuccessful. As before, reacting the metal with benzyl alcohol in order to produce a metal benzyl alkoxide solution, produced only turbid solutions (thus with unknown concentration) which were therefore useless.

The coprecipitation of oxalates method was used to attempt the synthesis of these compounds, but like in the case of barium, was unsuccessful both in the case of **$CaFeO_3$** and **$CaFe_2O_4$**: all products obtained consisted of multiple of crystalline phases. The different synthetic parameters employed are summarised in table A1.2.3.

Sample	Fe/M/acid nominal molar ratio	TENOH/ml	Basification protocol	Calcination temperature (protocol number)
Ca001	1/1/3	2	A	900°C (6)
Ca002	2/1/4.5	2	A	900°C (6)
Ca003	1/1/3	2	B	900°C (6)
Ca004-a	2/1/4.5	2	B	900°C (6)
Ca004-b	2/1/4.5	2	B	1100°C (7)
Ca005-a	2/1/4.5	2	A	600°C (2)
Ca005-b	2/1/4.5	2	A	400°C (1)
Ca006	1/1/3	2	A	600°C (2)

Table A1.2.3 - *Experimental parameters for the syntheses of calcium ferrites via coprecipitation of oxalates*

Appendix 2

This appendix reports the XRD graphs relative to unsuccessful synthetic attempts.

A2.1 - Barium ferrite

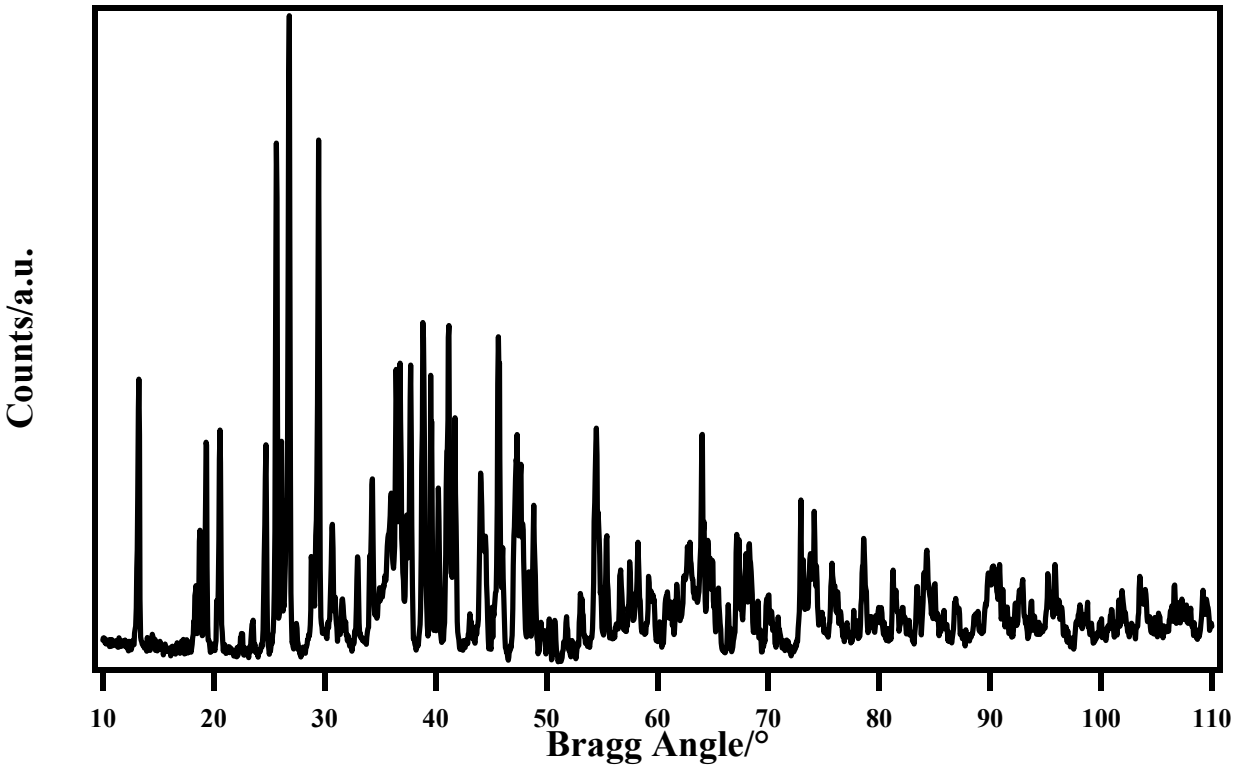

Figure A2.1.1 - *XRD pattern for sample S-Ba018-4*

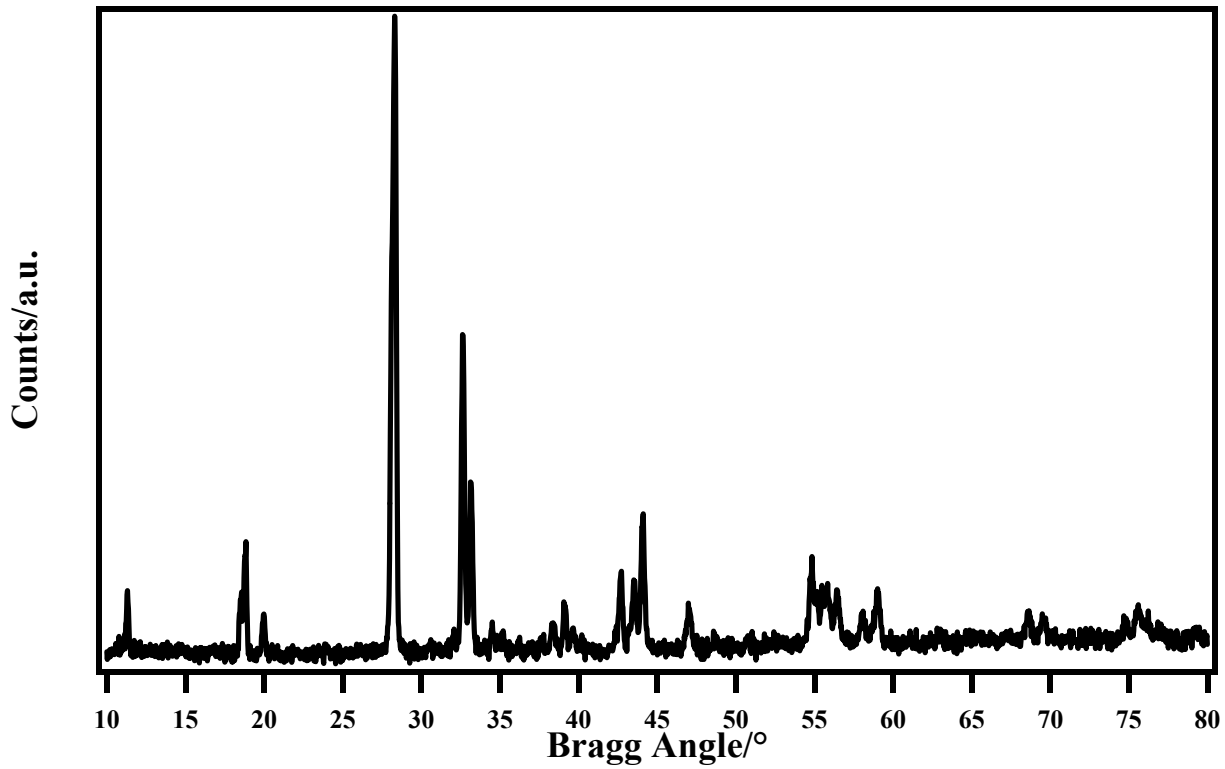

Figure A2.1.2 - *XRD pattern for sample Ba002*

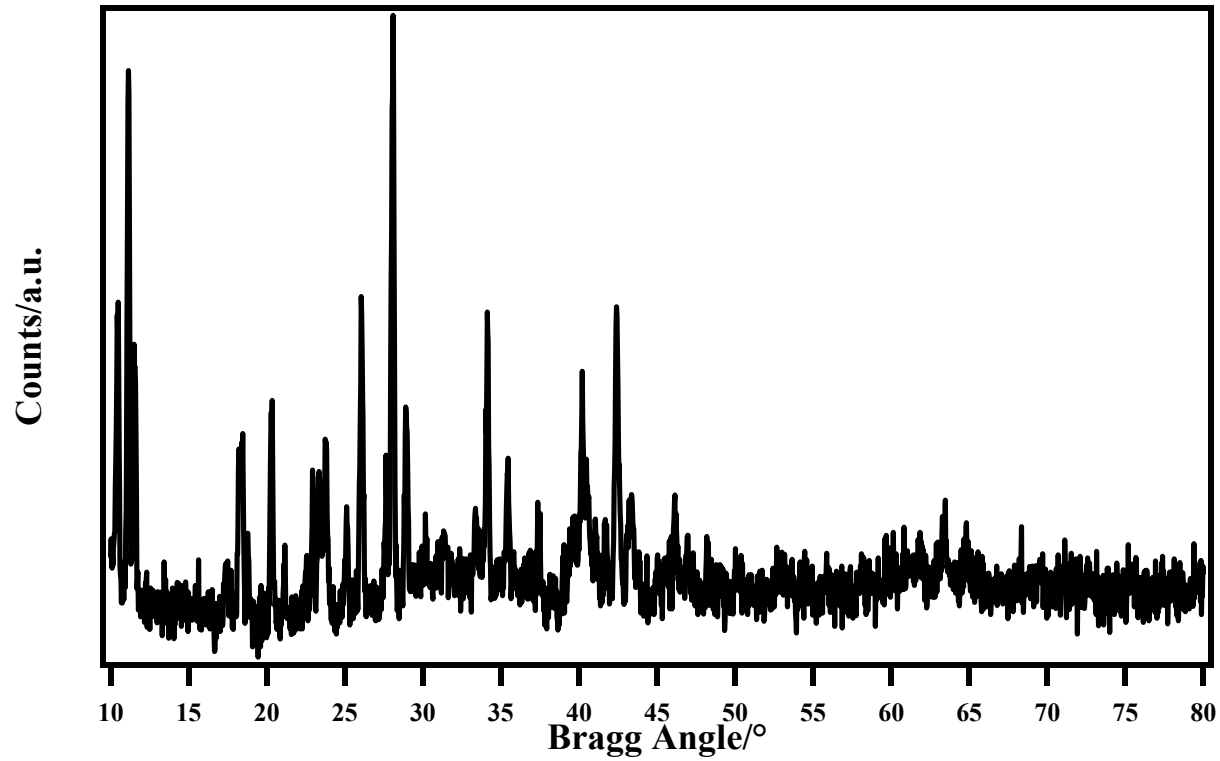

Figure A2.1.2 - *XRD pattern for sample I-Ba002*

A2.2 - Calcium ferrite

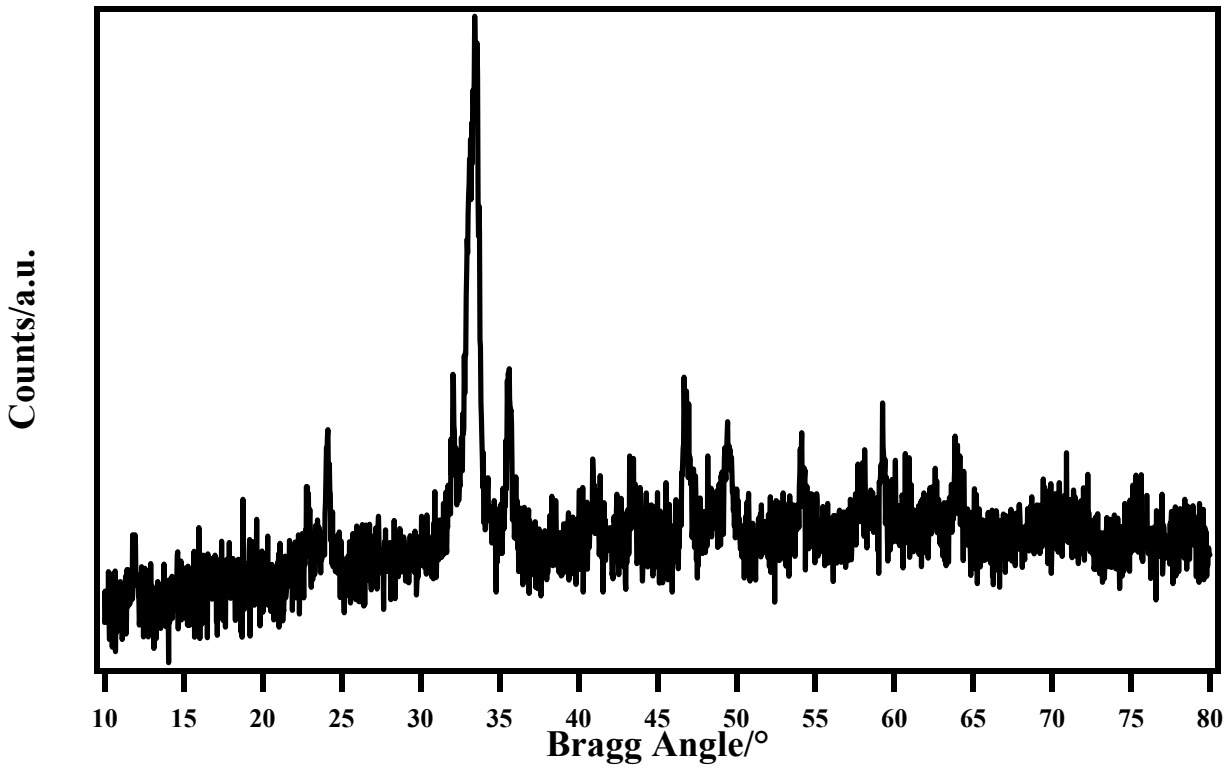

Figure A2.2.1 - *XRD pattern for sample Ca005-a*

A2.3 - Magnesium ferrite

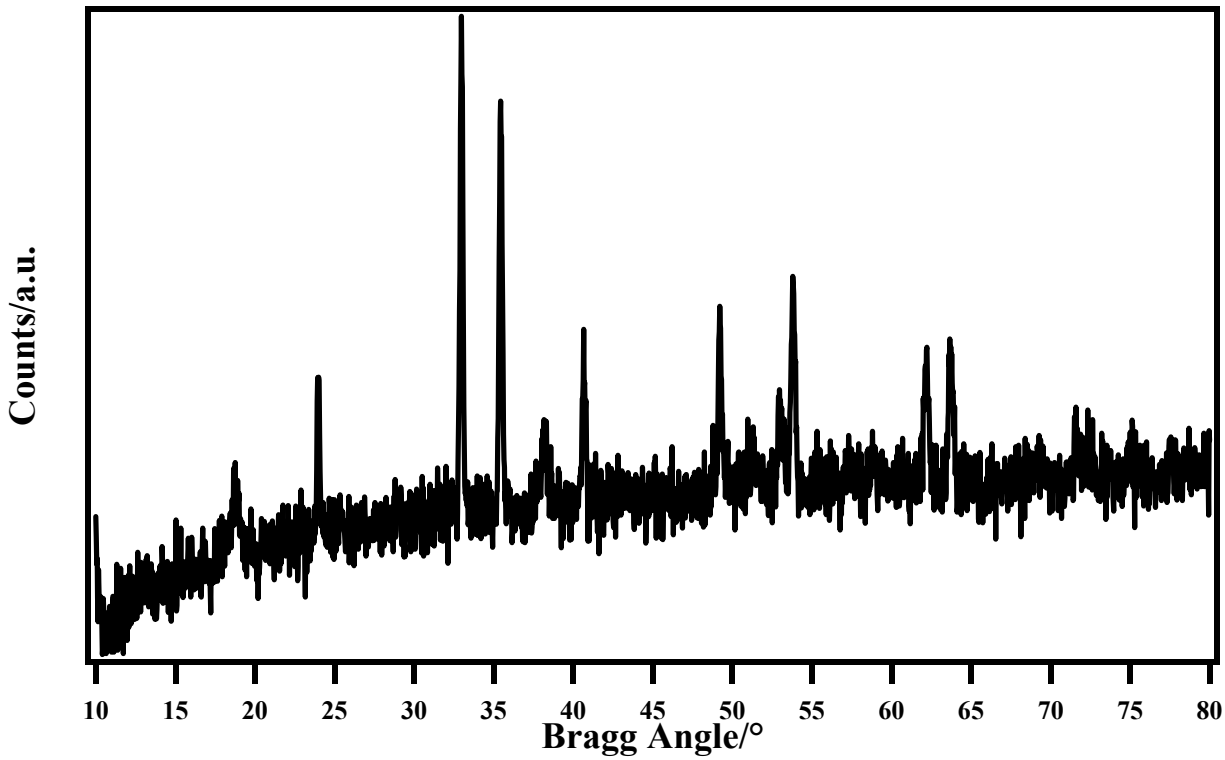

Figure A2.3.1 - *XRD pattern for sample I-Mg004*

A2.4 - Strontium ferrite

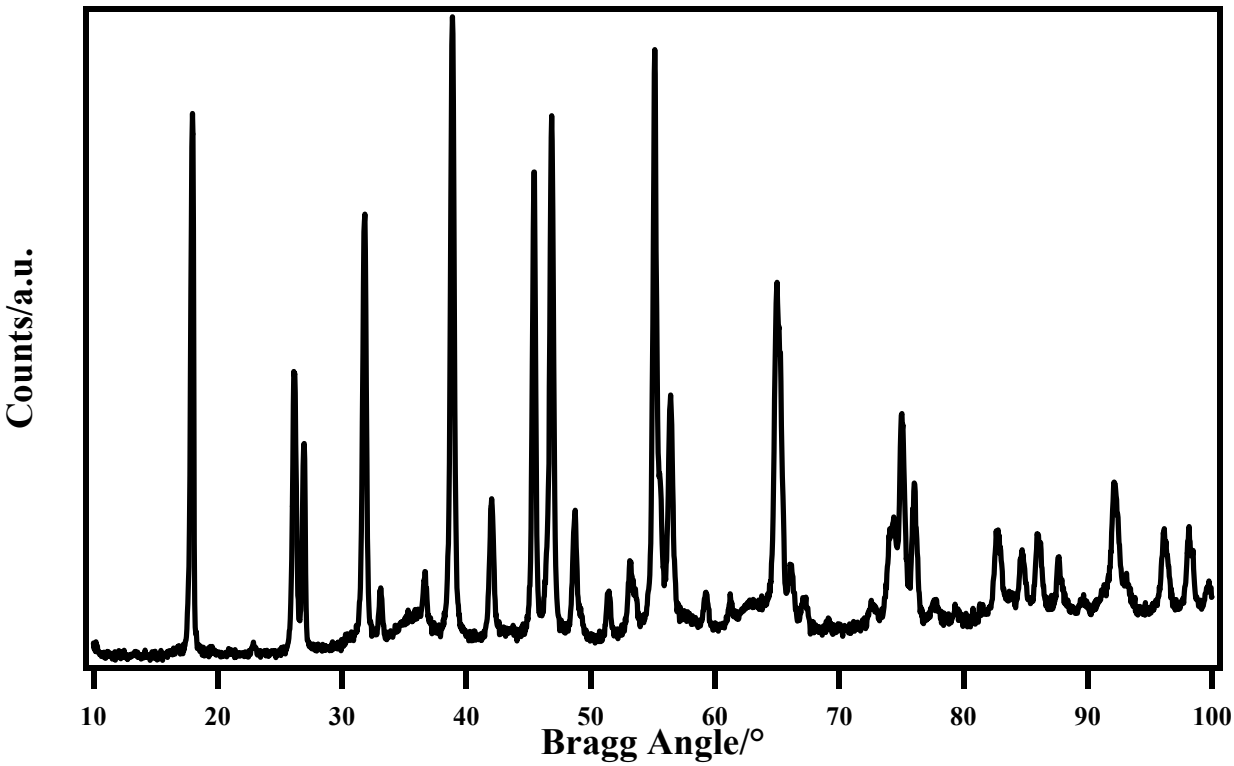

Figure A2.4.1 - *XRD pattern for sample S-Sr035-4*

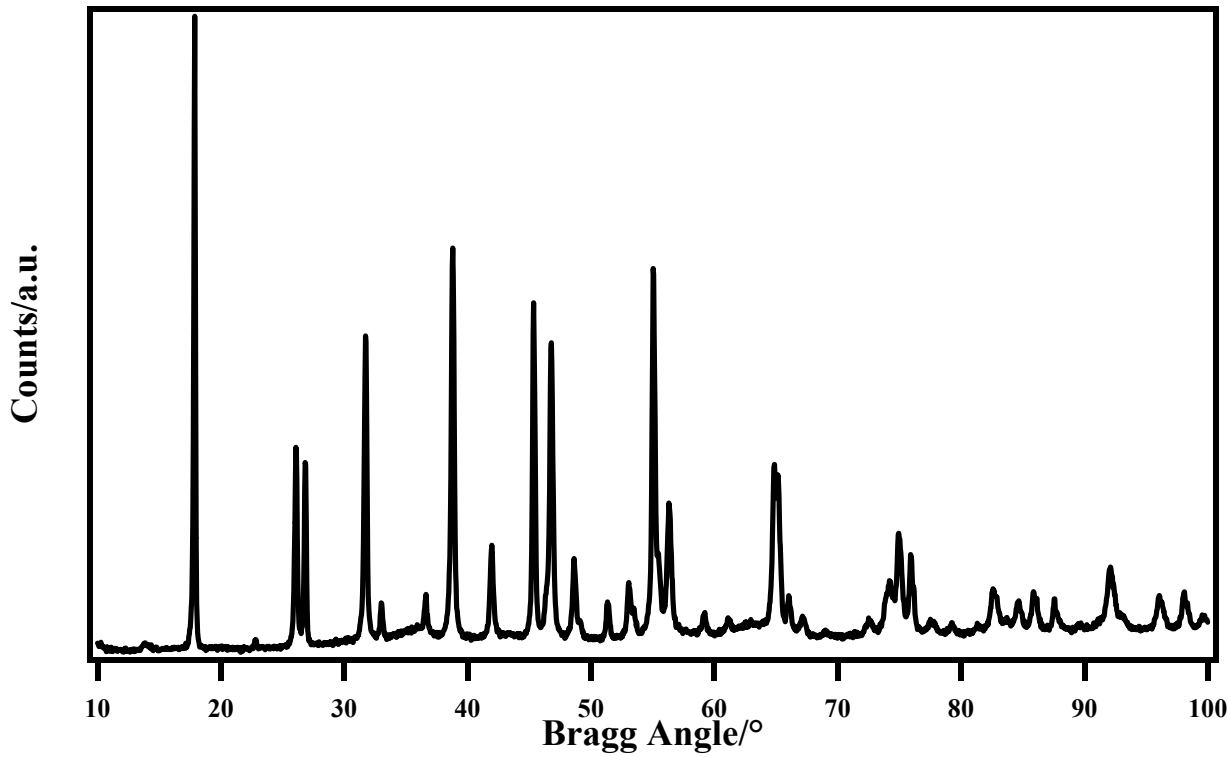

Figure A2.4.2 - *XRD pattern for sample S-Sr036-4*

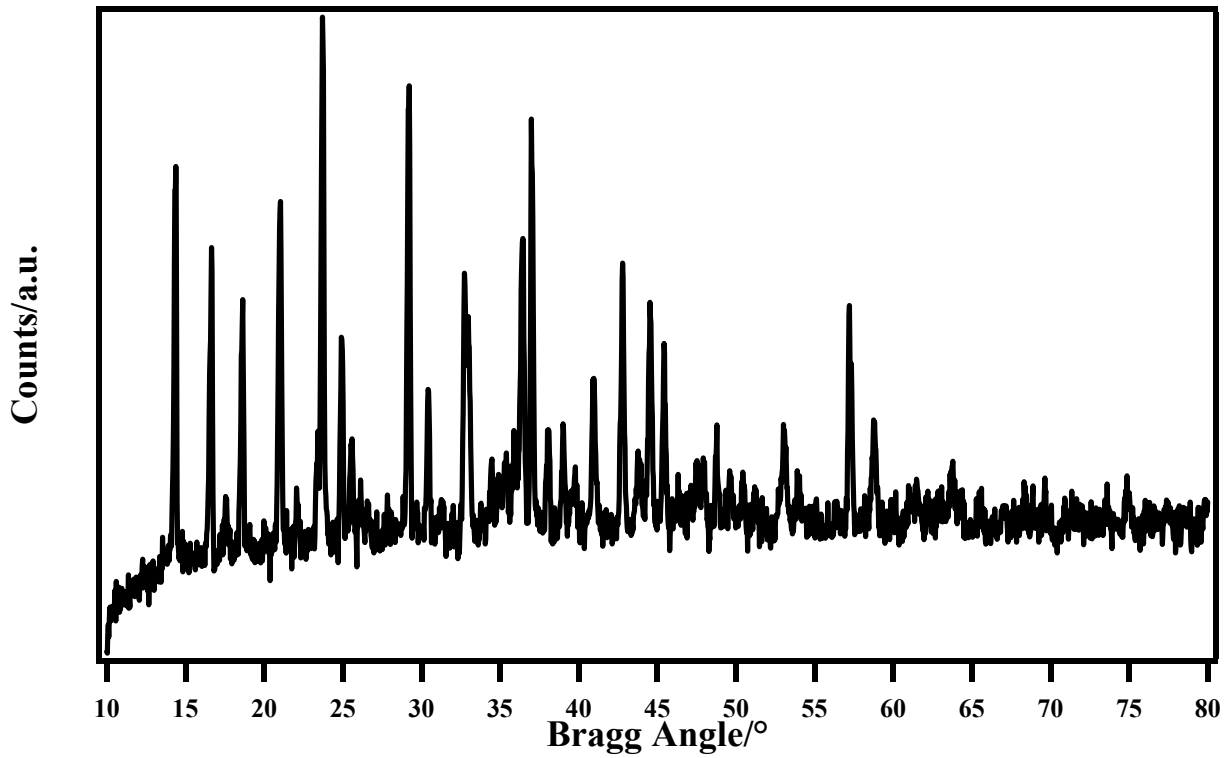

Figure A2.4.3 - *XRD pattern for sample I-Sr001*

ISI publications

Highly crystalline strontium ferrites $SrFeO_{3-\delta}$: an easy and effective wet-chemistry synthesis
S. Diodati; L. Nodari; M.M. Natile; U. Russo; E. Tondello; L. Lutterotti; S. Gross
Dalton Trans. 2012, **41**, 5517-5525

Green, unprecedented, low temperature hydrothermal assisted synthesis of nanocrystalline transition metal ferrites
S. Diodati; L. Pandolfo; S. Gialanella; S. Gross
Paper in preparation

Inorganic chemistry in a nanoreactor: doped ZnO nanostructures by miniemulsion
P. Dolcet; F. Latini; M. Casarin; A. Speghini; E. Tondello; C. Foss; S. Diodati; L. Verin; A. Motta; S. Gross
Accepted by Eur. J. Inorg. Chem. DOI: 10.1002/ejic.201201474

Transition metal iron ferrites investigated by XPS
S. Diodati; S. Gross
Submitted to Surface Science Spectra

Divalent metal ferrites, a RIXS investigation
S. Diodati; M. Bauer; S. Gross
Paper in preparation

Nanosized ferrites: an easy and effective wet-chemistry synthesis
S. Diodati; L. Nodari; M.M. Natile; A. Caneschi; C. Hoffmann; S. Kaskel; V. di Noto; A. Lieb; S. Mascotto; S. Gross
Paper in preparation

Effective stoichiometric control by wet synthesis of mixed ferrites
S. Diodati; L. Nodari; V. Di Noto; S. Gross
Paper in preparation

Acknowledgements

I must gratefully thank my mentor Dr. Silvia Gross (ISTM-CNR, Dip. Scienze Chimiche, Università degli Studi di Padova) for her support during the entirety of my studenthood (and Ph.D.) and for giving me the opportunity to undertake this Ph.D.

Scuola di Dottorato in Scienze Molecolari (Dip. Scienze Chimiche, Università degli Studi di Padova) is thanked for financial support.

Most sincere thank go to Prof. Markus Niederberger (ETH Zürich) for letting me stay in his work group for the majority of the first year of my Ph.D. and for his enlightening inputs to my research. Also, thanks go to all members in his workgroup for the assistance and friendship they extended to me. Particular thanks go to Dr. Idalia Bilecka who supervised my work during my stay and taught me the nonaqueous sol-gel synthetic approach, Dr. Florian Heiligtag who performed TEM measurements and especially Rafael Da Silva and Rafael Libanori who gave me a place to stay when I was homeless.

I also want to express my gratitude to all the people from the University of Padova who contributed to this work by carrying out analyses on my samples and data interpretation. In particular, Dr. Luca Nodari who carried Mössbauer spectroscopy measurements and data interpretation, Dr. Marta Maria "Mara" Natile who performed TPR analyses, Prof. Vito Di Noto (and his whole work group) who carried ICP-AES analyses and BES measurements and Dr. Roberta Saini who performed TGA-DSC measurements.

Grateful thanks also go to all the people from outside this institute who contributed data to this work. In particular, Prof. Andrea Caneschi and Dr. César de Julián Fernández (Università degli Studi di Firenze) are gratefully thanked for SQUID measurements and data interpretation, Dr. Simone Mascotto (Università degli Studi di Trento) is thanked for sample calcination, Dr. Alexandra Lieb (OGVU, Magdeburg) is thanked for TPXRD measurements, Prof. Stefan Kaskel and Claudia Hoffman (TU Dresden) are thanked for CH_4-TPO measurements, Prof. Urška Lavrenčič Štangar and Dr. Fernando Fresno García (University of Nova Gorica) are gratefully thanked for conducting photocatalytic tests on my compounds (results pending), Prof. Matthias Bauer (TU Kaiserslautern) is thanked for EXAFS measurements, Prof. Stefano Gialanella (Università degli Studi di Trento) is thanked for his help on TEM theory and, last but most definitely not least, Dr. Gloria Ischia (Università degli Studi di Trento) is also thanked for TEM measurements.

Prof. Luciano Pandolfo (Dip. Scienze Chimiche, Università degli Studi di Padova) is gratefully thanked for his useful suggestions and insights on hydrothermal synthesis.

A special mention goes to my master thesis supervisor, Prof. Eugenio Tondello (Dip. Scienze Chimiche; Università degli Studi di Padova), who is gratefully thanked for his support.

Finally, Deutsces Electronen-Syncrotron (DESY) is thanked for financially supporting my beamtime period and stay at Hamburg